Dietmar Haba

Toughening of epoxy with WS_2 nanoparticles

PhD Thesis

MONTAN UNIVERSITÄT
WWW.UNILEOBEN.AC.AT

Empa
Materials Science and Technology

Toughening of epoxy with WS_2 nanoparticles

A Thesis
in Polymer Engineering and Science

presented to the Department Polymer Engineering and Science
of the Montanuniversitaet Leoben
in partial fulfillment of the requirements for the degree of
Doctor of Montanist Sciences (Dr. mont.)

by Dietmar Haba

September 2016

This cumulative dissertation is authored by

Dipl.-Ing. Dietmar Haba

born July 6th 1987

in Steyr, Austria

Submitted to

Chair of Materials Science and Testing of Polymers

Department Polymer Engineering and Science

Montanunitversitaet Leoben, Austria

Conducted at

Empa – Swiss Federal Laboratories for Materials Science and Technology

Laboratory Mechanical Systems Engineering

Dübendorf, Switzerland

Academic Supervisor

Univ.-Prof. Dipl.-Ing. Dr.mont. Gerald Pinter

Professor for Materials Science and Testing of Polymers

Affidavit

I declare in lieu of oath that I wrote this thesis and performed the associated research myself, using only literature cited therein.

Dietmar Haba
Zürich, September 2016

"The duty of the man who investigates the writings of scientists, if learning the truth is his goal, is to make himself an enemy of all that he reads, and ... attack it from every side. He should also suspect himself as he performs his critical examination of it, so that he may avoid falling into either prejudice or leniency."

– Alhazen, approx. 1000 AD

– I dedicate this work to my future children. –

Preamble

Acknowledgement

I want to express my gratitude to all persons who supported my work while performing this thesis.

First and foremost I want to thank my internal supervisors at Empa, Dr. Andreas J. Brunner and Dr. Michel Barbezat. They always had open ears and were generally great advisers. Moreover, I always felt that finding the scientific truth and helping me in creating a good thesis was more important to them than just putting their names on author lists.

Secondly, I want to thank my supervising professors, Prof. Gerald Pinter and Prof. Christian Teichert. They as well are mostly interested in good scientific work and collaboration, not simply in their personal benefit.

I want to thank my other co-authors, Dr. Katharina Resch, Dr. Josef Kaufmann, Prof. Thomas Griesser, Dr. Ulrich Müller, Dr. Santhosh Ayalur-Karunakaran, Dr. Sandra Schlögl and Dr. Andreas Hausberger for their support.

I highly acknowledge the support of several colleagues that helped me in everyday laboratory work, in particular that of Marcel Rees, Anja Huch, Beatrice Fischer, Dr. Arndt Remhof and Dr. Lassi J. Karvonen. Likewise, I want to thank my colleagues from the laboratory for Mechanical Systems Engineering at Empa for the pleasant social atmosphere.

I want to thank my partner Katharina who supported me all the time during this work and who gave me hope when I needed it most. I want to thank both my family and hers for their great support. I thank my friends for helping me to distracting myself, it particular Zuzana, Lukas, Mandy and Felix. I also want to thanks my Bundesbrüder who paved my way towards where I am today, in particular Robert, Wolfgang, Andreas and Thomas.

Finally, I want to thank the peoples of Austria and Switzerland for financing my education and my scientific work with their taxes. I hope that I could fulfill their expectations and that I will be able to finance young talents as well.

Abstract

This Thesis deals with the toughening effect of tungsten disulfide (WS_2) nanoparticles (NPs) on epoxy, in particular that of inorganic, fullerene-like WS_2 (IF-WS_2) NPs. IF-WS_2 was treated with three different chemical modifiers, two of which functionalized the NPs successfully. When the NPs were dispersed within ethanol by sonication, the surface functionalization significantly deteriorated the dispersion quality. The final agglomerate size of 200 nm is obtained after 10 min of sonication. The primary particle size is significantly smaller (approx. 100 nm), but aggregation seems to limit the dispersibility. Sonication is ineffective in dispersing the NPs within an epoxy resin, while three-roll milling gives good and well reproducible dispersion quality. Flaky WS_2 exhibits larger agglomerate sizes than IF-WS_2, but improves the fracture toughness more effectively.

The elastic modulus distribution in epoxy can be measured with a novel atomic force microscopy (AFM) technology, provided that the investigated surface is smooth enough. Reported *nodules* are likely AFM artifacts caused by too rough surfaces. It is unlikely that epoxy has modulus inhomogeneities that differ by more than 150 MPa from the bulk modulus and that are larger than 10 nm in size. The epoxy's modulus in the vicinity of IF-WS_2 NPs does not seem to differ from its bulk modulus.

The addition of either kind of WS_2 NPs considerably improves the fracture toughness of certain epoxy systems, but other epoxy systems are hardly affected by them or even embrittle. The NP surface functionalization does not seem to improve the dispersion quality nor the toughening effect. IF-WS_2 leads to the formation of secondary cracks, which create additional fracture surface. This might be an important toughening mechanism. However, the fracture surface increases even if the toughening effect of the NPs is negative, so that more complex mechanisms are more likely.

The two major factors determining the toughening effect are the type of curing agent and its quantity. If only polyetheramine-cured epoxy systems are concerned, the toughening effect tends to be higher for sub-stoichiometric epoxy systems, but the same is not true for some other curing agent types. It is unlikely that this is due to the resulting higher fraction of molecular network defects. For a given epoxy system, IF-WS_2 NPs do not seem to differ significantly from other kinds of NPs with respect to their toughening effect.

Zusammenfassung

Diese Arbeit beschäftigt sich mit dem Zähigkeits-Erhöhungseffekt von Wolframdisulfid (WS_2) Nanopartikeln (NP) in Epoxid, insbesondere dem von anorganischen, fullerenartigen WS_2 (IF-WS_2) NP. IF-WS_2 wurde mit drei verschiedenen chemischen Modifikatoren behandelt, wovon zwei die NP erfolgreich funktionalisierten. Wenn die NP mittels Ultraschallbeschallung in Ethanol dispergiert wurden, verschlechterte die Funktionalisierung die Dispersionsqualität deutlich. Die Endgröße der Agglomerate von 200 nm wird nach 10 min Ultraschallbehandlung erreicht. Die Primärpartikelgröße ist deutlich kleiner (ca. 100 nm), aber Aggregate scheinen die Dispergierbarkeit zu beschränken. Ultraschall ist nicht effektiv darin, die NP im Epoxidharz zu dispergieren, während Dispergierung im Dreiwalzenstuhl gute und gut reproduzierbare Dispersionsqualität liefert. Plättchenförmiges WS_2 bildet größere Agglomerate als IF-WS_2, verbessert die Bruchzähigkeit aber effektiver.

Die Elastizitätsmodulverteilung im Epoxid kann mit einer neuen Rasterkraftmikroskopietechnik gemessen werden, falls die untersuchte Oberfläche glatt genug ist. Anderswo beobachtete *nodulare Strukturen* sind wahrscheinlich Artefakte der Rasterkraftmikroskopie aufgrund zu rauher Oberflächen. Es ist unwahrscheinlich, dass Epoxid Modulinhomogenitäten aufweist, die um mehr als 150 MPa vom Modul der Masse abwei-

chen und die mehr als 10 nm groß sind. Der Modul des Epoxids in der Nähe der IF-WS_2 NP scheint sich nicht vom Modul seiner Masse zu unterscheiden.

Die Zugabe jedweder Art von WS_2 NP verbesserte die Bruchzähigkeit bestimmter Epoxidsysteme beträchtlich, aber andere Epoxidsysteme werden kaum von ihnen beeinflusst oder verspröden sogar. Die NP-Oberflächenfunktionalisierung scheint weder die Dispersionsqualität noch den Zähigkeits-Erhöhungseffekt nicht zu verbessern. IF-WS_2 führt zur Bildung von Sekundärbrüchen, die zusätzliche Bruchfläche erzeugen. Dies könnte ein wichtiger Zähigkeits-Erhöhungsmechanismus sein. Allerdings vergrößert sich die Bruchfläche selbst dann, wenn die NP das Material verspröden, sodass komplexere Mechanismen wahrscheinlicher sind.

Die zwei Hauptfaktoren, die den Zähigkkeitsanstieg bestimmen, sind die Art und die Menge des Härters. Solange nur Polyetheramin-gehärtete Epoxidsysteme betrachtet werden, ist der Zähigkeitsanstieg bei substöchiometrischen Epoxidsystemen tendenziell höher, doch das ist bei manchen anderen Härtertypen nicht der Fall. Es ist unwahrscheinlich, dass der Grund dafür der verursachte höhere Anteil an molekularen Fehlstellen ist. Für ein gegebenes Epoxidsystem scheinen sich IF-WS_2 NP in ihrem Zähigkeitserhöhungseffekt nicht deutlich von anderen Arten von NP zu unterscheiden.

Conventions followed throughout this Thesis

This Thesis follows in all respects the 8th edition of *The International System of Units* (SI) as published by the *International Bureau of Weights and Measures* (French: *Bureau International des Poids et Measures*, BIPM). It also follows the standards published by the International Organization for Standardization (ISO), whenever applicable.

SI units and chemical symbols are never defined throughout the Thesis. Chemical symbols and formulas like WS_2 or EtOH are written in a different font type in order to facilitate their discrimination from other acronyms.

Measurement uncertainties are given by adding the standard deviation of the results of a measurement series after their mean and a plus-minus sign. In a few cases, the standard deviation was instead given in brackets after the mean. For instance, the result of a measurement series with a mean of 176.4 and a standard deviation of 32.0 is given either as 176.4 ± 32.0 or as 176.4(320).

The term *room temperature* stands for a temperature in the range of 18 °C to 25 °C. Whenever the temperature of a process is unmentioned, it took place at room temperature. Mechanical tests took always place at a nominal temperature of 23 °C and a relative humidity of 50 % as required by ISO 291.

Several technical terms in this Thesis are often used somewhat interexchangeably both in the related literature and in industry. In order to avoid confusion, some of these are defined here. The terms *thermoset, thermosetting polymer, epoxy, epoxy resin, epoxy system, epoxide* and *DGEBA* are defined in section 1.2.1. The term *cross-link* is explained in section 1.2.2. The terms *nanoparticles, nanocomposites* and *master batch* are described in section 1.3.

Contents

1 Introduction

1.1 Motivation

Global climate change is potentially one of the biggest issues for the future of humanity. In 2015, the General Assembly of the United Nations declared *Urgent actions to combat climate change and its impacts* to be one of its 17 *Sustainable Development Goals* [1]. It is currently believed that human energy consumption is at least one of the dominant factors causing climate change, mainly by increasing the atmospheric CO_2 concentration [2]. Reducing energy consumption is thus of highest priority.

Transportation stays among the most energy-consumptive sectors of human technology: In 2012, 26 % of the energy consumption in the European Union was due to road transportation and further 6 % due to other types of transportation [3]. Likewise, 28 % of the energy consumed in the United States of America in 2014 was used for transportation [4]. These figures vary little over time.

Reducing the weight of means of transportation is a very effective way to improve their energy efficiency, which is in particular true for aircraft: As a rule of thumb, a 1 % reduction in an airplane's weight results in a 0.75 % to 1 % reduction in its energy consumption [5]. Fiber-reinforced polymers (FRPs) are a very effective way to reduce the weight of means of transportation. In particular C-fiber-reinforced polymers (CFRPs) possess high specific strength and

modulus and can thus greatly reduce the mass of material necessary. Consequently, aeronautics industry is steadily increasing the planes' CFRP percentage, with the current leader being the recently introduced *Airbus A350 XWB*, which consists by 53 % by mass of CFRP. As a result, this airplane consumes 25 % less energy compared to its current long-range competitors that use Al alloys [6, 7].

The use of FRPs is strongly increasing in the automotive industry as well. CFRPs has been used for the chassis of racing and high-end cars for decades, but recently also finds application in mass-produced cars: The German automobile manufacturing company *BMW* was the first to launch a volume production vehicle on the market, featuring CFRPs for the passenger compartment of their model *i3* [8, 9]. In fact, the automotive industry is seen by some as the CFRP market with the most growth potential, with a predicted annual growth rate of approx. 34 % [9].

Of course, there are also plenty of applications of FRPs besides the automotive and aerospace industry, for example in the civil engineering sector or in the sports industry. Many of these applications are safety-relevant and thus require high confidence in a material's reliability. FRPs have good tensile strength in the dimension of the fiber direction, but their compressive and shear strength are weak points. The strong fibers take only a certain fraction of the forces in these cases while most of the force has to be taken by the rather weak polymer matrix. The frequent bending loads express themselves as a combination of tensile stresses and compressive stresses, so that compressive stresses are hard to avoid. Hence, the polymer matrix will have to withstand stresses in most applications.

Currently, the matrix materials of high-quality FRPs are predominantly thermosetting polymers, although thermoplastic matrix materials are increasing in importance. For higher-quality applications, especially for CFRPs, epoxy is the usual choice. Epoxy has a series of good properties, especially

when compared with other polymers, but like most thermosetting polymers, it is very brittle. This low fracture toughness is the epoxy's major weakness and limits its use for many applications. The toughening of epoxy is therefore key to future development of FRP applications and as a consequence for the future of human mobility.

1.1.1 Epoxy as a material for the future

In 1872, Baeyer [10] formed the basis for the later development of the first fully synthetic plastics by Baekeland three decades later [11]. These phenolic resins are thermosetting polymers that cure in a polycondensation reaction, releasing H_2O. Condensation products like these are usually unwanted as they can cause voids, act as plasticizers and result in cure shrinkage. Phenolic resins are still used today in various applications, but they have been mostly replaced by other thermosetting polymers by now. The need for thermosetting polymers that cure without any condensation products and with low cure shrinkage lead to the invention of epoxy resins by Schlack [12] and Castan [13] in the 1930s.

Epoxy industry began to evolve after World War II, focusing mainly on the use for coatings. In the 1970s and 1980s, the use of epoxies for fiber-reinforced polymers (FRPs) became another important industrial sector. The versatility of epoxy allowed industrial companies to modify its properties in order to fit various different applications, e.g., increased high-temperature resistivity, improved weathering characteristics, flame retardancy, toxicologic harmlessness, enhanced resistance to hard-to-hold corrosive chemicals, moisture resistance, purity, enhanced processibility, and many more. [14]

Epoxy stands out from the entirety of polymers in a series of properties, namely its [14]

- excellent mechanical properties,

- outstanding chemical, moisture and corrosion resistance,
- good thermal properties,
- excellent adhesion,
- very good electrical properties,
- low cure shrinkage,
- low viscoelasticity,
- good dimensional stability and
- good processability.

However, like most thermosetting polymers, epoxy is also known for its inherent brittleness. The fracture toughness K_{Ic} of neat epoxy is usually at the magnitude of 1 MPa $\sqrt{m}$, which is comparable to that of polystyrene or soda-lime glass and significantly inferior to that of most engineering polymers. Details on the definition and measurement of fracture toughness are given in section 1.6.5.

Nowadays still more than 50 % of the world's epoxy is used in protective coatings, the next most important applications being printed circuit board laminates, semiconductor encapsulants, FRPs, tooling, molding, casting, flooring and adhesives [14]. Among these, the mentioned low fracture toughness is a major issue for the use in FRPs and adhesives.

In fact, the use of FRPs is frequently discouraged simply due to the matrix's low fracture toughness. Nevertheless, FRPs are constantly increasing in use for high-performance applications. Especially the CFRP market is currently growing fast, with an annual growth rate of 10.6 %, and is expected to grow even stronger over the years to come, at 11.4 % to 12.3 % per year [15, 16]. The need for tougher epoxy is thus higher than ever.

1.1.2 Toughening strategies

The fracture toughness of neat epoxy can be optimized to some extent by careful selection of the curing agent and its relative quantity or by fine-tuning the cure cycle (all of which will be discussed in sec. 1.2.2 and sec. 1.2.3), but much higher improvements are obtained with toughening agents. Commonly applied toughening agents include, among others, liquid rubbers [17], spherical rubber particles [18], core–shell particles [19, 20], glass beads [21, 22], microvoids [23, 24], hyperbranched polymers [25] and combinations thereof [26], as well as C nanotubes (NTs) [27] and other NPs [28].

The most notable toughening effect is usually obtained with modifiers that are less rigid than the epoxy matrix, e.g., with rubber particles. However, these modifiers tend to degrade other properties, in particular the Young's modulus E and the glass-transition temperature T_g. In contrast, rigid particles generally do not affect the epoxy's T_g and can even increase its E. Their toughening effect is still significant, but less pronounced than that of rubber particles.

Micrometer-sized rigid particles and rubbery fillers share one disadvantage that limits their applicability severely: They both increase the viscosity of the uncured epoxy and thus restrict its processability, which is of particular importance in the manufacturing of FRPs, where good flow control is crucial. This viscosity increase can only barely be accounted for by selecting an epoxy system with lower viscosity or by increasing the processing temperature. In fact, the maximum filler loading, and thus the maximum toughening effect, is often limited by the acceptable viscosity.

The significantly smaller viscosity increase is one of the major advantages of spherical (*zero-dimensional*) NP fillers. While their toughening effect is not outstanding, they show this toughening effect already at significantly lower filler loading, so that there is only a minor viscosity increase. Even at rather high filler contents, zero-dimensional NPs increase the viscosity of a suspen-

sion only marginally, and the viscosity increase is the smaller the better dispersed they are [29]. Epoxy toughening with NPs will be discussed in detail in sec. 1.3.1.

1.2 Epoxy chemistry

1.2.1 Epoxy and epoxy resins

The term *epoxy* describes both a basic component and the cured end product of epoxy resins and is also often used as a colloquial name for the *epoxide* functional chemical group (also called *oxirane*, see fig. 1.1). In this Thesis, however, these terms are used separately in order to avoid confusion: The term *epoxy resin* is used for the basic, unreacted component that consists of molecules with mostly unreacted epoxide groups that are not reacting, and the term *epoxy* will be used for the cured, solid end product. In addition, the terms *uncured epoxy* or *curing epoxy* describe epoxy that is curing but currently not yet fully cured.

Epoxy is a *thermoset*, or more precisely, a *thermosetting polymer*, that is to say, it is a polymer that does not melt upon heating like thermoplastic polymers do, but that stays solid until its degradation[1]. This is because it consists of a three-dimensional molecular network of covalent bonds. In fact, it

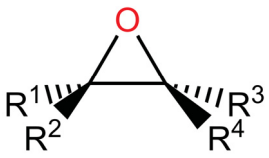

Figure 1.1: Epoxide functional group

[1] However, most thermosetting polymers soften considerably at elevated temperatures.

is possible to produce thermoplastic epoxy by restricting the polymerization reaction (henceforth called *cure reaction*) to only one dimension, but these materials have little importance in practice and shall thus not be considered in this Thesis.

While there are different kinds of epoxy resins available, this Thesis deals exclusively with 2,2'-(((propane-2,2-diylbis(4,1-phenylene))-bis(oxy))bis(methylene))bis(oxirane), which is better known as *bisphenol-A-diglycidylether* or *diglycidyl ether of bisphenol A (DGEBA)*. The latter name is the most common and will thus be used in this Thesis. DGEBA accounts for more than 75 % of the epoxy resin volume used worldwide [14] so that the conclusions drawn in this Thesis are very generally applicable. DGEBA is an oligomer and its degree of polymerization determines its viscosity. In its most common form, it has a degree of polymerization n of approx. 0.2 (see fig. 1.2), resulting in an epoxide group concentration of approx. 5.4 mol/kg. With this degree of polymerization, DGEBA forms a transparent liquid[2] with a viscosity of 11 Pa s to 16 Pa s [14]. This particular type of DGEBA epoxy resin has become popular under *Shell Chemical*'s trade name *Epon 828* and is the epoxy resin that is exclusively used in this Thesis.

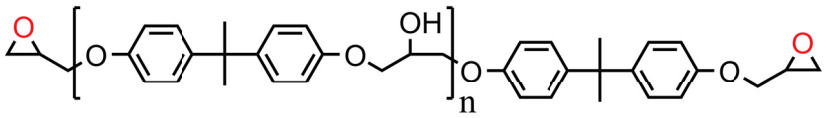

n = 0 (88%); n = 1 (10%); n = 2 (2%)

Figure 1.2: Diglycidylether of bisphenol A (DGEBA)

[2] Strictly speaking, this form of DGEBA is a solid at room temperature. However, it crystallizes extremely slowly and the crystals melt easily upon stirring, so that it can be considered a liquid for most practical purposes.

1.2.2 Cure reaction

Epoxy is formed in the cure reaction of the epoxy resin with another chemical substance, the *curing agent* (the types of curing agents applied in this Thesis and their particular cure reactions will be described in section 1.2.3). The resulting three-dimensional molecular network consists of linear molecular chains that are interconnected by *cross-links*. The *International Union of Pure and Applied Chemistry* (IUPAC) defines a cross-link as "a small region in a macromolecule from which at least four chains emanate" [30]. However, this definition was not found to be very useful for the present Thesis, which is why an alternative definition was formulated that suits the description of highly cross-linked networks better: For this Thesis, a cross-link is defined as *a single atom* from which at least *three* molecular chains emanate that all connect this atom individually to the molecular network (see fig. 1.3). This definition usually results in the same number of cross-links as the IUPAC's definition, but it facilitates calculations.

The cure reaction often requires heating of the mixture to an appropriate cure temperature. Typical cure temperatures range from room temperature to 200 °C, but also higher temperatures are sometimes used for fast cure reactions or high-temperature epoxy. The cure temperature affects the cure kinetics and thus the material's final properties, and so do the heating and cooling rates to some extent. The combination of the epoxy system and the cure temperature determines the cure time, which can be as short as a few seconds and as long as several days.

The *glass-transition temperature* T_g is the temperature above which the mobility of a material's molecular chains increases drastically. As a consequence, the material softens considerably, so that the T_g limits its operation temperature for most practical purposes. The T_g of unreacted epoxy is usually below room temperature but increases steadily with cure conversion. The cure reac-

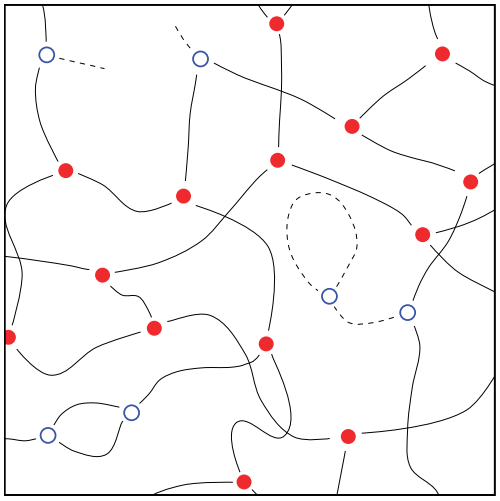

Figure 1.3: Schematic of a molecular network, where the lines stand for molecular chains and the circles stand for atoms where these molecular chains interconnect. The filled circles are atoms that have at least three individual connections to the molecular network, while the open circles have fewer. According to the IUPAC's definition of a cross-link, each of the lines connecting two filled circles would represent a cross-link. In this work, however, the filled circles themselves are seen as the cross-links. The dashed lines are molecular chains that are not part of the molecular network.

tion stops as soon as the epoxy's T_g becomes higher than the cure temperature or if no reactants remain. In the latter case, the material is fully cured and has reached its final T_g, irrespectively of the actual cure temperature.

Complete cure is usually desired, so that the cure temperature must be higher than the epoxy's final T_g. However, a too high cure temperature in the early stages of the cure reaction can result in a too vigorous exothermic cure reaction and consequently in a non-perfect molecular network and possibly incipient thermal degradation. This is why a non-constant cure temperature is often applied. In this Thesis, all materials were cured in a two-step cure process, where the reactive mixture is first heated to one temperature level that is high enough to make the material solidify, and then to a higher tempera-

ture level that is higher than the material's final T_g to ascertain complete cure. As the epoxy can be demolded and machined already after the first cure step, this second cure step additionally helps to relax the internal stresses from the restricted cure shrinkage.

1.2.3 Curing agents

An epoxy resin must be mixed with an appropriate curing agent to produce cured epoxy. A curing agent (also called *hardener* or *curative*) is a chemical substance that is miscible with the epoxy resin and that contains functional groups that react with the epoxide groups to form covalent bonds. Most curing agents are liquid at room temperature, but some need to be heated to melt them so that they can be mixed properly with the epoxy resin.

The chosen curing agent is just as important for the properties of the final material as the epoxy resin itself. The combination of the epoxy resin, its curing agent and possibly added catalysts, and the respective quantities thereof, cured with a certain temperature profile, will be called the *epoxy system* as the properties of the final material are really just determined by this entire combination.

Variations in the epoxy system allow great variability in the properties of the resulting epoxy. Two of the most dependent properties are the glass-transition temperature T_g and the fracture toughness. The T_g of epoxy ranges from below ambient temperature (the produced epoxy is then a rubbery solid) to above 300 °C. The fracture toughness of fully cured, stoichiometric, neat epoxy is usually contrary to the T_g, i.e., epoxy with high T_g has often low fracture toughness.

Epoxide groups have good reactivity towards both nucleophilic and electrophilic species and are thus receptive to a wide range of reagents. The curing agents used in this Thesis are amine and anhydride curing agents.

Amines are the most commonly used curing agents for epoxies. Primary and secondary amines react with epoxide groups in a stepwise polyaddition reaction, where each amino hydrogen reacts with one epoxide group (see fig. 1.4). For aliphatic amines both primary and secondary amino hydrogens have approximately the same reactivity [31]. If the amount of epoxide groups is equal to or lower than the amount of amino hydrogens, side reactions do not take place [31]. When there is an excess of epoxide groups, a third reaction can compete with the two previous ones (fig. 1.5) [31]. However, this reaction is insignificant at temperatures below 150 °C in the absence of a catalyst [32].

The second largest class of curing agents for epoxy resins is formed by (cyclic organic acid) anhydrides [31], which are usually used in combination with a Lewis-base catalyst (usually a tertiary amine). The exact mechanism of this cure reaction is still a matter of controversy [33]. It is proposed that the catalyst (also called *initiator* or *accelerator*) reacts with the epoxide group to form a zwitter-ion that immediately reacts with an anhydride group; the reaction then proceeds strictly alternating as a chainwise polymerisation (see fig. 1.6) [33, 34]. At high temperatures, the epoxy can react with the anhydride curing agent without any catalyst or undergo an anionic autopolymerization reaction initiated by the Lewis base without the anhydride curing agent, but neither of these reactions is relevant at moderate temperatures. [31]

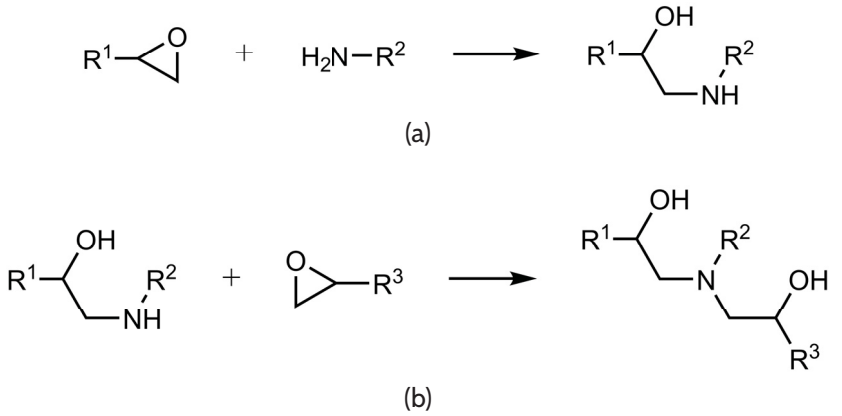

Figure 1.4: Cure reaction of an epoxide group with (a) a primary and (b) a secondary amine, respecively

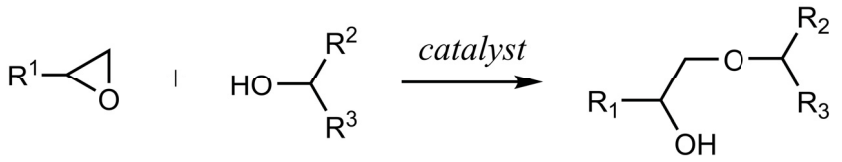

Figure 1.5: Catalytic etherification reaction of an epoxide group with a hydroxyl group

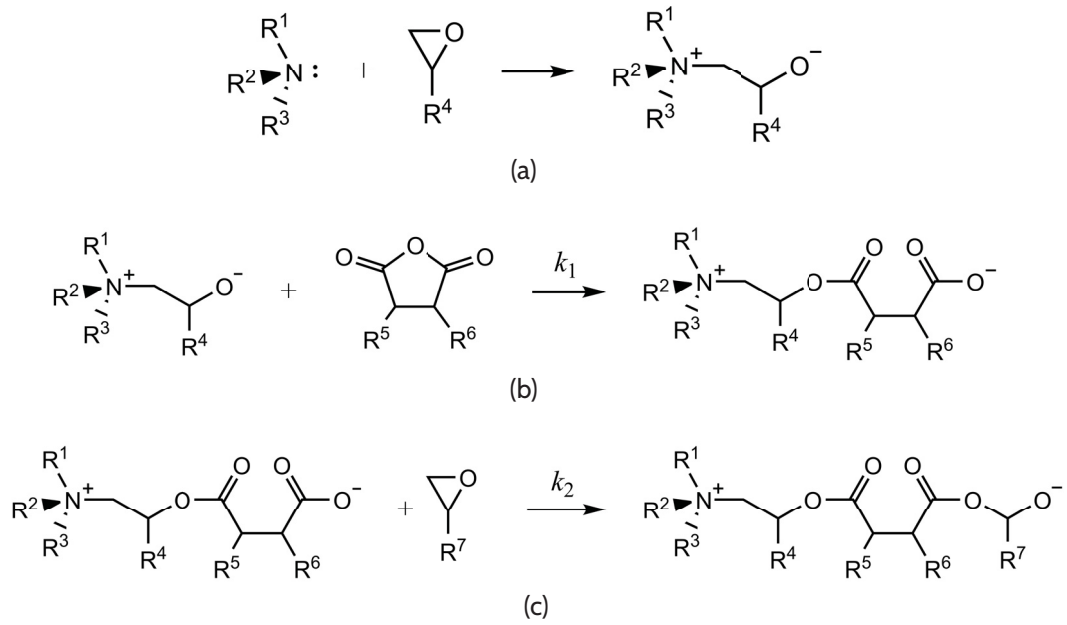

Figure 1.6: Initiation reaction of an epoxide group with a tertiary amine initiator (a) and the subsequent cure reactions with an anhydride (b) and another epoxide group (c); $k_1 \ggg k_2$ [31]

1.3 Epoxy nanocomposites in general

If a polymer is filled with particles, the diameter d of these particles is of major importance for the composite's properties. As the nanoscience pioneer Eric Drexler pointed out, confusing the micron scale with the nanoscale "is like confusing an elephant with a ladybug" [35, 36]. Indeed, a moderate change in d results in very significant differences in the particles' volumes V, their specific surface area (SSA), their number density n (i.e., their number per unit volume) and their mean distance $2c$ to each other, among others (see fig. 1.7). These size effects are the main reasons for the characteristics of nanocomposites that differentiate them from conventional composite materials.

Besides their sizes, the effects of NPs are mostly determined by their aspect ratio, that is to say, by the ratio of their side lengths. If the NPs are comparable in size in all three dimensions, they are called *zero-dimensional* or *three-dimensional*. If they are significantly longer in one dimension than in the other two, they are called *one-dimensional* and if they are significantly longer in two dimensions than in the third, they are called *two-dimensional*. The IF-WS_2 used in this Thesis are zero-dimensional, while WS_2 NTs are one-dimensional and flaky WS_2 are two-dimensional.

A nanocomposite is a "composite in which at least one of the phase domains has at least one dimension of the order of nanometres" [30]. Most standardization organizations agree that the *nanoscale* is the length range approximately from 1 nm to 100 nm [37, 38]. The meaning of the term *nanoparticle* (NP) varies depending on the defining organization. The major standardization organizations agree that NPs are particles with sizes in the nanoscale, but definitions vary with regards to how many of a particle's dimensions have to be in the nanoscale [38]. This Thesis uses the definition of the ISO [37], stating that objects with at least one dimension in the nanoscale are called *nano-*

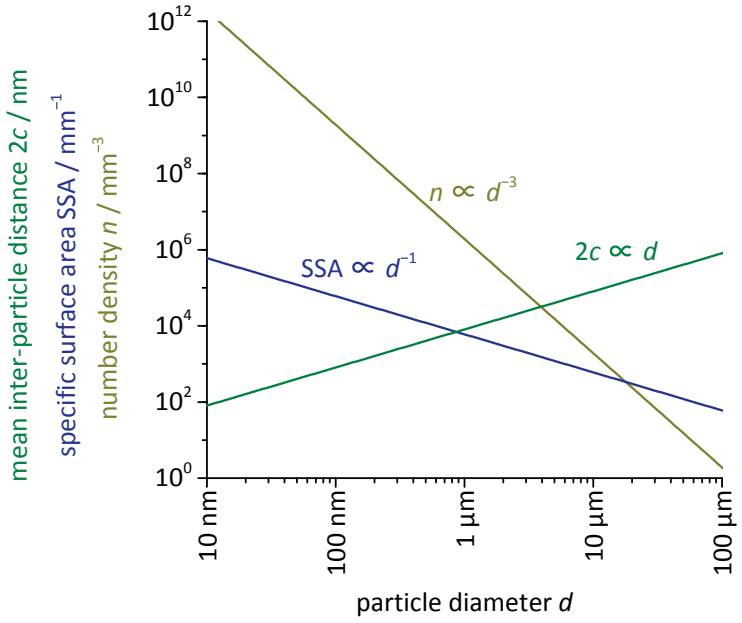

Figure 1.7: Number density n, specific surface area (SSA) and mean inter-particle distance $2c$ over the diameter d of particles, assuming a spherical shape and a particle volume fraction of $0.1\,\%$

objects, and only nano-objects with all dimensions in the nanoscale are called *nanoparticles*.

However, these NPs can still interconnect with each other, forming larger structures, so-called *agglomerates*. The IUPAC defines an *agglomerate* as a "cluster of primary particles held together by physical interactions", where a *primary particle* is the "smallest discrete identifiable entity observable by a specified identification technique", e.g., by electron microscopy [30]. These physical interactions can be quite strong or very weak, down to the strength of van-der-Waals forces. An *aggregate*, in contrast, is defined to be a "cluster of primary particles interconnected by chemical bonds" [30]. Several aggregates can again be held together by physical interactions, forming an *agglomerate of*

aggregates. Aggregates are usually interconnected much more strongly than agglomerates.

In practice, it is quite difficult to discern aggregates from agglomerates, which is why some scientists call a cluster of particles *agglomerate*, if it can be broken up with usual dispersion techniques (e.g., by sonication), and *aggregate* otherwise. For similar practical reasons, all clusters of particles will be called *agglomerates* in this Thesis, while the term *aggregate* will only be used if suitable microscopy techniques suggest that a cluster is interconnected by chemical bonds.

NPs are produced either by separating larger particles into smaller ones down to the nanoscale (*top-down approach*) or by growing them from precursor molecules (*bottom-up approach*). The bottom-up approach is usually more expensive but tends to produce more homogeneous NPs. In some cases it is even possible to grow the NPs *in situ* directly in the epoxy resin, which yields monodisperse particle size distribution and outstanding dispersion quality, so that the resulting nanocomposites have very well defined properties [39].

The NPs are usually dispersed in the epoxy resin rather than in the curing agent or in a mixture of both because of the usually higher viscosity of the epoxy resin, which stabilizes the dispersion. This dispersion is often called a *master batch*, even if it is used only once.

1.3.1 Toughening of epoxy by nanoparticles

As pointed out in sec. 1.1.2, NPs are an effective way to increase an epoxy's fracture toughness without reducing its processability. Toughness improvements usually range up to 120 % to 160 % in the critical stress-intensity factor K_{Ic} and to 240 % to 350 % in the critical strain-energy release rate G_{Ic} [28, 40–42] (the definition and measurement of these values is described in sec-

tion 1.6.5). The maximum increase is usually obtained at the highest investigated filler loadings which were usually around 15 % to 30 % by volume.

However, one of the major advantages of NPs is their good toughening effect at low loadings (i.e., 0.1 % to 5 % by volume) where they outclass micrometer-sized rigid particles. For each percent of zero-dimensional nanoparticles (NPs) added by volume, the critical energy release rate G_{Ic} of epoxy typically increases by up to 15 % to 75 % and the critical stress-intensity factor K_{Ic} by up to 5 % to 30 % [28, 40–42].

The exact mechanisms by which the NPs toughen the polymer matrix depend on NPs' shapes and dimensions, their surface chemistry and morphology, the dispersion quality and on the polymer matrix. Most scientists name the following keywords to describe the toughening mechanisms of NPs in epoxy nanocomposites:

- crack deflection [28, 40, 43, 44]
- microcracking [28, 43]
- void formation and yielding [40, 43–49]
- residual stress fields [28]
- crack (tip) pinning [28, 40, 43, 44, 50]
- immobilized polymer [40]
- crack bridging [43]
- plastic deformation of the matrix [28, 40, 43, 44, 50]
- matrix–particle debonding [28, 44]

Details on the meaning of these keywords can be found in the respective literature. However, it is likely to be the case that several of these keywords describe the same phenomena or effects caused by the same phenomena, or possibly even apparent phenomena. Likewise, the same keywords have possibly been used for different phenomena. Also, some of these keywords describe toughening mechanisms in one-dimensional nanocomposites only

or mechanisms that were adapted from microcomposites to nanocomposites without a thorough critical investigation on whether the same explanations hold true at the nanoscale.

Attempts were made to model the toughening effect of some of these mechanisms, with varying success [40, 51, 52]. These attempts usually focus on the effects of plastic deformation of the matrix, of matrix–particle debonding and of void formation and yielding [52]. Despite the large efforts, however, it is still not fully understood to date, which of the epoxy's material properties are determining for the toughening effect.

1.4 Tungsten disulfide

Tungsten disulfide (WS_2, more precisely called *tungsten(IV) sulfide*) is a chemical compound that occurs naturally as the rare mineral *tungstenite* and belongs to the group of *transition metal dichalcogenides*. Metal dichalcogenides are dark, diamagnetic solids that are insoluble in all solvents, exhibit semiconducting properties and are highly covalent. [53]

The most common metal dichalcogenide is MoS_2, which shares many characteristics with WS_2. Both adopt a layered molecular structure with strong covalent bondings between the metal and the S atoms but only weak van-der-Waals forces between the layers. Like MoS_2, WS_2 occurs mostly in three different polytypes, namely in the hexagonal polytype with two layers per unit cell (2H), in the rhombohedral with three layers per unit cell (3R) polytype and the trigonal polytype with one layer per unit cell (1T).

Both MoS_2 and WS_2 exhibit outstanding tribologic properties, which is why they are used as tribologic additives for lubricating oils and polymers [54, 55]. Besides that, they are used as semiconductors and as catalysts [53].

1.4.1 Inorganic, fullerene-like WS_2 (IF-WS_2) and WS_2 nanotubes

The layered structure of metal dichalcogenides closely resembles that of (C) graphite. It has been known from the 1980s that C can also form closed polyhedra known as *fullerenes* (C_{60}, C_{70}, etc.). If the polyhedra are formed by multiple concentric shells, (i.e., they form a *nano-onion* [37]) they are called *nested fullerene nanoparticles* [53]. Both single-wall and multi-wall structures are also found in a one-dimensional form, forming single-wall or multi-wall C nanotubes (NTs).

In 1991, similar hollow, closed structures were found for WS_2 (and also for MoS_2 and several other compounds), which are now known as *inorganic WS_2 NTs* and *inorganic, fullerene-like WS_2* (IF-WS_2). The numerous interesting properties of these materials has driven the development of their production processes. While approx. 300 g of IF-WS_2 could be produced per batch in the early states of its commercialization, the process has been scaled up to currently 100 kg to 300 kg per batch, so that it is now possible to use it as an additive for lubricants [56] or other applications, often outperforming flaky WS_2 [55, 57–59].

It was shown that WS_2-NTs do not fail due to their defect statistic (weak links), but keep their elastic behavior almost to the point where the chemical bonds fail [60]. With about 15 GPa to 22 GPa, they exhibit a strength several times higher than that of para-aramid (*Kevlar*) or C fibers, although it is still much lower than that of C NTs [61].

The maximum allowed shock pressure that IF-WS_2 NPs can hold was suggested to be as high as 25 GPa, making them the toughest cage molecules known so far [62, 63]. The compressive strength of these NPs is 1 GPa to 2.5 GPa [64]. The good mechanical properties of IF-WS_2 and WS_2-NTs and their high crystalline quality, in combination with their good availability,

arouse consequently scientific interest into their use in polymer nanocomposites [65, 66].

1.5 Epoxy–IF-WS_2 nanocomposites

There are only a few articles published that deal with the use of IF-WS_2 in epoxy. The first reported use of IF-WS_2 in epoxy was in 2004 by Rapoport *et al.* [58]. They mixed IF-WS_2 into epoxy, cured with diethylenetriamine (DETA) and reported significantly improved tribologic properties. At 10 % by mass, however, the filler loading was quite high and no dispersion was done besides stirring, so that the produced material was most likely rather different from the materials investigated in the present Thesis. [58]

The first approach to enhance epoxy's fracture toughness with IF-WS_2 was undertaken by Buchman *et al.* in 2009 [67]. Two very different epoxy systems were investigated, where one of the curing agents was Jeffamine T-403 (*Huntsman Co.*, UK), which is the most frequently used curing agent in the present Thesis. However, from the information given it seems that the investigated epoxy systems were non-stoichiometric. The IF-WS_2 was dispersed within the epoxy resin by sonication with unstated power. Their results indicated that low IF-WS_2 loadings of 0.3 % to 0.5 % by mass resulted in the best toughening effect for both investigated epoxy systems, providing outstanding G_{Ic} increases of up to five-fold. Unfortunately, the reported G_{Ic} values are possibly questionable since they have never been reproduced in another publication and Buchman *et al.* did not succeed in providing a good hypothesis for the origin of the reported toughening effect. [67]

This work was followed up by Shneider *et al.* in 2010 [68]. The investigated epoxy system was the same as one of the systems used by Buchman *et al.* Dispersion was obtained by thorough stirring only. The authors claim that more

intense stirring for longer times resulted in better dispersion quality, but the presented peel strength values and SEM images do not show a significant effect. Improvements in the peel strength were found to peak at a filler loading of 0.5 % by mass. Notably, the authors claim that the S atoms that form the outermost layers of the IF-WS_2 had reacted with the epoxy resin to form C – S bonds as their infrared (IR) spectra might indicate. However, it is unclear which chemical reaction would make the rather strong W – S bonds break to form C – S bonds. [68]

Shneider and co-workers published two further articles in this field in 2013. One of them deals with the tribologic properties of epoxy–IF-WS_2 nanocomposites [70]. The authors showed that epoxy's wear and to some extent its coefficient of friction can be significantly reduced by adding small loadings of various types of various WS_2 nanoparticles, namely 2H-WS_2, IF-WS_2 and WS_2 NTs. The lowest wear was obtained with 0.5 % IF-WS_2, which reduced the epoxy's wear by up to 83 %. The authors explain this outstanding improvement with the NPs' good tribologic properties, as well as the improved fracture toughness of the nanocomposite, which might reduce the material's susceptibility to small wear-induced cracks. [70]

The present Thesis was first and foremost inspired by the third article of Shneider and co-workers [69]: This article deals with the toughening effect of surface-functionalized IF-WS_2 on epoxy and its origin. The chosen epoxy system was a DGEBA cured with Jeffamine T-403, which is why primarily this epoxy system was used in the present Thesis as well. From the information given, it seems that the amount of curing agent used was sub-stoichiometric. The NPs were dispersed by sonication with unstated power. [69]

The surface functionalization with different silane modifiers was done in order to improve the NPs' dispersibility within epoxy as well as to provide covalent bonding between the NPs and the epoxy matrix. Despite the almost inert nature of WS_2 [66], X-ray photoelectron spectroscopy (XPS) analy-

sis suggested that the silanization reaction was successful [69]. However, it is not clear which chemical reaction bonded the silane modifiers to the NPs, nor whether this bonding was of chemical or rather of physical nature, in which case the bonding would be very weak. Likewise, it is doubtful whether the acryloxy functionalization was capable of forming a covalent bond to the epoxy network.

The measured G_{Ic} of the nanocomposites was up to 70 % higher than that of the neat epoxy, where the best improvement was obtained with the alkylsilane-functionalized NPs. These improvements are notable, as only 0.5 % IF-WS_2 had been added by mass, corresponding to only 0.09 % by volume. This corresponds to a G_{Ic} increase of over 800 % per percent of NPs added by volume. The authors explain this outstanding improvement with the hypothetical formation of a *nodular morphology* that they claim to see in SEM images of fracture surfaces. In other words, they assume that there is a region of enhanced modulus in the vicinity of the nanoparticles which might enhance the material's fracture toughness [69]. The existence of such nodular morphology is, however, subject to a controversial debate [71, 72] and will be investigated critically in chapter 2. The hypothetically inhomogeneous modulus distribution in the vicinity of the NPs is an interesting assumption that will be put to test in chapter 4.

In a nutshell, the published literature suggests that IF-WS_2 NPs are capable of improving the fracture toughness and the tribologic properties of epoxy considerably, where 0.5 % IF-WS_2 by mass seems to be a good choice. Nevertheless, there are still several open questions, and it is the objective of the present Thesis to clearly state and answer them.

1.6 Characterization techniques

This section gives a brief introduction into the underlying principles of the most important characterization techniques that were used in several of the chapters in this Thesis. It does not cover characterization techniques that were applied only in single chapters (like nuclear magnetic resonance or the plane-strain compression test) nor those that are of less importance for the understanding of the chapters (like titration or mass-density measurement). Details on the used equipment and adjustments as well as on characterization techniques that are not covered here can be found in the respective chapters and in the applied standards.

1.6.1 Dynamic light scattering (DLS)

Dynamic light scattering (DLS, also known as *photo-correlation spectroscopy* or *quasi-elastic light scattering*) is a technique that allows determining the size distribution of small particles in a suspension or of polymers in a solution. As epoxy is insoluble, only the investigation of particles is of interest for the present work.

Small particles in suspension are subject to Brownian motion, that is to say, they move in a random pattern within the liquid, permanently changing both their position and their velocity vector. As larger particles have higher inertia than smaller particles, they change their velocity less drastically and thus they move more slowly. The Stokes–Einstein–Sutherland equation describes how the translational diffusion coefficient D of a spherical particle, which corresponds to the velocity of Brownian Motion, is affected by the particle's diameter d and the liquid's temperature T and its viscosity η (k_B is the Boltzmann constant):

$$D = \frac{k_B T}{3\pi\eta d} \tag{1.1}$$

A DLS spectrometer measures D by investigating the temporal fluctuations of light that is scattered by the suspended particles: The faster the signal fluctuates, the smaller the particles in the suspension are (see fig. 1.8). In order to avoid multiple scattering, the particle volume fraction in the suspension should preferably be very low (usually 10^{-5} to 10^{-4} [73]), which means that they barely affect the liquid's viscosity and the viscosity of the neat liquid can be used for the calculation. The temperature must be controlled very well as it is not only a factor in eq. (1.1) itself, but also strongly affects the viscosity, which is a factor therein as well.

DLS is a first-principle method, that is to say, the results are directly derived from basic physical equations without needing any models or calibrations. There is hence no need to calibrate the DLS spectrometer prior to a measurement. DLS is best suited for particles of diameters between 5 nm and 1000 nm [73], but can potentially measure particle diameters between 0.1 nm and 10 000 nm. However, sedimentation and low signal-to-noise ratio severely restrict the usefulness of DLS for larger particles (> 500 nm) [73]. This is particularly critical for NPs with high mass densities like WS_2.

The particle diameter $\bar{x}_{\mathrm{DLS}}$ measured by DLS is the *intensity-weighted* average of the *hydrodynamic* diameter. The hydrodynamic diameter is the diameter of spherical particles that have the same translational diffusion speed as the investigated particles. This is important for the present work as the investigated particles are not perfectly spherical and they appear mostly in agglomerates (see sec. 1.3). Thus, the measured diameter represents the size of the agglomerates. The intensity-weighted average diameter is always somewhat larger than the volume-weighted average diameter, which in turn is higher than the number-average diameter. While the latter two are much more representative of the physical reality, determining them requires some model assumptions, which reduces their usefulness and limits their comparability. This is why ISO 22412 recommends using only the intensity-weighted aver-

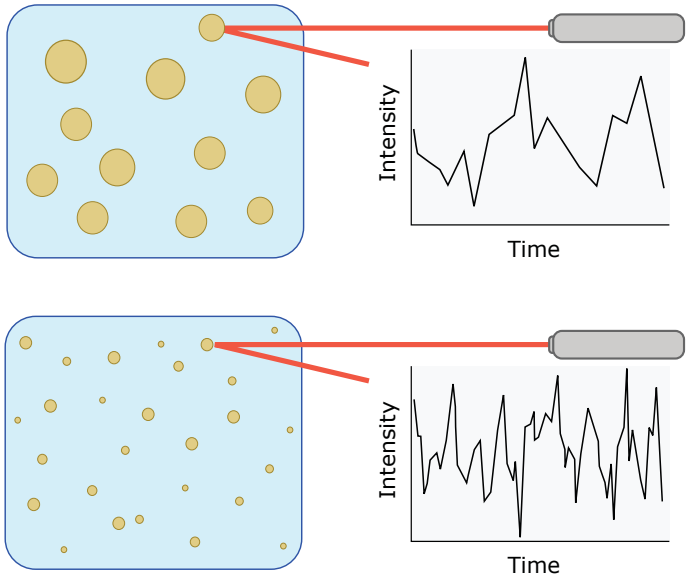

Figure 1.8: DLS measurement principle: suspended particles scatter the incident monochromatic light. The fluctuation speed of the scattered light can be correlated to the particle size distribution.

age diameter $\bar{x}_{\mathrm{DLS}}$ [74], and this recommendation was followed throughout this Thesis. It must therefore be kept in mind that the majority of the agglomerates are likely smaller than $\bar{x}_{\mathrm{DLS}}$. DLS can also measure the breadth of the agglomerate size distribution, but that information is not used in this Thesis.

1.6.2 Dynamic mechanical analysis (DMA)

Dynamic mechanical analysis (DMA, also known as *dynamic mechanical spectroscopy* or *dynamic mechanical thermal analysis*) is a material characterization technique that quantifies the viscoelastic behavior of solids at varying temperatures. In its most common form, it applies sinusoidal mechanical strains on a material and measures the resulting mechanical stresses, or vice versa. In this Thesis, exclusively tensile strains were applied.

If the investigated material is viscoelastic, the measured mechanical response will lag behind its stimulation by a certain phase angle δ, the *loss angle*, which quantifies how viscoelastic the material is (see fig. 1.9). Together with the stress amplitude σ_0 and the strain amplitude ϵ_0, δ allows calculating both the elastic part of the material's modulus, the *storage modulus* E', and its viscous part, the *loss modulus* E'':

$$E' = \frac{\sigma_0}{\epsilon_0} \cos\delta \tag{1.2}$$

$$E'' = \frac{\sigma_0}{\epsilon_0} \sin\delta \tag{1.3}$$

These, in turn, are often combined into the *complex modulus* E^*. The most convenient way to describe a material's viscoelastic behavior is by giving the *damping factor* $\tan\delta$ and the absolute of the complex modulus $|E^*|$:

$$E^* = E' + iE'' \tag{1.4}$$

$$\tan\delta = E''/E' \tag{1.5}$$

$$|E^*| = \sqrt{E'^2 + E''^2} \tag{1.6}$$

DMA is frequently used to characterize the thermal behavior of a material. The measurement is then performed while the material is heated or cooled, typically at rates at the order of magnitude of 1 °C/min. One important purpose of this is determining a material's glass-transition temperature T_g. There are several different possibilities for how to extract a value for the T_g from a DMA measurement. In this Thesis, the temperature at which E'' was maximum is taken as the T_g. Figure 1.10 shows E', E'' and $\tan\delta$ curves as they are typically measured in a DMA measurement of epoxy and the temperature that is used as T_g.

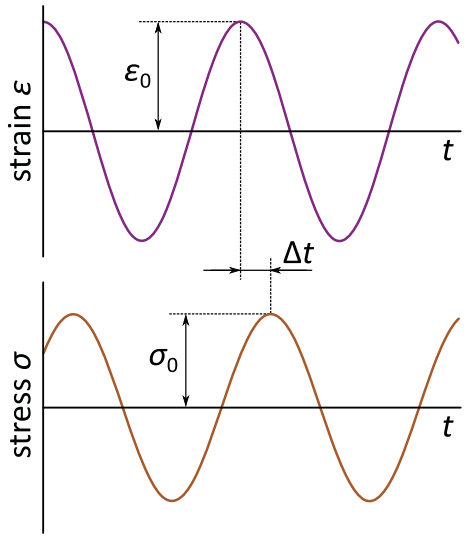

Figure 1.9: Phase shift in a DMA measurement. The measured stress σ lags behind the applied strain ϵ by the time lag Δt, which is used to calculate the loss angle $\delta = \Delta t \cdot 2\pi f$, where f is the constant frequency.

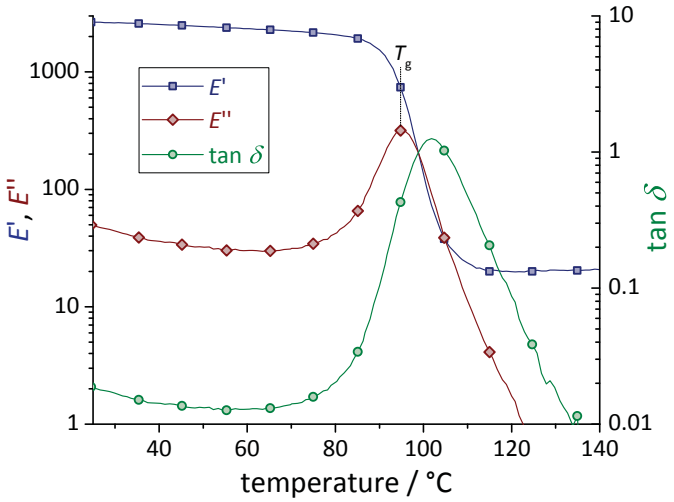

Figure 1.10: Typical curves of the storage modulus E', the loss modulus E'' and the loss factor $\tan\delta$ of an epoxy over the temperature as measured via DMA, and the T_g as determined in this Thesis

Besides that, the DMA data is used to calculate the epoxy's *rubber equilibrium modulus* E_r, that is to say, its modulus in the rubbery state, i.e., at a temperature above T_g. E_r can be used to roughly estimate a material's cross-link density [75]. For this Thesis, E_r was defined as the average complex modulus at temperatures between $T_{\min(E)}-5\,°C$ and $T_{\min(E)}+5\,°C$ during a DMA measurement, where $T_{\min(E)}$ is the temperature where the complex modulus is minimum. This indirect measurement of the cross-link density is used and discussed in chapters 5 and 6.

1.6.3 Atomic force microscopy (AFM)

Atomic force microscopy (AFM, also called *Scanning Force Microscopy*) is a scanning-probe microscopy technique that investigates surfaces by measuring the contact forces between them and a scanning probe at the nanoscale. The main purpose is measuring the surface's topography on the nanoscale, but certain AFM modes allow mapping various material properties at the same time, e.g., mechanical properties, the friction coefficient, electrical and magnetic properties, the chemical composition and many more, all at the nanoscale. [76]

For usual topographic investigation, the scanning AFM probe is a sharp tip (typical tip radii around 1 nm to 10 nm), mounted on a flexible cantilever (typical spring constants around 0.1 N/m to 100 N/m). Forces between this tip and the investigated surface cause the cantilever to deflect. This deflection can be measured at the nanoscale with various methods, the currently most frequently used being a laser and a photodiode (see fig. 1.11). The acting contact forces can then be calculated from the deflection via the cantilever's spring constant.

The sample is moved both vertically and laterally by fine piezoelectric scanners[3]. The lateral movement is usually carried out line-by-line, so that the sample moves quickly back and forth in one lateral direction (usually called *fast scan axis* or *X axis*) and slowly in the other (*slow scan axis* or *Y axis*). The vertically moving piezoelectric scanner (*Z-piezo*) permanently adjusts the sample's height to keep the maximum force between the probe and the surface constant. The vertical distance between the probe and the surface is usually additionally varied at a higher frequency by an additional piezoelectric scanner, depending on the mode the AFM is used in.

In the present Thesis, AFM was performed exclusively in air at room temperature[4] in the *Peak-Force Tapping* mode. This non-resonant, intermittent-contact AFM mode is a trade mark of the company *Bruker* that was introduced to the market in 2010. However, similar modes are used by other companies under different designations, e.g., *pulsed force* mode. This AFM mode allows measuring the interacting forces directly (i.e., in Nanonewtons) during the measurement at every single contact event at a high frequency of usually 2 kHz. Earlier AFM modes were measuring the forces at very low frequencies of a few Hertz, which made them unsuitable for highly resolved images.

In the Peak-Force Tapping mode, the AFM sample is moved vertically once per pixel in a sinusoidal movement, while the force is permanently measured at a high sampling rate (see fig. 1.12). As a result, a complete force–distance curve is measured in every single contact event. These force–distance curves allow finely controlling the contact force directly, keeping it constant and low. Moreover, certain mechanical properties can be deduced: For example, the maximum attractive force is a measure for the adhesion between the probe and the surface at the respective position. Most importantly, however, certain

[3] In some AFM systems, the probe is moved by the piezoscanners instead of the sample.

[4] Some applications favor or require scanning within a liquid or at other temperatures, but this is not relevant for this Thesis.

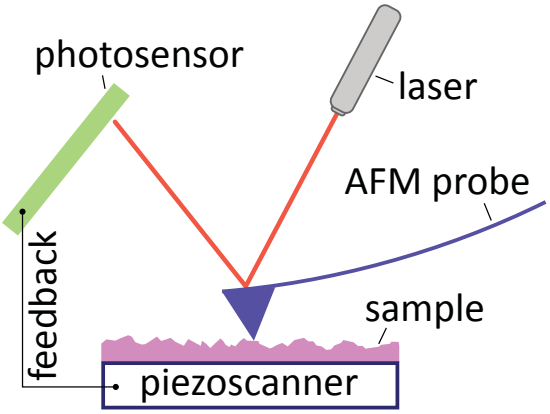

Figure 1.11: Basic principle of an AFM. The AFM probe deflects on contact with the sample, deflecting the reflected laser light, which is detected by the photosensor. The X- and Y-scanner make the probe scan the surface and the feedback electronics adjust the Z-piezo in a way that the maximum force between the AFM probe and the sample stays constant.

models can be fitted to the force–distance curves, yielding the modulus of the sample at the respective position. AFM modulus measurement requires relatively high contact forces, at the scale of 50 nN, while the topography can be measured as well or even better at lower contact forces of below 1 nN. Likewise, the spring constant of the used probes must be suited for the investigated material. For materials with moduli in the range of 2 GPa to 3 GPa, like epoxy, *Bruker* recommends AFM probes with spring constants of 40 N/m to 100 N/m [77]. It is currently not clear, which modulus differences can be measured at which lateral resolution, and how exactly the material's modulus, the contact force, the probe's spring constant and the surface roughness affect this resolution.

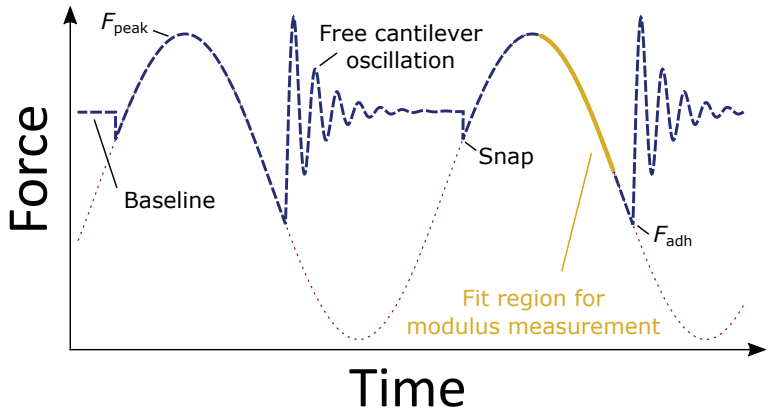

Figure 1.12: Principle of the Peak-Force Tapping AFM mode. The blue, dashed curve is the probe–sample force curve as calculated from the cantilever deflection that the photosensor measures, and the red, dotted curve shows what the force curve would look like if the probe did not detach from the surface. The baseline is where the force is zero. As the probe tip approaches the sample surface, at some point it is attracted strongly enough to snap to the surface. The modulus is determined by fitting an appropriate model to the falling flank of the force curve in the repulsive regime, given by the yellow, solid curve. The maximum attractive force is used as the adhesion force. The probe is usually in contact only for a smaller fraction of the time than shown here.

1.6.4 Electron microscopy

An electron microscope is a microscope that uses a beam of accelerated electrons as its source of illumination. This electron beam interacts with the investigated sample and the resulting signals can be detected and combined into images. Due to the small wavelength of electrons, its theoretical spatial resolution is considerably better than that of light microscopes.

The electron beam is thermoionically emitted from an electron gun fitted with a W filament cathode. Modern electron microscopes use field-emission electron guns, which provide a very narrow beam-energy spread, resulting in good resolution. In this Thesis, *Schottky*-type field-emission electron guns are

used, which can produce high electron beam currents thanks to their sharp ZrO_2-coated W tips [78]. Electron-microscopy investigation is generally done in vacuum, and high vacuum tends to provide the best image resolution. All electron-microscopy images presented in this Thesis were gathered in high vacuum (approx. 10^{-4} Pa). The variants of the electron microscope used in this Thesis are the scanning electron microscope (SEM) and the transmission electron microscope (TEM).

Scanning electron microscopy

In an SEM, the electron beam is scanned over a surface to investigate it. The electrons have usually rather low kinetic energies of 1 keV to 30 keV. When they interact with the sample, they produce various signals that can be detected and used to form an image pixel-by-pixel. One of the major advantages of the SEM over the light microscope is its 100 to 500 times greater depth-of-field, which allows it to produce completely in-focus micrographs even of relatively rough surfaces at high magnifications [78].

All SEM images used in this Thesis use secondary electrons (SEs) as detected signal. These electrons are ejected from the sample's atoms by inelastic scattering interactions with the beam electrons. Due to their low energy of less than 50 eV, only SEs from the top few nanometers can escape from the sample and be collected by a detector. The SEM was used both in the standard imaging mode using an Everhart-Thornley detector (ETD) and in the *immersion lens mode*, using a through-the-lens detector (TLD). The latter mode provides even better spatial resolution, but does not reveal fine surface topography.

A sample must be electrically conductive to enable its investigation in an SEM so that the introduced electrons can be discharged. If nonconductive samples shall be investigated, they must be coated with a thin layer of a conductive material. All samples investigated over the course of this Thesis were

nonconductive and therefore coated with a few nanometers of Pt or Au prior to the investigation. Only a few powdery samples were investigated without any coating as the small dimensions of the powdery particles limit the electrons' path lengths and thus make coating unnecessary.

Despite the conductive coating, the investigated region of the sample is damaged irreversibly by the electron beam[5]. As this effect could not be fully avoided, the presented SEM images were all gathered *blind*, i.e., the investigated regions had not been irradiated at all before.

While the best SEMs can provide a spatial resolution of below 0.5 nm [78], the resolution is substantially worse if coated, nonconductive samples are investigated, with resolutions below 100 nm being hard to obtain.

Transmission electron microscopy

In a TEM, the electron beam is transmitted through an ultra-thin specimen at a usually much higher kinetic energy of 100 keV to 300 keV. In this Thesis, TEM is used in its most common mode of operation, the *bright-field mode*, in which the contrast is provided by the absorption of electrons by the material, so that thicker regions or regions with a higher atomic number appear dark.

TEM can provide even much better lateral resolution than SEM – the best spatial resolution obtained with a TEM so far was below 50 pm [79]. The actual resolution, however, depends strongly on the sample and its preparation. In this Thesis, TEM samples were produced exclusively by placing drops of WS_2 NP suspensions on TEM grids. Thanks to the high atomic number of W, the contrast was always very good.

[5] This region is often permanently darkened

1.6.5 Linear-elastic fracture mechanics (LEFM)

Fracture mechanics is the field of mechanics that deals with the propagation of cracks in materials. If exclusively linear-elastic materials and brittle fracture processes are concerned, as is the case in this Thesis, the concepts of linear-elastic fracture mechanics can be applied.

Fracture processes are divided by the type of crack-opening stress into mode I (tensile stress), mode II (shear stress perpendicular to the crack front) and mode III (shear stresses parallel to the crack front). The only load mode considered in this Thesis is the mode-I fracture mode, i.e., the cracks are opened by tensile stresses only. The stress state within a material during fracture is a combination of plane stress and plane strain. In LEFM experiments, the specimens must be thick enough so that plane strain deformation predominates. As epoxy is rather brittle, this is relatively easily achieved.

Cracks cannot be described by the linear elasticity theory as it would predict infinitely high stresses at the crack tip. In reality, a small region around the crack tip yields even in brittle materials, forming a plastic zone. In order to circumvent the problems associated with determining the actual stresses, the mode-I stress-intensity factor K_I is used to describe the stress state in the proximity of a crack tip. The value of K_I depends on the crack length a in relation to a specimen's width w and the nominal normal stress σ_{yy} and is calculated via a dimensionless geometry factor $f(a/w)$ that depends on the particular specimen's geometry:

$$K_\mathrm{I} = \sqrt{a\pi}\,\sigma_{\mathrm{yy}} \cdot f(a/w) \tag{1.7}$$

The *critical stress-intensity factor* K_Ic is the plain-strain K_I at which the crack propagation velocity becomes critical and sudden fracture occurs, that is to

say, as K_I approaches K_{Ic}, the crack propagation velocity goes to infinity[6]. K_{Ic} is the most important measure for a material's fracture toughness.

Another measure for a fracture process is the *strain-energy release rate* G, which is the change in the elastic potential energy U over the change in the fracture surface area A:

$$G = -\frac{\partial U}{\partial A} \tag{1.8}$$

The *critical strain-energy release rate* G_{Ic} is the mode-I G for plane strain at which the crack propagation velocity becomes critical and sudden fracture occurs. G_{Ic} is thus another measure for the fracture toughness that can be seen as an alternative to K_{Ic}. The G_{Ic} is related to the K_{Ic} via the Young's modulus E and the Poisson's ratio ν:

$$G_{Ic} = K_{Ic}^2 \cdot \frac{1-\nu^2}{E} \tag{1.9}$$

The G_{Ic} can often be determined more easily than the K_{Ic}, in particular when macroscopically heterogeneous materials are investigated (e.g., FRPs), for which the determination of the K_{Ic} is very difficult, which is why G_{Ic} data are sometimes easier to obtain. However, the G_{Ic} is of little use in structural applications, which is why the K_{Ic} is usually favored. In practice, it is advisable to determine both values independently and check whether they agree with eq. (1.9).

The fracture-mechanics measurements reported in this Thesis were all done as single-edge-notched bending (SENB) tests according to ISO 13586 [80]. This test has the advantage that the sample preparation is relatively facile and that rather little material is required. This means that more samples can be measured with a given amount of material, which is

[6] Of course, the effective crack propagation velocity will still be limited by other physical laws, for example, by the limited velocity of wave propagation in the investigated material.

very important for fracture-mechanics tests that usually suffer from high scatter.

In an SENB test, a notched, pre-cracked bar is bent until fracture. The K_{Ic} is then calculated from the force at fracture, the pre-crack length and the sample geometry, and the G_{Ic} is calculated from the area below the force–displacement curve until fracture, the pre-crack length and the sample geometry. [80]

One of the most critical factors determining the usefulness of SENB results is the quality of the pre-crack. For this Thesis, the pre-cracks were made at room temperature by tapping a fresh blade into the notch using a hammer. As the crack tip was always well distant from the blade, these pre-cracks were assumed to be comparable to natural cracks. ISO 13586 states two validity recommendations that were often not met over the course of this Thesis. First, it recommends that ratio of the specimen width w to the pre-crack length a_0, is between 0.45 and 0.55. Secondly, the standard recommends that the length of pre-cracks should not differ by more than 10 % over the sample's thickness. As the pre-cracking was done by tapping, which makes controlling the exact pre-crack length difficult, many of the pre-cracks did not fulfill these requirements. However, the results did not seem to be affected critically by these issues. As none of these recommendations are strict requirements, all

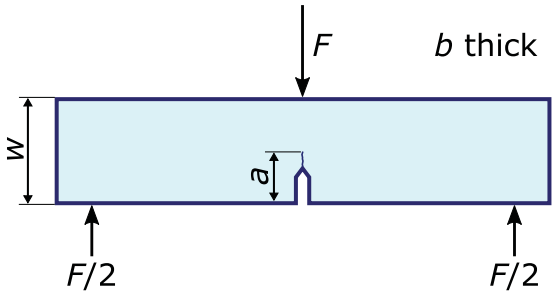

Figure 1.13: Schematic drawing of an SENB specimen

fracture-toughness results were considered valid as long as they did not differ strongly from the results of all other samples for a given material. In order to enable the readers to review the effect of this procedure, detailed fracture toughness results are listed in chapter 8.

1.7 Dispersion techniques

The dispersion of NPs within viscous liquids like epoxy resins requires the introduction of dispersion energy, the magnitude of which depends on the interfacial interaction between the NPs and the liquid. The most simple dispersion technique is mixing. However, even high-speed mixers are usually incapable of providing good dispersion quality. While all investigated epoxy systems were mixed with the NPs at relatively high speeds, more sophisticated dispersion techniques were applied additionally, namely sonication and three-roll milling (3RM).

1.7.1 Sonication

Sonication is agitating particles in a liquid with sound energy, usually at ultrasonic frequencies (20 kHz to 400 kHz), which is why it is often also called *ultrasonication*. It may be done for various reasons, e.g., for degassing or for cell disruption; in this Thesis it is used exclusively for dispersing WS_2 NPs within ethanol or epoxy.

The sound waves are essentially alternating high-pressure and low-pressure cycles. High-intensity ultrasonic waves create small voids in the liquid during the low-pressure cycle. Once these voids reach a certain volume, they cannot absorb any additional energy anymore and collapse violently during a high-pressure cycle. This process results in very high local temperatures (approx. 5000 K) and pressures (approx. 2000 bar) and causes the liquid

to form liquid jets of velocities up to 280 m/s [81]. These extreme conditions cause NP agglomerates to break up, but they can also damage primary NPs as well as the liquid they are suspended in.

Sonciation can be done using *ultrasonic baths* or *ultrasonic probes* (see fig. 1.14). Ultrasonic baths are mostly used for cleaning purposes. They consist of a chamber that is usually filled with water and that is excited with ultrasonic waves from the outside. Some ultrasonic baths can be heated. Flasks with sample liquids can then be sonicated by simply placing them into the bath. The sonication power of ultrasonic baths usually ranges from 50 W to 1000 W and scales with their size. The sonication effect is of relatively low intensity and unevenly spread within the chamber. The repeatability and scalability of this process are both very poor.

Ultrasonic probes consist essentially of metal bars (usually straight or conical), which are exciting their surroundings with ultrasonic waves. These probes are normally submerged into the sample liquid by only a few millimeters and thus concentrate their ultrasonic power to a smaller volume than ultrasonic baths. As they are usually also driven at a higher power (usually 300 W to 3000 W), ultrasonic probes deliver significantly higher power densities than ultrasonic baths do.

1.7.2 Three-roll milling

A *three-roll mill* (3RM) is a machine that applies high shear stresses to a viscous liquid, gel or paste that is processed with it in order to mix it or to disperse something therein. Although the 3RM has been invented already in the 19th century, it is still increasingly used today, in particular in the epoxy and nanocomposite science, as can be seen in fig. 1.15. This statistic is somewhat biased as earlier publications are often not completely entered in the electronic databases and as the number of publications overall increases over

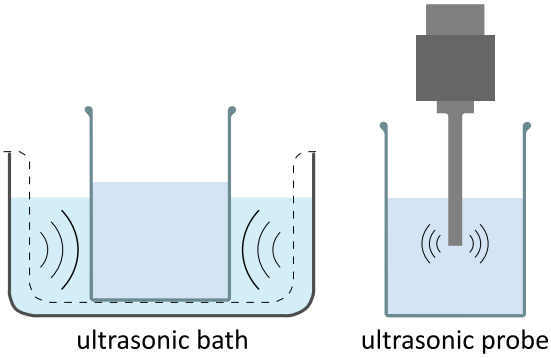

Figure 1.14: Schematic drawings of the used sonication techniques. The circular segments indicate ultrasonic wave propagation.

time as well. Nevertheless, it is clear that the use of 3RMs is more prevailing in these scientific disciplines than it was ever before.

A 3RM consists of three rolls (usually made of steel or ceramic and often temperature-controlled) that are mounted close and in parallel to each other and that turn at different rotational speeds (see fig. 1.16). The gaps between the rolls can either be set to a certain distance or controlled by the applied force between the rolls and the rheological properties of the processed material, which was exclusively done in the present Thesis. The apron roll can be separated from the other two so that the material is only mixed between these. This step serves for mixing rather than for dispersing as the material can simply re-flow between the two rolls without passing the gap once. The dispersing takes place mainly in the gap between the center roll and the apron roll. However, as the material passes this gap only once before being collected by a knife, it might be necessary to pass it through the 3RM several times to achieve a certain dispersion quality.

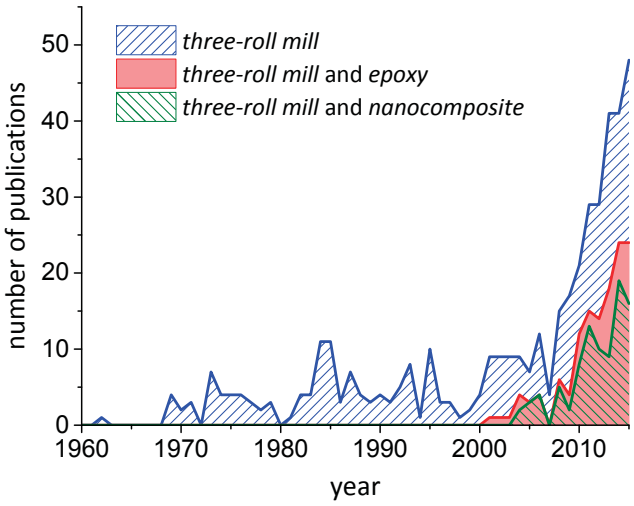

Figure 1.15: Number of published articles per year with the phrase *three-roll mill* and its combination with either *epoxy* or *nanocomposite* in any field as found in the database of Scopus

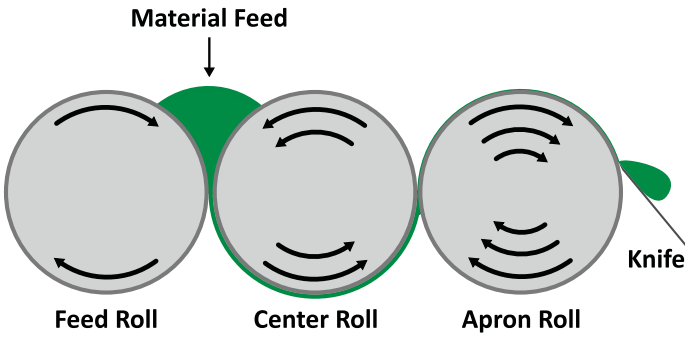

Figure 1.16: Scheme of a 3RM. The dispersion takes place mainly between the center roll and the apron roll.

1.8 Objectives and Outline of the Thesis

1.8.1 Objectives

The general objective of this Thesis is to give an idea on whether IF-WS_2 is a suitable toughening agent for epoxy and what mechanisms are responsible for the toughening effect. In doing so, the findings of others should be reviewed critically and alternative explanations should be proposed and validated whenever necessary. In particular, the following specific questions should be answered:

- Shneider *et al.* have reported that epoxy could be toughened considerably by the addition of IF-WS_2 NPs [69]. Is this toughening effect reproducible and can it be generalized for different epoxy systems?

- Shneider *et al.* have explained the toughening effect with the formation of a nodular morphology, resulting in a region with enhanced modulus [69]. Can the existence of such nodular morphology be confirmed in epoxy? Can the modulus distribution in epoxy be measured at the nanoscale, and if so, is there a modulus variation in the vicinity of dispersed IF-WS_2 NPs?

- What role does the fullerene-like geometry of IF-WS_2 play for the toughening effect? Are the commercial IF-WS_2 NPs used in most reference works comparable to laboratory-made IF-WS_2 NPs from another source?

- Is the reported surface functionalization of the IF-WS_2 NPs reproducible and can it be confirmed that it is helpful for the dispersibility and/or the toughening effect?

- Are there suitable alternatives to sonication for dispersing IF-WS_2 within epoxy resin?
- Are there additional techniques to quantify the dispersion quality of IF-WS_2 within epoxy, besides microscopy methods?
- What role do the epoxy system's composition and its properties play for its toughening ability?

1.8.2 Outline

This Thesis consists of eight chapters, where this introduction forms the first one. The next five chapters describe the scientific work that lead to the conclusions that are summed up in chapter 7:

Chapter 2 focuses on the claimed existence of inhomogeneities and a nodular morphology in neat epoxy. AFM is used to measure the topography and modulus distribution at the nanoscale on differently prepared neat-epoxy surfaces and an alternative interpretation of the claimed nodular morphology is presented. Suggestions are made for which requirements must be fulfilled to measure modulus distributions in epoxy reliably and to avoid AFM artifacts showing apparent nodular morphology.

Chapter 3 covers the surface functionalization of IF-WS_2 NPs with silane modifiers and its characterization, the subsequent dispersion of these NPs within ethanol and the quantification of the dispersion quality with DLS. A model is presented that approximates the dispersion quality over sonication time.

Chapter 4 discusses the dispersion of functionalized and unfunctionalized IF-WS_2 NPs within an epoxy resin by sonication and with a 3RM as well as the resulting dispersion quality and fracture mechanics properties. AFM is used to measure the modulus distribution in epoxy–IF-WS_2 nanocomposites,

in particular in the vicinity of an IF-WS_2 NP. A model toughening mechanism is presented that is a possible alternative to the mechanisms listed in section 1.3.1.

Chapter 5 investigates the significance of the epoxy network properties for the toughening effect of IF-WS_2. Varying the relative quantity of curing agent (i.e., producing a sub-stoichiometric material) results in a variation of cross-link densities and molecular network defects. Moreover, the IF-WS_2 are compared with flaky WS_2 in order to investigate the significance of the fullerene-like geometry.

Chapter 6 discusses the significance of the epoxy's properties for the toughening effect of the IF-WS_2 from another perspective. By varying both the type and the amount of curing agent, epoxies with varying properties are produced, with less inter-correlation between their material properties. This allows discerning the effects of the individual material properties for the toughening effect. Furthermore, another source of IF-WS_2 is used for these investigations in order to allow more general statements on the effect of IF-WS_2 on epoxy.

The Annex can be found in chapter 8. It contains supporting information that is not necessary but useful for the understanding of the previous chapters.

References

[1] United Nations, "Transforming our world: The 2030 agenda for sustainable development", Resolution adopted by the general assembly, 2015. [Online]. Available: https://sustainabledevelopment.un.org/post2015/transformingourworld/publication (visited on 08/08/2016).

[2] Intergovernmental panel on climate change, *Climate change 2013: The physical science basis*, T. F. Stocker, Q. D., G.-K. Plattner, *et al.*, Eds. Cambridge, United Kingdom and New York, USA: Cambridge University Press, 2013, 1535 pp., Contribution of working group I to the fifth assessment report of the intergovernmental panel on climate change.

[3] Eurostat, *Energy, transport and environment indicators*, 2014 edition. Luxembourg: Publications Office of the European Union, 2014, ISBN: 978-92-79-41256-1.

[4] U.S. Energy Information Administration, "Energy consumption by sector", in *Monthly energy review*. Jul. 2016. [Online]. Available: http://www.eia.gov/totalenergy/data/monthly (visited on 08/08/2016).

[5] K. E. Ohrn, "Aircraft energy use", in *Encyclopedia of energy engineering and technology*, B. L. Capehart, Ed. CRC Press, 2007, ch. 4, pp. 24–30, ISBN: 978-1-4398-7482-0. DOI: 10.1201/9780849338960.

[6] Airbus S.A.S. (Jan. 4, 2016). A350 XWB, [Online]. Available: http://www.airbus.com/aircraftfamilies/passengeraircraft/a350xwbfamily.

[7] "Airbus readies first A350", *Reinf. Plast.*, vol. 58, no. 6, p. 6, 2014. DOI: 10.1016/S0034-3617(14)70225-5.

[8] BMW. (Jan. 5, 2016). The dawn of a new era, Building cars with CFRP, [Online]. Available: http://www.bmwgroup.com/e/0_0_www_bmwgroup_com/produktion/BMW_I/life_modul_aus_cfk.html.

[9] A. Jacob, "Carbon fibre and cars – 2013 in review", *Reinf. Plast.*, vol. 58, no. 1, pp. 18–19, 2014. DOI: 10.1016/S0034-3617(14)70036-0.

[10] A. v. Baeyer, "Ueber die Verbindungen der Aldehyde mit den Phenolen und aromatischen Kohlenwasserstoffen [on the compounds of aldehydes with phenols and aromatic hydrocarbons]", in German, *Berichte der deutschen chemischen Gesellschaft*, vol. 5, no. 2, pp. 1094–1100, 1872. DOI: 10.1002/cber.187200502157.

[11] L. H. Baekeland, "Verfahren zur Herstellung von Kondensationsprodukten aus Phenolen und Formaldehyd [process for the preparation of condensation products from phenols and formaldehyde]", in German, Deutsches Reichspatent 233 803, Jan. 1908.

[12] P. Schlack, in German, Deutsches Reichspatent 676 117, Dec. 1934.

[13] P. Castan, in German, Schweizer Patent 211 116, Aug. 1938.

[14] H. Q. Pham and M. J. Marks, "Epoxy resins", in *Ullmann's Encyclopedia of Industrial Chemistry*. Wiley–VCH Verlag, 2000, ISBN: 9783527306732. DOI: 10.1002/14356007.a09_547.pub2.

[15] "Report predicts strong growth in carbon fiber consumption", *Reinf. Plast.*, vol. 59, no. 5, p. 214, 2015. DOI: 10.1016/j.repl.2015.08.039.

[16] "12% growth in carbon fiber predicted", *Reinf. Plast.*, vol. 59, no. 5, p. 220, 2015. DOI: 10.1016/j.repl.2015.08.019.

[17] S. Kar and A. K. Banthia, "Use of acrylate-based liquid rubbers as toughening agents and adhesive property modifiers of epoxy resin", *J. Appl. Polym. Sci.*, vol. 92, no. 6, pp. 3814–3821, 2004. DOI: 10.1002/app.20397.

[18] R. Bagheri and R. A. Pearson, "Role of particle cavitation in rubber-toughened epoxies: Ii. inter-particle distance", *Polymer*, vol. 41, no. 1, pp. 269–276, 2000. DOI: 10.1016/S0032-3861(99)00126-3.

[19] R. J. Day, P. A. Lovell, and A. A. Wazzan, "Toughened carbon/epoxy composites made by using core/shell particles", *Comp. Sci. Technol.*, vol. 61, no. 1, pp. 41–56, 2001. DOI: 10.1016/S0266-3538(00)00169-X.

[20] H. J. Sue, E. I. Garcia Meitin, D. M. Pickelman, and C. J. Bott, "Fracture mechanisms in rigid core-shell particle modified high performance epoxies", *Colloid and Polym. Sci.*, vol. 274, no. 4, pp. 342–349, 1996. DOI: 10.1007/BF00654054.

[21] J. Lee and A. F. Yee, "Inorganic particle toughening II: Toughening mechanisms of glass bead filled epoxies", *Polymer*, vol. 42, no. 2, pp. 589–597, 2001. DOI: 10.1016/S0032-3861(00)00398-0.

[22] J. Lee and A. F. Yee, "Effect of rubber interlayers on the fracture of glass bead/epoxy composites", *J. Mat. Sci.*, vol. 36, no. 1, pp. 7–20, 2001. DOI: 10.1023/A:1004814002344.

[23] R. Bagheri and R. A. Pearson, "The use of microvoids to toughen polymers", *Polymer*, vol. 36, no. 25, pp. 4883–4885, 1995. DOI: 10.1016/0032-3861(95)99306-F.

[24] Y. Huang and A. J. Kinloch, "The toughness of epoxy polymers containing microvoids", *Polymer*, vol. 33, no. 6, pp. 1330–1332, 1992. DOI: 10.1016/0032-3861(92)90785-U.

[25] R. J. Varley and W. Tian, "Toughening of an epoxy anhydride resin system using an epoxidized hyperbranched polymer", *Polym. Int.*, vol. 53, no. 1, pp. 69–77, 2004. DOI: 10.1002/pi.1324.

[26] J. Fröhlich, H. Kautz, R. Thomann, H. Frey, and R. Mülhaupt, "Reactive core/shell type hyperbranched blockcopolyethers as new liquid rubbers for epoxy toughening", *Polymer*, vol. 45, no. 7, pp. 2155–2164, 2004. DOI: 10.1016/j.polymer.2004.01.065.

[27] F. H. Gojny, M. H. G. Wichmann, B. Fiedler, and K. Schulte, "Influence of different carbon nanotubes on the mechanical properties of epoxy matrix composites – a comparative study", *Compos. Sci. Technol.*, vol. 65, no. 15–16, pp. 2300–2313, 2005. DOI: 10.1016/j.compscitech.2005.04.021.

[28] B. Wetzel, P. Rosso, F. Haupert, and K. Friedrich, "Epoxy nanocomposites – fracture and toughening mechanisms", *Eng. Fract. Mech.*, vol. 73, no. 16, pp. 2375–2398, 2006. DOI: 10.1016/j.engfracmech.2006.05.018.

[29] P. Cassagnau, "Melt rheology of organoclay and fumed silica nanocomposites", *Polymer*, vol. 49, no. 9, pp. 2183–2196, 2008. DOI: 10.1016/j.polymer.2007.12.035.

[30] J. Alemán, A. V. Chadwick, J. He, *et al.*, "Definitions of terms relating to the structure and processing of sols, gels, networks, and inorganic–organic hybrid materials, Iupac recommendations 2007", *Pure Appl. Chem.*, vol. 79, 10 2007. DOI: 10.1351/pac200779101801.

[31] J.-P. Pascault, H. Sautereau, J. Verdu, and R. J. J. Williams, "Chemistry of crosslinked polymer synthesis", in *Thermosetting polymers*, CRC Press, 2002, ch. 2, ISBN: 978-0-203-90840-2. DOI: 10.1201/9780203908402.ch2.

[32] C. C. Riccardi and R. J. J. Williams, "Kinetic scheme for an amine–epoxy reaction with simultaneous etherification.", *J. Appl. Polym. Sci.*, vol. 32, no. 2, pp. 3445–3456, 1986.

[33] P. Musto, M. Abbate, G. Ragosta, and G. Scarinzi, "A study by Raman, near-infrared and dynamic-mechanical spectroscopies on the curing behaviour, molecular structure and viscoelastic properties of epoxy/anhydride networks", *Polymer*, vol. 48, no. 13, pp. 3703–3716, 2007. DOI: 10.1016/j.polymer.2007.04.042.

[34] J. Rocks, L. Rintoul, F. Vohwinkel, and G. George, "The kinetics and mechanism of cure of an amino-glycidyl epoxy resin by a co-anhydride as studied by FT-Raman spectroscopy", *Polymer*, vol. 45, no. 20, pp. 6799–6811, 2004. DOI: 10.1016/j.polymer.2004.07.066.

[35] A. F. Rawle, "Micron sized nano-materials", *Powder Technol.*, vol. 174, no. 1–2, pp. 6–9, 2007. DOI: 10.1016/j.powtec.2006.10.012.

[36] E. Regis, *Nano: The emerging science of nanotechnology : Remaking the world-molecule by molecule*, 1st edition. Little, Brown and Co., 1995, pp. 207–208, ISBN: 0-316-73858-1.

[37] "ISO 80004-2. nanotechnologies – vocabulary – part 2: nano-objects", International Organization for Standardization, Geneva, CH, Standard, Jun. 2015.

[38] S. Horikoshi and N. Serpone, "Introduction to nanoparticles", in *Microwaves in nanoparticle synthesis: Fundamentals and applications*, S. Horikoshi and N. Serpone, Eds. Weinheim, Germany: Wiley-VCH, 2013. DOI: 10.1002/9783527648122.ch1.

[39] S. Sprenger, "Epoxy resin composites with surface-modified silicon dioxide nanoparticles: A review", *J. Appl. Polym. Sci.*, vol. 130, no. 3, pp. 1421–1428, 2013. DOI: 10.1002/app.39208.

[40] B. B. Johnsen, A. J. Kinloch, R. D. Mohammed, A. C. Taylor, and S. Sprenger, "Toughening mechanisms of nanoparticle-modified epoxy polymers", *Polymer*, vol. 48, no. 2, pp. 530–541, 2007. DOI: 10.1016/j.polymer.2006.11.038.

[41] H.-Y. Liu, G.-T. Wang, Y.-W. Mai, and Y. Zeng, "On fracture toughness of nanoparticle modified epoxy", *Composites, Part B*, vol. 42, no. 8, pp. 2170–2175, 2011. DOI: 10.1016/j.compositesb.2011.05.014.

[42] D. J. Bray, P. Dittanet, F. J. Guild, *et al.*, "The modelling of the toughening of epoxy polymers via silica nanoparticles: The effects of volume fraction and particle size", *Polymer*, vol. 54, no. 26, pp. 7022–7032, 2013. DOI: 10.1016/j.polymer.2013.10.034.

[43] M. M. Shokrieh, S. M. Ghoreishi, and M. Esmkhani, "Toughening mechanisms of nanoparticle-reinforced polymers", in *Toughening mechanisms in composite materials*, Q. Qin and J. Ye, Eds., Woodhead Publishing, 2015, ch. 11, pp. 295–320, ISBN: 978-1-78242-279-2. DOI: 10.1016/B978-1-78242-279-2.00011-1.

[44] M. Quaresimin, M. Salviato, and M. Zappalorto, "Toughening mechanisms in nanoparticle polymer composites: Experimental evidences and modeling", in *Toughening mechanisms in composite materials*, Q. Qin and J. Ye, Eds., Woodhead Publishing, 2015, pp. 113–133, ISBN: 978-1-78242-279-2. DOI: 10.1016/B978-1-78242-279-2.00004-4.

[45] H. Zhang, Z. Zhang, K. Friedrich, and C. Eger, "Property improvements of in situ epoxy nanocomposites with reduced interparticle distance at high nanosilica content", *Acta Materialia*, vol. 54, no. 7, pp. 1833–1842, 2006. DOI: 10.1016/j.actamat.2005.12.009.

[46] G. M. Odegard, T. C. Clancy, and T. S. Gates, "Modeling of the mechanical properties of nanoparticle/polymer composites", *Polymer*, vol. 46, no. 2, pp. 553–562, 2005. DOI: 10.1016/j.polymer.2004.11.022.

[47] J. Lee and A. F. Yee, "Fracture of glass bead/epoxy composites: On micro-mechanical deformations", *Polymer*, vol. 41, no. 23, pp. 8363–8373, 2000. DOI: 10.1016/S0032-3861(00)00187-7.

[48] T. Kawaguchi and R. A. Pearson, "The effect of particle–matrix adhesion on the mechanical behavior of glass filled epoxies. Part 2. A study on fracture toughness", *Polymer*, vol. 44, no. 15, pp. 4239–4247, 2003. DOI: 10.1016/S0032-3861(03)00372-0.

[49] A. J. Kinloch and A. C. Taylor, "The toughening of cyanate-ester polymers, Part I Physical modification using particles, fibres and woven-mats", *J. Mater. Sci.*, vol. 37, no. 3, pp. 433–460, 2002. DOI: 10.1023/A:1013735103120.

[50] A. J. Kinloch and R. J. Young, "Toughened multiphase plastics", in *Fracture behaviour of polymers*. London, New York: Elsevier Applied Science, 1988, ch. 11, pp. 421–467, ISBN: 0-85334-186-9.

[51] T. H. Hsieh, A. J. Kinloch, K. Masania, A. C. Taylor, and S. Sprenger, "The mechanisms and mechanics of the toughening of epoxy polymers modified with silica nanoparticles", *Polymer*, vol. 51, no. 26, pp. 6284–6294, 2010. DOI: 10.1016/j.polymer.2010.10.048.

[52] M. Quaresimin, K. Schulte, M. Zappalorto, and S. Chandrasekaran, "Toughening mechanisms in polymer nanocomposites: From experiments to modelling", *Comp. Sci. Technol.*, vol. 123, pp. 187–204, 2016. DOI: 10.1016/j.compscitech.2015.11.027.

[53] C. O. Oriakhi and M. M. Lerner, "Layered metal chalcogenides", in *Handbook of layered materials*, S. M. Auerbach, K. A. Carrado, and P. K. Dutta, Eds. CRC Press, 2004, ch. 10.

[54] G. W. Stachowiak and A. W. Batchelor, "Wear of non-metallic materials", in *Engineering tribology*, 4th. Waltham: Butterworth-Heinemann, 2014, ch. 16, pp. 651–704, ISBN: 978-0-12-397047-3.

[55] K. Hu, X. Hu, Y. Xu, X. Sun, and Y. Jing, "Tribology of MoS_2-based nanocomposites", in *Tribology of nanocomposites*, J. P. Davim, Ed., Berlin Heidelberg: Springer, 2013, pp. 41–60, ISBN: 978-3-642-33881-6. DOI: 10.1007/978-3-642-33882-3.

[56] A. Zak, L. Sallacan-Ecker, A. Margolin, M. Genut, and R. Tenne, "Insight into the growth mechanism of WS_2 nanotubes in the scaled-up fluidized-bed reactor", *Nano*, vol. 4, no. 2, pp. 91–98, 2009. DOI: 10.1142/S1793292009001551.

[57] M. Chhowalla and G. A. J. Amaratung, "Thin films of fullerene-like MoS_2 nanoparticles with ultra-low friction and wear", *Nature*, vol. 407, pp. 164–167, 2000. DOI: 10.1038/35025020.

[58] L. Rapoport, O. Nepomnyashchy, A. Verdyan, *et al.*, "Polymer nanocomposites with fullerene-like solid lubricant", *Adv. Eng. Mater.*, vol. 6, no. 1–2, pp. 44–48, 2004. DOI: 10.1002/adem.200300512.

[59] C. Shahar, D. Zbaida, L. Rapoport, *et al.*, "Surface functionalization of WS_2 fullerene-like nanoparticles", *Langmuir*, vol. 26, no. 6, pp. 4409–4414, 2010. DOI: 10.1021/la903459t.

[60] R. Tenne and M. Redlich, "Recent progress in the research of inorganic fullerene-like nanoparticles and inorganic nanotubes", *Chem. Soc. Rev.*, vol. 39, no. 5, pp. 1423–1434, 2010. DOI: 10.1039/B901466G.

[61] I. Kaplan-Ashiri, S. R. Cohen, K. Gartsman, *et al.*, "On the mechanical behavior of WS_2 nanotubes under axial tension and compression", *PNAS*, vol. 103, no. 3, pp. 523–528, 2006. DOI: 10.1073/pnas.0505640103.

[62] Y. Q. Zhu, T. Sekine, Y. H. Li, *et al.*, "WS_2 and MoS_2 inorganic fullerenes–super shock absorbers at very high pressures", *Adv. Mat.*, vol. 17, no. 12, pp. 1500–1503, 2005. DOI: 10.1002/adma.200401962.

[63] Y. Q. Zhu, T. Sekine, Y. H. Li, *et al.*, "Shock-absorbing and failure mechanisms of WS_2 and MoS_2 nanoparticles with fullerene-like structures under shock wave pressure", *J. Am. Chem. Soc.*, vol. 127, no. 46, pp. 16 263–16 272, 2005. DOI: 10.1021/ja054715j.

[64] O. Tevet, O. Goldbart, S. R. Cohen, *et al.*, "Nanocompression of individual multilayered polyhedral nanoparticles", *Nanotechnology*, vol. 21, no. 36, p. 365 705, 2010. DOI: 10.1088/0957-4484/21/36/365705.

[65] A. Zak, L. Sallacan-Ecker, A. Margolin, *et al.*, "Scaling up of the WS_2 nanotubes synthesis", *Fullerenes, Nanotubes, Carbon Nanostruct.*, vol. 19, no. 1–2, pp. 18–26, 2010. DOI: 10.1080/1536383X.2010.488594.

[66] M. Naffakh, A. M. Díez-Pascual, C. Marco, G. J. Ellis, and M. A. Gómez-Fatou, "Opportunities and challenges in the use of inorganic fullerene-like nanoparticles to produce advanced polymer nanocomposites", *Prog. Polym. Sci.*, vol. 38, no. 8, pp. 1163–1231, 2013. DOI: 10.1016/j.progpolymsci.2013.04.001.

[67] A. Buchman, H. Dodiuk-Kenig, A. Dotan, R. Tenne, and S. Kenig, "Toughening of epoxy adhesives by nanoparticles", *J. Adhes. Sci. Technol.*, vol. 23, no. 5, pp. 753–768, 2009. DOI: 10.1163/156856108X379209.

[68] M. Shneider, H. Dodiuk, S. Kenig, and R. Tenne, "The effect of tungsten sulfide fullerene-like nanoparticles on the toughness of epoxy adhesives", *J. Adhes. Sci. Techn.*, vol. 24, no. 6, pp. 1083–1095, 2010. DOI: 10.1163/016942409X12584625925268.

[69] M. Shneider, H. Dodiuk, R. Tenne, and S. Kenig, "Nanoinduced morphology and enhanced properties of epoxy containing tungsten disulfide nanoparticles", *Polym. Eng. Sci.*, vol. 53, no. 12, pp. 2624–2632, 2013. DOI: 10.1002/pen.23517.

[70] M. Shneider, L. Rapoport, A. Moshkovich, *et al.*, "Tribological performance of the epoxy-based composite reinforced by WS_2 fullerene-like nanoparticles and nanotubes", *Phys. Status Solidi A*, vol. 210, no. 11, pp. 2298–2306, 2013. DOI: 10.1002/pssa.201329162.

[71] J. Duchet and J.-P. Pascault, "Do epoxy–amine networks become inhomogeneous at the nanometric scale?", *J. Polym. Sci., Part B: Polym. Phys.*, vol. 41, no. 20, pp. 2422–2432, 2003. DOI: 10.1002/polb.10585.

[72] C. M. Sahagun and S. E. Morgan, "Thermal control of nanostructure and molecular network development in epoxy–amine thermosets", *ACS Appl. Mater. Interfaces*, vol. 4, no. 2, pp. 564–72, 2012. DOI: 10.1021/am201515y.

[73] H. G. Merkus, "Dynamic light scattering", in *Particle size measurements*, H. G. Merkus, Ed. Springer, 2009, ch. 12, pp. 299–317, ISBN: 978-1-4020-9015-8. DOI: 10.1007/978-1-4020-9016-5.

[74] "ISO 22412:2008(E). particle size analysis – dynamic light scattering (DLS)", International Organization for Standardization, Geneva, CH, Standard, May 2008.

[75] L. E. Nielsen, "Cross-linking-effect on physical properties of polymers", *J. Macromol. Sci., Part C: Polym. Rev.*, vol. 3, no. 1, pp. 69–103, 1969. DOI: 10.1080/15583726908545897.

[76] E. Meyer, H. J. Hug, and R. Bennewitz, *Scanning probe microscopy: The lab on a tip*. Berlin: Springer, 2003, ISBN: 3-540-43180-2.

[77] B. Pittenger, N. Erina, and C. Su, *Application note # 128, Quantitative mechanical property mapping at the nanoscale with PeakForce QNM*, Bruker, 2012. [Online]. Available: https://www.bruker.com/fileadmin/user_upload/8-PDF-Docs/SurfaceAnalysis/AFM/ApplicationNotes/AN128-RevB0-Quantitative_Mechanical_Property_Mapping_at_the_Nanoscale_with_PeakForceQNM-AppNote.pdf (visited on 02/01/2013).

[78] A. E. Vladár and M. T. Postek, "The scanning electron microscope", in *Handbook of charged particle optics*, 2nd edition, CRC Press, 2009, ch. 9, pp. 437–496, ISBN: 978-1-4200-4554-3.

[79] R. Erni, M. D. Rossell, C. Kisielowski, and U. Dahmen, "Atomic-resolution imaging with a sub-50-pm electron probe", *Phys. Rev. Lett.*, vol. 102, no. 9, p. 096 101, 2009. DOI: 10.1103/PhysRevLett.102.096101.

[80] "ISO 13586:2000(E). plastics – determination of fracture toughness (G_{IC} and K_{IC}) – linear elastic fracture mechanics (LEFM) approach", International Organization for Standardization, Geneva, CH, Standard, Mar. 2000.

[81] K. S. Suslick, "Sonoluminescence and sonochemistry", in *Ultrasonics symposium, 1997. Proceedings., 1997 IEEE*, vol. 1, 1997, 523–532 vol.1. DOI: 10.1109/ULTSYM.1997.663076.

2 Publication 1

2.1 Bibliographic Information

2.1.1 Title

Observation of elastic modulus inhomogeneities in thermosetting epoxies using AFM – Discerning facts and artifacts

2.1.2 Authors

- Dietmar Haba [1]
- Josef Kaufmann [1]
- Andreas J. Brunner [1]
- Katharina Resch [2]
- Christian Teichert [2]

[1] Empa – Swiss Federal Laboratories for Materials Science and Technology, Dübendorf, Switzerland

[2] Montanuniversität Leoben, Austria

2.1.3 Publication details

Published in: *Polymer*, vol. 55, no. 16, pp. 4032–4040, 2014
DOI: 10.1016/j.polymer.2014.06.030

Statement with regard to publication: The manuscript presented here is an adapted version of the accepted manuscript to fit the formatting of the Thesis and does not necessarily reflect exactly the actually published version.

2.2 Abstract

Observations of a nanometer-scale *nodular morphology* on differently prepared surfaces of thermosets have frequently been interpreted as a sign for an inhomogeneous molecular network, which would result in an inhomogeneous modulus distribution within those thermosets. To test this hypothesis, the Peak-Force Tapping AFM mode was used on fracture surfaces and ultramicrotome cuts of epoxy and other polymers using different AFM probes.

The nodular morphology is quite likely caused by an AFM artifact, which also seems to cause an apparently inhomogeneous modulus distribution; a variation in the tip–sample contact area could explain this effect. Smooth surfaces are necessary in order to reduce the contribution from this artifact. Ultramicrotome cutting currently seems to be the most appropriate surface preparation technique for the measurement of modulus distribution at the nanometer scale.

All investigated materials seem to be homogeneous on a scale on the order of 10 nm to 1000 nm. If modulus inhomogeneities are present, their amount or their lateral size is too small to be unambiguously measurable with this technique. From this data, it seems unlikely that epoxy exhibits an inhomogeneous molecular network.

Keywords: Epoxy; Nodular morphology; Inhomogeneity

2.2.1 Graphical Abstract

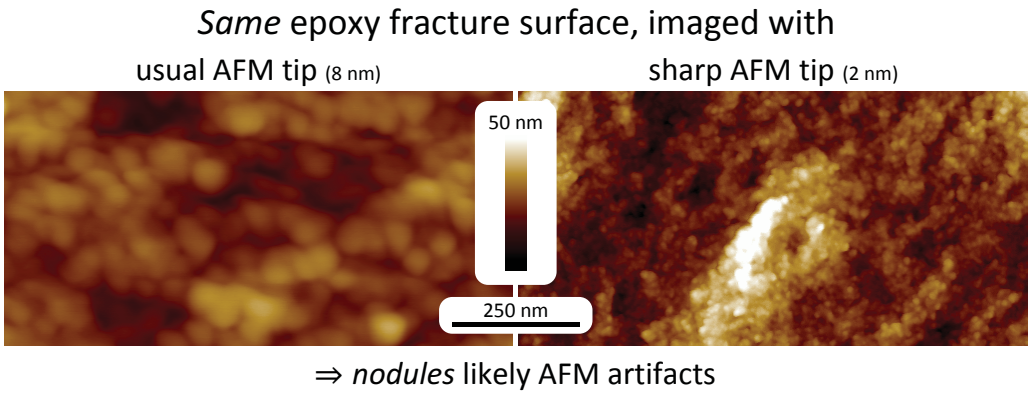

2.3 Introduction

The good performance of thermosetting epoxy polymers made them suitable for high-quality products at reasonable prices. The possible applications are, however, still limited by their rather low fracture toughness. In contrast to thermoplastic polymers, the morphology of thermosets is essentially fixed once they are fully cured. Their final properties are hence determined by the molecular network built up during the cure reaction. This molecular network is generally supposed to be completely homogeneous.

However, it has been speculated that both the low fracture toughness of epoxy and its limited strength could be due to an inhomogeneous network structure, consisting of differently densely cross-linked areas: A high percentage of intra-molecular cross-links in the early stages of the cure reaction could lead to small, highly cross-linked macromolecules within the unreacted monomer in the early stages of cure. Those inhomogeneities could then be partly reduced in the later stages of the cure reaction, but some inhomo-

geneities might still remain. According to this hypothesis, cured thermosets consist of hard regions enclosed in a soft matrix. [1]

Early scanning electron microscopy studies on fracture surfaces of thermosets suggested a *nodular morphology*, i.e., there appeared small spherical bumps with diameters in the range of 50 nm [2]. In the late 1970s, higher resolved transmission electron microscopy images of C–Pt replicas of fracture surfaces of mostly amine-cured epoxy contributed to the hypothesis that a nodular morphology was formed in the fracture process [3–7]. Similar nodular structures were observed on surfaces created by chemical etching [3, 5], microtomy [8], as well as on surfaces created by removal of a substrate and on free surfaces [3].

This nodular morphology was in these cases interpreted as an indication of an inhomogeneous molecular network structure. It was suggested that a crack propagating through epoxy would follow a low-energy path, breaking as few cross-links as possible. The crack would therefore propagate through the areas with the lower cross-link density. Similar hypotheses were invoked to explain why a nodular morphology was visible on differently prepared surfaces (e.g. surfaces from chemical etching).

However, most published indications for an inhomogeneous network structure in epoxies are contradicted by other reports or can be interpreted in different ways. For example, some small-angle electron or neutron scattering measurements yielded the conclusion that epoxy was inhomogeneous [9–11], while others using similar epoxy systems led to the opposite conclusion [12, 13].

Dušek *et al.* [14, 15] explained the observed nodular morphology with artifacts arising from the sample preparation and/or the investigation by electron microscopy. They showed that similar – apparently nodular – electron microscopy images were obtained when replicas of etched fracture surfaces of amorphous thermoplastics were investigated, which are generally supposed

to be homogeneous [16]. Based on this set of investigations, it was concluded that there was neither nodular morphology nor inhomogeneous cross-link density in cured epoxy. [14, 15]

Atomic force microscopy (AFM) was used for the first time by VanLandingham *et al.* to investigate the nanometer-scale morphology of epoxy. They studied the influence of the amine content on the nodular morphology [17]. This work was followed by several investigations of thermoset fracture surfaces with AFM [9, 10, 18–22]. Recently, Sahagun and coworkers published a series of detailed investigations on the nodular morphology on fracture surfaces of cured epoxy resins by AFM [1, 23–27]. Duchet and Pascault showed, however, that apparently nodular structures might as well be due to an inevitable AFM artifact that is caused by worn or contaminated AFM tips and rough surfaces [28].

Besides the experimental work, theoretical explanations for possible inhomogeneous curing of thermosets were discussed. It was argued that thermosets cured in a step-growth polymerization, like amine-cured epoxies, may not generally exhibit an inhomogeneous network structure, while those cured in a chain-growth polymerization, like polyester resins cured with free radicals, do so [15, 29, 30]. This was explained with the mechanism of the chain-growth polymerization process.

The aim of this work was to stress the hypothesis that a nodular morphology forms in chain-growth polymerized epoxy which results in an inhomogeneous modulus distribution. The recently developed AFM mode *Peak-Force Tapping* was used to measure moduli at the nanometer scale. Special attention was drawn to the detection of possible AFM artifacts. For that purpose, differently prepared surfaces (i.e., with different surface roughness) of the same material were compared, as well as different AFM probes and contact forces which were supposed to affect the results. Finally, supposedly differently inhomogeneous polymers were compared.

2.4 Experimental

2.4.1 Materials

The chosen epoxy system was an anhydride-cured epoxy, catalyzed by a tertiary amine. The chemical structures of its components are given in fig. 2.1. The epoxy resin was a diglycidyl ether of bisphenol A (DGEBA, trade name *Epikote 828 LVEL*) with an epoxide group content of 5.4 mol/kg, the curing agent was a methyl-tetrahydrophthalic anhydride (MTHPA, with the trade name *Epikure 3601*) with an anhydride group content of 6.0 mol/kg and 1-methyl imidazole (trade name *Epikure Catalyst 201*) was used as the tertiary amine catalyst. All materials were delivered by *Momentive* (USA).

The cure reaction is initiated by the reaction of the imidazole with the epoxy ring, creating a zwitterion. This reacts with an anhydride group that, in turn, reacts with an epoxide group again, and so on. The reaction is strictly alternating. It is important to mention that its exact course is still subject to debate [31]. As the used epoxy is bi-functional, the reaction results in a three-dimensional molecular network.

Most measurements were conducted on samples from one single epoxy plate in order to avoid possible influence of the material's production process. Unless mentioned, all presented images are from this plate. For its production stoichiometric amounts of DGEBA (100 parts) and MTHPA (89.2 parts) were stirred for 10 min with a mechanical overhead mixer at 6000 rpm in vacuum. Afterwards, 2.00 parts of the imidazole catalyst were stirred in for further 10 min at 6000 rpm in vacuum. The material was cast into a $120 \times 160 \times 4\,\mathrm{mm}^3$ steel mold and cured at 120 °C for 8 h.

Furthermore, the same process was repeated with only 0.100 parts imidazole catalyst in order to test if a low catalyst content (corresponding to a

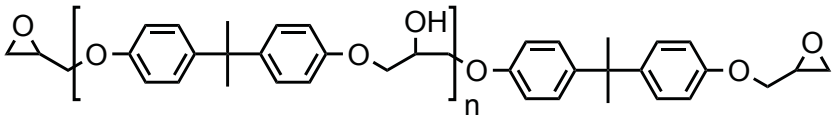

n = 0 (88%); n = 1 (10%); n = 2 (2%)

(a) DGEBA epoxy resin

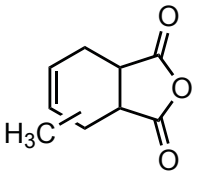

(b) MTHPA

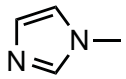

(c) imidazole

Figure 2.1: The chemical structures of the investigated epoxy system's components

low initiation rate) leads to the formation of a more inhomogeneous network structure, as it was assumed for chain-growth polymerizations [30, 32].

Besides that, polystyrene (PS) and polymethylmethacrylate (PMMA) were investigated as examples of amorphous thermoplastics, as well as an unsaturated polyester (UP) resin and a inter-penetrating network (IPN). Their manufacturing is explained in the Supporting Information section.

2.4.2 Surface preparation

Fracture surfaces were produced by manual fracturing. For that purpose, roughly $5 \times 5 \times 30\,mm^3$ bars were cut from the plates and a pre-crack of about 3 mm was introduced with a sharp blade. The unfractured samples were glued to an AFM sample holder disc with an instant adhesive before. They were fractured immediately before the AFM measurement by slowly bending them until fracture.

The manually-fractured samples were compared with fracture surfaces created in single-edge-notched bending (SENB) tests, which were performed

according to the respective ISO standard [33] and no qualitative differences could be observed, suggesting that manual fracturing provides representative fracture surfaces. Likewise, retests after several weeks showed no qualitative differences in the AFM results, suggesting that time is not a critical factor.

Ultramicrotome cutting was done in order to obtain as flat and smooth surfaces as possible with as little contamination and shearing as possible. Instead of keeping the ultramicrotome-cut sections, the remaining stub was used for AFM investigation. Ultramicrotome cuts of approx. $200 \times 200\,\mu m^2$ were made at room temperature with a *Reichert-Jung Ultracut ultramicrotome* using a *Diatome Ultra* 35° diamond blade at 1 mm/s. The quality of the used ultramicrotome blade was determining for the resulting surface roughness.

2.4.3 AFM operation

AFMs are primarily used to obtain topographic information of solid surfaces at the nanometer scale and below. A sharp tip mounted on a cantilever touches the surface which causes the cantilever to deflect. This deflection is proportional to the forces acting between the AFM tip and the investigated surface; the proportionality factor is the cantilever's *spring constant*. The magnitude of these forces can provide additional, non-topographic information on the sample's properties. [34]

All AFM measurements presented here were done on a *MultiMode 8* AFM from *Bruker* in the *Peak-Force Tapping* mode. This mode allows measuring not only the topography of a surface, but also some of its mechanical properties.

The *peak force* F_{peak} is the maximum force between the AFM tip and the sample in a single contact event. In the Peak-Force Tapping mode, F_{peak} is controlled during the scan, which allows scanning at given (low) contact

forces. Moreover, force–distance curves are recorded for every single contact between the AFM tip and the sample. This mode is essentially an extension of the *pulsed-force mode* with improved force resolution [35].

Besides the sample height Z, the most important measured values for this work are the Young's modulus E_s (hereafter called *modulus*) and the adhesion force F_{adh} (hereafter called *adhesion*), which is the maximum attractive force in a contact event. The modulus is determined by fitting the force–distance curves to a Derjaguin–Muller–Toporov (DMT) model [36]. This model approximates the AFM tip as a sphere with radius R pressing into a flat surface and links the contact force $F(d)$ and deformation $(d_0 - d)$ to the material's reduced modulus E^*:

$$F(d) = \frac{4}{3} E^* \sqrt{R \cdot (d_0 - d)^3} - F_{adh} \tag{2.1}$$

E_s was calculated by $E_s = E^*/(1-\nu_s^2)$ assuming a Poisson's ratio of $\nu_s = 0.35$. The DMT fit was applied to the *retract* curve in the range where $(F + F_{adh})$ was within 30 % and 90 % of $(F_{peak} + F_{adh})$ (see fig. 2.2). For a more detailed explanation of the Peak-Force Tapping technique the reader is referred to the literature [35, 37].

All images presented here have 512×256 pixels and a scan size of $1000 \times 500\,\mathrm{nm}^2$; they were obtained at a scan rate of 1000 nm/s. The AFM measures each scan line twice; the first scan is called *trace* and the second one, which runs in the opposite direction, *retrace*. For all images presented here, the two scans were in good agreement with each other. If not mentioned explicitly, all presented images and curves were taken from the retrace scan.

The measurements were recorded with two different AFM probes, both of which had been manufactured by *Bruker AFM Probes* (USA). The trade name of the first probe is *ScanAsyst-Air*. It has a relatively soft triangular silicon-nitride cantilever, with a nominal spring constant of 0.4 N/m, and a very sharp

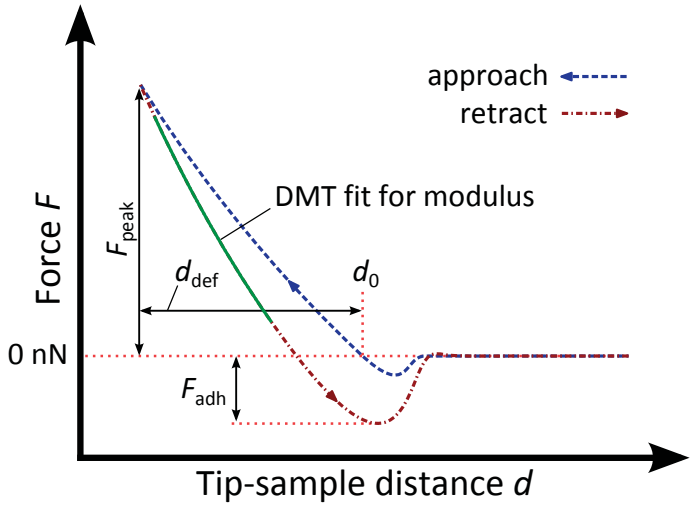

Figure 2.2: Peak-Force Tapping evaluation from the AFM force–distance curves (schematic). The software calculates the sample's height Z, the peak force F_{peak}, the adhesion force F_{adh} and the peak deformation d_{def}. The reduced modulus E^* is calculated from the DMT fit of the retract curve.

nominal tip radius of 2 nm. Whenever this probe was used, the contact force was kept below 1 nN to avoid that the tip gets blunt and to conserve the high lateral resolution it can provide. This will hereafter be called *soft contact* scanning. It is not possible to measure a modulus at these low forces due to the low d_{def} and accordingly bad agreement with the DMT model.

The second probe has the trade name *RTESPA*, a nominal spring constant of 40 N/m and a nominal tip radius of 8 nm. This is a frequently used rectangular silicon probe type for the investigation of epoxies. This probe was used at contact forces around 50 nN, which will hereafter be called *hard contact* scanning.

In order to measure a sample's modulus, the spring constant of the probe's cantilever must be chosen in a way that the sample and the cantilever deform by comparable displacements in a usual contact process. The cantilever of the

RTESPA probe deformed approximately twice as much as the epoxy sample in a usual contact process, which is why this probe was considered to be suitable.

In order to calculate the actual contact forces, the spring constant of the probe's cantilever is needed. It was estimated with the *thermal sweep* method [38]. While the exact spring constant of stiff cantilevers cannot be determined by this method [39], it can serve as a rough estimate and help to estimate the actually occurring forces better than by using the nominal spring constants. This is important for the adhesion force measurements.

However, such a rough estimation would not be sufficient to estimate a sample's modulus. As there are several influential factors affecting the modulus measurement with the Peak-Force Tapping technique, it is recommended to do a calibration measurement on a reference sample with known modulus, and to adjust the fit parameters in a way that this modulus is obtained. A purpose-made PS calibration reference sample with a nominal modulus of 2.7 GPa was used here. The contact forces were chosen in a way that the average peak deformation d_{def} was between 2 nm and 3 nm. The standard deviations in the modulus $s(E_{\mathrm{s}})$ measured on clean regions on this sample were in the range of 4 % to 9 % of the image's mean modulus $\bar{E}_{\mathrm{s}}$. Hence, a coefficient of variation $\hat{c}_{\mathrm{v}}(E_{\mathrm{s}}) = s(E_{\mathrm{s}})/\bar{E}_{\mathrm{s}}$ as low as that is representative of the measurement inaccuracy.

It must be emphasized that the moduli obtained after such a calibration are only relative values, i.e. the absolute modulus values presented here might differ considerably from the samples' real moduli [35]. Moreover, the AFM tip radius may change during the measurement. This is why the average moduli in images presented below vary. Nevertheless, the relative modulus differences within single images are representative.

On the nanometer scale, no qualitative differences were found between different regions of the fracture surfaces, independently of their distance to the pre-crack. Relatively flat regions were chosen for the investigation as slanted

surfaces are a major challenge for AFM investigation. The scan angle was chosen in a way that there was a small height difference in the fast scan axis, i.e. the slow scan axis was parallel to the sample's height gradient. That way the sample tracking quality was maximized.

All automatic AFM image post-processing was turned off. Every AFM height image was manually post-processed by a linear *line fit* procedure. This procedure removes each scan line's tilt individually and subtracts its mean height value. This step works as an improved plane fit. None of the non-topographic output images was post-processed.

In order to give additional information of the investigated samples' surface roughnesses the arithmetic average roughness R_a was calculated from these post-processed AFM height images via $R_a = N^{-1} \sum_{n=1}^{N} |\Delta Z_n|$. Here, n are the individual pixels in the image, N is the total number of pixels, and ΔZ_n is the difference between the height Z of n and the image's mean height. While more sophisticated roughness parameters exist [40], we chose R_a as it was also used by Duchet and Pascault [28] and can therefore be compared with their work more easily. It must be mentioned that roughness values can be ambiguous as they depend on the way the images were created. Moreover, the calculated roughness value depends strongly on the image size and on the number of pixels. Hence, R_a will be given here only for rough statements on the surface roughness, and only for images with a scan size of $1000 \times 500\,\mathrm{nm}^2$ and 512×256 pixels.

2.5 Results and Discussion

2.5.1 Measurements on fracture surfaces

Scanning the epoxy fracture surface with hard contact yields the results presented in fig. 2.3. The fracture surfaces are relatively rough for highly-resolved

AFM investigation ($R_a = 3.6\,\text{nm}$). The height image seems to show a clear nodular morphology, similar to what has been reported in literature. Both the modulus and the adhesion image seem to show strong inhomogeneities ($\hat{c}_v(E_s) = 24\,\%$).

However, there seems to be a soft-in-hard structure on this surface, which is in contrast to several statements in the literature which claim that there was a hard-in-soft structure [17, 21, 41]. This contradiction is crucial, as it cannot be explained by the hypothesis that the nodular morphology is caused by highly cross-linked regions within a weakly cross-linked matrix.

An entirely different image is obtained when the same surface (and approximately the same region on that surface) is scanned with soft contact. In this mode, it is not possible to measure moduli anymore, but one can use significantly sharper AFM tips (2 nm instead of 8 nm nominal tip radius), providing much higher spatial resolution. An image taken in that mode is presented in fig. 2.4. The surface appears rougher compared to the less sharp AFM probe ($R_a = 6.0\,\text{nm}$), suggesting that more surface details were observed now. For the same reason the z-scale is extended in this image.

Again, there seems to be a nodular morphology, but the nodules appear much smaller now when compared to the hard contact image, although the very same surface was scanned at approx. the same position. This shows that the apparent nodules in fig. 2.3 are imaging effects rather than surface features, as these would yield comparable images independently of the imaging mode.

This can easily be explained by a well-known AFM artifact, called *tip convolution* or *dilation* [42]: The AFM tip has a finite diameter, so that the measured shapes of surface features are always a combination of their real shapes and the shape of the AFM tip. Fig. 2.5 schematically shows how a rough surface (e.g., a fracture surface) appears to consist of small spheres when it is scanned by an AFM tip of comparable dimensions. Further, it can be speculated that

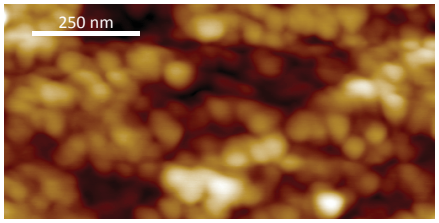

(a) Height Z

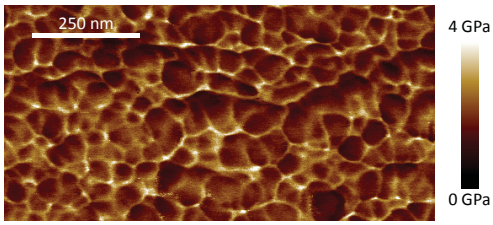

(b) Modulus E_s

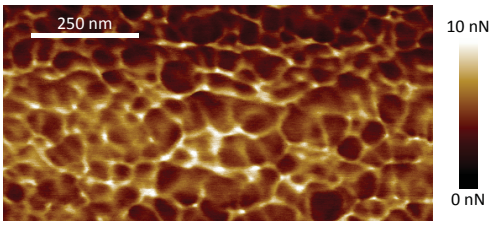

(c) Adhesion F_{adh}

Figure 2.3: Typical Peak-Force Tapping images of an epoxy fracture surface for hard contact scanning. The height image seems to exhibit a nodular structure and both modulus and adhesion seem to show distinct inhomogeneities. Notice that the modulus image appears to indicate soft regions in a hard matrix.

the apparently nodular morphology in fig. 2.4 is possibly due to the same artifact as well, albeit at another size.

It is important to understand that the tip-convolution artifact is not only caused by the relatively large AFM tip radii, but also by the relatively rough surface. If the investigated surfaces were smoother, this artifact would widely disappear, even if measured with the same AFM tip. It is important to emphasize that the observed nodules do reflect real surface features, but their shape might be different. However, it is the apparently nodular shape that was frequently interpreted as a sign for inhomogeneities in literature.

Already a decade ago, Duchet and Pascault showed that the morphology of surfaces imaged via AFM appears to be nodular if the investigated surfaces are not sufficiently smooth and if the used AFM tip is not freshly cleaned [28].

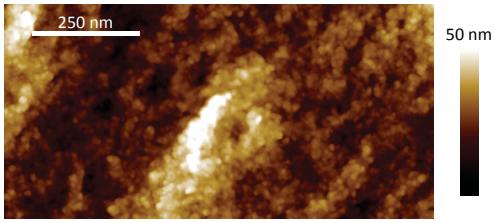

Figure 2.4: Peak-Force Tapping height image of the same surface as in fig. 2.3, scanned with soft contact. The nodular morphology appears again, but the nodules are smaller this time.

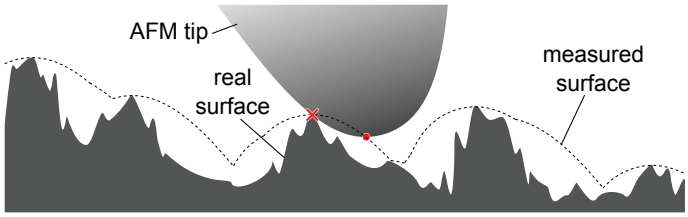

Figure 2.5: Schematic illustration of tip convolution when scanning a rough surface. The small red circle (●) highlights the supposed contact point, while the red cross (✕) highlights the real contact point between the AFM tip and the sample.

Indeed, the images here indicate that also sharp, fresh AFM tips will cause a rough surface to appear nodular, though on another scale. Cleaning the AFM tips as recommended by Duchet and Pascault reduces this artifact, but it cannot be avoided completely.

The tip-convolution artifact is critical exclusively if the interaction geometry of the AFM tip is comparable to the geometry of the features on the investigated surface. It plays only a minor role if the surface features are either much smaller or much larger than the AFM tip. Hence, the material's morphology appears to be nodular if the surface roughness is within a given range for a given AFM tip radius.

This is probably the reason why there is only scant literature reporting a correlation between material properties and the formation of a nodular mor-

phology [1, 17, 19, 26]. It is possible that in those few cases differently brittle materials, and hence differently rough surfaces were compared with each other.

Etching of epoxy surfaces with ion beams was frequently used as a surface preparation method for subsequent investigation via AFM [22, 43, 44]. It must, however, still be proven that the presented structures are more than just artifacts, considering how common artifacts are on etched polymer surfaces [45]. As the created surfaces are often very rough, it is indeed likely that the images are afflicted by tip convolution.

It is very likely that all or at least most reports in literature on the nodular morphology of epoxy fracture surfaces measured by AFM are afflicted by the tip-convolution artifact. However, various authors reported a similar nodular morphology which they found in electron microscopy images. Highly resolved images at that time were usually obtained by C–Pt replication [3–7]. It should be investigated if this replication process could result in a similar artifact that causes non-spherical features to appear nodular as well.

2.5.2 Artificially inhomogeneous modulus and adhesion

The emphasis of this work lies on investigating modulus inhomogeneity in cured epoxy thermosets, as it seems to be visible in fig. 2.3b. However, there is a strong correlation between the height image and both the modulus and the adhesion. It is known that non-topographic AFM images (e.g. phase-contrast images) must be interpreted cautiously if they correlate strongly with the topography [34].

A clearer impression of these correlations can be deduced from line profiles, like the one presented in fig. 2.6. From those curves, it is obvious that both the modulus and the adhesion are highest in topographic valleys (for both trace and retrace scans). As has been pointed out, these apparent valleys are prob-

ably afflicted by tip convolution and their real shape might deviate strongly from the one we measured. It is therefore likely that also the non-topographic output data are afflicted by the same artifact.

This assumption is supported by Peak-Force Tapping images of fractured amorphous thermoplastics. In fig. 2.7 the fracture surface of PMMA is depicted as an example. Due to its higher fracture toughness K_{IC} ($K_{IC,PMMA} \approx 2 \cdot K_{IC,epoxy}$), the PMMA's fracture surface is much rougher than that of epoxy ($R_{a,PMMA} = 11.5\,nm$). We can easily recognize an apparently nodular morphology analogous to that on epoxy fracture surfaces. PS fracture surfaces were still much rougher ($R_{a,PS} = 69\,nm$, images given in the Supporting Information), so that their measurement with AFM was even more problematic. As amorphous thermoplastics are not cross-linked, these apparently nodular morphologies cannot be explained by inhomogeneous cross-linking.

This observation is in good agreement with the findings of Dušek *et al.* [14] and contradicts the findings of Sahagun [23] who claimed that there was no nodular morphology on PS fracture surfaces. It must be mentioned that the AFM scans presented by Sahagun showed a very smooth fracture surface. It is possible that the type of PS was in this case much more brittle than the one used here, resulting in the smooth fracture surface and therefore in the absence of an apparently nodular morphology. [14, 23]

Moreover, there are also apparent inhomogeneities visible in the modulus of the PMMA ($\hat{c}_v(E_s) = 23\,\%$). It seems rather unlikely that the modulus of PMMA is in fact that strongly inhomogeneous [16]. This suggests that not only the nodular morphology is (at least partly) due to artifacts, but also the measured modulus inhomogeneities.

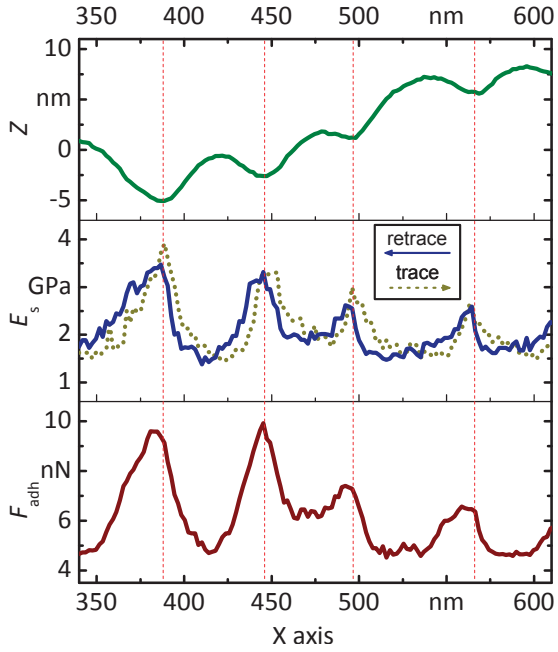

Figure 2.6: Line profiles of the height Z, the modulus E_s and the adhesion F_{adh} from part of one line of the image in fig. 2.3. The measured moduli in the two scan directions agree rather well with each other. Both modulus and adhesion are highest in topographic valleys.

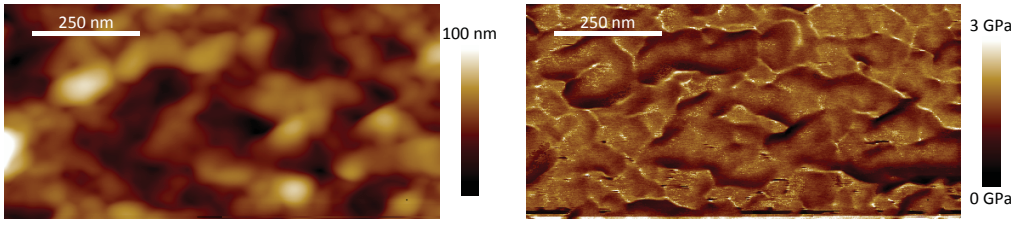

(a) Height Z (b) Modulus E_s

Figure 2.7: Peak-Force Tapping images of fractured PMMA. Although PMMA is supposed to be homogeneous [16], there are strong apparent inhomogeneities measurable.

2.5.3 Origin of apparent modulus inhomogeneities

One might argue that the apparent modulus inhomogeneities may be due to variations in F_{peak}. It will be discussed in the Supporting Information why this seems unlikely to be the case.

The origin of these apparent inhomogeneities becomes clear from the schematic in fig. 2.8: In fig. 2.8a the AFM tip touches the rough surface in only one single contact point. The touching feature on the surface will deform relatively strongly, giving the appearance of a relatively soft material. In fig. 2.8b, in contrast, there are two contact points, so that there is a stronger resistance against deformation. The material appears stiffer here.

It is well-known that the tip–sample contact area is of major importance for the determination of moduli via AFM [46]. This variation in the tip–sample contact area is supposedly the reason for the measured modulus appearing higher in topographic valleys. Likewise, the differently large contact area leads to different measured adhesions as well [47, 48], as adhesion is related to the tip–sample contact area. Hence, also the apparent inhomogeneity in the adhesion can be explained by this hypothesis.

2.5.4 Measurement of ultramicrotome cuts

Many of the artifacts mentioned above are caused by the high surface roughness of the fracture surfaces. The PS reference sample the AFM was calibrated on has a surface roughness of $R_{\text{a,ref}} \approx 0.5\,\text{nm}$. In order to measure modulus distributions reliably, similarly smooth surfaces are necessary.

Duchet and Pascault were criticized for using free surfaces as these might not represent the bulk material's properties [10, 28]. In order to dispel such doubts a representative cross-section of the material is necessary. However, most surface-preparation techniques that are used to provide smooth cross-

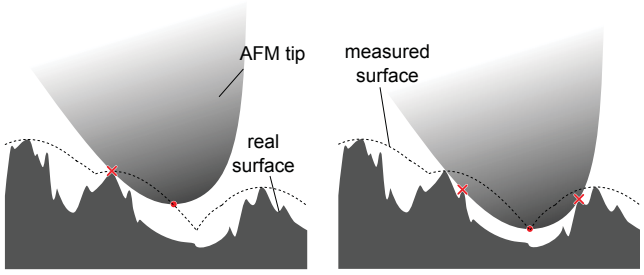

(a) *Soft* region (b) *Hard* region

Figure 2.8: Scheme of an AFM tip scanning a rough surface. The small red circles (●) highlight which point is supposed to touch the sample surface; the red crosses (✕) highlight the actual contact points between the AFM tip and the sample. In apparent valleys, like in (b) the AFM tip touches the sample in several points at once.

sections contaminate the created surface, shear it strongly, or heat it up; each of these effects is undesired. Moreover, most did not result in sufficiently low roughness.

Surfaces created by focused-ion-beam milling, for example, were smooth only in the direction parallel to the ion beam and might be contaminated with Ga. Surfaces from Ar^+-ion etching were very smooth at the nanometer scale but not sufficiently flat at the micrometer scale. Moreover, both techniques heat the treated surface and it cannot be excluded that this affects the material's chemistry. Mechanical polishing contaminates the surface with water and shears it strongly, and the resulting surface roughness was in the best cases around $R_{\mathrm{a,polished}} \approx 1.4\,\mathrm{nm}$. In contrast, ultramicrotome cutting is a technique that provides very smooth surfaces at minimal shear and without contamination or heating. We suppose, therefore, that it provides the most representative cross-sectional information for the bulk material.

AFM topography images of one single epoxy ultramicrotome cut were gathered both with soft contact (fig. 2.9) and with hard contact (fig. 2.10a). Both

images confirm that the surface is very smooth ($R_{a,soft} = 0.38\,nm$, $R_{a,hard} = 0.29\,nm$).

In contrast to the claims of Aspbury and Wake [8] there was no nodular morphology visible on most ultramicrotome cuts. However, if the used ultramicrotome blade was not sufficiently sharp, the resulting surface roughness was much higher ($R_a > 1\,nm$). In these cases the surface appeared to be nodular indeed. However, this morphology changed strongly depending on the used AFM tip, suggesting that it is, again, not a material property but an artifact caused by the higher surface roughness. Smooth ultramicrotome-cut samples ($R_a < 0.5\,nm$) never appeared to be nodular.

There are many tiny bumps visible with soft contact scanning that do not appear for hard contact. Comparison of trace and retrace images shows that these bumps are not due to noise, but they represent real surface features. Supposedly, these bumps are compressed when imaged at hard contact and therefore only visible at soft contact. Nevertheless, these surfaces are considered sufficiently smooth for modulus measurements as they are of similarly low roughness as the PS reference sample.

The modulus and adhesion distribution on the epoxy ultramicrotome cut, as given in fig. 2.10, are very homogeneous. The coefficient of variation $\hat{c}_v(E_s)$ in the modulus is 4.9 % and therefore as low as the one measured on the PS ref-

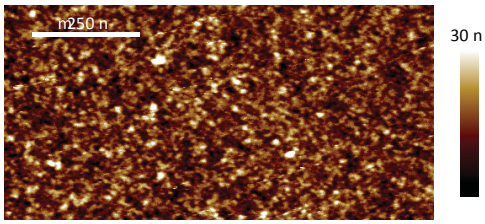

Figure 2.9: AFM height image of an epoxy ultramicrotome cut, scanned with soft contact. Although the surface roughness is very low, there are small features that are not visible when scanned with hard contact.

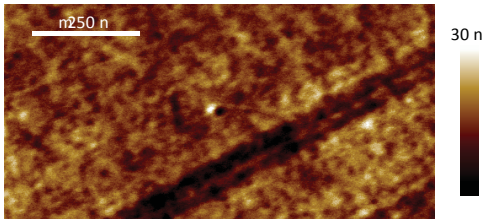

(a) Height Z

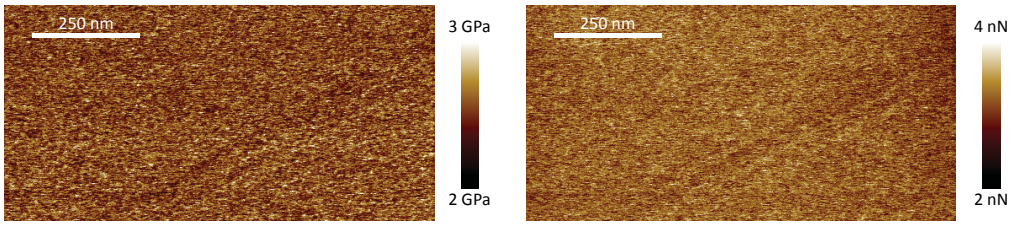

(b) Modulus E_s (c) Adhesion F_{adh}

Figure 2.10: Peak-Force Tapping images of an epoxy ultramicrotome cut, scanned with hard contact. The surface was very smooth. A scratch from the ultramicrotome cutting is visible and has a slight influence on the measured modulus and adhesion. The modulus variations were as low as on the PS reference sample.

erence sample. The discrepancy between these images and those obtained on fracture surfaces shows that the surface preparation has substantial influence on the measured modulus distribution. The images of the ultramicrotome cuts are probably much more representative than images of rougher surfaces.

2.5.5 Further investigated thermosets

Subsequently, thermoset materials were investigated that have been claimed to be inhomogeneous in literature: For example, it was frequently reported that thermosetting polymers cured in a chain-growth polymerization cure reaction exhibit inhomogeneities in their molecular network structure [15, 29, 30, 32]. In particular, inhomogeneities are expected if the materials are cured at low initiator contents [30, 32]. As presented, we could not verify that

there were modulus inhomogeneities in anhydride-cured epoxy when cured at usual catalyst contents. Fig. 2.11 shows the Peak-Force Tapping images of an epoxy with low catalyst content. Again, the material does not appear to be inhomogeneous ($\hat{c}_v(E_s) = 4.3\,\%$).

Likewise, UP resins were often mentioned as an example of inhomogeneously curing thermosetting polymers [29, 30]. A Peak-Force Tapping image of such a UP resin ($R_{a,UP} = 0.25\,\text{nm}$) is given in fig. 2.12; once again, there are no inhomogeneities visible ($\hat{c}_v(E_s) = 8.7\,\%$).

The supposedly most inhomogeneous material we investigated was the IPN, a mixture of epoxy and UP-resin, cured simultaneously. Such IPNs were found elsewhere to exhibit strong inhomogeneities at scales around 50 nm [22]. The resulting Peak-Force Tapping images are presented in fig. 2.13. The variations are once again very low ($R_{a,UP} = 0.31\,\text{nm}$, $\hat{c}_v(E_s) = 6.5\,\%$). As the modulus variations are in the same range as those in the PS reference sample, we cannot conclude from these images that the material is inhomogeneous.

The histograms of the modulus images are summarized in fig. 2.14. Mind that the average modulus values are not representative. For example, the real modulus of the low-catalyst-content epoxy is most likely comparable to the one of the standard epoxy. In contrast, the relative scattering allows con-

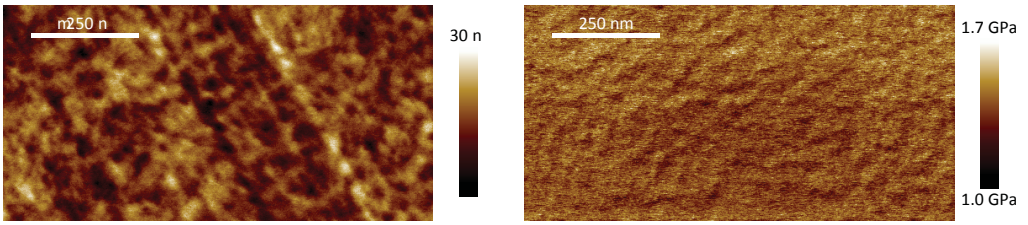

(a) Height Z (b) Modulus E_s

Figure 2.11: Peak-Force Tapping images of an ultramicrotome cut of an epoxy cured with a low catalyst content.

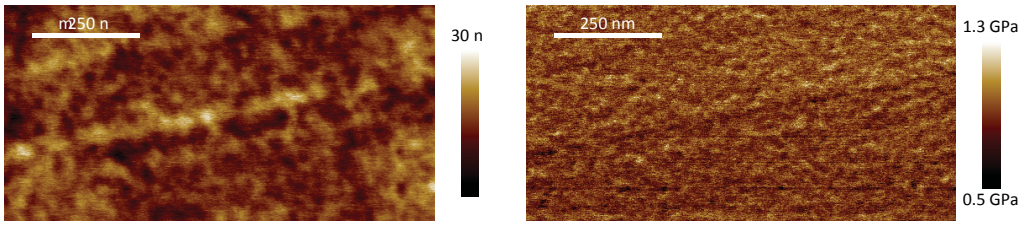

(a) Height Z (b) Modulus E_s

Figure 2.12: Peak-Force Tapping images of an ultramicrotome cut of an UP-resin.

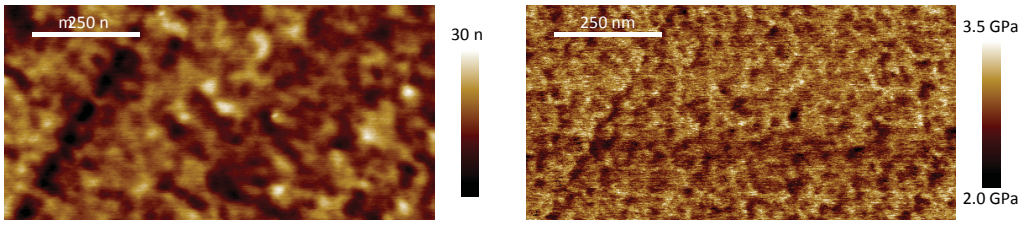

(a) Height Z (b) Modulus E_s

Figure 2.13: Peak-Force Tapping images of an ultramicrotome cut of a IPN, a mixture of epoxy and UP-resin, cured simultaneously. This material was supposed to be particularly inhomogeneous. However, only minor variations in the modulus could be observed.

clusions on the homogeneity of the material. Clearly, modulus images from fracture surfaces appear much more inhomogeneous than those from ultramicrotome cuts do. The scatter of the modulus values of all ultramicrotome cuts was comparable to the one of the PS reference. In the image of the UP resin ultramicrotome cut, the modulus values were more discrete than in the others, but the scatter was still low. The modulus values of the most images approximate a normal distribution, suggesting that deviations from the mean are mostly statistical.

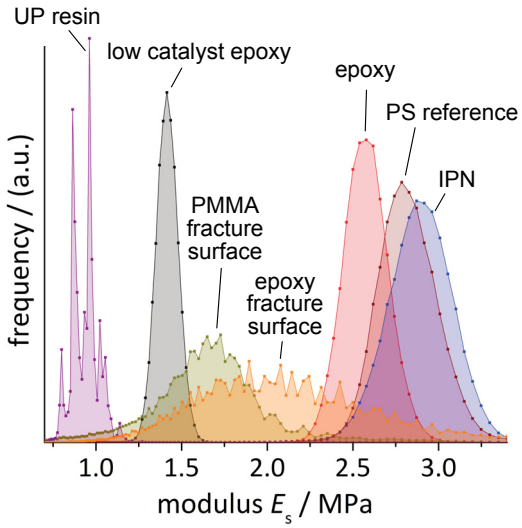

Figure 2.14: Histograms of the presented modulus images, plus the one of the PS reference sample. Except for the fracture surfaces and the PS reference sample, all histograms are from modulus images of ultramicrotome cuts.

2.5.6 Are cured thermosets inhomogeneous?

The comparison with ultramicrotome cuts shows that fracture surfaces, like all rough surfaces, are not suitable for measuring the modulus distribution in a material. This is probably due to the variations in the tip–sample contact area and a consequently poor agreement with the DMT model. Observations of an inhomogeneous modulus distribution on rough thermoset surfaces measured by AFM phase-contrast imaging [17, 28] must, therefore, be interpreted carefully.

No ordered inhomogeneities beyond the scale of the PS reference sample could be detected on any of the investigated surfaces. Thus, the investigated materials are considered homogeneous, or else the possibly existing inhomogeneities are too small in their magnitude or in their lateral dimensions to be measured with the Peak-Force Tapping technique.

Future work dealing with AFM imaging of possible inhomogeneities shall avoid that results are afflicted by artifacts. For that purpose, the following measures are proposed:

- Apparently nodular morphologies should be verified by measurements with differently sharp AFM probes in order to detect a possible tip-convolution artifact.
- Non-topographic AFM results should be verified on smooth surfaces, e.g. ultramicrotome cuts.
- It may be worthwhile to compare supposedly inhomogeneous materials with identically prepared homogeneous materials, e.g. amorphous thermoplastics.

2.6 Conclusion

It has long since been speculated that thermosets, in particular epoxy, exhibit a *nodular morphology*, that is to say, that they consist of hard regions of higher cross-link density enclosed in soft regions of lower cross-link density. In order to measure this hypothetically inhomogeneous modulus distribution, epoxy surfaces from fracture and ultramicrotome cuts and other polymers were investigated with AFM in the *Peak-Force Tapping* mode. The following conclusions can be drawn:

- The reported nodular morphology on differently prepared epoxy surfaces is most likely due to an AFM artifact. This has be demonstrated by imaging of the same surface with differently sharp AFM tips.
- A variation in the tip–sample contact area causes an apparently inhomogeneous modulus distribution on rough surfaces. Even amorphous

thermoplastics appear to be inhomogeneous if the investigated surface is not sufficiently smooth.

- Ultramicrotome cutting seems to be a suitable alternative for the preparation of a smooth cross section for further measurement of the modulus distribution in epoxy. It yields very smooth surfaces at minimum shearing and without contamination.
- Neither the investigated epoxy system, regardless of its catalyst content, nor any of the other investigated polymers seems to be inhomogeneous in their modulus.

Future work on the determination of inhomogeneities in thermosetting polymers via AFM should compare differently sharp AFM tips as well as differently prepared surfaces. Supposedly homogeneous materials should be used as counterexamples.

Acknowledgments

We would like the acknowledge Anja Huch for her experimental support with the ultramicrotome cutting and Ulrich Müller for fruitful discussions on AFM.

Supporting information

Supporting information related to this chapter can be found in section 8.1.

References

[1] C. M. Sahagun and S. E. Morgan, "Thermal control of nanostructure and molecular network development in epoxy–amine thermosets", *ACS Appl. Mater. Interfaces*, vol. 4, no. 2, pp. 564–72, 2012. DOI: 10.1021/am201515y.

[2] E. H. Erath and R. A. Spurr, "Occurrence of globular formations in thermosetting resins", *J. Polym. Sci.*, vol. XXXV, pp. 391–399, 1959. DOI: 10.1002/pol.1959.1203512907.

[3] J. L. Racich and J. A. Koutsky, "Nodular structure in epoxy resins", *J. Appl. Polym. Sci.*, vol. 20, pp. 2111–2129, 1976. DOI: 10.1002/app.1976.070200808.

[4] J. L. Racich, "Thermoset layers in thermoset adhesives", PhD Thesis, University of Wisconsin–Madison, 1977.

[5] J. S. Mijović and J. A. Koutsky, "Correlation between nodular morphology and fracture properties of cured epoxy resins", *Polymer*, vol. 20, pp. 1095–1107, 1979. DOI: 10.1016/0032-3861(79)90301-X.

[6] J. S. Mijović and J. A. Koutsky, "The effect of postcure time on the fracture properties and nodular morphology of an epoxy resin", *J. Appl. Polym. Sci.*, vol. 23, no. 4, pp. 1037–1042, 1979. DOI: 10.1002/app.1979.070230408.

[7] J. S. Mijović and L. Tsay, "Correlations between dynamic mechanical properties and nodular morphology of cured epoxy resins", *Polymer*, vol. 22, pp. 902–906, 1981. DOI: 10.1016/0032-3861(81)90265-2.

[8] P. J. Aspbury and W. C. Wake, "The supermolecular structures found in cured epoxy resins", *Br. Polym. J.*, vol. 11, no. March, pp. 17–27, 1979. DOI: 10.1002/pi.4980110105.

[9] X. Gu, D. Raghavan, D. L. Ho, *et al.*, "Nanocharacterization of surface and interface of different epoxy networks", in *MRS Proceedings*, vol. 710, 2002, pp. DD10.9.1–DD10.9.6. DOI: 10.1557/PROC-710-DD10.9.1.

[10] X. Gu, T. Nguyen, M. Oudina, *et al.*, "Microstructure and morphology of amine-cured epoxy coatings before and after outdoor exposures—an AFM study", *JCT Research*, vol. 2, no. 7, pp. 547–556, 2005. DOI: 10.1007/s11998-005-0014-x.

[11] R. J. Matyi, D. R. Uhlmann, and J. A. Koutsky, "Structure of glassy polymers. VII. Small-angle X-ray scattering from epoxy resins", *J. Polym. Sci., Part B: Polym. Phys.*, vol. 18, no. 5, pp. 1053–1063, 1980. DOI: 10.1002/pol.1980.180180512.

[12] S. J. Bai, "Crosslink distribution of epoxy networks studied by small-angle neutron scattering", *Polymer*, vol. 26, no. 7, pp. 1053–1057, 1985. DOI: 10.1016/0032-3861(85)90228-9.

[13] J. D. LeMay and F. N. Kelley, "Structure and ultimate properties of epoxy resins", in *Epoxy resins and composites III*, ser. Advances in polymer science, vol. 78, Springer, 1986, pp. 117–118, ISBN: 978-3-540-15936-0. DOI: 10.1007/BFb0035359.

[14] K. Dušek, J. Pleštil, F. Lednický, and S. Luňák, "Are cured epoxy resins inhomogeneous?", *Polymer*, vol. 19, pp. 393–397, 1978. DOI: 10.1016/0032-3861(78)90243-4.

[15] K. Dušek, "Are cured thermoset resins inhomogeneous?", *Angew. Makromol. Chem.*, vol. 240, pp. 1–15, 1996. DOI: 10.1002/apmc.1996.052400101.

[16] E. W. Fischer, J. H. Wendorff, M. Dettenmaier, G. Lieser, and I. Voigt-Martin, "Chain conformation and structure in amorphous polymers as revealed by X-ray, neutron, light and electron diffraction", *J. Macromol. Sci., Part B: Phys.*, vol. 12, no. 1, pp. 41–59, 1976. DOI: 10.1080/00222347608215172.

[17] M. R. VanLandingham, R. F. Eduljee, and J. R. Gillespie, "Relationships between stoichiometry, microstructure, and properties for amine-cured epoxies", *J. Appl. Polym. Sci.*, vol. 71, pp. 699–712, 1999.

[18] T. Nguyen, X. Gu, M. R. VanLandingham, *et al.*, "Characterization of coating system interphases with phase imaging AFM", in *24th annual meeting of the adhesion society*, 2001, pp. 68–70.

[19] M. Giraud, T. Nguyen, X. Gu, and M. R. VanLandingham, "Effects of stoichiometry and epoxy molecular mass on wettability and interfacial microstructures of amine-cured epoxies", in *Adhesion society meeting*, 2001, pp. 260–262.

[20] X. Gu, D. Raghavan, T. Nguyen, M. R. VanLandingham, and D. Yebassa, "Characterization of polyester degradation using tapping mode atomic force microscopy: Exposure to alkaline solution at room temperature", *Polym. Degrad. Stab.*, vol. 74, no. 1, pp. 139–149, 2001. DOI: 10.1016/S0141-3910(01)00138-0.

[21] X. Gu, T. Nguyen, L. Sung, *et al.*, "Advanced techniques for nanocharacterization of polymeric coating surfaces", *JCT Research*, vol. 1, no. 3, pp. 191–200, 2004. DOI: 10.1007/s11998-004-0012-4.

[22] O. Gryshchuk and J. Karger-Kocsis, "Influence of the type of epoxy hardener on the structure and properties of interpenetrated vinyl ester/epoxy resins", *J. Polym. Sci., Part A: Polym. Chem.*, vol. 42, no. 21, pp. 5471–5481, 2004. DOI: 10.1002/pola.20371.

[23] C. M. Sahagun, "Molecular network development of a thermosetting epoxy–amine polymer", PhD Thesis, University of Southern Mississippi, 2012.

[24] C. M. Sahagun and S. E. Morgan, "A nanoscale investigation of epoxy resin nodule development", in *International SAMPE technical conference*, 2009.

[25] C. M. Sahagun, K. M. Knauer, and S. E. Morgan, "Understanding network growth in thermosetting epoxy systems", in *International SAMPE technical conference*, 2010.

[26] C. M. Sahagun, K. M. Knauer, and S. E. Morgan, "Molecular network development and evolution of nanoscale morphology in an epoxy–amine thermoset polymer", *J. Appl. Polym. Sci.*, vol. 126, pp. 1394–1405, 2012. DOI: 10.1002/app.36763.

[27] C. M. Sahagun and S. E. Morgan, "Molecular network connectivity in epoxy–amine thermosets", in *ANTEC*, 2012, pp. 875–878.

[28] J. Duchet and J.-P. Pascault, "Do epoxy–amine networks become inhomogeneous at the nanometric scale?", *J. Polym. Sci., Part B: Polym. Phys.*, vol. 41, no. 20, pp. 2422–2432, 2003. DOI: 10.1002/polb.10585.

[29] K. Dušek, H. Galina, and J. Mikeš, "Features of network formation in the chain crosslinking (co)polymerization", *Polym. Bull.*, vol. 3, no. 1–2, pp. 19–25, 1980. DOI: 10.1007/BF00263201.

[30] J.-P. Pascault, H. Sautereau, J. Verdu, and R. J. J. Williams, "Are cured thermosets inhomogeneous?", in *Thermosetting polymers*, CRC Press, 2002, ch. 7, ISBN: 978-0-203-90840-2. DOI: 10.1201/9780203908402.ch7.

[31] J. Rocks, L. Rintoul, F. Vohwinkel, and G. George, "The kinetics and mechanism of cure of an amino-glycidyl epoxy resin by a co-anhydride as studied by FT-Raman spectroscopy", *Polymer*, vol. 45, no. 20, pp. 6799–6811, 2004. DOI: 10.1016/j.polymer.2004.07.066.

[32] H. M. J. Boots, "Inhomogeneous network formation studied by the kinetic gelation model", *Physica A*, vol. 147, no. 1–2, pp. 90–98, 1987. DOI: 10.1016/0378-4371(87)90099-9.

[33] "ISO 13586:2000(E). plastics – determination of fracture toughness (G_{IC} and K_{IC}) – linear elastic fracture mechanics (LEFM) approach", International Organization for Standardization, Geneva, CH, Standard, Mar. 2000.

[34] E. Meyer, H. J. Hug, and R. Bennewitz, *Scanning probe microscopy: The lab on a tip*. Berlin: Springer, 2003, ISBN: 3-540-43180-2.

[35] T. J. Young, M. A. Monclus, T. L. Burnett, *et al.*, "The use of the PeakForce^{TM} quantitative nanomechanical mapping AFM-based method for high-resolution Young's modulus measurement of polymers", *Meas. Sci. Technol.*, vol. 22, no. 12, p. 125 703, 2011. DOI: 10.1088/0957-0233/22/12/125703.

[36] B. V. Derjaguin, V. M. Muller, and Y. P. Toporov, "Effect of contact deformations on the adhesion of particles", *J. Colloid Interface Sci.*, vol. 53, no. 2, pp. 314–326, 1975. DOI: 10.1016/0021-9797(75)90018-1.

[37] P. Trtik, J. Kaufmann, and U. Volz, "On the use of peak-force tapping atomic force microscopy for quantification of the local elastic modulus in hardened cement paste", *Cem. Concr. Res.*, vol. 42, no. 1, pp. 215–221, 2012. DOI: 10.1016/j.cemconres.2011.08.009.

[38] J. L. Hutter and J. Bechhoefer, "Calibration of atomic-force microscope tips", *Rev. Sci. Instrum.*, vol. 64, no. 7, pp. 1868–1873, 1993. DOI: 10.1063/1.1143970.

[39] B. Ohler, "Cantilever spring constant calibration using laser Doppler vibrometry.", *The review of scientific instruments*, vol. 78, no. 6, 2007. DOI: 10.1063/1.2743272.

[40] C. Teichert, "Self-organization of nanostructures in semiconductor heteroepitaxy", *Phys. Rep.*, vol. 365, no. 5–6, pp. 335–432, 2002. DOI: 10.1016/S0370-1573(02)00009-1.

[41] J. Feng, K. R. Berger, and E. P. Douglas, "Water vapor transport in liquid crystalline and non-liquid crystalline epoxies", *J. Mater. Sci.*, vol. 39, no. 10, pp. 3413–3423, 2004. DOI: 10.1023/B:JMSC.0000026944.85440.f3.

[42] J. S. Villarrubia, "Morphological estimation of tip geometry for scanned probe microscopy", *Surf. Sci.*, vol. 321, no. 3, pp. 287–300, 1994. DOI: 10.1016/0039-6028(94)90194-5.

[43] B. Wetzel, P. Rosso, F. Haupert, and K. Friedrich, "Epoxy nanocomposites – fracture and toughening mechanisms", *Eng. Fract. Mech.*, vol. 73, no. 16, pp. 2375–2398, 2006. DOI: 10.1016/j.engfracmech.2006.05.018.

[44] S. Grishchuk, A. Bonyár, J. Elsäßer, *et al.*, "Toward reliable morphology assessment of thermosets via physical etching: Vinyl ester resin as an example", *EXPRESS Polym. Lett.*, vol. 7, no. 5, pp. 407–415, 2013. DOI: 10.3144/expresspolymlett.2013.38.

[45] L. C. Sawyer, D. T. Grubb, and G. F. Meyers, *Polymer microscopy*. Springer, 2008, ISBN: 978-0-387-72628-1. DOI: 10.1007/978-0-387-72628-1.

[46] S. N. Magonov, V. Elings, and M.-H. Whangbo, "Phase imaging and stiffness in tapping-mode atomic force microscopy", *Surf. Sci.*, vol. 375, no. 2–3, pp. L385–L391, 1997. DOI: 10.1016/S0039-6028(96)01591-9.

[47] O. Behrend, L. Odoni, J. L. Loubet, and N. A. Burnham, "Phase imaging: Deep or superficial?", *Appl. Phys. Lett.*, vol. 75, no. 17, pp. 2551–2553, 1999. DOI: 10.1063/1.125074.

[48] M. Kolahdoozan, M. Hamedi, and M. Nikkhah-Bahrami, "A novel model for the effect of geometric properties of micro/nanoscale asperities on surface adhesion", *Int. J. Adhes. Adhes.*, vol. 48, pp. 280–287, 2014. DOI: 10.1016/j.ijadhadh.2013.09.035.

3 Publication 2

3.1 Bibliographic Information

3.1.1 Title

Comparative investigation of different silane surface functionalizations of fullerene-like WS_2

3.1.2 Authors

- Dietmar Haba [1]
- Thomas Griesser [2]
- Ulrich Müller [1]
- Andreas J. Brunner [1]

[1] Empa – Swiss Federal Laboratories for Materials Science and Technology, Dübendorf, Switzerland

[2] Montanuniversität Leoben, Austria

3.1.3 Publication details

Published in:	*Journal of Materials Science*, vol. 50, pp. 5125–5135, 2015
DOI:	10.1007/s10853-015-9039-4

Statement with regard to publication: The manuscript presented here is an adapted accepted manuscript in order to fit the formatting of the thesis and does not necessarily reflect exactly the actually published version.

3.2 Abstract

Inorganic, fullerene-like WS_2 (IF-WS_2) nanoparticles are useful additives for polymers and lubricating agents, in particular when their surfaces are functionalized by silane modifiers. However, both the success of such a silanization reaction and its effect on the final dispersion quality are still doubtful. In this work, IF-WS_2 are functionalized using three different silane modifiers and investigated with X-ray photoelectron spectrometry, infrared spectroscopy, titration, thermogravimetric analysis and mass spectroscopy. Eventually, they are dispersed within ethanol by sonication to compare the dispersing behavior.

The combination of the different analytical techniques revealed that the IF-WS_2 surfaces can be functionalized with two of the used silane modifiers while the third one was repeatedly unsuccessful. The amount of Si on the particles seems to be a fairly clear indication for the success of the functionalization reaction. The IF-WS_2 seems to oxidize during the functionalization process, probably producing acidic SO_2 or SO_3, which can fully acidify a basic surface modifier. The executed treatment without any added silane modifier improved the dispersibility of the IF-WS_2 within ethanol to some extent, but added modifiers deteriorated it significantly. TEM images indicate that IF-WS_2 particles form aggregates, which might be the reason for the limited dispersibility.

Keywords: Silane surface functionalization; Tungsten disulfide; Dispersion; Sonication

3.3 Introduction

Inorganic, fullerene-like tungsten disulfide (IF-WS_2) nanoparticles are a relatively new class of nanomaterials. They are best known for their outstanding lubricating effect [1, 2], but there are also promising reports on their use as a nanofiller for various polymers [3]. While most research in this field was done on thermoplastics, a few publications dealt with epoxy–IF-WS_2 nanocomposites and showed substantial improvements in adhesion fracture toughness and other mechanical properties [4, 5].

Despite the rather inert nature of IF-WS_2 nanoparticles, it was indicated that it is possible to graft silane surface modifiers onto them in order to improve their dispersibility within lubricating oils [2] and epoxy resins [4], respectively. The lubricating and toughening effects of silane-functionalized IF-WS_2 were superior to those of unfunctionalized IF-WS_2. While the exact course of this silanization reaction is not known, it was assumed that H_2O located at defect sites of the IF-WS_2 plays an important role. Besides the reported improvements, however, a few X-ray photoelectron spectroscopy (XPS) and infrared (IR) spectroscopy measurements are the only indications that the silanization reaction did take place. [2, 4]

In this work we investigate the feasibility of a surface functionalization of IF-WS_2 with selected silane modifiers for later use as a nanofiller in epoxy nanocomposites. The aim of the functionalization was to improve the dispersibility of the IF-WS_2 as well as their bonding to an epoxy matrix. Special emphasis was given to detailed characterization of the obtained powders with various analytical methods.

Chlorosilanes are known to be much more reactive than alkoxysilanes, which is beneficial for the modification process, but also limits the available functional groups, as many would react with the chlorosilane themselves. Alkoxysilanes, in contrast, are available with various functional end groups

and are usually much more easy to handle, which is an important requirement for a possible industrial application.

In this work, treated and untreated IF-WS_2 are dispersed within ethanol by sonication for different time periods. The aim was not to obtain optimum dispersion quality but rather to investigate the effect of the surface functionalization on it. Sonication was chosen as it is a rather well defined process and as it is a frequently reported technique for dispersing IF-WS_2 in organic liquids [2–4, 6–8]. A later publication will deal with the dispersion of these particles within epoxy and the resulting properties.

3.4 Experimental

3.4.1 Materials

The black IF-WS_2 powder with the trade name *Nanolub R* was received from *NanoMaterials Ltd.* (Israel); this source has been used in earlier research published by other groups [2, 4, 5, 9]. According to the manufacturer, it was produced by high-temperature solid–gas synthesis, the primary particles had diameters of 40 nm to 300 nm and they consisted of 10 to 100 WS_2 layers, with an interlayer spacing of 0.62 nm [10].

The silane surface modifiers are depicted in fig. 3.1. The chosen chorosilane was hexyltrichlorosilane (HTCS, 85 % purity); its rather short carbon chain is expected to interact well with a fairly polar epoxy resin. Moreover, it does not act as a plasticizer as strongly as long carbon chains do. The chosen alkoxysilane modifiers were 3-glycidoxypropyltrimethoxysilane (GTMS, 98 % purity) and 3-(2-aminoethylamino)propyltrimethoxysilane (AATMS, 80 % purity). Both are expected to improve the miscibility of nanoparticles with epoxy resin and their functional groups should react with either epoxy or the amine

hardener, promising good bonding between the nanoparticles and the epoxy resin. All silane modifiers were obtained from *Sigma-Aldrich* (USA).

3.4.2 Processing

For the surface functionalization with the chlorosilane HTCS, chloroform ($CHCl_3$) was used as a solvent (stabilized with 1 % ethanol, 99 % purity), while for the functionalization with the alkoxysilanes GTMS and AATMS, ethanol (EtOH) was used (denaturated with 5 % isopropyl alcohol, 99.9 % purity). Approx. 100 ml of these solvents were added to 1.00 g IF-WS_2 and sonicated for 1 min with a 200 W ultrasonic wave generator (*Bandelin Sonoplus HD 2200*) oscillating a Ti_6Al_4V sonotronde (⌀3 mm) at maximum intensity. Within a few seconds, the temperature rose to the boiling point of the respective solvent. In the case of the $CHCl_3$ suspension, all subsequent steps were done under exclusion of air as the highly reactive chlorosilane might otherwise react with air moisture.

The suspensions were further sonicated in an ultrasonic bath at the boiling temperature of the respective solvent while being stirred with a PTFE-mantled overhead stirrer. In separate flasks, 100 mg of the respective surface modi-

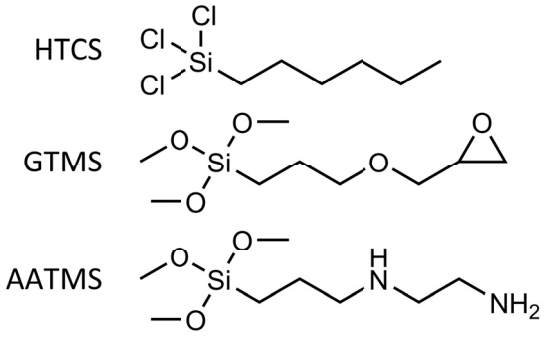

Figure 3.1: Used silane surface modifiers

fier were dissolved within the respective solvents; these solutions were then added dropwise to the suspensions with a syringe. After 60 min, the sonication was stopped and the suspensions were further stirred with magnetic stirrers. The EtOH suspensions were stirred overnight at 90 °C under reflux while the $CHCl_3$ suspensions were stirred closed at room temperature.

The day after, the particles were separated from the solvent by centrifuging at 2000*g* for 3 min per pass. The liquid phase was decanted and kept for further analysis. When all the solvent was removed, fresh solvent was added, the suspensions were mixed thoroughly, and then centrifuged again. This was done three times in order to properly remove the remaining unreacted modifier as well as soluble reaction products. When the liquid phase showed still a gray color tone after centrifuging, the centrifuging step was redone at higher speed and longer times, up to 4000*g* for 30 min. The remaining slurries were heated to 50 °C in vacuum for 1 h to remove the remaining solvent. The powder was then ground with a mortar and a pestle. Finally, the powders were tempered at 100 °C in vacuum for 1 h to make the residual unreacted silane groups react.

These processes were repeated both with three times the amount of surface modifier and without surface modifier. Table 3.1 gives an overview over all treated IF-WS_2 powders. All powders were stored in a desiccator over calcium chloride in vacuum (at approx. 5 mbar).

Suspensions of treated and untreated IF-WS_2 within EtOH were sonicated in order to determine which average agglomerate size can be obtained that way. For that purpose, 50 ml of EtOH were added to 18 mg IF-WS_2 in a round-bottom flask (particle volume fraction $\varphi_p \approx 5 \times 10^{-5}$). The suspensions were sonicated the same way as mentioned above for up to 60 min.

Table 3.1: Overview over all treated IF-WS_2 powders

denomination	surface modifier type	mass / mg	solvent
Ref-EtOH			EtOH
Ref-$CHCl_3$			$CHCl_3$
GTMS-1	GTMS	100	EtOH
GTMS-3	GTMS	300	EtOH
AATMS-1	AATMS	100	EtOH
AATMS-3	AATMS	300	EtOH
HTCS-1	HTCS	100	$CHCl_3$
HTCS 3	HTCS	300	$CHCl_3$

3.4.3 Characterization

Transmission IR specta were obtained from 4000 cm^{-1} to 400 cm^{-1} with 1.9 cm^{-1} step size (64 scans, *Bruker Tensor 27*). Approx. 0.5 mg of IF-WS_2 powders were ground in a mortar together with 150 mg KBr (trade name *Spectranal*, delivered by *Fluka*) and subsequently compressed at 0.75 GPa for 2 min.

All treated IF-WS_2 powders were investigated using an XPS spectrometer (*Physical Electronics Quantum 2000*) to gather additional information on the success of the silanization reaction. The machine uses monochromatic Al K_α X-rays ($h\nu = 1486.7$ eV) and operates at a pressure of 3×10^{-7} Pa at room temperature. The electron take-off angle was 45° and the analyzer was operated in the constant pass energy mode at 58.7 eV. The beam diameter chosen was around 150 µm and spectra were recorded with a step size of 0.25 eV. The powders were pressed into an In foil and kept in vacuum at least 16 h before the measurement. Electron and Ar^+ neutralizers were used to compensate for possible surface charging. The samples were measured in randomized order. The spectra were analyzed using the software *MultiPak 8.2B*. A Shirley back-

ground subtraction was done on every peak, before its area was calculated by numerical integration. As the W_{4f} peaks overlap with a $W_{5p3/2}$ peak, their areas were instead calculated by fitting those curves with a Gaussian–Lorentzian function, and only the area belonging to the W_{4f} peaks was used. The atomic fractions of the individual elements were calculated from these peak areas using the corrected relative sensitivity factors calculated by the software.

As one of the chosen silane surface modifiers, AATMS, contains two basic amine groups, its content is measurable by acid–base titration. This was done on AATMS, on the AATMS-treated IF-WS_2 powders and on the EtOH rest from the two AATMS modifications (called *AATMS-X-rest-EtOH*). For the titration, 100 mg of AATMS were dissolved in 25 ml of EtOH and another 25 ml of H_2O were added; 100 mg of the AATMS-treated IF-WS_2 powders were dispersed in 25 ml of H_2O; and 25 ml of the AATMS-X-rest-EtOH were mixed with 25 ml of H_2O. The titration was done with 10 mmol/l HCl or NaOH in H_2O using a calibrated pH probe. This H_2O had been freshly purified to Grade 1 (*Thermo Scientific Barnstead NanoPure*) [11]. The titration curves were evaluated using the *CurTiPot* software [12].

Thermogravimetric analysis (TGA) was performed in order to determine how effective the silanization had worked (*Perkin Elmer TGA 7*). Before the measurement, the powders were heated to 50 °C in vacuum for several hours in order to assure that they were dry. Roughly 6 mg of treated IF-WS_2 powders were heated with 20 °C/min under He flow (purity 4.6). At 600 °C, the gas was switched to O_2 (purity 2.5).

In order to get more information on the origin of the mass loss in the TGA, 100 mg of HTCS-3 and AATMS-3 were further investigated by TGA combined with mass spectrometry (TG/MS, *Netzsch STA 409 CD with QMS 403 C*) at 20 °C/min under He flow (purity 4.6).

Scanning electron microscopy (SEM) images were taken to determine the agglomerate sizes of treated and untreated powders after various sonication

times. For this purpose, EtOH suspensions were applied dropwise to a Si wafer and dried at room temperature as it had been done earlier [2]. Images were gathered with a *FEI NovaNanoSEM 230* with a Schottky field emission electron source operating at 5 kV, imaging secondary electrons with a through-the-lens detector at 3×10^{-4} Pa pressure.

Dynamic light scattering (DLS) measurements were performed at 25.0 °C (*Malvern Zetasizer Nano Z*, laser wavelength 534 nm). While this technique is best suited for the measurement of the diameters of well-dispersed spherical primary particles with sizes of 1 nm to 1000 nm [13], it has also been successfully used for quantifying agglomerate sizes [14–18]. EtOH suspensions were diluted with additional EtOH 1:10 (resulting particle volume fraction $\varphi_p \approx 5 \times 10^{-6}$). The viscosity of neat EtOH was used for the calculation of particle diameters. Presented values are the means of 15 individual measurements of 30 s each. As recommended by the respective ISO standard [19], the intensity-weighted average particle diameter $\bar{x}_{DLS}$ was used for evaluation.

For transmission electron microscopy (TEM), a drop of EtOH–IF-WS_2 suspension (sonicated for 60 min) was placed on a TEM grid and allowed to dry. The images were gathered in a Schottky field emission TEM (*JEOL 2200FS TEM/STEM*) operating at 200 kV.

3.5 Results and Discussion

As mentioned above, there are two reports indicating that IF-WS_2 can be functionalized with chlorosilane or alkoxysilane surface modifiers [2, 4]. As the underlying chemical reaction is, however, not fully understood so far, particular emphasis was given to a critical characterization with different methods.

3.5.1 IR spectroscopy

According to literature reports, the presence of surface modifier on IF-WS_2 can be detected by transmission IR spectroscopy, where IR bands at 2962 cm^{-1}, 2922 cm^{-1} and 2852 cm^{-1} were attributed to $-CH_3$ and $-CH_2-$ groups [2]. Indeed, all treated IF-WS_2 showed IR bands at exactly these positions, even Ref-EtOH, which has no surface modifier on it; moreover, these bands were also observed in fresh KBr (data given in the Supporting Information). Thus, these IR signals originate most likely from small impurities in the KBr powder rather than from an organic modifier. There was no significant increase observed from the fresh KBr to any of the samples of treated IF-WS_2. This might be due to the high absorptivity of IF-WS_2: Possible IR signals from the functionalization might have been reduced to below the noise level.

3.5.2 XPS

XPS survey scans showed that the elements present on the surfaces of the treated IF-WS_2 powders were mostly those expected: W, S, C, O, Si and N. Besides these, there was a small signal of In, which stems from the used foil, and a small signal of Se, which is in traces often present in transition metal dichalcogenides. No signal of residual Cl was detected around 200 eV, indicating that no unreacted HTCS was left.

The highly resolved XPS scans are given in fig. 3.2. The W_{4f} peaks did not change for any sample, indicating that the surface functionalization did not alter the chemical state of the W. A WO_x signal might be seen as a shoulder around 36.0 eV as was stated earlier [2, 4], but it is too small to draw a clear conclusion from.

The shape of the S_{2p} peaks did not change either, but a side peak formed at higher binding energy in some cases. Späth et al. have already reported such

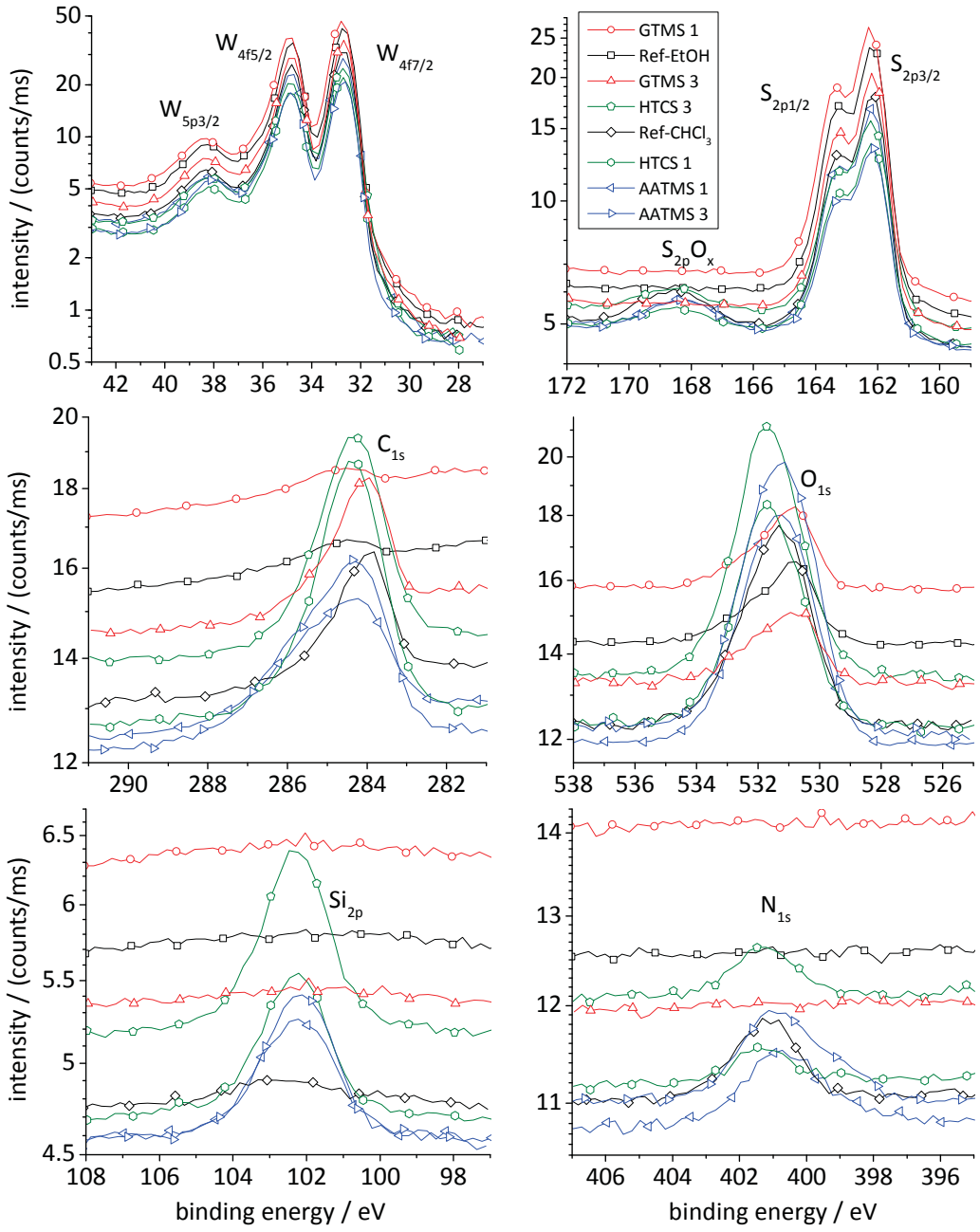

Figure 3.2: XPS spectra of all treated IF-WS_2 powders with the presumed assignment

a side peak in untreated, but aged IF-WS_2 and attributed it to SO_x [9], and this interpretation is shared in the present work. As it was assumed that this side peak came from S_{2p} as well, its area was composed in the measurement of the S content.

Both O_{1s} and C_{1s} are compounded of at least two different peaks each, the ratio of which varies among the samples. The binding energy of Si_{2p} of approx. 102.4 eV is in good agreement with that reported for siloxanes [20]. A broad, low-intensity peak appeared to be present for all samples overlapping with the Si_{2p} peak (see fig. 3.2); as this peak was assumed to be a signal from the W, it was removed by background subtraction before calculation of the Si_{2p} peak area.

The measured atomic fractions of the individual elements are given in table 3.2. Note that the absolute measurement uncertainty of atomic fractions determined by XPS is usually in the range of ±10 %, while the relative differences between the individual samples might be measured more accurately. The detection limit depends on the investigated signal and on the background and lies usually at atomic fractions below 1.0 %.

The S/W ratio was generally slightly lower than 2. This might be explained with the substitution of some S atoms by Se, or by the fact that some IF-WS_2 nanoparticles might be broken up and WO_3 from their core might have been measured. Given the limited accuracy of XPS with respect to quantification of composition, however, no further conclusions can be drawn from that. Even though the measurement order was random, the high correlation between similarly treated powders suggests that the S/W ratio is indeed affected by the used modifier and/or the used solvent.

The increase in C_{1s} content might be used as an indication for a successful functionalization as it has been done earlier [2, 4]. However, while the C content is very low in Ref-EtOH, it is much higher in Ref-$CHCl_3$; this shows that an increase in the C_{1s} peak alone does not necessarily provide proof of suc-

Table 3.2: Atomic fractions of the investigated elements as calculated from the curves in fig. 3.2 and ratios thereof.

	W at.%	S at.%	C at.%	O at.%	Si at.%	N at.%	S/W	SO_x/S %
Ref-EtOH	31.4	55.2	3.0	10.4	*	*	1.76	*
Ref-$CHCl_3$	19.1	37.4	17.4	21.2	*	4.4	1.96	8.9
GTMS-1	30.8	54.5	4.7	9.3	*	*	1.77	*
GTMS-3	25.2	44.1	21.9	8.4	*	*	1.75	*
AATMS-1	15.8	30.8	22.6	23.4	3.4	4.0	1.94	7.1
AATMS-3	11.3	21.5	31.7	26.1	4.2	5.2	1.90	11.1
HTCS-1	12.3	22.9	38.3	20.7	4.3	1.5	1.86	6.2
HTCS 3	13.3	24.7	31.1	23.0	5.6	2.3	1.85	6.5

*Signal below the detection limit.

cessful functionalization. Due to the high surface sensitivity of XPS, already small amounts of contaminants affect the measurement considerably, and C is known to be a ubiquitous contaminant. The shift in the C_{1s} peak of Ref-$CHCl_3$ is not significantly different from that of the functionalized powders neither.

The same is true for the O_{1s} peak: While it increases strongly and shifts after functionalization, an increase or shift alone is not sufficient to tell whether the functionalization was successful. The strong N_{1s} peak of the AATMS-functionalized powders agrees well with the assumed presence of amines and thus indicates that those powders have been functionalized successfully. However, Ref-$CHCl_3$ and some powders functionalized with N-free modifiers showed clear N_{1s} peaks as well, which is again presumably due to contaminants.

In contrast, the Si_{2p} peak is clearly measurable for some samples and not detectable for others. It hence seems that this peak provides clear evidence on whether the functionalization process was successful. It can therefore be concluded that both functionalization reactions with GTMS were unsuccess-

ful, while those with AATMS and those with HTCS were all successful. It is unclear why the functionalization with AATMS should be successful when that with GTMS is not as the type of reaction is the same, but the increase in the C_{1s}, O_{1s} and N_{1s} peaks support this interpretation. Moreover, it is not clear whether the silane modifiers attach to the IF-WS_2 by chemical bonds or just by physisorption.

The presence of the SO_x peak correlates strongly with the O content, indicating that it is indeed due to oxidized S. While Späth et al. showed that IF-WS_2 oxidize upon exposure to ambient air for long time periods (three years) [9], we can see here that the performed treatment can cause oxidation as well; the SO_x peak of Ref-$CHCl_3$ shows that the presence of silanes was not necessary for an oxidation reaction. Rather, the reason for this oxidation might lie in the short sonication at the beginning of the treatment. The high local temperatures during the sonication of up to 5000 K [21] might lead to the degradation of the IF-WS_2 or the used solvents and the resulting formation of oxidative degradation products. Späth et al. assumed that the oxidized S might be present in the form of SO_4^{2-}. In order to test that, small amounts of treated IF-WS_2 powders and of EtOH rests left from the treatment were mixed with H_2O and $BaCl_2$. As no precipitate formed in any of these cases, the presence of SO_4^{2-} seems unlikely.

Due to the contaminations with C, O and N, only limited conclusions can be drawn from the atomic ratios of these. Analyzing the amount of shifting of the C_{1s} and the O_{1s} peaks did not yield conclusive facts neither.

3.5.3 Titration

The well-reproducible titration curve of AATMS shows two pH steps as it is typical for diprotic bases. However, significantly more than double the amount of HCl had to be added until the second pH step than until the first

one, namely 2.4 times that much (see fig. 3.3). This indicates that some portion of the AATMS molecules, namely 34 %, had been monoprotonated already before their delivery, making one of their amine groups an ammonium group. This is not unexpected, given the limited purity of the AATMS and the fact that amines are easily protonated.

The amine group content in AATMS can be quantified by subtracting the amount of HCl necessary until the first pH step (where half of the molecules are protonated once) from that necessary until the second pH step (where half of the molecules are protonated twice). More precise results were obtained with the titration curve fitting software. The measured acid disscociation constants K_a calculated by curve fitting were $10^{-6.57}$ and $10^{-9.77}$ and therefore similar to $10^{-6.86}$ and $10^{-9.92}$ which are stated for ethylenediamine [22]. The amine group content was as high as 9.5 mmol/g and hence higher than the theoretically expected value of 9.0 mmol/g. It seems, therefore, that some diamine was present in the form of the AATMS's precursor, that is to say, without a trimethoxysilane group. Once again, this is not unexpected given AATMS's limited purity. All subsequent calculations were done assuming an amine group content of 9.5 mmol/g.

A comparable titration was done on AATMS-3-rest-EtOH. The titration curve was again well reproducible, and once again showed two pH steps at the same pH values, indicating that there was still AATMS left in the EtOH after centrifugation. This time, the results indicate that 92 % of the AATMS molecules have been protonated already once, which is significantly more than before the treatment. Thus, acidic groups have been added or created during the treatment. Considering the XPS results, this is most likely due to the SO_x surface groups that were sometimes produced during the treatment. It is worth noting that untreated IF-WS_2 leads to acidic pH when dispersed within H_2O which may stem for the H_2S-rich atmosphere usually used for their synthesis [23, 24], possibly resulting in SO_x surface groups as well. Consider-

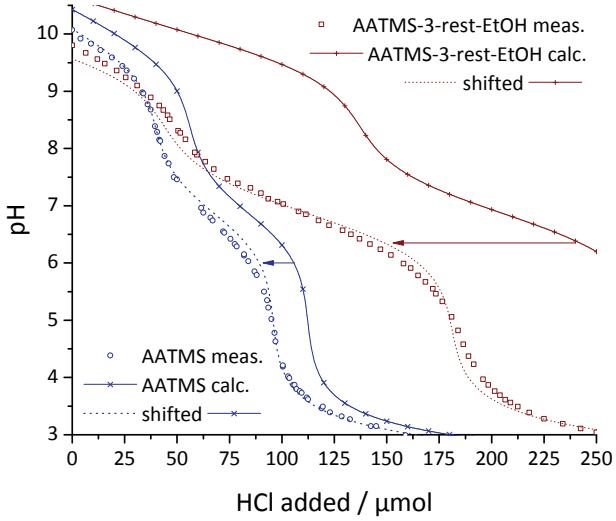

Figure 3.3: Measured and calculated titration curves of AATMS and AATMS-3-rest-EtOH

ing the titration curves, 0.63 mmol acid groups were present before or created during the AATMS-3 functionalization process. The titration indicates that 1.1 mmol AATMS was left in the used EtOH, which corresponds to 74 % of the amount added initially. Assuming that the residual 26 % of the AATMS molecules adhered to the IF-WS_2 particles, one can estimate the maximum organic mass fraction of AATMS-3 to 7.2 %.

In the case of AATMS-1-rest-EtOH, the pH is acidic right from the beginning; the titration was therefore done with 10 mmol/l NaOH instead. The well reproducible curve shape is similar to those reported above, as there are once again two pH steps at the same pH values (data given in the Supporting Information). This indicates that AATMS modifier was present in AATMS-1-rest-EtOH, but more acid groups had been present before or created during the treatment than base groups had been added in the form of AATMS, namely 0.93 mmol. Hence, AATMS-1 is functionalized with diammonium molecules

rather than with diamines. The amount of diammonium measured in the sample corresponds to 47 % of the nominally added AATMS. Assuming that the other 53 % adhered on the IF-WS_2 particles, one can estimate the maximum organic mass fraction of AATMS-1 to 5.8 %.

Comparable titrations were done on the modified powders AATMS-1 and AATMS-3 as well (data given in the Supporting Information). AATMS-3 results in a basic pH value when dispersed within H_2O while AATMS-1 results in an acidic pH value, which is in good agreement with the results of the respective EtOH rests. However, the obtained titration curves were not as well defined as those and the measured diamine contents far exceeded the expected amounts. This is most likely due to the participation of the IF-WS_2 in the acid–base reaction during the titration, e.g., with their oxidized S groups, thereby wrongly indicating very high modifier contents. Quantitative titration results must therefore be interpreted cautiously.

3.5.4 TGA

In inert atmosphere, IF-WS_2 are stable to above 1000 °C [10], while organic molecules decompose between 200 °C and 600 °C; it was therefore expected that the organic content of the treated powders could be measured by TGA. Fig. 3.4 shows the mass of all treated IF-WS_2 powders over temperature. The largest mass loss occurs at 600 °C, when the flow gas is switched to O_2; here, the W of the outermost WS_2 layers oxidizes to WO_3 and the S oxidizes, e.g., to SO_2, and vaporizes. The yellow color of the residual powder after the measurement indicates WO_3 as well.

Even though the powders had been stored in a vacuum exsiccator and dried in a vacuum oven just before the measurement, all treated powders, whether functionalized or not, lost 0.8 % to 1.5 % of their mass below 220 °C. This is most likely due to firmly bound H_2O molecules that are either hard to remove

or that are taken up quickly after drying. The presence of H_2O on IF-WS_2 has been reported earlier and was explained with H_2O molecules in the voids in the center of the IF-WS_2 as well as in defects in the IF-WS_2 structure [25].

Generally, powders that were treated similarly show similar mass loss behavior, showing that the mass loss is affected by the silane treatment. However, Ref-$CHCl_3$ shows significant mass loss as well, even though it contains no surface modifier. This shows that the TGA mass loss alone is not sufficient as a measure for the organic content of IF-WS_2. In contrast, these results once again indicate that the used solvent affects the powders, as the TGA curve of Ref-$CHCl_3$ is very similar that of the HTCS-modified powders, which have been treated within $CHCl_3$ as well.

The AATMS-modified powders are the only ones whose mass loss behavior is significantly different from that of all other powders, including the reference curves. The significant mass loss around 290 °C indicates the decomposition of the supposed ammonium in the AATMS molecule, which might work similar to a Hofmann elimination. Thermal loss of ammonium modifiers has been reported earlier to take place at roughly that temperature [26]. This again indicates that the functionalization with AATMS was successful.

Interestingly, the TGA mass loss correlates strongly with the C, O, N and SO_x contents measured by XPS (see table 3.2). This is in good agreement with the assumption that the TGA mass loss is mainly due to removal of CO_2, H_2O, SO_x and ammonium compounds. Note that the TGA curves of the HTCS-modified powders are entirely different if the tempering step is omitted as unreacted chlorosilanes might then react during the measurement, releasing HCl (details given in the Supporting Information).

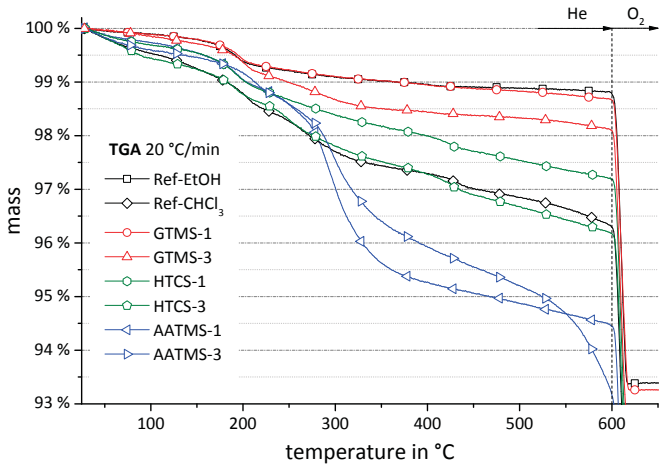

Figure 3.4: TGA curves of all treated powders

3.5.5 TG/MS

The composition of the gas produced during a TGA measurement was analyzed via TG/MS measurements on AATMS-3 and HTCS-3 in order to obtain additional information on the origin of the mass loss; the analyzed ratios of ion mass m to ion charge q were chosen in a way to analyze possible traces of CO_2, H_2O, HCl and ammonium compounds in the gas.

The results support the assumption that the mass loss is mainly due to H_2O and CO_2, and in the case of AATMS-3 possibly also due to succession of ammonium compounds (detailed results and discussion given in the Supporting Information). No traces of HCl were detected, indicating that no unreacted chlorosilanes were left after tempering at 100 °C. The detected CO_2 indicates that organic species were present on both samples and hence that these powders had been functionalized successfully. The detection of ammonium compounds further supports this assumption for AATMS-3.

3.5.6 Sonication of untreated IF-WS_2 powders

During sonication, agglomerates are split into two or more differently large parts until a final agglomerate size is reached. As agglomerates can also reform during sonication, it is possible that not all agglomerates will be split even after infinitely long sonication times, hence the final average number of primary particles per agglomerate n_{end} might be more than unity. It is assumed here that the reduction of the average number of particles per agglomerate n over time t is proportional to the difference between n and n_{end}:

$$\tau \cdot \frac{\mathrm{d}n}{\mathrm{d}t} = -[n(t) - n_{\mathrm{end}}] \tag{3.1}$$

with the proportionality factor τ being called *time constant*. Integrating gives:

$$n(t) = n_{\mathrm{end}} + (n_0 - n_{\mathrm{end}}) \cdot e^{-\frac{t}{\tau}} \tag{3.2}$$

with $n_0 = n(t = 0)$. Due to $n_0 \gg n_{\mathrm{end}}$ this can be rewritten to:

$$n(t) = n_{\mathrm{end}} + n_0 \cdot e^{-\frac{t}{\tau}} \tag{3.3}$$

The time t_α until a certain ratio α of the final dispersion quality is reached can be calculated:

$$1 - \alpha = \frac{n(t_\alpha) - n_{\mathrm{end}}}{n_0 - n_{\mathrm{end}}} \approx \frac{n(t_\alpha) - n_{\mathrm{end}}}{n_0} = e^{-\frac{t_\alpha}{\tau}} \tag{3.4}$$

$$t_\alpha = -\tau \cdot \ln(1 - \alpha) \tag{3.5}$$

The n in eq. (3.3) can be substituted by the average agglomerate volume V or the average agglomerate diameter d due to $n \propto V \propto d^3$:

$$d^3(t) = d_{\mathrm{end}}^3 + d_0^3 \cdot e^{-\frac{t}{\tau}} \tag{3.6}$$

In order to measure agglomerate sizes after sonication, SEM imaging was used in a first attempt as it was done in an earlier work [2]. Some differences are visible between SEM images of samples sonicated for very short and very long time periods, respectively (e.g., for 10 s and 60 min; see fig. 3.5, additional images in the Supporting Information): While individual primary particles can be seen in most samples, agglomerates of micrometer dimensions are visible more often in samples that had been sonicated for shorter time periods, which shows that sonication is generally able to break agglomerates. However, nanoparticles tend to reagglomerate upon drying due to their van-der-Waals interaction, which is the stronger the smaller the particles are. The IF-WS_2 agglomerates had hence quite likely been significantly smaller within the EtOH suspension before it dried. Moreover, SEM images are very difficult to quantify sensibly. In contrast, DLS is done directly on suspensions and is statistically much more useful, which is why it was considered a superior tool for measuring agglomerate size distributions.

The IF-WS_2 suspension became dark black within a few seconds of sonication, indicating successful dispersion. Nevertheless, large agglomerates were visible as well, even after 60 min of sonication. Hence, it seems that the sonication resulted in a polydisperse, bimodal agglomerate size distribution.

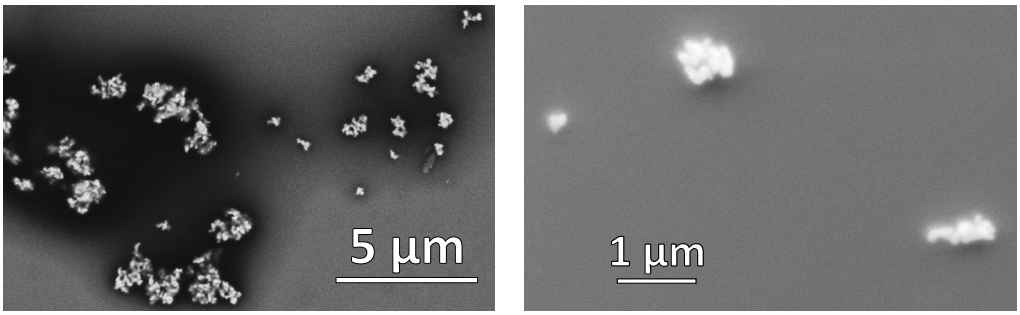

Figure 3.5: SEM images of dried Ref-EtOH after sonication for 10 s (left) and 60 min (right), respectively, showing IF-WS_2 agglomerates

DLS is very sensitive to polydispersity; already few large agglomerates will result in a measurement outlier. Such outliers appeared very frequently, even though most large agglomerates sedimented quickly and thus did not affect the DLS measurement. Unfortunately, the automatic outlier detection by the DLS software did not work reliably enough, which is why some outliers had to be excluded manually. Fig. 3.6 shows the measured $\bar{x}_{\mathrm{DLS}}$ after two different sonication set-ups (different probe diameter, with and without stirring). The empty points indicate excluded data. The remaining data were fitted to eq. (3.6) and the fit is given in fig. 3.6 with its 95-%-confidence interval.

Each sample was measured twice with the DLS, and the results normally agreed well. This shows that the repeatability of the DLS was reasonable, but that some of the samples contained large agglomerates that caused problems. Interestingly, the results appeared to be better when a probe of smaller diameter was used and when the liquid was not stirred. However, this is probably just because the large agglomerates were mostly sedimented on the bottom of the beaker and hence fewer of them were collected for measurement. These results are thus probably not representative for the real agglomerate size distribution.

Fig. 3.6 shows that eq. (3.6) fits the *selected* data points quite well and seems to be more appropriate than models suggested elsewhere [15]. The fit parameters are listed in table 3.3: Independently of the set-up, τ was below 2 min. Inserting these values into eq. (3.5) gives $t_{0.99} < 10\,\mathrm{min}$, meaning that 99 % of the final dispersion quality will be obtained within 10 min for both investigated sonication set-ups. The d_{end} agrees very well for both sonication set-ups, but in both cases it is still much larger than the diameter of the primary particles. Thus, it seems that agglomerates remain even after long sonication times.

The agglomerate sizes visible in TEM images agree reasonably well with the SEM and DLS results: While individual primary particles do exist, there are

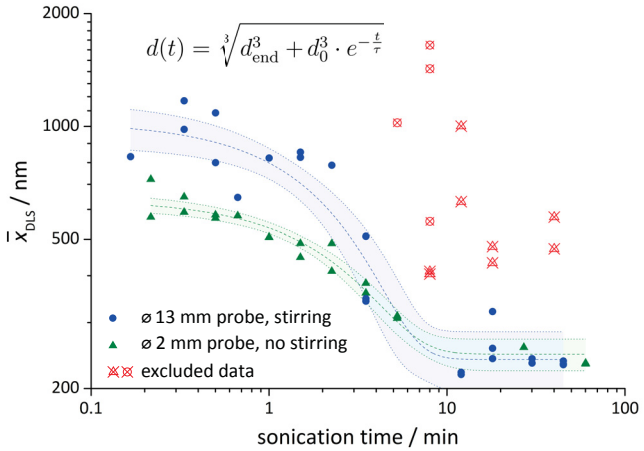

Figure 3.6: $\bar{x}_{\text{DLS}}$ over sonication time of IF-WS_2 within EtOH as measured by DLS with two different sonication set-ups. The data were fitted using eq. (3.6); the bands represent the 95 %-confidence interval.

Table 3.3: Fit parameters of the curves in fig. 3.6, giving the final average diameter of particles after sonication d_{end}, their initial diameter d_0 and the time constant τ as modeled with eq. (3.6).

probe ⌀	d_{end} / nm	d_0 / nm	τ / min
13 mm	239 ± 21	1020 ± 67	1.29 ± 0.22
2 mm	247 ± 11	626 ± 16	1.75 ± 0.18

also agglomerates of different sizes even after 60 min of sonication. It seems as if some of the particles were broken up; however, it cannot be stated if these particles had broken up during sonication or if they were broken up already before. Likewise, it is unclear to what extent the nanoparticles had reagglomerated upon drying on the TEM grid, analogous to the possible reagglomeration on the Si wafers as observed via SEM.

Two of the primary IF-WS_2 particles in fig. 3.7 share some WS_2 layers with each other. Hence, the adhesion between them is not just due to van-der-

Waals forces but they are conjoined by covalent bonds. Such conjoined nanoparticles could be observed several times. Thus, it seems as if some agglomerates are rather aggregates, or agglomerates of aggregates. The fact that the final agglomerate diameter is significantly larger than that of the primary particles supports the assumption that a significant fraction of the IF-WS_2 is present in the form of aggregates.

3.5.7 Sonication of treated IF-WS_2 powders

The treated powders were sonicated within EtOH the same way as the untreated ones (examples given in fig. 3.8). Once again, some measurement results had to be excluded arbitrarily, but the data generally obey eq. (3.6). The fitting parameters are given in table 3.4.

The reference powders and the nominally GTMS-functionalized powders show strongly reduced d_{end}, d_0, and with one exception, τ. Thus, the treatment improved the initial dispersion quality as well as the dispersibility of the powders, even though there was no modifier added to the reference powders and the GTMS functionalization was probably unsuccessful. The improvements are most likely due to the short sonication and the grinding with mortar and pestle during the treatment.

In contrast, the successfully functionalized powders had an increased d_0 and with one exception an increased d_{end} when compared to the untreated powders; moreover, the scatter was strongly increased. Hence, the silane functionalization deteriorated the dispersibility of IF-WS_2 rather than to improve it, even though the treatment itself was shown to improve the dispersion quality significantly. It seems, therefore, that the silane modifiers caused the IF-WS_2 agglomerates to stick together.

These results indicate that surface functionalization of IF-WS_2 with organic molecules is possible, but does not necessarily improve its dispersibility in

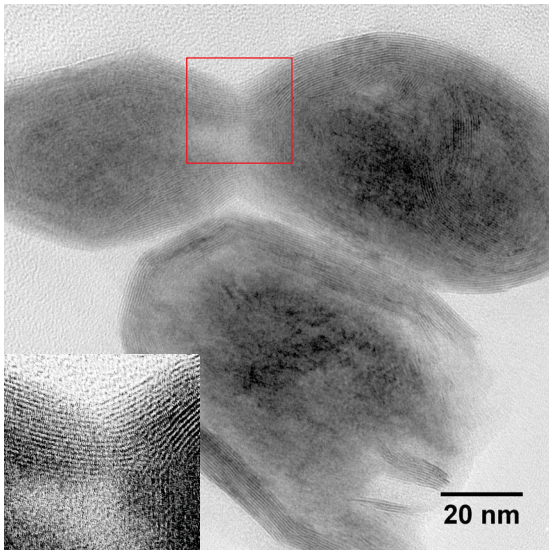

Figure 3.7: TEM image of IF-WS_2 nanoparticles after $60\,\mathrm{min}$ of sonication in EtOH. The framed area is magnified in the bottom left corner with enhanced contrast.

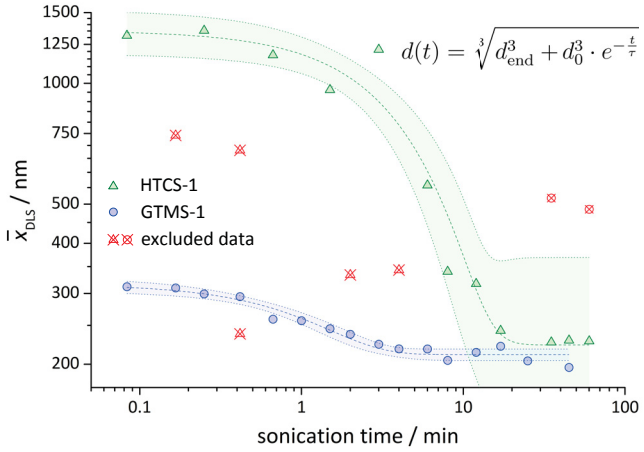

Figure 3.8: $\bar{x}_{\mathrm{DLS}}$ over sonication time of two treated IF-WS_2 within EtOH as measured by DLS. The data were fitted using eq. (3.6); the bands represent the $95\,\%$-confidence interval.

Table 3.4: Fit parameters of the DLS measurement results of all treated IF-WS_2 dispersed within EtOH, fitted by eq. (3.6)

	d_{end} / nm	d_0 / nm	τ / min
Ref-EtOH	210 ± 4	306 ± 12	0.73 ± 0.13
Ref-$CHCl_3$	228 ± 11	384 ± 27	0.70 ± 0.24
GTMS-1	211 ± 4	282 ± 8	0.99 ± 0.15
GTMS-3	222 ± 3	345 ± 7	1.85 ± 0.22
AATMS-1	422 ± 34	1226 ± 145	1.76 ± 0.23
AATMS-3	620 ± 52	1714 ± 204	1.41 ± 0.14
HTCS-1	223 ± 64	1350 ± 75	2.43 ± 0.45
HTCS-3	309 ± 36	1844 ± 440	0.11 ± 0.04

fairly polar solvents like EtOH. The forces holding the individual IF-WS_2 particles together are very small to begin with and are hence not reduced by silane surface modifiers. Possible positive effects of the surface functionalization on the long-term dispersion stability [2] might not be related to improved dispersion quality. Likewise, the enhanced properties of IF-WS_2-epoxy nanocomposites [4] might be caused by other factors.

3.6 Conclusion and Outlook

This work deals with three types of silane surface functionalization of IF-WS_2, their characterization and their dispersion within EtOH. Various measurements indicate that the modifications with HTCS and AATMS were successful while that with GTMS was not. The most direct evidence for successful modification was the presence of the Si_{2p} peak in the XPS curves, while the increase in the C, O or N contents were considered inconclusive.

The performed treatment, both with and without silane modifiers added, resulted in the formation of SO_x groups, most likely SO_2 or SO_3. These de-

crease the pH of the suspension and can hence partially or fully protonate the surface modifier. As long as this effect is taken into account, acid–base titration of the residual solvent left from the treatment can be used to determine indirectly the presence and to some extent the quantity of basic or acidic surface modifier on the nanoparticles.

Strongly bound H_2O was still present on the IF-WS_2 powders after drying them at 50 °C in vacuum for several hours. Together with the evaporation of SO_x, this complicates the determination of organic contents with TGA. Only the amine-functionalized IF-WS_2 could be clearly discriminated from the references.

The powders were dispersed within EtOH by sonication down to agglomerate diameters of approx. 200 nm, which is still larger than the nominal average primary particle size (around 100 nm). The development of agglomerate sizes over sonication time could be measured by DLS reasonably well, although several outliers had to be excluded, likely caused by bimodal polydispersity. Equation (3.6) approximated the evolution of the measured agglomerate size over sonication time reasonably well. After 10 min, further sonication does not seem to reduce the agglomerate sizes any further. TEM images show that some of the primary particles were conjoined with each other, forming aggregates; this might explain why the agglomerate size could not be reduced any further.

The performed treatment *can* hence help to limit the initial agglomerate size and to accelerate the size reduction upon sonication, but barely reduces the final agglomerate size. Moreover, the successfully functionalized powders showed significantly inferior dispersibility in EtOH to the unfunctionalized references. This shows that the chemical interaction between the IF-WS_2 and the dispersion solvent is not the factor limiting the dispersion quality.

In an upcoming work, these IF-WS_2 powders will be used to manufacture epoxy nanocomposites with special focus on the resulting fracture tough-

ness. Special emphasis will be given to the obtained dispersion quality and the bonding between the IF-WS_2 particles and the epoxy matrix.

Acknowledgments

The authors would like to thank Anja Huch, Beatrice Fischer, Jörg Patscheider, Lassi Karvonen and Matthias Nagel for their experimental and theoretical support.

Supporting information

Supporting information related to this chapter can be found in section 8.2.

References

[1] L. Rapoport, Y. Bilik, Y. Feldman, *et al.*, "Hollow nanoparticles of WS_2 as potential solid-state lubricants", *Nature*, vol. 387, pp. 791–793, 1997. DOI: 10.1038/42910.

[2] C. Shahar, D. Zbaida, L. Rapoport, *et al.*, "Surface functionalization of WS_2 fullerene-like nanoparticles", *Langmuir*, vol. 26, no. 6, pp. 4409–4414, 2010. DOI: 10.1021/la903459t.

[3] M. Naffakh, A. M. Díez-Pascual, C. Marco, G. J. Ellis, and M. A. Gómez-Fatou, "Opportunities and challenges in the use of inorganic fullerene-like nanoparticles to produce advanced polymer nanocomposites", *Prog. Polym. Sci.*, vol. 38, no. 8, pp. 1163–1231, 2013. DOI: 10.1016/j.progpolymsci.2013.04.001.

[4] M. Shneider, H. Dodiuk, R. Tenne, and S. Kenig, "Nanoinduced morphology and enhanced properties of epoxy containing tungsten disulfide nanoparticles", *Polym. Eng. Sci.*, vol. 53, no. 12, pp. 2624–2632, 2013. DOI: 10.1002/pen.23517.

[5] A. Buchman, H. Dodiuk-Kenig, A. Dotan, R. Tenne, and S. Kenig, "Toughening of epoxy adhesives by nanoparticles", *J. Adhes. Sci. Technol.*, vol. 23, no. 5, pp. 753–768, 2009. DOI: 10.1163/156856108X379209.

[6] S. M. Ghoreishi, S. S. Meshkat, M. Ghiaci, and A. A. Dadkhah, "Nanoparticles synthesis of tungsten disulfide via AOT-based microemulsions", *Mater. Res. Bull.*, vol. 47, no. 6, pp. 1438–1441, 2012. DOI: 10.1016/j.materresbull.2012.02.042.

[7] M. Shneider, L. Rapoport, A. Moshkovich, *et al.*, "Tribological performance of the epoxy-based composite reinforced by WS_2 fullerene-like nanoparticles and nanotubes", *Phys. Status Solidi A*, vol. 210, no. 11, pp. 2298–2306, 2013. DOI: 10.1002/pssa.201329162.

[8] F. Xu, C. Yan, Y.-T. Shyng, *et al.*, "Ultra-toughened nylon 12 nanocomposites reinforced with IF-WS_2", *Nanotechnology*, vol. 25, no. 32, p. 325 701, 2014. DOI: 10.1088/0957-4484/25/32/325701.

[9] B. Späth, F. Kopnov, H. Cohen, *et al.*, "X-ray photoelectron spectroscopy and tribology studies of annealed fullerene-like WS_2 nanoparticles", *Phys. Status Solidi B*, vol. 245, no. 9, pp. 1779–1784, 2008. DOI: 10.1002/pssb.200779531.

[10] *Material safety data sheet NanoLub R, WS_2 lubricant nanopowder*, version 4, NanoMaterials, Mar. 2011.

[11] "ISO 3696:1987. water for analytical laboratory use – specification and test methods", International Organization for Standardization, Geneva, CH, Standard, Oct. 1987.

[12] I. G. R. Gutz, *CurTiPot – pH and acid–base titration curves: Analysis and simulation freeware*, version 4.

[13] H. G. Merkus, "Dispersion of powders in air and in liquids", in *Particle size measurements*, H. G. Merkus, Ed. Springer, 2009, ch. 5, pp. 117–136, ISBN: 978-1-4020-9015-8. DOI: 10.1007/978-1-4020-9016-5.

[14] B. Bittmann, F. Haupert, and A. K. Schlarb, "Preparation of TiO_2 epoxy nanocomposites by ultrasonic dispersion and resulting properties", *J. Appl. Polym. Sci.*, vol. 124, no. 3, pp. 1906–1911, 2012. DOI: 10.1002/app.34493.

[15] B. Bittmann, F. Haupert, and A. K. Schlarb, "Ultrasonic dispersion of inorganic nanoparticles in epoxy resin", *Ultrason. Sonochem.*, vol. 16, no. 5, pp. 622–628, 2009. DOI: 10.1016/j.ultsonch.2009.01.006.

[16] B. Bittmann, F. Haupert, and A. K. Schlarb, "Preparation of TiO_2/epoxy nanocomposites by ultrasonic dispersion and their structure property relationship", *Ultrason. Sonochem.*, vol. 18, no. 1, pp. 120–126, 2011. DOI: 10.1016/j.ultsonch.2010.03.011.

[17] M. Englert, B. Bittmann, F. Haupert, and A. K. Schlarb, "Scaling-up of the dispersion process of nanoparticle-agglomerates in epoxy resin with an innovative continuous ultrasonic flow-through-cell dispersion system", *Polym. Eng. Sci.*, vol. 52, no. 1, pp. 102–107, 2012. DOI: 10.1002/pen.22051.

[18] M. Englert, F. Haupert, and A. K. Schlarb, "Verification of a dispersion model to describe the dispersion of nanoparticle agglomerates in epoxy resin with a stirred bead mill", *J. Dispersion Sci. Technol.*, vol. 33, no. 8, pp. 1240–1246, 2012. DOI: 10.1080/01932691.2010.505112.

[19] "ISO 22412:2008(E). particle size analysis – dynamic light scattering (DLS)", International Organization for Standardization, Geneva, CH, Standard, May 2008.

[20] M. R. Alexander, R. D. Short, F. R. Jones, *et al.*, "An X-ray photoelectron spectroscopic investigation into the chemical structure of deposits formed from hexamethyldisiloxane/ oxygen plasmas", *J. Mater. Sci.*, vol. 31, no. 7, pp. 1879–1885, 1996. DOI: 10.1007/BF00372203.

[21] E. B. Flint and K. S. Suslick, "The temperature of cavitation", *Science*, vol. 253, no. 5026, pp. 1397–1399, 1991. DOI: 10.1126/science.253.5026.1397.

[22] W. M. Haynes, "Dissociation constants of organic acids and bases", in *CRC handbook of chemistry and physics*, 95th, Boca Raton: CRC Press, 2014, pp. 5–94, ISBN: 978-1-4822-0867-2.

[23] Y. Feldman, A. Zak, R. Popovitz-Biro, and R. Tenne, "New reactor for production of tungsten disulfide hollow onion-like (inorganic fullerene-like) nanoparticles", *Solid State Sci.*, vol. 2, no. 6, pp. 663–672, 2000. DOI: 10.1016/S1293-2558(00)01070-0.

[24] R. Tenne and G. Seifert, "Recent progress in the study of inorganic nanotubes and fullerene-like structures", *Annu. Rev. Mater. Res.*, vol. 39, no. 1, pp. 387–413, 2009. DOI: 10.1146/annurev-matsci-082908-145429.

[25] A. M. Panich, F. Kopnov, and R. Tenne, "Nuclear magnetic resonance study of fullerene-like WS_2", *J. Nanosci. Nanotechnol.*, vol. 6, no. 6, pp. 1678–1683, 2006. DOI: 10.1166/jnn.2006.211.

[26] D. Chattopadhyay, I. Galeska, and F. Papadimitrakopoulos, "A route for bulk separation of semiconducting from metallic single-wall carbon nanotubes", *J. Am. Chem. Soc.*, vol. 125, no. 11, pp. 3370–3375, 2003. DOI: 10.1021/ja028599l.

4 Publication 3

4.1 Bibliographic Information

4.1.1 Title

Dispersion of fullerene-like WS_2 nanoparticles within epoxy and the resulting fracture mechanics

4.1.2 Authors

- Dietmar Haba [1]
- Andreas J. Brunner [1]
- Gerald Pinter [2]

[1] Empa – Swiss Federal Laboratories for Materials Science and Technology, Dübendorf, Switzerland

[2] Montanuniversität Leoben, Austria

4.1.3 Publication details

Published in:	*Composites Science and Technology*, vol. 119, pp. 55–61, 2015
DOI:	10.1016/j.compscitech.2015.09.013

Statement with regard to publication: The manuscript presented here is an adapted accepted manuscript in order to fit the formatting of the thesis and does not necessarily reflect exactly the actually published version.

4.2 Abstract

Fullerene-like WS_2 (IF-WS_2) nanoparticles (NPs), some with silane-based surface functionalization, were dispersed within epoxy as toughening agents. Dispersion by sonication resulted in a broad and likely bimodal agglomerate size distribution and in thermo-oxidative degradation. In contrast, three-roll milling gave good and well reproducible dispersion quality as measured by dynamic light scattering (DLS). The fracture toughness increased considerably, independently of the functionalization. Atomic-force microscopy indicated that the epoxy's modulus close to the NPs did not differ from the bulk modulus, thus modulus inhomogeneities cannot explain the toughness increase. Fracture surfaces show curved crack lines several hundred nanometers distant from the NPs, which are likely due to secondary cracks induced at the nanoparticle surfaces. The resulting increase in the fracture surface area and possible shear fracture are likely toughening mechanisms.

Keywords: Nano composites; Fracture; Crack; Atomic force microscopy (AFM); Fractography

4.3 Introduction

Epoxy is a polymeric material known for its high strength and modulus, but also for its limited fracture toughness, which is why it is frequently toughened by fillers. In recent years, particular attention is given to nanofillers, as already small amounts can toughen epoxy considerably: For each percent of zero-

dimensional nanoparticles (NPs) added by volume, the critical energy release rate G_{Ic} of epoxy typically increases by 15 % to 75 % and the critical stress-intensity factor K_{Ic} by 5 % to 30 % [1–4].

Inorganic, fullerene-like tungsten disulfide (IF-WS_2) is a relatively new class of NPs. It is best known for its outstanding lubricating effect [5], but there are also promising reports on its use as a nanofiller for polymers [6]. While most work in this field was done on thermoplastics, a few papers dealt with epoxy–IF-WS_2 nanocomposites and showed substantial improvements in adhesion fracture toughness and other mechanical properties [7, 8]. Shneider *et al.* showed that the G_{Ic} of epoxy increases by more than 40 % upon addition of 0.5 % by mass of IF-WS_2, corresponding to appox. 0.09 % by volume [8]. This corresponds to a G_{Ic} increase of more than 500 % per percent of untreated IF-WS_2 added by volume.

Despite the rather inert nature of IF-WS_2, it was indicated that it is possible to graft silane surface modifiers onto them in order to improve their miscibility with oils [9] or epoxy resins [8], as confirmed recently [10]. By addition of 0.5 % by mass of functionalized IF-WS_2 NPs, a G_{Ic} increase of 70 % could be achieved [8], corresponding to an increase of 800 % per percent of IF-WS_2 added by volume.

Among the numerous factors that affect the properties of nanocomposites, the dispersion quality is one of the key factors: Unless homogeneous and reproducible dispersion quality are guaranteed, the measured results must be considered somewhat arbitrary and cannot be generalized. If the dispersion quality is poor, i.e., the NPs appear in large agglomerates, then the filler acts like a conventional microfiller and less expensive fillers might provide comparable improvements. So far, IF-WS_2 NPs were dispersed within epoxy by simple mechanical mixing [11, 12] and in some cases by additional sonication [7, 8]. Agglomerates were observed microscopically in each of these works, but

their size distribution was not quantified. It is thus unclear to what extent the reported effects were caused by nanoscale effects.

Shneider *et al.* have shown crack lines on epoxy–IF-WS_2 nanocomposite fracture surfaces that were several hundred nanometers distant from the NPs and often roughly parabolic in shape. These were interpreted as indicating *nodules*, i.e., for regions around the IF-WS_2 NPs where the epoxy's modulus was higher than in the bulk material. This inhomogeneous modulus distribution was assumed to be the main toughening mechanism [8]. It is unclear which effects could cause such modulus inhomogeneity. Liu *et al.* hypothesized that the epoxy–amine group ratio was imbalanced in the vicinity of NPs [13], which might result in an inhomogeneous modulus distribution. Further possible causes are preferred cure initiation at the NP surfaces, inhibited cure shrinkage or a plasticizing effect of the NP surface modifier. As significant surface moisture has been measured on the NPs [10], this might also affect the cure reaction or plasticize the epoxy. However, no modulus inhomogeneities have been measured so far. Moreover, for unfilled epoxy it has been questioned if such nodules do actually exist [14].

The aim of the present work is to investigate the toughening effects of (partly surface-functionalized) IF-WS_2 NPs in epoxy nanocomposites, as well as the significance of the dispersion quality and the NP surface chemistry for them. Sonication is compared to three-roll mill (3RM), with regards to their effects on the neat epoxy and the resulting dispersion quality and fracture mechanics. The origin of the mentioned crack lines is investigated by SEM and topographic and nanomechanical AFM imaging, and alternative hypotheses are proposed to explain their formation.

4.4 Experimental

4.4.1 Materials

The epoxy resin is a diglycidyl ether of bisphenol A (DGEBA, trade name *Epikote 828 LVEL* from *Momentive*, USA) with an epoxide group content of 5.4 mol/kg and a viscosity of 11 Pa s. The curing agent is a polyetheramine (trade name *Jeffamine T-403* from *Huntsman*, USA) with an amine group content of 6.3 mol/kg.

The IF-WS_2 NP powder (trade name *Nanolub R*) was obtained from the same supplier (*NanoMaterials Ltd.*, Israel) as that used in research published by others earlier [7–9]. However, changes in the manufacturing process with time or unintentional variation from batch to batch cannot be excluded. According to the manufacturer, this powder was produced by high-temperature solid–gas synthesis, the primary particles had diameters of 50 nm to 150 nm and they consisted of 10 to 100 WS_2 layers, with an interlayer spacing of 0.62 nm. Representative transmission electron microscopy images of these particles are given in an earlier work [10] as well as in the Supporting Information of this chapter.

These powders were functionalized with the silane surface modifiers 3-glycidoxypropyltrimethoxysilane (GTMS), 3-(2-aminoethylamino)propyltrimethoxysilane (AATMS) and hexyltrichlorosilane (HTCS) (structure formulas given in the Supporting Information); the preparation procedure is given in table 4.1. The exact functionalization process and the outcome are described elsewhere [10]. Note that the results there indicate that the surface functionalizations with AATMS and with HTCS were successful while that with GTMS might not have been.

Table 4.1: Overview over all treated IF-WS_2 powders

denomination	surface modifier type	mass / mg	solvent
Ref-EtOH			EtOH
Ref-$CHCl_3$			$CHCl_3$
GTMS-1	GTMS	100	EtOH
GTMS-3	GTMS	300	EtOH
AATMS-1	AATMS	100	EtOH
AATMS-3	AATMS	300	EtOH
HTCS-1	HTCS	100	$CHCl_3$
HTCS 3	HTCS	300	$CHCl_3$

4.4.2 Processing

For the preparation of the DGEBA–IF-WS_2 master batches, 0.7 parts by mass (pbm) of the IF-WS_2 powders were mixed with 100 pbm of DGEBA first manually with a spatula and then with an overhead stirrer turning at 2000 min^{-1} for 5 min. Dispersing was done either by sonication or in a 3RM. Sonication was executed for up to 60 min with a 200 W ultrasonic wave generator (*Sonoplus HD 2200* from *Bandelin*, Germany) equipped with a Ti_6Al_4V sonotronde (⌀13 mm) at maximum intensity. In doing so, the suspension was stirred with a magnetic stirrer and was held in a stirred water bath for temperature control. Its temperature increased to roughly 90 °C within about 5 min. The effective sonication power was in the range of 100 W as measured by the electric energy consumption. The same procedure was done on neat DGEBA in order to determine the sonication-induced material damage (see Supporting Information).

The rolls (200 mm wide, ⌀150 mm) of the 3RM (*SDY-200* from *Bühler*, Switzerland) were permanently cooled to 20 °C and turned at 45 min^{-1}, 110 min^{-1} and 220 min^{-1}, respectively. For the first 5 min, the fastest roll was

separated from the other two, so that the suspension was only sheared between these. This step serves mainly for mixing rather than for dispersing. Afterwards, the fastest roll was pressed onto the middle roll with a force of 12 kN so that the suspension was sheared in between them. The material was collected and passed through the 3RM two further times.

Afterwards, either 100 pbm of neat DGEBA or 100.7 pbm of the processed DGEBA–IF-WS_2 master batches were mixed with 40 pbm of polyetheramine curing agent, resulting in a NP loading of 0.5 % by mass or approx. 0.09 % by volume. This substoichiometric epoxide–amine group ratio was chosen for the sake of comparability with an earlier work [8]; for a stoichiometric mixture, 43.9 pbm of curing agent would have been necessary. Mixing was done first manually with a spatula and then with an overhead stirrer turning at 2000 min^{-1} for 5 min. Afterwards, the mixture was poured into a wide beaker (⌀140 mm) and degassed in a vacuum oven at 80 °C to approx. 30 mbar. The mixtures had to reach approx. 70 °C until the air bubbles broke, which took approx. 7 min. Subsequently, the mixture was poured into a steel mold of $160 \times 120 \times 4$ mm^3, the surfaces of which had been coated with a mold release agent (trade name *QZ 13* from *Huntsman*, USA). The mold was placed in a pre-heated oven at 80 °C for 4 h and then cooled down slowly. The cured plates were demolded and machined to appropriate geometries for testing. Subsequently, these samples were heated at 1 °C/min to 100 °C, held there for 3 h, and then cooled at 1 °C/min. This was done to finish the cure reaction and to let the internal stresses relax; there was no measurable change in the geometry of the samples. The glass-transition temperature T_g of the produced epoxy plates was around 85 °C as measured by the maximum in the loss modulus in dynamic-mechanical analyses and did not change significantly in a second measurement. This indicated that the post-curing temperature of 100 °C was high enough to complete the cure reaction. All samples were stored in a desiccator over calcium chloride in vacuum until testing.

4.4.3 Characterization

Dynamic light scattering DLS measurements were done at 25.0 °C (device *Zetasizer Nano Z* from *Malvern*, UK). The master batches were dissolved in acetone (approx. 1:100 by mass, resulting particle volume fraction $\varphi_p \approx 10^{-6}$). The viscosity of neat acetone was used for the calculation of particle diameters. Presented values are the means of 15 individual measurements of 30 s each. As recommended by the respective ISO standard [15], the intensity-weighted average particle diameter $\bar{x}_{DLS}$ is used for evaluation.

The fracture toughness of the nanocomposites was measured in single-edge-notched bending (SENB) tests on specimens of $65 \times 15 \times 4\,mm^3$ at a test speed of 5 mm/min according to ISO 13586 [16]. A pre-crack was introduced by tapping a sharp blade into the machined notch. The pre-cracks of most samples did not fulfill the prerequisites of the ISO 13586 with regards to their length or symmetry; however, these samples were nevertheless tested and used for evaluation. Measurements were rejected if the sample's pre-crack was split into diverging pre-cracks. As a consequence, at least eight out of twelve specimens measured per material were valid. The Supporting Information lists the results for all individual samples as well as their validity.

For investigation of fracture surfaces with a scanning electron microscope (SEM), the nanocomposite samples were sputter-coated with 2 nm Pt (sputtering machine *EM ACE600 High Vacuum Sputter Coater* from *Leica*). The SEM (*NovaNanoSEM 230* from *FEI*) had a Schottky field emission electron source operating at 5 kV, imaging secondary electrons with an Everhart-Thornley detector at roughly 3×10^{-4} Pa pressure. All images were taken from regions close to the pre-crack.

Ultramicrotomy was done in order to obtain smooth surfaces for later investigation by atomic force microscopy (AFM). Ultramicrotome cuts of approx. $200 \times 200\,\mu m^2$ were made at room temperature with an ultramicrotome

(*Ultracut* from *Reichert-Jung*) using a diamond blade (*Ultra* 35° from *Diatome*) at 1 mm/s. The surfaces of the stubs remaining after ultramicrotome cutting were used for AFM investigation.

The AFM (*MultiMode 8* from *Bruker*) was used with a 10 µm scanner in the *Peak-Force Tapping* mode in order to measure the surface topography of fracture surfaces as well as the modulus distribution on ultramicrotome cuts of several nanocomposites. The AFM probes used for the topographic imaging of fracture surfaces trade name *ScanAsyst-Air* had a relatively soft triangular silicon-nitride cantilever (nominal spring constant $k = 0.4\,\mathrm{N/m}$) and a very sharp tip (nominal tip radius $r_{\mathrm{tip}} = 2\,\mathrm{nm}$). Whenever these probes were used, the contact force was kept below 1 nN. In contrast, rectangular silicon AFM probes (trade name *RTESPA*, $k = 40\,\mathrm{N/m}$, $r_{\mathrm{tip}} = 8\,\mathrm{nm}$) were used for nanomechanical imaging at contact forces around 50 nN, thus deforming the epoxy samples by 2 nm to 3 nm. The modulus was gathered assuming a Derjaguin–Muller–Toporov (DMT) model [17]. For detailed information on AFM and the Peak-Force Tapping mode the reader is referred to an earlier work [14].

4.5 Results and Discussion

4.5.1 Nanoparticle dispersion by sonication

After dispersing IF-WS_2 within DGEBA by sonication, large agglomerates were visible with the naked eye. When samples from the suspension were dissolved in acetone for the DLS measurement, these large agglomerates sedimented immediately and were therefore not measured. Hence the DLS measures only the sizes of those agglomerates that sediment sufficiently slowly. Nevertheless, the apparent $\bar{x}_{\mathrm{DLS}}$ was still in the range of 400 nm to 1600 nm with limited reproducibility even after 60 min of sonication, and both visual and microscopic inspection support these results.

The obtained dispersion quality is significantly worse than that obtained after sonication within EtOH when $\bar{x}_{DLS}$ around 240 nm were obtained [10]. It seems that the high viscosity of the DGEBA limits the effectiveness of the sonication as it was assumed earlier [18]. However, others reported reasonable NP dispersion quality after sonication within DGEBA [8, 18, 19] for different kinds of NPs, and it is unclear what causes the difference.

The real polydispersity of partly sedimenting powders cannot be quantified by DLS. However, it was observed that both large agglomerates and individual primary particles were present after sonication, hence the agglomerate size distribution was very broad and probably bimodal. Fig. 4.1 outlines a possible mechanism that might result in such a bimodal agglomerate size distribution: Instead of splitting large agglomerates into comparably large parts, it seems that sonication rather *erodes* the agglomerates, that is to say, it causes small agglomerates to break off a large one, which in turn barely changes in its size. Such a mechanism would per se result in a broad, bimodal agglomerate size distribution.

Besides resulting in insufficient dispersion quality, sonication also causes a yellowing of the DGEBA, indicating thermo-oxidative degradation (see Supporting Information). In a nutshell, sonication does not seem to be the optimum dispersion technique.

4.5.2 Dispersion quality after 3RM

In contrast to sonication, the driving forces for dispersion in a 3RM are intense shear stresses for short time periods. Thus, the total induced energy is rather low so that little material damage is expected. Nevertheless, a temperature increase to up to 50 °C was measured, even though the rolls were permanently cooled. There was no color change observed, neither visually nor by UV/Vis

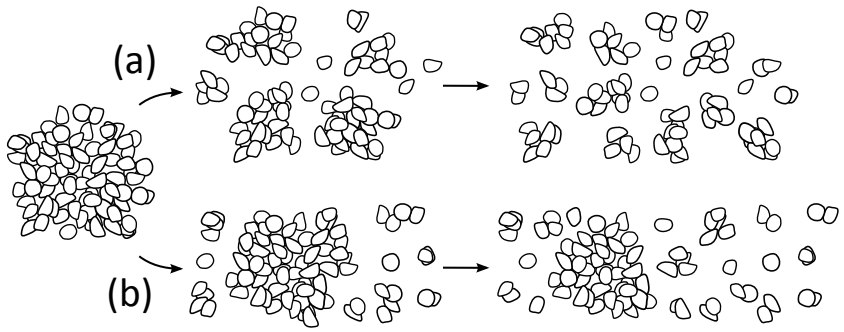

Figure 4.1: Schematic drawing of two different dispersion mechanisms. In (a) agglomerates are preferably split into smaller agglomerates of comparable sizes, while in (b) smaller agglomerates erode from a larger one. The particle size distribution in (b) is bimodal.

spectroscopy, after up to five passes of neat DGEBA in the 3RM, indicating that degradation was insignificant.

No agglomerates were visible anymore after just one single pass of untreated IF-WS_2 in DGEBA through the 3RM. The measured $\bar{x}_{DLS}$ was 193 nm, 180 nm and 177 nm after 1, 2 and 3 passes through the 3RM, respectively, with very good reproducibility. Hence, the obtained dispersion quality is clearly superior to that achieved by sonication for 60 min, even though the $\bar{x}_{DLS}$ after 3RM is still somewhat larger than the assumed average primary particle diameter ($\approx$ 100 nm). As 3RM is also much more easily scalable to industrial scale, it is clearly preferable to sonication. Consequently, the functionalized powders were dispersed within DGEBA exclusively by 3RM for the further investigations.

4.5.3 Influence of surface functionalization

It was speculated that the surface functionalization improves the IF-WS_2 NPs' miscibility with DGEBA and therefore grants better dispersion quality. In or-

der to test that, DLS measurements were done on all DGEBA–IF-WS_2 master batches after 0, 1, 2 and 3 passes in the 3RM.

With the exception of the two master batches made with AATMS-modified powders, there are only small differences in the $\bar{x}_{DLS}$ of all 3RMed master batches, independently of the surface modifier (see fig. 4.2). After 1, 2 and 3 passes through the 3RM, the $\bar{x}_{DLS}$ of those master batches were (186 ± 13) nm, (170 ± 10) nm and (167 ± 8) nm, respectively.

Both the unprocessed master batches (i.e., those with zero passes in the 3RM) and the master batches made with AATMS-modified IF-WS_2 behaved entirely differently. Large sedimenting agglomerates were visible after dissolving them in acetone. Accordingly, the DLS results of these samples do not represent the real average agglomerate size, but only that of the non-sedimenting fraction. In order to emphasize that, these data points were plotted unfilled and connected with dashed lines in fig. 4.2. The measured $\bar{x}_{DLS}$ of these samples was much higher, with large scatter and poor reproducibility.

It may seem surprising that the AATMS-processed powders behaved so much poorer than unprocessed IF-WS_2. This could be explained by a curing reaction that had taken place already before the DLS measurements: Even though the DLS measurements of the master batches were done just a few hours after processing them, it is hypothesized that the AATMS's amine/ammonium groups had already reacted with the DGEBA's epoxide groups. Even if the dispersion quality was good after the 3RM, such a reaction would result in large agglomerate networks, which would remain after dissolving the master batches in acetone. However, these large agglomerates might not necessarily be present in the cured nanocomposites, as for the production of these, the master batches were mixed with the amine curing agent just several minutes after processing them. The fact that both AATMS-treated powders behaved differently from all others strongly suggests that they had

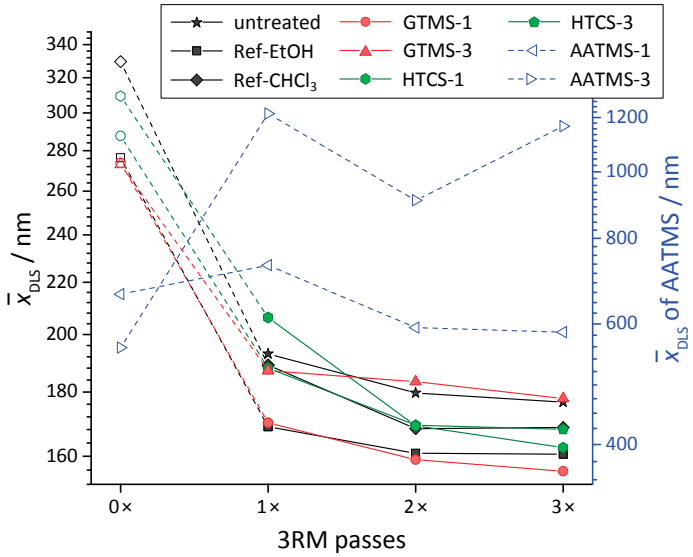

Figure 4.2: Average agglomerate diameter of all treated IF-WS_2 powders after mixing them with DGEBA and different numbers of passes through the 3RM. Note that the results of AATMS-1 and AATMS-3 are scaled according to the right axis. Unfilled symbols indicate measurements where sedimentation was observed.

been functionalized successfully and that the functional groups do indeed react with the DGEBA.

The low scattering of most DLS results shown in fig. 4.2 indicates that both the 3RM process and the DLS measurement are well reproducible. Already a single pass through the 3RM can be sufficient to obtain a rather good dispersion quality, significantly superior to that obtained by sonication within DGEBA or ethanol [10]. Further 3RM passes improve this dispersion quality slightly; the final agglomerate diameter is nevertheless still larger than that of the individual primary particles (approx. 100 nm).

In a nutshell, it seems that the functionalization did not affect the dispersion quality of the produced master batches, unless reactive groups reacted with the DGEBA before the DLS measurement forming insoluble agglomer-

ates. As earlier measurements have indicated that the surface functionalization with HTCS was successful [10], this result indicates that an alkyl surface coating does not improve the miscibility of IF-WS_2 with DGEBA. This is in contrast to the findings of Shahar *et al.* who found that HTCS improved the miscibility of IF-WS_2 with paraffin oil [9]. On the other hand, the surface of IF-WS_2 is already very nonpolar so that further hydrophobic treating might be unnecessary.

4.5.4 Fracture toughness

Table 4.2 shows the SENB test results of neat DGEBA and the DGEBA nanocomposites with the differently functionalized IF-WS_2 at a mass fraction of 0.5 % each. All nanocomposites show increased fracture toughness. The smallest improvement was obtained when the dispersion was done by 60 min of sonication. Dispersing untreated IF-WS_2 by 3RM lead to much higher improvements, but also to high scatter. Nanocomposites made of treated IF-WS_2 gave improvements of 45 % to 62 % in G_{Ic} and of 15 % to 25 % in K_{Ic}, irrespecively of the particular treatment. This corresponds to an increase of approx. 500 % in G_{Ic} and of approx. 200 % in K_{Ic} per percent of IF-WS_2 added by volume. These values are comparable to those presented in an earlier work [8], even though those were measured with another fracture toughness test method. Other than in this earlier work, however, no significant correlation was observed with the nominal surface functionalization nor with the XPS results of the respective powders [14], indicating that the surface treatment does not play a significant role in the toughening effect. This contradiction to an earlier finding [8] might partly be explained with possible differences in the pristine NPs used; even though the supplier was the same, manufacturing variations or process variability cannot be excluded. Lacking di-

rect comparative characterization, e.g., by transmission electron microscopy, however, there is no clear evidence for such effects.

4.5.5 SEM fractography

The fracture surfaces of all tested nanocomposites were investigated by SEM. There were both very small and very large agglomerates present in the nanocomposite produced by sonication, which is consistent with the observation that sonication leads to a bimodal agglomerate size distribution. In contrast, the agglomerate sizes were homogeneously distributed in nanocomposites produced by 3RM. Selected SEM images are given in fig. 4.3 and additional images are given in the Supporting Information. Most visible particles were present in the form of small agglomerates consisting of a few primary particles, but individual primary particles were also visible, as well as large agglomerates with diameters of up to a few micrometers, all of which is in good agreement with the DLS results.

The SEM images show a clear difference between dispersion by sonication (fig. 4.3a) and 3RM (fig. 4.3b), but also certain differences between the individual 3RM-dispersed nanocomposites. For instance, the fracture surface of EP/GTMS-3 seems to be relatively smooth and its fairly homogeneously dispersed NPs tend to detach from the epoxy matrix (fig. 4.3c). In contrast, the fracture surface of EP/HTCS-1 seems to be much rougher, with multiple crack lines, and the less perfectly dispersed NPs tend to adhere to the matrix (fig. 4.3d). This is in contrast to the observations of Shneider *et al.*, who reported that cavitation takes place more frequently around IF-WS_2 functionalized with alkyl groups [8].

The large agglomerate size measured in EP/AATMS-3 by DLS does not reflect in the SEM images (fig. 4.3f), which supports the assumption that the large, insoluble networks observed by DLS had not formed prior to mixing the

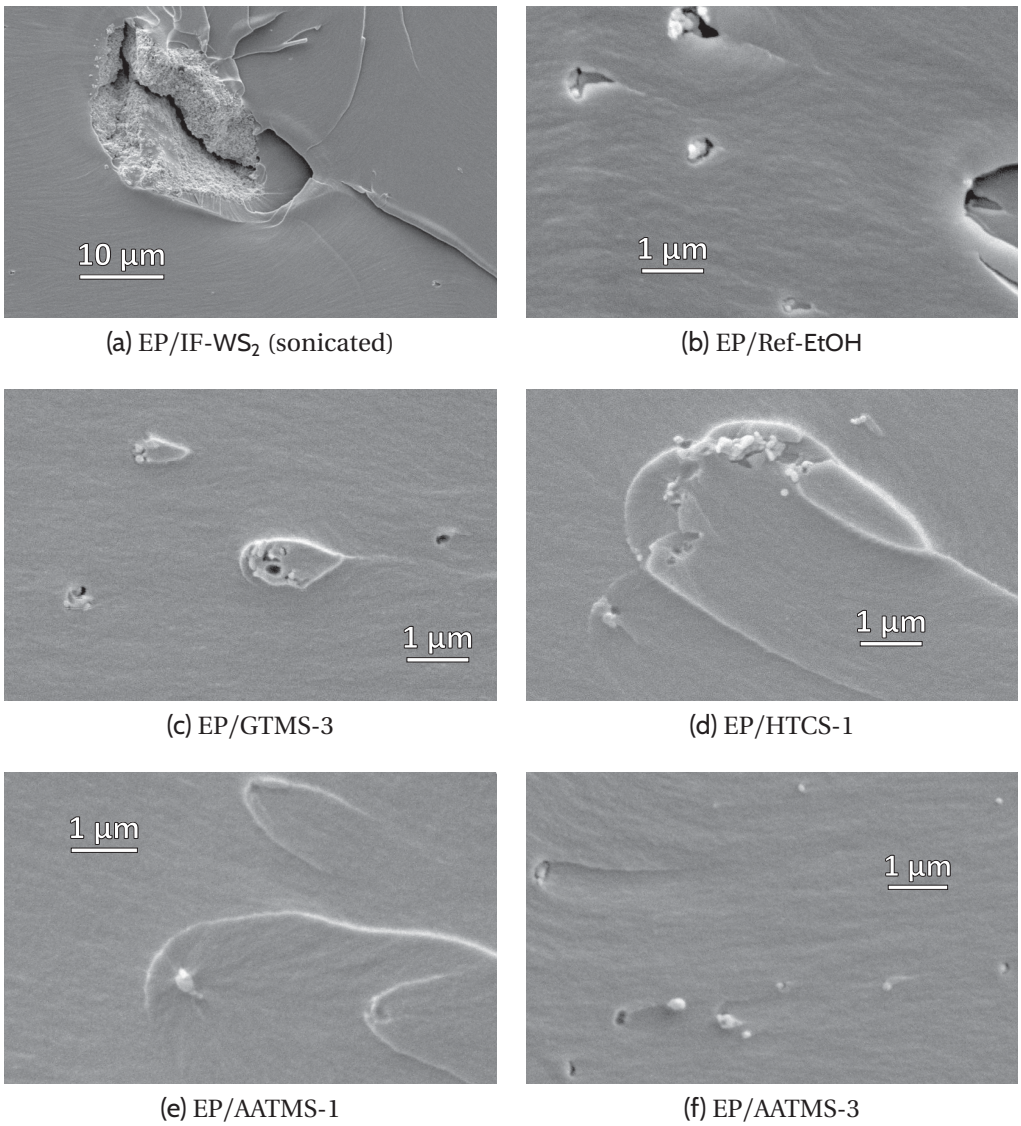

(a) EP/IF-WS_2 (sonicated)

(b) EP/Ref-EtOH

(c) EP/GTMS-3

(d) EP/HTCS-1

(e) EP/AATMS-1

(f) EP/AATMS-3

Figure 4.3: SEM images of selected fracture surfaces (note the different scales). The direction of crack propagation is from left to right.

Table 4.2: Fracture toughness results

	G_{Ic} / (J/m^2)	$\frac{\langle G_{Ic}\rangle - \langle G_{Ic,neat}\rangle}{\langle G_{Ic,neat}\rangle}$	K_{Ic} / (MPa$\sqrt{m}$)	$\frac{\langle K_{Ic}\rangle - \langle K_{Ic,neat}\rangle}{\langle K_{Ic,neat}\rangle}$
neat epoxy 1	144.9 ± 22.7		0.698 ± 0.057	
neat epoxy 2	139.1 ± 16.3		0.677 ± 0.038	
IF-WS_2 sonic.	160.8 ± 10.9	13 %	0.742 ± 0.025	8 %
IF-WS_2 3RM	206.7 ± 51.1	46 %	0.791 ± 0.096	15 %
Ref-EtOH	213.3 ± 31.3	50 %	0.804 ± 0.056	17 %
Ref-$CHCl_3$	230.1 ± 24.7	62 %	0.858 ± 0.055	25 %
GTMS-1	217.1 ± 30.1	53 %	0.804 ± 0.055	17 %
GTMS-3	224.6 ± 11.5	58 %	0.834 ± 0.019	21 %
HTCS-1	206.3 ± 27.8	45 %	0.799 ± 0.063	16 %
HTCS-3	214.5 ± 21.4	51 %	0.827 ± 0.038	20 %
AATMS-1	206.9 ± 24.5	46 %	0.793 ± 0.052	15 %
AATMS-3	216.5 ± 32.0	52 %	0.826 ± 0.073	20 %

master batches with the amine curing agent. In contrast, the agglomerates in EP/AATMS-1 appear to be relatively large in the SEM images (given in the Supporting Information). The clear difference between these two samples is surprising, considering the similar DLS results and the good reproducibility of the 3RM process. Notably, the fracture toughness values of all 3RM-dispersed nanocomposites is comparable, indicating that the seemingly different dispersion qualities visible on SEM images are not representative for the bulk material or not critical at this level.

4.5.6 Modulus distribution

Several fractographic images show crack lines with several hundred nanometers distance to the NPs and a conic-section shape (e.g., fig. 4.3e). As men-

tioned, it was hypothesized elsewhere that these crack lines originated from a region of increased modulus in the vicinity of the IF-WS_2 NPs [8].

In order to test this hypothesis, the modulus distribution in the vicinity of the IF-WS_2 NPs was measured on ultramicrotome-cut surfaces of selected samples with AFM. Fig. 4.4 shows an example of simultaneously gathered AFM height and modulus images of an IF-WS_2 agglomerate in EP/AATMS-1. This agglomerate was not removed or split by the ultramicrotome, but stuck to the nanocomposite stub and hence results in a round elevation of 80 nm height in the otherwise very smooth surface.

For the interpretation it must be noted that the AFM modulus measurement is valid only on plane areas as only these agree with the underlying DMT deformation model [14]. Therefore, the modulus inhomogeneity in the region of the elevation in the center must be considered invalid. Except for the elevation, the modulus in fig. 4.4 seems to be very homogeneous. AFM imaging of cryo-ultramicrotome cuts of commercial acrylonitrile–styrene–acrylate showed that modulus variations in the range of a few hundred MPa can be measured on smooth regions with this AFM technique if they are present (shown in the Supporting Information). Such modulus inhomogeneities are absent in the smooth regions in fig. 4.4.

The profile curves of the highlighted rectangle in fig. 4.4 are given in fig. 4.5. The measured bulk modulus is quite constant at 3.1 GPa to 3.4 GPa, which compares well with the modulus values of 2.9 GPa to 3.4 GPa gathered in the SENB tests. Approaching the NP, the first pixels that deviate from this range are already in the topographic curvature and therefore invalid. Similar results were obtained for other nanocomposites with both functionalized and unfunctionalized IF-WS_2.

It is possible that modulus inhomogeneities are present, but smaller in magnitude than what is resolved with this technique (approx. 300 MPa) and/or their lateral dimensions (approx. 10 nm). Moreover, it is possible that

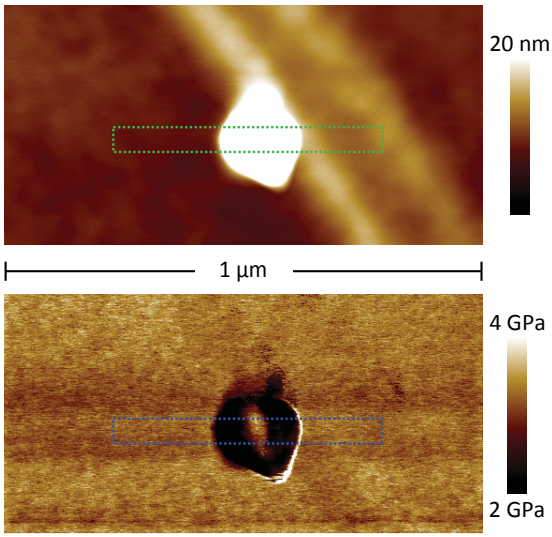

Figure 4.4: Nanomechanical AFM height (top) and modulus (bottom) image of an ultramicrotome cut of the EP/AATMS-1 nanocomposite. No modulus inhomogeneity is visible in smooth regions.

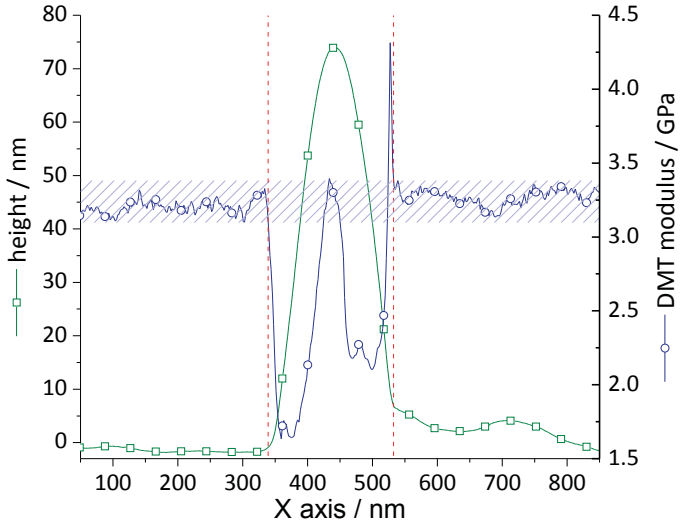

Figure 4.5: Average value of the profiles within the highlighted rectangle in fig. 4.4. The shaded area highlights the bulk modulus. No deviations from this area were measured in smooth regions.

modulus inhomogeneities were present but have relaxed upon ultramicrotomy. It is nevertheless unlikely that the observed crack lines were indeed caused by epoxy modulus inhomogeneities and thus an alternative explanation is proposed.

4.5.7 Crack lines

It is worth noting that similar crack lines have long since been recognized in unfilled polymers, mostly in PMMA, but also in unfilled epoxy [20, 21], and were usually explained by the formation of *secondary* cracks that form ahead of the propagating *primary* crack [22]. Wetzel *et al.* observed similar crack lines in NP-filled epoxy systems and explained them with *crack pinning* or *crack front bowing*, but also mentioned the possibility of secondary cracks being formed [1].

It is hence suggested that the crack lines visible here originate from secondary cracks as well. These might initiate at the NP surfaces as the primary crack approaches the rigid NPs and the stresses concentrate around them. Such secondary cracks would then propagate radially in all lateral directions. Once a secondary crack overlaps with the primary crack in the main stress axis, the material between them can experience shear fracture, forming a clearly visible crack line.

When the primary crack propagates at a constant velocity v_p and a secondary crack at a constant velocity v_s, their ratio determines whether the resulting crack line is elliptic ($v_s < v_p$), parabolic ($v_s = v_p$) or hyperbolic ($v_s > v_p$) in shape. Each of these shapes was observed on SEM images (derivation in the Supporting Information). However, as v_s will generally not be constant, most crack lines will not form ideal conic sections.

AFM height images of fracture surfaces provide further insight into the nature of the crack lines. As shown in fig. 4.6, the region enclosed by the crack

line is at another height level than the main fracture plane. The border between these two regions is almost vertical, i.e., parallel to the main stress direction during the fracture process, which is a very unfavorable crack propagation direction in a mode I fracture mechanics test. The height difference measured at this crack line was 80 nm, but other crack lines had height differences of up to 300 nm.

Besides the visible secondary cracks, it is assumed that many additional subsurface secondary cracks are created during a fracture process. The additional energy necessary for producing these secondary crack surfaces and the shear cracks might also contribute to the G_{Ic} increase. Likewise, NPs and secondary cracks from the pre-cracking result in an inhomogeneous stress field at the crack tip before fracture, which might explain the K_{Ic} increase.

4.6 Conclusion

This work deals with the dispersion of IF-WS_2 within DGEBA and the fracture mechanics of the resulting nanocomposites. Sonication-induced dispersion resulted in limited dispersion quality with a broad and probably bimodal agglomerate size distribution, as was already visible with the naked eye and confirmed by SEM investigation. The hypothesis that sonication leads to erosion of NPs rather than their splitting might explain the poor effectiveness of the dispersion process. Moreover, sonication seems to cause thermo-oxidative degradation of the DGEBA resin.

In contrast, 3RM resulted in a reasonable and very well reproducible dispersion quality as evidenced by DLS measurements and SEM images. DLS proved to be a suitable technique for measuring sizes of agglomerates of zero-dimensional NPs, provided that the polydispersity is low enough. Obtainable average agglomerate diameters after 3RM lie at approx. 160 nm and are hence

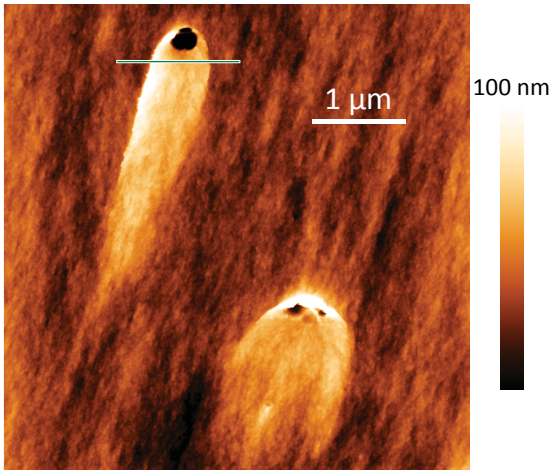

Figure 4.6: Topographic AFM image of the fracture surface of EP/AATMS-3 showing crack lines produced by two IF-WS_2 NP agglomerates.

still somewhat larger than the diameters of the individual primary particles, i.e., the particles are still mostly present in the form of small agglomerates.

Untreated IF-WS_2 NPs were compared with IF-WS_2 NPs that had been treated with various silane surface modifiers as described elsewhere [10]. The various functionalizations had no significant effect on the obtained average agglomerate diameter. An exception are the two AATMS-modified samples, which seemed to have strongly increased agglomerate diameters after 3RM as measured by DLS, most likely due to the fact that their functional groups had already reacted with the DGEBA. However, this did not seem to affect the dispersion quality of the cured nanocomposites.

The addition of 0.5 % of IF-WS_2 by mass increased the K_{Ic} by 15 % to 25 % and the G_{Ic} by 45 % to 62 %, respectively, independently of the particular functionalization, provided that the processing was done in the 3RM, while the improvements after sonication were significantly smaller. SEM images confirmed that the dispersion quality was reasonable after 3RM, even though there were still agglomerates left. Other than stated elsewhere [8], no signifi-

cant correlation was observed between the surface functionalization and the fracture mechanics of the nanocomposites.

Crack lines were observed with a few hundred nanometers distance to the NPs, which have been interpreted elsewhere as a result of an inhomogeneous modulus distribution in the vicinity of IF-WS_2 NPs [8]. This hypothesis was investigated by AFM imaging, but cannot be supported as the modulus was measured to be homogeneous up to the NP border. Topographic AFM images showed that the height difference between the two sides of the crack lines was up to 300 nm.

Considering the essentially conic-section-like shape of the observed crack lines, a plausible explanation for them is the formation of radially propagating secondary cracks at the NP surfaces. When secondary cracks overlap with the primary crack, the matrix material between them can experience shear fracture, thus dissipating energy. Together with the additional surface area for both surface and subsurface secondary cracks, this is suggested to be the explanation for the fracture toughness increase.

Acknowledgments

The authors would like to thank Anja Huch and Beatrice Fischer for their experimental work and Alan F. Rawle and Christian Teichert for their precious theoretical support. Furthermore, we acknowledge the support of Maja M. Günthert and ScopeM/Swiss Federal Institute of Technology ETHZ. Finally, we want to thank BASF and Huntsman Corporation for kindly delivering materials.

Supporting Information

Supporting Information related to this chapter can be found in section 8.3.

References

[1] B. Wetzel, P. Rosso, F. Haupert, and K. Friedrich, "Epoxy nanocomposites – fracture and toughening mechanisms", *Eng. Fract. Mech.*, vol. 73, no. 16, pp. 2375–2398, 2006. DOI: 10.1016/j.engfracmech.2006.05.018.

[2] B. B. Johnsen, A. J. Kinloch, R. D. Mohammed, A. C. Taylor, and S. Sprenger, "Toughening mechanisms of nanoparticle-modified epoxy polymers", *Polymer*, vol. 48, no. 2, pp. 530–541, 2007. DOI: 10.1016/j.polymer.2006.11.038.

[3] H.-Y. Liu, G.-T. Wang, Y.-W. Mai, and Y. Zeng, "On fracture toughness of nanoparticle modified epoxy", *Composites, Part B*, vol. 42, no. 8, pp. 2170–2175, 2011. DOI: 10.1016/j.compositesb.2011.05.014.

[4] D. J. Bray, P. Dittanet, F. J. Guild, *et al.*, "The modelling of the toughening of epoxy polymers via silica nanoparticles: The effects of volume fraction and particle size", *Polymer*, vol. 54, no. 26, pp. 7022–7032, 2013. DOI: 10.1016/j.polymer.2013.10.034.

[5] L. Rapoport, Y. Bilik, Y. Feldman, *et al.*, "Hollow nanoparticles of WS_2 as potential solid-state lubricants", *Nature*, vol. 387, pp. 791–793, 1997. DOI: 10.1038/42910.

[6] M. Naffakh, A. M. Díez-Pascual, C. Marco, G. J. Ellis, and M. A. Gómez-Fatou, "Opportunities and challenges in the use of inorganic fullerene-like nanoparticles to produce advanced polymer nanocomposites", *Prog. Polym. Sci.*, vol. 38, no. 8, pp. 1163–1231, 2013. DOI: 10.1016/j.progpolymsci.2013.04.001.

[7] A. Buchman, H. Dodiuk-Kenig, A. Dotan, R. Tenne, and S. Kenig, "Toughening of epoxy adhesives by nanoparticles", *J. Adhes. Sci. Technol.*, vol. 23, no. 5, pp. 753–768, 2009. DOI: 10.1163/156856108X379209.

[8] M. Shneider, H. Dodiuk, R. Tenne, and S. Kenig, "Nanoinduced morphology and enhanced properties of epoxy containing tungsten disulfide nanoparticles", *Polym. Eng. Sci.*, vol. 53, no. 12, pp. 2624–2632, 2013. DOI: 10.1002/pen.23517.

[9] C. Shahar, D. Zbaida, L. Rapoport, *et al.*, "Surface functionalization of WS_2 fullerene-like nanoparticles", *Langmuir*, vol. 26, no. 6, pp. 4409–4414, 2010. DOI: 10.1021/la903459t.

[10] D. Haba, T. Grießer, U. Müller, and A. J. Brunner, "Critical investigation of the silane surface functionalization of fullerene-like WS_2", *J. Mater. Sci.*, vol. 50, no. 15, pp. 5125–5135, 2015. DOI: 10.1007/s10853-015-9039-4.

[11] L. Rapoport, O. Nepomnyashchy, A. Verdyan, *et al.*, "Polymer nanocomposites with fullerene-like solid lubricant", *Adv. Eng. Mater.*, vol. 6, no. 1–2, pp. 44–48, 2004. DOI: 10.1002/adem.200300512.

[12] M. Shneider, H. Dodiuk, S. Kenig, and R. Tenne, "The effect of tungsten sulfide fullerene-like nanoparticles on the toughness of epoxy adhesives", *J. Adhes. Sci. Techn.*, vol. 24, no. 6, pp. 1083–1095, 2010. DOI: 10.1163/016942409X12584625925268.

[13] G. Liu, H. Zhang, D.-j. Zhang, *et al.*, "On depression of glass transition temperature of epoxy nanocomposites", *J. Mater. Sci.*, vol. 47, no. 19, pp. 6891–6895, 2012. DOI: 10.1007/s10853-012-6633-6.

[14] D. Haba, J. Kaufmann, A. J. Brunner, K. Resch, and C. Teichert, "Observation of elastic modulus inhomogeneities in thermosetting epoxies using AFM – discerning facts and artifacts", *Polymer*, vol. 55, no. 16, pp. 4032–4040, 2014. DOI: 10.1016/j.polymer.2014.06.030.

[15] "ISO 22412:2008(E). particle size analysis – dynamic light scattering (DLS)", International Organization for Standardization, Geneva, CH, Standard, May 2008.

[16] "ISO 13586:2000(E). plastics – determination of fracture toughness (G_{IC} and K_{IC}) – linear elastic fracture mechanics (LEFM) approach", International Organization for Standardization, Geneva, CH, Standard, Mar. 2000.

[17] B. V. Derjaguin, V. M. Muller, and Y. P. Toporov, "Effect of contact deformations on the adhesion of particles", *J. Colloid Interface Sci.*, vol. 53, no. 2, pp. 314–326, 1975. DOI: 10.1016/0021-9797(75)90018-1.

[18] B. Bittmann, F. Haupert, and A. K. Schlarb, "Preparation of TiO_2 epoxy nanocomposites by ultrasonic dispersion and resulting properties", *J. Appl. Polym. Sci.*, vol. 124, no. 3, pp. 1906–1911, 2012. DOI: 10.1002/app.34493.

[19] M. Englert, B. Bittmann, F. Haupert, and A. K. Schlarb, "Scaling-up of the dispersion process of nanoparticle-agglomerates in epoxy resin with an innovative continuous ultrasonic flow-through-cell dispersion system", *Polym. Eng. Sci.*, vol. 52, no. 1, pp. 102–107, 2012. DOI: 10.1002/pen.22051.

[20] I. Narisawa, T. Murayama, and H. Ogawa, "Internal fracture of notched epoxy resins", *Polymer*, vol. 23, no. 2, pp. 291–294, 1982. DOI: 10.1016/0032-3861(82)90319-6.

[21] R. E. Robertson, M. G. Sporer, T.-Y. Pan, and V. E. Mindroiu, "Plasticity of brittle epoxy resins during debonding failures", *J. Mat. Sci.*, vol. 24, no. 11, pp. 4106–4113, 1989. DOI: 10.1007/BF01168982.

[22] W. Döll, "Fractography and failure mechanisms of amorphous thermoplastics", in *Fractography and failure mechanisms of polymers and composites*, A. C. Roulin-Moloney, Ed., Elsevier Applied Science, 1989, ch. 10, pp. 397–399, ISBN: 1-85166-296-0.

5 Publication 4

5.1 Bibliographic Information

5.1.1 Title

Significance of epoxy network properties for the toughening effect of flaky and fullerene-like WS_2 nanoparticles

5.1.2 Authors

- Dietmar Haba [1]
- Michel Barbezat [1]
- Santhosh Ayalur-Karunakaran [2]
- Sandra Schlögl [2]
- Andreas J. Brunner [1]
- Gerald Pinter [3]

[1] Empa – Swiss Federal Laboratories for Materials Science and Technology, Dübendorf, Switzerland

[2] Polymer Competence Center Leoben, Leoben, Austria

[3] Montanuniversität Leoben, Leoben, Austria

5.1.3 Publication details

Published in: *Journal of Polymer Science, Part B: Polymer Physics*, vol. 54, no. 17, pp. 1738–1747, 2016
DOI: 10.1002/polb.24077

Statement with regard to publication: The manuscript presented here is an adapted accepted manuscript in order to fit the formatting of the Thesis and does not necessarily reflect exactly the actually published version.

5.2 Abstract

This work deals with the toughening effect of flaky WS_2 and fullerene-like WS_2 (IF-WS_2) nanoparticles on epoxy with varying network properties. Reducing the amount of curing agent resulted in decreased cross-link density as measured by dynamic-mechanic analysis and double-quantum nuclear magnetic resonance spectroscopy. While that lead to moderate changes in the epoxy's tensile properties, its fracture toughness dropped drastically, probably due to an increased defect fraction. IF-WS_2 could be dispersed significantly more effectively within epoxy resin than flaky WS_2, possibly due to its spherical shape, but caused less toughening. IF-WS_2 tended to debond from the epoxy, while flaky WS_2 introduced more secondary cracks. Both increased the fracture toughness of the (brittle) sub-stoichiometric, but not that of the (tough) stoichiometric epoxy, possibly due to their interaction with molecular defects. Whatever mechanism resulted in the toughening effect, its effectiveness depended strongly on the epoxy matrix.

Keywords: Epoxy, Stoichiometry, Cross-link density, Nanocomposites, Fracture

5.2.1 Graphical Table of Contents

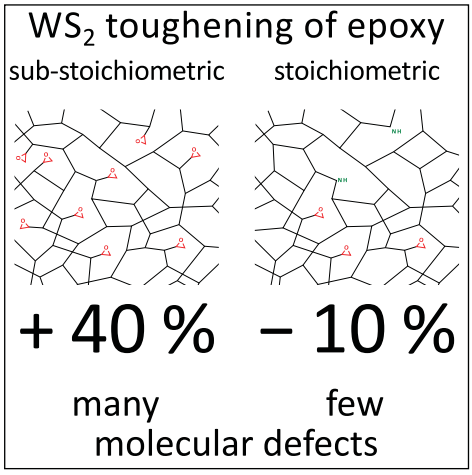

Two types of WS_2 nanoparticles were used to toughen epoxy systems made with different amounts of curing agent. As a consequence, these systems differed in their crosslink density and the density of molecular defects. The sub-stoichiometric epoxy system was much more brittle then the stoichiometric one. However, it could be toughened much more effectively by the WS_2 nanoparticles, highlighting how important the properties of the reference system are.

5.3 Introduction

Epoxy is a thermosetting polymer that is well known for its interesting mechanical and chemical properties and its good processibility, and is therefore frequently used as a matrix in fiber-reinforced composites. However, its applications are limited by its inherent brittleness. Scientists are hence constantly researching ways to improve the epoxy's fracture toughness, recently more and more by the introduction of nanoparticles (NPs).

Two recent publications showed that inorganic fullerene-like WS_2 (IF-WS_2) NPs can increase the fracture toughness of epoxy considerably [1, 2], so that they seem an interesting alternative to (carbon) fullerenes which have been used elsewhere [3]. Likewise, flaky WS_2 NPs can be seen as an inorganic analogy to graphite (see fig. 5.1). Nanodispersed, flaky WS_2 is expected to behave somewhat similarly to IF-WS_2 when used as a nanofiller due to the similar surface chemistry and the similar primary particle size, the most significant

difference being the crystal structure. However, due to their spherical shape, IF-WS_2 NPs can roll off each other [4], so that they are potentially easier to disperse. A comparison of IF-WS_2 with nanodispersed, flaky WS_2 might show to what extent the fullerene-like shape of the IF-WS_2 NPs affects their dispersibility and their toughening effect. A more detailed discussion on the morphology of IF-WS_2 and WS_2 NPs can be found in the related literature [5–7].

Much effort has been dedicated to determine the toughening effect of the NP type, morphology and functionalization [8], but relatively little attention has been given to the significance of the properties of the neat epoxy system. It is currently not clear, which properties of an epoxy system affect its potential to be toughened by NPs. In this work, the term *epoxy system* will be used to describe unique proportions of a specific epoxy resin with a specific curing agent, cured with a given temperature profile, as only this entire combination determines the properties of the final material.

Hsieh *et al.* [9] used a complex model to estimate the fracture toughness increase of epoxy with NP addition. This model suggests higher relative increases for epoxy systems with high initial fracture strain and high initial fracture toughness as well as for low cross-link density. In contrast, a recent work found higher fracture toughness increases for epoxy systems with high cross-link density [10].

The two initially mentioned references reporting a toughening effect of IF-WS_2 NPs used a *sub-stoichiometric* epoxy system [1, 2], as the ratio λ of amine hydrogen atoms to epoxide groups was only approx. 0.93. Sub-stoichiometric systems have significantly lower fracture toughness than stoichiometric systems [11, 12], possibly due to their lower cross-link density and the higher amount of molecular defects like dangling bonds. The toughening effect of NPs depends both on the fracture toughness of the neat epoxy

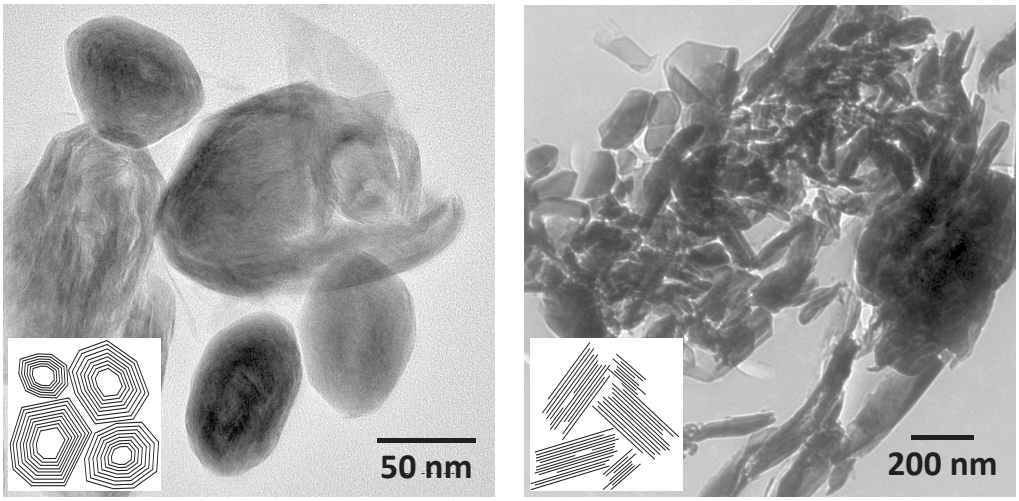

(a) IF-WS_2 (b) flaky WS_2

Figure 5.1: Transmission electron microscopy images of NP agglomerates. The insets are schematic drawings of the NPs' crystal structures.

system and on its cross-link density [9, 10]. It is thus likely that the potential toughening effect of NPs depends strongly on λ.

One argument for using slightly sub-stoichiometric systems is that these can have a higher strength σ and a higher Young's modulus E [13], both of which can be crucial depending on the application. However, varying λ can also be interesting for purely scientific reasons, as it allows varying the epoxy's cross-link density without changing the chemical reactants. Fig. 5.2 schematically shows the differences between a stoichiometric and a sub-stoichiometric epoxy network. In a stoichiometric network, both the cross-link density and the chemical conversion are maximum, although a certain number of secondary amine groups and dangling bonds from unreacted epoxide groups will always remain. In a sub-stoichiometric network, the cross-link density will be lower and hardly any secondary amine groups but significantly more dangling bonds from unreacted epoxide groups will re-

main. Varying the curing agent content is thus expected to allow varying the cross-link density while keeping the used reactants the same.

It should be noted that the unreacted epoxide groups can undergo an autopolymerization reaction to form ether linkages, which might increase the cross-link density of the sub-stoichiometric epoxy system. However, this reaction is insignificant at temperatures below 150 °C in the absence of a catalyst [14], so that it is not expected to take place in the investigated epoxy systems.

Measuring the cross-link density of a thermosetting polymer is a rather difficult issue as the rubber elasticity theory does not apply to these highly cross-linked materials. One of the most promising ways to measure the molecular mass per cross-link M_c (basically the inverse of the cross-link density) is by relating it to the rubber equilibrium modulus E_r (i.e., the Young's modulus above the glass-transition temperature T_g) and to the mass density ρ: [9, 15, 16]

$$\log_{10} \frac{E_r}{3\ \mathrm{MPa}} = 293 \frac{\rho}{M_c} \frac{\mathrm{mol}}{\mathrm{cm}^3} \tag{5.1}$$

A less well known method to measure the cross-link density is the (low-field) double-quantum nuclear magnetic resonance (DQ NMR) spectroscopy. In the recent years, it has been successfully applied to characterize the network structure of elastomers [17, 18], hydrogels [19] and ionomers [20], however it has not been applied to thermosets like epoxy until recently [21]. This method allows measuring a material's residual dipolar coupling D_{res}, which corresponds to the overall rigidity of the network chains after delineating it from the effect of the more mobile non-network or defect chains. Furthermore, it facilitates the determination of the mole fraction of non-network chains in a network sample. This is of particular interest for sub-stoichiometric epoxy formulations where significant fractions of dangling unreacted epoxide groups can be expected. Details of the application of this

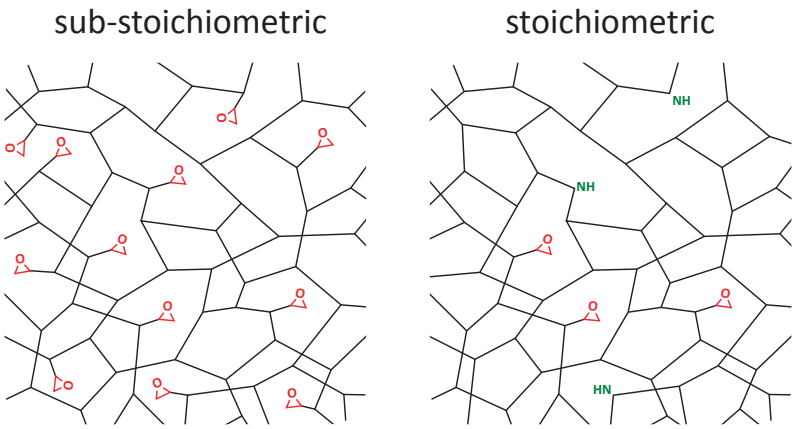

Figure 5.2: Schematic drawing of a sub-stoichiometric and a stoichiometic epoxy network. In sub-stoichiometic networks, the cross-link density is lower, the number of unreacted epoxide groups is much higher and there are barely any secondary amine groups left.

method especially to elastomers can be found elsewhere [18, 22] and a brief discussion of the application, the data processing and analysis can be found in the Supporting Information of the present article.

The aim of the present work was to investigate how the toughening effect of both IF-WS_2 and flaky WS_2 NPs depends on the properties of the used epoxy system, in particular on its cross-link density. For this purpose, epoxy nanocomposites were manufactured with various loadings of both IF-WS_2 and flaky WS_2 NPs, using epoxy systems with various amounts of curing agents.

5.4 Experiments

5.4.1 Materials

The epoxy resin was a diglycidyl ether of bisphenol A (DGEBA, trade name *Epikote 828 LVEL* from *Momentive*) with a viscosity of 11 Pa s and a nominal epoxide group content of 5.34 mol/kg to 5.50 mol/kg. The curing agent T403 was a polyetheramine (trade name *Jeffamine T-403* from *Huntsman*) with a nominal amine group content of 6.1 mol/kg to 6.6 mol/kg. The chemical structures are given in fig. 5.3.

The IF-WS_2 NP powder (trade name *Nanolub R*) was obtained from the same supplier (*NanoMaterials Ltd.*, Israel) as that used in research published by others earlier [1, 2, 23, 24]. However, changes in the manufacturing process with time or unintentional variation from batch to batch cannot be excluded. According to the manufacturer, this powder was produced by high-temperature solid–gas synthesis, the primary particles had diameters of 50 nm to 150 nm and they consisted of 10 to 100 WS_2 layers, with an interlayer spacing of 0.62 nm. The powder had been stored at ambient conditions for 22 months before processing.

According to its supplier (*Graphene Laboratories Inc.*, USA), the flaky WS_2 NP powder had a purity of 99.0 %, an average particle size of approx. 90 nm, approx. 30 m^2/g specific surface area, nearly spherical morphology and a true

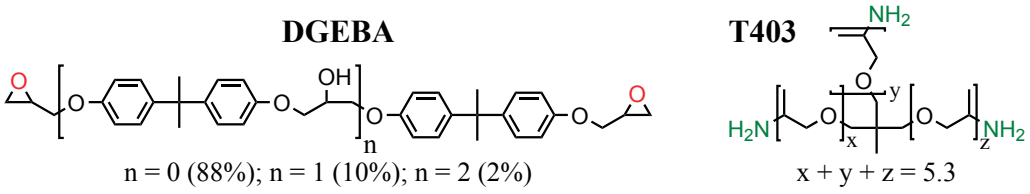

Figure 5.3: Chemical structures of the epoxy resin DGEBA and the curing agent T403

density of 7.50 g/cm^3. Thus, the size and shape are comparable to the IF-WS_2 powder, even though the crystal structure is different. X-ray crystallography showed that the flaky WS_2 consisted of WS_2 with two different crystal structures (2H and 3R), contaminated with traces of WO_3 and SO_2 (see Supporting Information for details). The powder had been stored at ambient conditions for 5 months before processing.

5.4.2 Processing

The materials were mixed in a way that the NP mass fractions w of the produced nanocomposites were 0.25 % and 0.50 % for IF-WS_2, and 0.25 %, 0.50 % and 1.00 % for flaky WS_2. The relative quantity W_{T403} of T403 necessary for a stoichiometric mixture is roughly 44 parts per hundred parts of DGEBA resin (phr) by mass according to the respective material data sheets. For 100.0 phr of DGEBA, 38.0 phr, 40.0 phr, 42.0 phr and 44.0 phr T403 were added. Two neat epoxy references were produced for each level of W_{T403}.

In order to facilitate the comparability of the individual mixtures, all nanocomposite materials were made out of two concentrated epoxy–NP master batches, one with IF-WS_2 and one with flaky WS_2 NPs. That way, the dispersion quality of all materials produced with one kind of NPs should be comparable. For the production of these master batches, 100.0 phr of DGEBA were mixed with 2.00 phr NPs first manually with a spatula and subsequently with high-speed shear mixer turning at 6000 min^{-1} for 5 min in vacuum.

Dispersion was done by passing these master batches three times through a three-roll mill (3RM) as this has been shown earlier to reproducibly provide reasonable dispersion quality [1]. The rolls (200 mm wide, ⌀150 mm) of the 3RM (*SDY-200* from *Bühler*, Switzerland) were permanently cooled to 25 °C and rotated at 45 min^{-1}, 110 min^{-1} and 220 min^{-1}, respectively. In every pass through the 3RM, the fastest roll was separated from the other two for the

first 5 min, so that the suspension was only sheared between these. This step served mainly for mixing rather than for dispersing. Afterwards, the fastest roll was pressed onto the middle roll with a force of 12 kN so that the suspension was sheared in between them. One neat epoxy reference material was produced with a W_{T403} of 44.0 phr after passing the DGEBA five times through the 3RM in order to analyze if this treatment had a significant effect on the material's properties.

The processed master batches were then mixed with respective amounts of additional DGEBA first manually with a spatula and then with an overhead stirrer turning at 2000 min^{-1} for 5 min. These mixtures were homogenized by passing them once more through the 3RM as mentioned above. They were then mixed with respective amounts of T403 first manually with a spatula and then with an overhead stirrer turning at 2000 min^{-1} for 5 min.

Afterwards, the mixtures were poured into a wide beaker (⌀140 mm) and degassed in a vacuum oven at 80 °C to approx. 30 mbar. They had to reach between 47 °C and 77 °C until the air bubbles broke, which took 5 min to 15 min. Subsequently, they were poured into a steel mold of $160 \times 120 \times 4\,mm^3$, the surfaces of which had been coated with a mold release agent (trade name *QZ 13* from *Huntsman*). The mold was placed in a pre-heated oven at 80 °C for 4 h and then cooled down slowly. The cured plates were demolded and machined to appropriate geometries for testing. After machining, these samples were post-cured in an oven that was heated at 1 °C/min to 125 °C held there for 3 h and then cooled down at 1 °C/min. This was done to finish the cure reaction and to let internal stresses relax; there was no measurable change in the geometry of the samples. All samples were stored in a desiccator over $CaCl_2$ in vacuum until testing.

5.4.3 Characterization

The epoxide content in the DGEBA was determined by titration according to ISO 3001 [25] and the amine group content in T403 was determined by titration with 10 mmol/l HCl.

The agglomerate size distribution in the master batches was measured via dynamic light scattering (DLS) at 25.0 °C (device *Zetasizer Nano Z* from *Malvern*, UK). For that purpose, the master batches were dissolved in acetone (approx. 1:100 by mass, resulting particle volume fraction $\varphi_p \approx 10^{-6}$). The viscosity of neat acetone was used for the calculation of particle diameters. Presented values are the means of 15 individual measurements of 30 s each. As recommended by the respective ISO standard [26], the intensity-weighted average particle diameter $\bar{x}_{DLS}$ is used for evaluation.

Dynamic mechanical analysis (DMA) was done in tension in a DMA equipment (*Eplexor 500* from *Gabo Qualimeter Testanlagen GmbH*, Germany) on samples of $60 \times 10 \times 4\,mm^3$. The specimens were deformed statically by 0.2 % and dynamically at 10 Hz by 0.015 % while heating them at 1 °C/min to 140 °C. T_g was defined as the temperature at which the loss modulus E'' was maximum. The rubber equilibrium modulus E_r, which is necessary for eq. (5.1), was defined as the average complex modulus at temperatures between $T_{min(E)}-5\,°C$ and $T_{min(E)}+5\,°C$ during a DMA measurement, where $T_{min(E)}$ is the temperature where the complex modulus is minimum.

The mass density ρ was determined at 22 °C using the immersion technique according to ISO 1183 Method A [27].

DQ NMR measurements were performed on a time-domain NMR spectrometer (*minispec mq20* from *Bruker*), operating at 0.47 T (^{1}H resonance frequency: 20 MHz). The 90° and 180° pulse lengths were 2.8 µs and 5.6 µs, respectively, and the receiver dead time was 9 µs. A temperature regulator (*BVT3000* from *Bruker*) was used for temperature control and dry air was used

for sample heating. Cured neat epoxy samples (⌀8 mm, 8 mm high) were placed inside NMR tubes, which were then flame-sealed in vacuum. The samples were measured at 160 °C after an equilibration time of at least 45 min. For the generation of DQ coherence, the 3-pulse [28] (sometimes called 5-pulse) sequence was used. From the real part of an in-phase, on-resonance signal, the data points between 5 µs and 10 µs were averaged to get the intensity of the experiment. Details on the measurement principle and the evaluation are given in the Supporting Information.

Tensile tests were performed on neat epoxy at 1 mm/min in accordance with ISO 527-1 [29]. Eight specimens per material were machined by water-jet cutting to geometry 1A as given in ISO 527-2 [30] before post-curing and their sides and edges were ground with P400 sand paper to remove notches. The mechanical energy density at yield U_y and at break U_b were calculated by numerically integrating the engineering stress σ over the engineering strain ϵ until the yield and break point, respectively.

The fracture toughness of the nanocomposites was measured in single-edge-notched bending (SENB) tests on specimens of $65 \times 15 \times 4$ mm^3 at a test speed of 5 mm/min according to ISO 13586 [31]. A pre-crack was introduced by manually tapping a sharp blade into the machined notch at room temperature. The pre-cracks of most samples did not fulfill the recommendations of the ISO 13586 with regards to their length or symmetry, but nevertheless all samples were tested and evaluated (details in the Supporting Information).

Selected nanocomposite fracture surfaces were sputter-coated with 2 nm Pt (sputtering machine *EM ACE600 High Vacuum Sputter Coater* from *Leica*) immediately before their investigation with a scanning electron microscope (SEM). The SEM (*NovaNanoSEM 230* from *FEI*) had a Schottky field-emission electron source operating at a voltage of 3 kV (beam current 220 pA), imaging secondary electrons with an in-lens detector at roughly 3×10^{-4} Pa pressure. All images were taken from regions close to the pre-crack.

The AFM (*MultiMode 8* from *Bruker*) was used with a 100 µm scanner in the *Peak-Force Tapping* mode in order to measure the surface topography of fracture surfaces. The used AFM probes (*ScanAsyst-Air* from *Bruker*) had a relatively soft triangular silicon-nitride cantilever (nominal spring constant 0.4 N/m) and a sharp tip (nominal tip radius 2 nm). All images were taken from regions close to the pre-crack.

5.5 Results and Discussion

5.5.1 Dispersion quality

The average agglomerate size $\bar{x}_{\mathrm{DLS}}$ measured by DLS after 0, 1, 2 and 3 passes through the 3RM was 942 nm, 486 nm, 285 nm and 272 nm for the flaky WS_2 masterbatch and 318 nm, 203 nm, 196 nm and 192 nm for the IF-WS_2 masterbatch, respectively. After diluting these masterbatches with additional DGEBA and passing them once more through the 3RM, the $\bar{x}_{\mathrm{DLS}}$ decreased further to 240 nm to 270 nm for flaky WS_2 mixtures and to 170 nm to 190 nm for IF-WS_2 mixtures. As the $\bar{x}_{\mathrm{DLS}}$ of the flaky WS_2 was significantly larger than its primary particles (nominally approx. 90 nm), we can expect that it is mostly present in agglomerates. The non-spherical shape of its primary particles should thus not affect the measurement significantly.

While the measured $\bar{x}_{\mathrm{DLS}}$ of IF-WS_2 is in good agreement with earlier reports [1], flaky WS_2 seems to form significantly larger agglomerates. As the primary particle size of the investigated NPs is similar, this indicates that IF-WS_2 can be dispersed more effectively within DGEBA than flaky WS_2, possibly due to their ability to roll off each other [4]. In contrast, the possible cohesive effect of H_2O traces on IF-WS_2 NP surfaces assumed elsewhere [23] seems to be insignificant in the present case.

5.5.2 Stoichiometry and cross-link density

From the material data sheets of the DGEBA and the T403, the W_{T403} necessary for a stoichiometric mixture ($\lambda = 1$) was estimated to be roughly 43.9 phr. Titration of DGEBA gave an epoxide group content of 5.38(1) mol/kg, which corresponds to a mass of DGEBA per amount of epoxide groups M_{EP} (also called *epoxy equivalent weight*, *EEW*) of 186.0(4) g/mol. Titration of T403 gave an amine group content of 6.23(3) mol/kg, which corresponds to a mass of curing agent per amount of amine groups M_{NH2} of 160.4(7) g/mol ($M_{NH2} = 2 \cdot AHEW$, where *AHEW* is the curing agent's *amine hydrogen equivalent weight*). Thus, the W_{T403} necessary for a stoichiometric mixture was 43.13(22) phr. The W_{T403} levels used in the present work correspond, therefore, to values of λ of approx. 0.88, 0.93, 0.97 and 1.02, respectively.

A higher cross-link density usually results in a higher T_g, so that the maximum T_g is expected at $\lambda = 1$. As shown in fig. 5.4, the T_g peaks at about 44 phr, indicating that this is where the cross-link density is maximum. The fact that the T_g reaches its maximum at $\lambda > 1$ has been observed earlier [11] and can possibly be explained with the limited mobility of secondary amines: Every T403 molecule can react up to six times, but as every reaction reduces the T403's mobility, some T403 will react only four or five times. In contrast, DGEBA can react only twice so that its mobility does not decrease that much. Consequently, a slightly higher than stoichiometric T403 content might help to maximize the cross-link density. From these data, we assume that $W_{T403} \approx$ 44.0 phr provides the maximum cross-link density.

The Supporting Information explains how the molecular mass per cross-link M_c of the investigated epoxy system was estimated to

$$M_c(\lambda) = \frac{6M_{EP} + 3\lambda \cdot M_{NH2}}{10\lambda - 6} \tag{5.2}$$

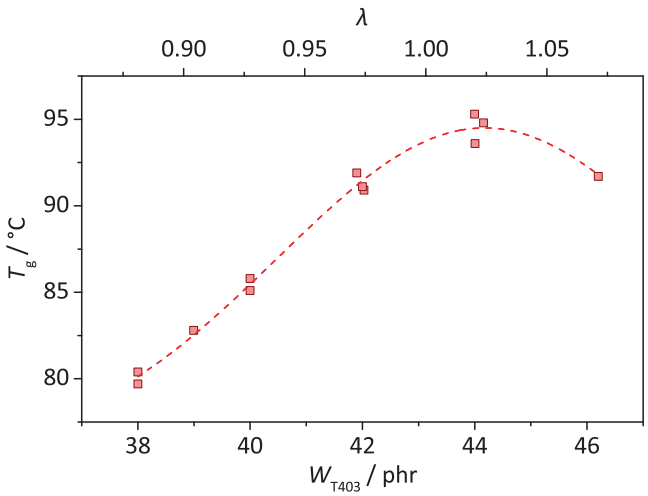

Figure 5.4: Glass-transition temperature $T_g = \arg\max E''(T)$ of neat epoxy over the amount of curing agent. The dashed line approximates the data.

under several assumptions (e.g., $0.5 \ll \lambda < 1.0$). Fig. 5.5 shows the values for M_c determined by DMA of neat epoxy samples via eq. (5.1) and compares these to the M_c estimated by eq. (5.2).

The measured M_c values show quite low scatter and a strong correlation with λ, which is not necessarily expected, given that this kind of calculation is considered to be a "rather crude empirical relationship" [15]. Likewise, it is noteworthy that eq. (5.2) agrees qualitatively with the measured values, even though several assumptions had to be made beforehand.

These results show that the cross-link density can be controlled by varying λ. Reducing W_{T403} from 44 phr to 38 phr resulted in an increase in M_c by 27 %, while the T_g decreased by only 15 °C. Thus, the M_c could be varied more effectively by varying λ than it was varied elsewhere by altering the type of curing agent, which was shown to result in a T_g drop of 118 °C while increasing M_c by only 18 % [9].

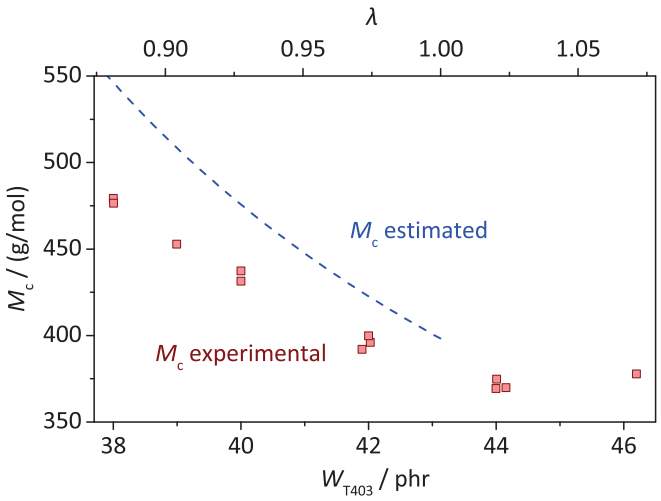

Figure 5.5: The trend in the molecular mass per crosslink M_c as estimated theoretically by eq. (8.16) agrees qualitatively well with that measured via DMA using eq. (5.1)

DQ NMR was used to further support these findings. As discussed in the Supporting Information, the results suggested that the epoxy's molecular network consisted of two differently flexible fractions, 1 and 2, which might represent a rather stiff DGEBA fraction and a rather flexible T403 fraction, respectively. Fig. 5.6 shows the D_{res} data for both fractions, which is related to a material's network rigidity. While it does not show the same clear trend as the DMA data, D_{res} decreased as W_{T403} was reduced, which supports the finding that the sub-stoichiometric system has a lower cross-link density.

5.5.3 Tensile properties of neat epoxy

Representative engineering stress–strain curves from tensile tests are given in fig. 5.7 and the results of all tested specimens are summarized in table 5.1. Decreasing λ resulted in a clear increase in the Young's modulus E and in the stress at yield σ_y, and in a clear decrease in the strain at yield ϵ_y and in the me-

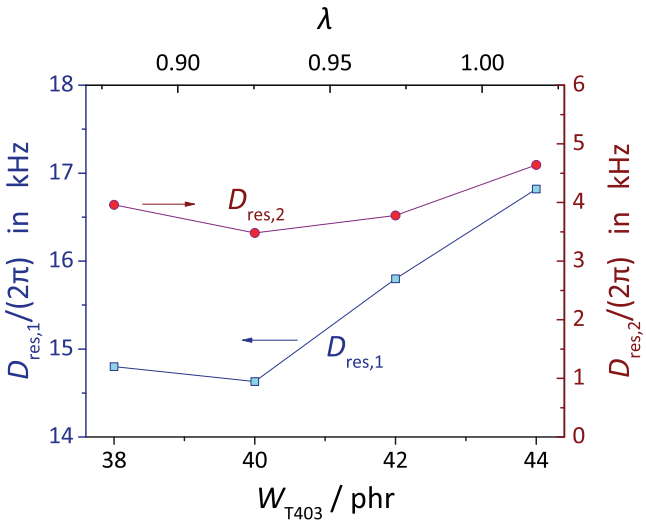

Figure 5.6: The parameter D_{res} measured via DQ NMR for the more (1) and the less (2) rigid part of the molecular network corresponds to the network rigidity, i.e., the cross-link density

chanical energy density at yield U_{y}. The strain at break ϵ_{b} and the mechanical energy density at break U_{b} did not show a clear dependence on W_{T403}. Processing the DGEBA with the 3RM did not affect the material's tensile properties significantly (fig. 5.7).

The fact that E and σ_{y} increase as W_{T403} is reduced might be unexpected given the decreased cross-link density, but can easily be explained by the higher flexibility of the T403 molecule compared to the DGEBA molecule.

5.5.4 Fracture mechanics results neat epoxy

In contrast to the tensile properties, the fracture toughness of neat epoxy dropped drastically as W_{T403} was reduced, as shown in fig. 5.8. Both the critical stress-intensity factor K_{Ic} and the critical stress-energy release rate G_{Ic} (data given in the Supporting Information) scatter strongly for sub-stoichiometric

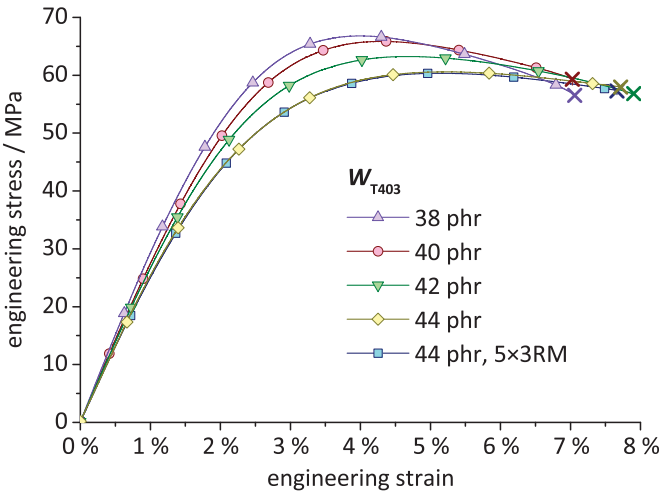

Figure 5.7: Representative tensile testing results of neat epoxy with different curing agent contents W_{T403}

materials, while they are fairly well defined for stoichiometric materials. Reducing W_{T403} from 44.0 phr to 42.0 phr, 40.0 phr and 38.0 phr reduced the K_{Ic} by 35 %, 51 % and 56 % and the G_{Ic} by 56 %, 79 % and 81 %, respectively. The fact that the fracture toughness was maximum at a λ slightly higher than 1 is consistent with an earlier report [11], although the measured fracture toughness drop for $\lambda < 1$ is even more pronounced in the present work. Processing the DGEBA in the 3RM did not affect the fracture toughness significantly.

The measured large fracture toughness differences are noteworthy, given the fairly small differences in the tensile properties. In particular, the variations in ϵ_{b}, U_{y} and U_{b} were rather small, which might arguably lead to the expectation that the fracture toughness should not vary strongly either.

The non-network signal from the mentioned DQ NMR measurements might help understanding these large fracture toughness variations. This signal gives a measure for the defect fraction of the material, i.e., the fraction that does not contribute to the molecular network. In the present system, this frac-

Table 5.1: Results of tensile tests on neat epoxy (eight specimens per material)

W_{T403} /phr	σ_y /MPa	ϵ_y /%	ϵ_b /%	U_y /(mJ/mm^3)	U_b /(mJ/mm^3)	E /MPa
38	67.0(1)	4.03(5)	6.97(38)	1.92(2)	3.69(23)	3034(42)
40	65.4(3)	4.31(5)	6.99(55)	2.07(5)	3.62(32)	2876(24)
42	63.0(3)	4.68(3)	7.94(28)	2.27(3)	4.04(16)	2737(43)
44	60.4(1)	5.20(4)	7.53(63)	2.58(3)	3.65(36)	2556(18)
44*	60.3(1)	5.13(5)	7.55(139)	2.49(4)	3.82(103)	2610(16)

* DGEBA passed through the 3RM five times

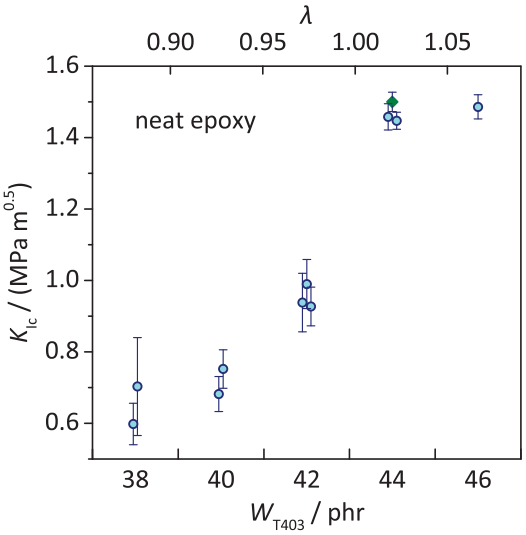

Figure 5.8: Measured fracture toughness of neat epoxy with different curing agent contents W_{T403}. The K_{Ic} drops drastically for $\lambda < 1$. Some data points are slightly offset horizontally to avoid overlapping. For the filled, diamond-shaped point, the DGEBA had been passed through the 3RM five times.

tion consists presumably mainly of dangling bonds with unreacted epoxide groups (cf. fig. 5.2). As shown in fig. 5.9, the defect fraction depends strongly on W_{T403}. Reducing W_{T403} to 42.0 phr, 40.0 phr and 38.0 phr increased the defect fraction to roughly 4, 7 and 12 times its value at 44.0 phr, respectively. This drastic increase in the number of molecular defects might explain the fracture toughness drop, for example if these defects act as stress concentrators.

5.5.5 Fracture mechanics results for nanocomposites

Given the strong dependency of the neat epoxy's fracture toughness on W_{T403}, the toughening effect of the NPs was expected to differ strongly as well. As mentioned, one toughening model suggests higher relative G_{Ic} increases for epoxy systems with high initial ϵ_b and high $G_{Ic,neat}$ as well as for higher NP loadings [9]. Consequently, one would expect that stoichiometric epoxy systems can be toughened much more effectively than sub-stoichiometric systems. However, the same source found the highest toughening effect for epoxy systems with a low T_g and a high M_c, which would be the sub-stoichiometric epoxy systems in the present study.

Table 5.2 lists the T_g and fracture toughness results of the various nanocomposites. As expected, adding any kind of WS_2 NPs did not affect the T_g significantly (cf. fig. 5.4). Both types of NPs tended to increase the fracture toughness for sub-stoichiometric epoxy systems when compared to the neat epoxy references (cf. fig. 5.8), while they decreased it for stoichiometric epoxy systems. Notably, flaky WS_2 had a superior toughening effect than IF-WS_2. With IF-WS_2 clear improvements in the fracture toughness were obtained only for $W_{T403} = 40$ phr and $w_{IF} = 0.50$ %, which is the combination for which the substantial improvements in earlier reports were obtained [1, 2]. This raises the question to what extent these improvements can be generalized.

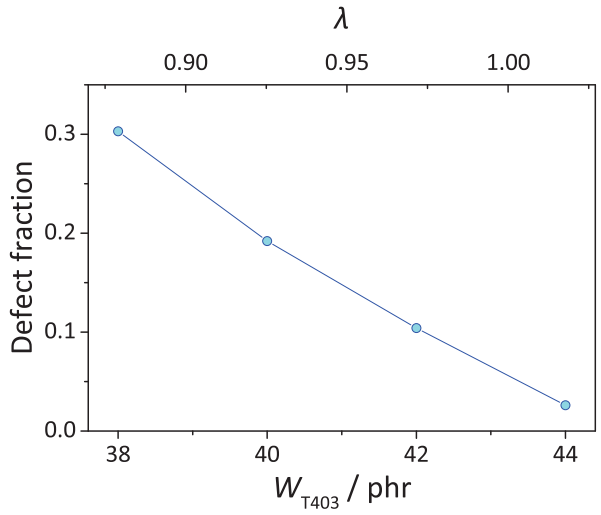

Figure 5.9: The defect fraction as measured by DQ NMR was rather small in the stoichiometric system but increased drastically as the curing agent content W_{T403} was reduced

Fig. 5.10 highlights the dependency of the toughening effect on W_{T403} graphically. Here, the change in the fracture toughness is given by $d_K = \big(\langle K_{\mathrm{Ic}}\rangle - \langle K_{\mathrm{Ic,neat}}\rangle\big)/\langle K_{\mathrm{Ic,neat}}\rangle$, where $\langle\ldots\rangle$ stands for the arithmetic mean. While it must be kept in mind that the uncertainty of these data is quite large (approx. 10 %), there is a clear trend showing a toughening effect for sub-stoichiometric epoxy only.

The results of both kinds of NPs do not confirm the expectations from the above-mentioned toughening model as the toughness of the epoxy systems with the highest $G_{\mathrm{Ic,neat}}$ and the highest ϵ_{y} was affected the most negatively. It seems, therefore, that the mentioned model is valid only for certain nanocomposite systems, e.g., with certain particle sizes or a certain surface chemistry. However, the present results agree with this earlier work in so far as the highest improvements were obtained for high M_{c}.

Table 5.2: T_g and fracture toughness results of nanocomposites

w	flaky WS_2			IF-WS_2		
	T_g /°C	K_{Ic} /(MPa$\sqrt{m}$)	G_{Ic} /(J/m^2)	T_g /°C	K_{Ic} /(MPa$\sqrt{m}$)	G_{Ic} /(J/m^2)
$W_{T403} = 38$ phr						
0.25 %	80.8	0.696(47)	146.2(205)	80.8	0.673(48)	142.0(195)
0.50 %	80.0	0.756(52)	167.2(236)	79.9	0.696(58)	143.8(205)
1.00 %	80.6	0.782(57)	183.8(266)			
$W_{T403} = 40$ phr						
0.25 %	85.7	0.748(67)	189.3(336)	85.9	0.733(53)	167.9(197)
0.50 %	85.9	0.745(82)	177.5(392)	84.8	0.815(95)	198.1(310)
1.00 %	86.0	0.737(56)	198.5(276)			
$W_{T403} = 42$ phr						
0.25 %	91.7	1.067(114)	378.0(871)	91.7	0.974(58)	306.8(400)
0.50 %	90.8	1.016(128)	362.7(897)	90.9	0.945(100)	323.9(756)
1.00 %	92.1	1.086(121)	386.4(843)			
$W_{T403} = 44$ phr						
0.25 %	94.0	1.478(42)	785.9(393)	94.6	1.415(56)	780.9(655)
0.50 %	95.3	1.409(86)	637.3(643)	94.1	1.420(76)	755.5(695)
1.00 %	94.6	1.410(68)	708.2(840)			

However, a similar investigation with an anhydride-cured epoxy system has recently come to the contrary result. After addition of silica NPs, Umboh *et al.* [10] report the highest fracture toughness increase for the stoichiometric system, which had the highest cross-link density, i.e., the lowest M_c. This contradiction might be explained by the different types of curing agent used. Anhydride curing agents are rather inflexible, so that anhydride-cured epoxy systems might be affected differently by NPs than epoxy systems cured with more flexible curing agents. This shows once again that the toughening effect of NPs can depend strongly on the investigated epoxy system.

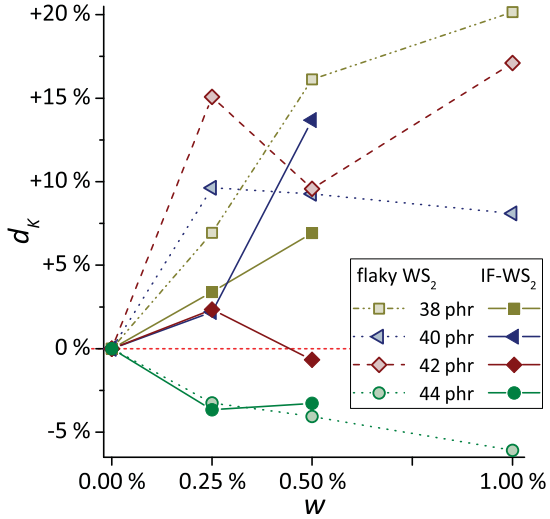

Figure 5.10: Relative fracture toughness change d_K over the mass fraction w of flaky WS_2 (open symbols) and IF-WS_2 (filled symbols) for all investigated levels of curing agent content W_{T403}. Fracture toughness increases were observed in sub-stoichiometric epoxy systems only, while the stoichiometric epoxy system ($W_{T403} = 44\,\text{phr}$) decreased in its fracture toughness.

It is noteworthy that the epoxy systems with the highest defect fraction (cf. fig. 5.9) could be toughened most effectively. This raises the question how and to what extent molecular defects affect the toughening effect of NPs. For example, molecular defects might concentrate around NPs, thus reducing in number in the bulk epoxy. Further investigations should clarify this aspect.

The results suggest that flaky WS_2 has a stronger effect on the epoxy's fracture toughness than IF-WS_2, both positive and negative. It seems that the superior toughening effect is due to the larger average agglomerate size of the flaky WS_2, although this contradicts the earlier finding that a good dispersion quality is beneficial [1].

5.5.6 Fractography

SEM images of nanocomposite fracture surfaces like those in fig. 5.11 confirm that IF-WS_2 was dispersed more effectively than flaky WS_2 (additional images in the Supporting Information). Agglomerates of various sizes could be observed in all investigated nanocomposites, but large agglomerates (i.e., with diameters in the micrometer range) were much more frequent in flaky WS_2 nanocomposites, whereas IF-WS_2 NPs were mostly present in small agglomerates that consisted of only a few primary particles. As the flaky WS_2 was still mostly present in the form of agglomerates, it seems that its primary particle size was not the limiting factor for its dispersibility.

The used type of NPs had a significant effect on the fracture morphology, independently of the level of W_{T403}: Flaky WS_2 produced more somewhat conic-section-shaped crack lines, whereas the IF-WS_2 NPs usually debonded from the epoxy matrix and the produced crack lines had only rarely a conic-section shape. Such conic-section shaped crack lines have been observed earlier and were often interpreted as an indication of a *crack bowing* mechanism [2, 32]. Other works, however, explained them with the formation of secondary cracks at the NP surfaces, which might result in a toughening effect as well [1, 33], and this viewpoint is shared in the present work. A possible interpretation of the presented images could thus be that flaky WS_2 have a much stronger tendency to form secondary cracks, which would explain their overall superior toughening effect. However, this might partly just be due to the larger size of its agglomerates.

Varying W_{T403} hardly affected the fracture morphology, despite the large fracture toughnesses differences. The most notable difference was the shape of the crack lines in flaky WS_2 nanocomposites: In stoichiometric systems, most crack lines were rather parabolic in shape and often several hundred nanometers separated from the NP agglomerates, whereas they were usually

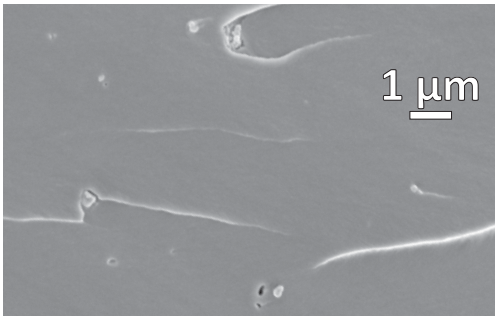

(a) $w_{\mathrm{IF}} = 0.50\,\%$, $W_{\mathrm{T403}} = 44\,\mathrm{phr}$

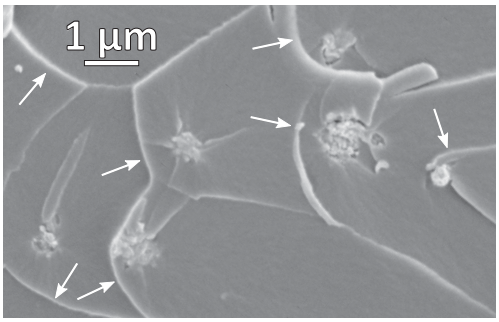

(b) $w_{\mathrm{flaky}} = 1.00\,\%$, $W_{\mathrm{T403}} = 44\,\mathrm{phr}$

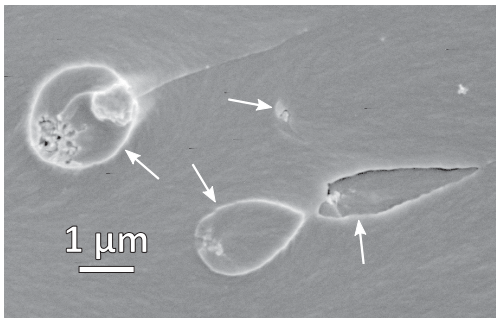

(c) $w_{\mathrm{flaky}} = 1.00\,\%$, $W_{\mathrm{T403}} = 40\,\mathrm{phr}$

Figure 5.11: Representative SEM images of fracture surfaces of nanocomposites. The cracks propagated from left to right. The white arrows highlight somewhat conic-section-shaped crack lines.

rather elliptic and close to the NPs in sub-stoichiometric systems (cf. fig. 5.11). The crack lines' shape and their distance to the NP agglomerates have been interpreted as an indication for how easily secondary cracks were formed and how fast they propagated with respect to the primary crack [1, 33]. According to this interpretation, secondary cracks were formed more easily and propagated faster with respect to the primary crack in the stoichiometric epoxy system.

There are contradicting reports in literature on how the fracture-surface roughness correlates with the fracture toughness [8]. Shtein *et al.* [34]. found

a coherent quantitative correlation for epoxy–WS_2 nanocomposites. Table 5.3 lists two different roughness parameters for fracture surfaces as investigated with AFM: R_{rms} is the root-mean-square roughness and $d_A = (A_{surf}/A_{proj}) - 1$, where A_{surf} is the measured surface area and A_{proj} is the projected image area. The roughness increase does not correlate with the toughness increase. In contrast, the nanocomposites with the highest relative toughness increase showed only moderate roughness increase. This shows that the toughness increases and decreases are not merely due to changes in the created fracture surface areas, but that the observed effects are more complex.

5.6 Conclusion

Altering W_{T403} is an effective way to vary an epoxy's cross-link density without changing the chemical components. An estimation of the cross-link density under several assumptions agrees qualitatively with its measurement via DMA and with the network rigidity measured by DQ NMR. Notably, the cross-link density changes strongly with W_{T403} while the T_g changes only moderately. Despite the decreased cross-link density, lowering W_{T403} increases the material's strength and modulus as DGEBA is less flexible than T403. A $\lambda < 1$ results

Table 5.3: Roughness of fracture surfaces as determined via AFM ($w = 0.50\,\%$)

W_{T403}	NP	R_{rms} / nm	d_A
40 phr	neat	8.0	0.13 %
	IF-WS_2	19.2	0.32 %
	flaky WS_2	89.2	0.62 %
44 phr	neat	15.7	0.04 %
	IF-WS_2	99.8	0.37 %
	flaky WS_2	114.0	1.60 %

in a rather moderate change in the material's tensile properties, but in a sudden drop in its fracture toughness. This might be due to the drastic increase in the defect fraction in the molecular network as measured via DQ NMR.

Both DLS measurements and fractographic images suggest that IF-WS_2 can be dispersed significantly more effectively within DGEBA with a three-roll mill than flaky WS_2, despite the similar primary particle size. It seems as if the fullerene-like shape facilitates the dispersibility, potentially due to the NPs' ability to roll off each other.

The toughening effect of NPs can depend strongly on the investigated epoxy system. The investigated epoxy systems with low cross-link density mostly increased in toughness after NP addition, while those with high cross-link density mostly decreased, even though the latter had higher strain at yield and significantly higher initial fracture toughness, both of which were supposed to facilitate a toughness increase. It is currently unclear how significant molecular defects are for the NPs' toughening effect.

Flaky WS_2 exhibited a larger agglomerate size than IF-WS_2 and tended to result in better fracture toughness improvements. Fractographic images suggest that IF-WS_2 tends to debond from the epoxy matrix, while flaky WS_2 tends to introduce more secondary cracks. These seemed to be initiated easier and propagated faster in stoichiometric than in sub-stoichiometric flaky WS_2 nanocomposites. AFM investigation of the fracture surfaces showed that fracture surfaces can become rougher even if the material's toughness decreases.

While the presented results question the usefulness of IF-WS_2 as a toughening agent for stoichiometric epoxy systems, its superior dispersibility means that it might be a useful additive for other applications, e.g., in tribology.

5.6.1 Acknowledgement

The authors would like to thank Arndt Remhof for his support with the X-ray diffraction, Brian Sinnet for his support with the DLS, Anja Huch for the TEM imaging, Christian Teichert for the fruitful discussions on roughness measurement via AFM and Kay Saalwächter for providing the DQ NMR pulse sequence and for useful tips on data acquisition. Part of the work was carried out at PCCL within the framework of the COMET-program of the Federal Ministry for Transport, Innovation and Technology and the Federal Ministry of Science, Research and Economy.

Supporting Information

Supporting Information related to this chapter can be found in section 8.4.

References

[1] D. Haba, A. J. Brunner, and G. Pinter, "Dispersion of fullerene-like WS_2 nanoparticles within epoxy and the resulting fracture mechanics", *Compos. Sci. Technol.*, vol. 119, pp. 55–61, 2015. DOI: 10.1016/j.compscitech.2015.09.013.

[2] M. Shneider, H. Dodiuk, R. Tenne, and S. Kenig, "Nanoinduced morphology and enhanced properties of epoxy containing tungsten disulfide nanoparticles", *Polym. Eng. Sci.*, vol. 53, no. 12, pp. 2624–2632, 2013. DOI: 10.1002/pen.23517.

[3] M. A. Rafiee, F. Yavari, J. Rafiee, and N. Koratkar, "Fullerene–epoxy nanocomposites-enhanced mechanical properties at low nanofiller loading", *J. Nanopart. Res.*, vol. 13, no. 2, pp. 733–737, 2011. DOI: 10.1007/s11051-010-0073-5.

[4] L. Rapoport, Y. Bilik, Y. Feldman, *et al.*, "Hollow nanoparticles of WS_2 as potential solid-state lubricants", *Nature*, vol. 387, pp. 791–793, 1997. DOI: 10.1038/42910.

[5] D. Haba, T. Grießer, U. Müller, and A. J. Brunner, "Critical investigation of the silane surface functionalization of fullerene-like WS_2", *J. Mater. Sci.*, vol. 50, no. 15, pp. 5125–5135, 2015. DOI: 10.1007/s10853-015-9039-4.

[6] R. Tenne and M. Redlich, "Recent progress in the research of inorganic fullerene-like nanoparticles and inorganic nanotubes", *Chem. Soc. Rev.*, vol. 39, no. 5, pp. 1423–1434, 2010. DOI: 10.1039/B901466G.

[7] M. Naffakh, A. M. Díez-Pascual, C. Marco, G. J. Ellis, and M. A. Gómez-Fatou, "Opportunities and challenges in the use of inorganic fullerene-like nanoparticles to produce advanced polymer nanocomposites", *Prog. Polym. Sci.*, vol. 38, no. 8, pp. 1163–1231, 2013. DOI: 10.1016/j.progpolymsci.2013.04.001.

[8] M. Quaresimin, K. Schulte, M. Zappalorto, and S. Chandrasekaran, "Toughening mechanisms in polymer nanocomposites: From experiments to modelling", *Comp. Sci. Technol.*, vol. 123, pp. 187–204, 2016. DOI: 10.1016/j.compscitech.2015.11.027.

[9] T. H. Hsieh, A. J. Kinloch, K. Masania, A. C. Taylor, and S. Sprenger, "The mechanisms and mechanics of the toughening of epoxy polymers modified with silica nanoparticles", *Polymer*, vol. 51, no. 26, pp. 6284–6294, 2010. DOI: 10.1016/j.polymer.2010.10.048.

[10] M. K. Umboh, T. Adachi, T. Nemoto, M. Higuchi, and Z. Major, "Non-stoichiometric curing effect on fracture toughness of nanosilica particulate-reinforced epoxy composites", *J. Mat. Sci.*, vol. 49, no. 21, pp. 7454–7461, 2014. DOI: 10.1007/s10853-014-8450-6.

[11] F. Fernandez-Nograro, A. Valea, R. Llano-Ponte, and I. Mondragon, "Dynamic and mechanical properties of DGEBA/poly(propylene oxide) amine based epoxy resins as a function of stoichiometry", *Eur. Polym. J.*, vol. 32, no. 2, pp. 257–266, 1996. DOI: 10.1016/0014-3057(95)00122-0.

[12] E. Crawford and A. J. Lesser, "The effect of network architecture on the thermal and mechanical behavior of epoxy resins", *J. Polym. Sci., Part B: Polym. Phys.*, vol. 36, no. 8, pp. 1371–1382, 1998.

[13] B. Burton, D. Alexander, H. Klein, *et al.*, *Epoxy formulations using Jeffamine polyetheramines*, Huntsman, USA, 2005.

[14] C. C. Riccardi and R. J. J. Williams, "Kinetic scheme for an amine–epoxy reaction with simultaneous etherification.", *J. Appl. Polym. Sci.*, vol. 32, no. 2, pp. 3445–3456, 1986.

[15] L. E. Nielsen, "Cross-linking-effect on physical properties of polymers", *J. Macromol. Sci., Part C: Polym. Rev.*, vol. 3, no. 1, pp. 69–103, 1969. DOI: 10.1080/15583726908545897.

[16] D. C. Timm, A. J. Ayorinde, and R. F. Foral, "Epoxy mechanical properties: Function of crosslink architecture", *Br. Polym. J.*, vol. 17, no. 2, pp. 227–232, 1984.

[17] M. Schneider, L. Gasper, D. E. Demco, and B. Blümich, "Residual dipolar couplings by ^{1}H dipolar-encoded longitudinal magnetization, double- and triple-quantum nuclear magnetic resonance in cross-linked elastomers", *J. Chem. Phys.*, vol. 111, no. 1, pp. 402–415, 1999. DOI: 10.1063/1.479291.

[18] K. Saalwächter, P. Ziegler, O. Spyckerelle, *et al.*, "^{1}H multiple-quantum nuclear magnetic resonance investigations of molecular order distributions in poly(dimethylsiloxane) networks: Evidence for a linear mixing law in bimodal systems", *J. Chem. Phys.*, vol. 119, no. 6, pp. 3468–3482, 2003.

[19] J. L. Valentín, D. López, R. Hernández, C. Mijangos, and K. Saalwächter, "Structure of poly(vinyl alcohol) cryo-hydrogels as studied by proton low-field NMR spectroscopy", *Macromolecules*, vol. 42, no. 1, pp. 263–272, 2009. DOI: 10.1021/ma802172g.

[20] M. A. Malmierca, A. González-Jiménez, I. Mora-Barrantes, *et al.*, "Characterization of network structure and chain dynamics of elastomeric ionomers by means of ^{1}h low-field NMR", *Macromolecules*, vol. 47, no. 16, pp. 5655–5667, 2014. DOI: 10.1021/ma501208g.

[21] M. Martin-Gallego, A. González-Jiménez, R. Verdejo, M. A. Lopez-Manchado, and J. L. Valentín, "Epoxy resin curing reaction studied by proton multiple-quantum NMR", *J. Polym. Sci., Part B: Polym. Phys.*, vol. 53, no. 18, pp. 1324–1332, 2015. DOI: 10.1002/polb.23767.

[22] K. Saalwächter, "Proton multiple-quantum NMR for the study of chain dynamics and structural constraints in polymeric soft materials", *Prog. Nucl. Magn. Reson. Spectrosc.*, vol. 51, no. 1, pp. 1–35, 2007. DOI: 10.1016/j.pnmrs.2007.01.001.

[23] C. Shahar, D. Zbaida, L. Rapoport, *et al.*, "Surface functionalization of WS_2 fullerene-like nanoparticles", *Langmuir*, vol. 26, no. 6, pp. 4409–4414, 2010. DOI: 10.1021/la903459t.

[24] A. Buchman, H. Dodiuk-Kenig, A. Dotan, R. Tenne, and S. Kenig, "Toughening of epoxy adhesives by nanoparticles", *J. Adhes. Sci. Technol.*, vol. 23, no. 5, pp. 753–768, 2009. DOI: 10.1163/156856108X379209.

[25] "ISO 3001:1999. platics – epoxide compounds – determination of epoxide equivalent", International Organization for Standardization, Geneva, CH, Standard, Oct. 1999.

[26] "ISO 22412:2008(E). particle size analysis – dynamic light scattering (DLS)", International Organization for Standardization, Geneva, CH, Standard, May 2008.

[27] "ISO 1183-1:2004. plastics – methods for determining the density of non-cellular plastics – part 1: Immersion method, liquid pyknometer method and titration method", International Organization for Standardization, Geneva, CH, Standard, Feb. 2004.

[28] M. A. Voda, D. E. Demco, J. Perlo, R. A. Orza, and B. Blümich, "Multispin moments edited by multiple-quantum NMR: Application to elastomers", *J. Magn. Reson.*, vol. 172, no. 1, pp. 98–109, 2005. DOI: 10.1016/j.jmr.2004.10.001.

[29] "ISO 527-1:2012. plastics – determination of tensile properties – part 1: General principles", International Organization for Standardization, Geneva, CH, Standard, Feb. 2012.

[30] "ISO 527-2:2012. plastics – determination of tensile properties – part 2: Test conditions for moulding and extrusion plastics", International Organization for Standardization, Geneva, CH, Standard, Feb. 2012.

[31] "ISO 13586:2000(E). plastics – determination of fracture toughness (G_{IC} and K_{IC}) – linear elastic fracture mechanics (LEFM) approach", International Organization for Standardization, Geneva, CH, Standard, Mar. 2000.

[32] B. Wetzel, P. Rosso, F. Haupert, and K. Friedrich, "Epoxy nanocomposites – fracture and toughening mechanisms", *Eng. Fract. Mech.*, vol. 73, no. 16, pp. 2375–2398, 2006. DOI: 10.1016/j.engfracmech.2006.05.018.

[33] D. Haba, M. Barbezat, and A. J. Brunner, "Secondary crack formation as fracture mechanism in nanocomposites of epoxy and fullerene-like WS_2", in *Proc. NAP (Lviv, Ukraine, September 2015)*, vol. 4, 2015, 02NNSA03-1–02NNSA03-3.

[34] M. Shtein, R. Nadiv, N. Lachman, H. D. Wagner, and O. Regev, "Fracture behavior of nanotube–polymer composites: Insights on surface roughness and failure mechanism", *Comp. Sci. Technol.*, vol. 87, pp. 157–163, 2013. DOI: 10.1016/j.compscitech.2013.07.016.

6 Publication 5

6.1 Bibliographic Information

6.1.1 Title

Correlation of epoxy material properties with the toughening effect of fullerene-like WS_2 nanoparticles

6.1.2 Authors

- Dietmar Haba [1]
- Andreas J. Brunner [1]
- Michel Barbezat [1]
- Dmitri Spetter [2]
- Wolfgang Tremel [2]
- Gerald Pinter [3]

[1] Empa – Swiss Federal Laboratories for Materials Science and Technology, Dübendorf, Switzerland

[2] Johannes Gutenberg Universität Mainz, Mainz, Germany

[3] Montanuniversität Leoben, Leoben, Austria

6.1.3 Publication details

Submitted to: *European Polymer Journal*

Statement with regard to publication: This is an adapted version of the submitted manuscript in order to fit the formatting of the Thesis and does not necessarily reflect exactly the actually published version.

6.2 Abstract

This work deals with the toughening effect of inorganic, fullerene-like WS_2 (IF-WS_2) nanoparticles (NPs) on epoxy. It has been hypothesized that this toughening effect depends on the epoxy's cross-link density, its molecular defect fraction or its reference fracture toughness K_{Ic}. Seven different epoxy systems were filled with 0.5 % laboratory-made IF-WS_2 NPs by mass and investigated in order to analyze which material properties are determining the toughening effect. These NPs were similar to commercially available IF-WS_2 NPs, but their agglomerates could not be broken up as successfully and they yielded less toughening effect. The cross-link density of the epoxies measured via dynamic-mechanical thermal analysis agreed reasonably well qualitatively with the theoretical estimation. The glass-transition temperature and the compressive yield stress were not affected significantly by the IF-WS_2 NPs. The toughening effect of IF-WS_2 depended entirely on the curing agent type and quantity. Polyetheramine-cured epoxies behaved differently from the others in their yielding behavior, but also in the IF-WS_2 NPs' toughening effect: While some of the investigated material properties correlate strongly with the toughening effect for polyetheramine-cured epoxies, the correlation for all investigated epoxies is rather low. Thus, none of the mentioned hypotheses could be clearly confirmed.

Keywords: Epoxy, Tungsten disulfide, Fracture mechanics, Nanocomposite, ANOVA

6.2.1 Graphical Abstract

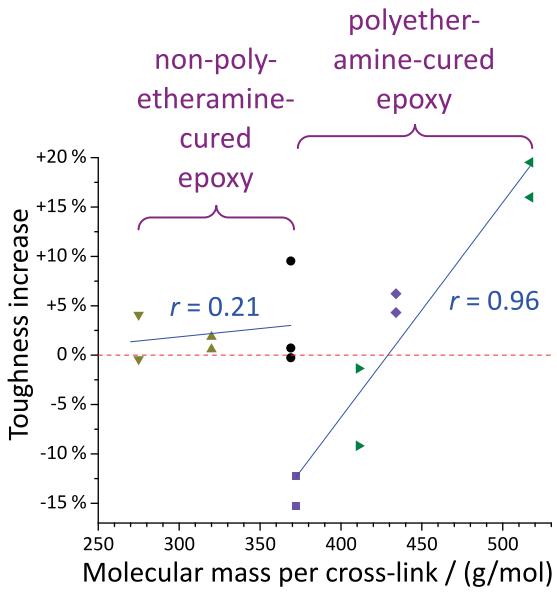

6.3 Introduction

Epoxy is a thermosetting polymer that is frequently used for high-performance applications like in fiber-reinforced polymers thanks to its good mechanical and chemical properties and its good processability. However, its applications are often limited by its low fracture toughness K_{Ic}. This is why epoxy is usually toughened by toughening additives like elastomeric or rigid particles. Recently, nanoparticle NP fillers have attracted much attention as already small quantities showed considerable toughening effects.

Inorganic, fullerene-like WS_2 (IF-WS_2) is a novel class of NPs that is known mostly for their outstanding tribologic properties [1–3]. When used as an additive in epoxy, IF-WS_2 can considerably improve not only its friction and wear

behavior [4, 5], but also its fracture toughness [6, 7]. The reported relative toughness increases are impressive (up to 69 % in the critical strain-energy release rate G_{Ic}), considering how little IF-WS_2 was usually added (less than 0.1 % by volume) [6].

However, a recent investigation [8] showed that significant fracture toughness improvements were only possible for certain epoxy systems. In particular, sub-stoichiometric epoxy systems increased in their K_{Ic} when IF-WS_2 was added, while stoichiometric epoxy tended to embrittle. It was consequently hypothesized that the effect of IF-WS_2 on the epoxy's K_{Ic} depended on its cross-link density or on its molecular defect fraction, that is to say, the fraction of the epoxy molecule that is not part of the molecular network [8]. Indeed, it was frequently assumed that the molecular network morphology, in particular the cross-link density, is an important factor determining the effectiveness of NP toughening agents [8–10]. Nevertheless, it is unclear whether a high cross-link density is beneficial [10] or detrimental [8, 9] for the toughening effect.

Likewise, some models predict that the epoxy's yield stress [9, 11], its strain at break [9] or its modulus [11] are determining for the toughening effect of NP additives. Finally, it is possible that the toughening effect depends simply on the K_{Ic} of the neat epoxy reference system [8, 9]. Indeed, combinations of these parameters could explain the mentioned dependency of the toughening effect on the curing agent concentration [8].

The aim of the present work is to separate these factors from each other by investigating several different epoxy systems. IF-WS_2 is dispersed within an epoxy resin that is then cured with various different curing agents, both stoichiometric and sub-stoichiometric. The resulting materials hence cover a wide range of cross-link densities and K_{Ic}'s, but they also exhibit different mechanical properties, molecular defect fractions, etc. The inter-correlation

between these factors is much lower than when only the stoichiometry is varied, which facilitates drawing conclusions.

Most published works on IF-WS_2 in epoxy may be somewhat biased by the fact that the used IF-WS_2 was often from the same commercial source (*Nanomaterials Ltd.*, Israel, formerly known as *ApNano*) [6–8, 12, 13]. Thus, it is possible that some of the reported effects are specific for NPs from this particular source rather than for IF-WS_2 in general. The present work uses laboratory-made IF-WS_2 from a different source in order to compare it with the earlier results from the commercial product and to allow more general statements on the effect of IF-WS_2 on epoxy properties.

6.4 Experimental

6.4.1 Materials

The used IF-WS_2 NPs were synthesized following a recently applied patent [14] via a solid–gas-phase reaction using quasi-spherical WO_3 NPs as precursors and H_2S/H_2 as reactive gases. The synthesis was carried out at 800 °C using a home-made quartz-class set up, which was designed to support a continuous production of WS_2 IF-NPs.

The epoxy resin was a diglycidyl ether of bisphenol A (DGEBA, trade name *EpiKote 828 LVEL* from *Momentive*) with a mass per amount of epoxide groups M_{EP} (also known as *epoxy equivalent weight, EEW*) of 186 g/mol as determined by titration according to ISO 3001 [15].

The methyl-tetrahydrophthalic anhydride (MTHPA, trade name *EpiKure 3601* from *Momentive*) had an *anhydride equivalent weight* M_{anh} of approx. 165 g/mol and was always used in combination with the tertiary amine catalyst 1-methyl imidazole (1MI, trade name *EpiKure Catalyst 201* from *Momentive*).

The diethylenetriamine (DETA) was delivered by *Sigma Aldrich* and had a purity of 99 % (molecular mass $M_{\mathrm{DETA}} = 103.2\,\mathrm{g/mol}$).

The polyetheramine (PEA) curing agents were the bifunctional D230 (trade name *Jeffamine D-230* from *Huntsman*) and the trifunctional T403 (trade name *Jeffamine T-403* from *Huntsman*), with *amine hydrogen equivalent weights* (*AHEW*) of approx. 59 g/mol and 80 g/mol, respectively, as determined by acid–base titration with 10 mmol/l HCl. The structure formulas of the DGEBA and the curing agents are given in the Supporting Information.

6.4.2 Processing

The DGEBA was mixed with MTHPA in an approximately stoichiometric ratio and with the three different amine curing agents in an approximately stoichiometric or in an approximately 10 % sub-stoichiometric ratio (i.e., with appox. 10 % lower amount of curing agent). Table 6.1 shows a list of the seven investigated epoxy systems with their respective type of curing agent and its relative mass W (given in mass parts per hundred mass parts of DGEBA resin, phr), as well as the respective post-cure temperature T_{post}. For each of these epoxy systems, at least two neat-epoxy reference plates and two IF-WS_2 nanocomposite plates were manufactured.

For the preparation of the DGEBA–IF-WS_2 suspensions, appropriate amounts of DGEBA and IF-WS_2 were mixed first manually with a spatula and then with an overhead stirrer at 2000 $\mathrm{min^{-1}}$ for 5 min. These mixtures were then processed with a three-roll mill (3RM) three times as this has been shown to reproducibly yield good dispersion quality [7, 8]. The rolls (200 mm wide, ⌀150 mm) of the 3RM (*SDY-200* from *Bühler*, Switzerland) were permanently cooled to 25 °C and rotated at 45 $\mathrm{min^{-1}}$, 110 $\mathrm{min^{-1}}$ and 220 $\mathrm{min^{-1}}$, respectively. For the first 5 min of each run, the fastest roll was separated from the other two, so that the suspension was only mixed between these. Afterwards, the

Table 6.1: Investigated epoxy systems. The relative mass W of curing agent added is given in mass parts per hundred mass parts of DGEBA resin (phr). T_{post} stands for the post-curing temperature. At least two IF-WS_2-filled materials and two neat-epoxy references were produced for each material type.

Denomination	Curing agent	W / phr	T_{post}
EP/MTHPA–89	MTHPA, 1MI	89.2, 2.00	160 °C
EP/DETA–10	DETA	10.0	160 °C
EP/DETA–11	DETA	11.1	160 °C
EP/T403–40	T403	40.0	125 °C
EP/T403–44	T403	44.0	125 °C
EP/D230–29	D230	29.0	125 °C
EP/D230–32	D230	32.0	125 °C

fastest roll was pressed onto the middle roll with a force of 12 kN and the suspension was dispersed between these rolls.

The neat DGEBA or these DGEBA–IF-WS_2 suspensions were mixed with the curing agents first manually with a spatula and then with an overhead stirrer at 2000 min^{-1} for 5 min. Afterwards, they were poured into a wide beaker (diameter 140 mm) and degassed in a vacuum oven at 80 °C to approx. 30 mbar. The mixtures had to reach between 47 °C to 75 °C until all air bubbles broke, which took approx. 3 min to 10 min. They were then poured into cold steel molds of $160 \times 120 \times 4\ \mathrm{mm}^3$, the surfaces of which had been treated with a silicone mold release agent (trade name *QZ 13* by *Huntsman*). The molds were than placed into a preheated oven at 80 °C for 4 h and then cooled down slowly.

One large neat-epoxy plate of $240 \times 210 \times 4\ \mathrm{mm}^3$ was produced for each epoxy system to cut the tensile-testing specimens out of. For that, the mixtures were mixed in a high-speed shear mixer at 6000 min^{-1} in vacuum (approx. 50 mbar) for 5 min and then molded and cured the same way.

After demolding, the epoxy plates were milled to appropriate geometries for the respective tests. Tensile testing specimens were produced by water-

jet cutting instead. The machined specimens were then post-cured for 3 h at 125 °C or for 1 h at 160 °C, respectively (cf. tab. 6.1). Heating and cooling ramps were 1 °C/min. All samples were stored in a desiccator over $CaCl_2$ in vacuum until testing.

6.4.3 Characterization

The agglomerate size distribution in the DGEBA–IF-WS_2 suspensions was measured via dynamic light scattering (DLS) at 25.0 °C (device *Zetasizer Nano Z* from *Malvern*, UK). For that purpose, they were dissolved in acetone (approx. 1:100 by mass, resulting particle volume fraction $\varphi_p \approx 10^{-6}$). The viscosity of neat acetone was used for the calculation of particle diameters. Presented values are the means of 15 individual measurements of 30 s each. As recommended by the respective ISO standard [16], the intensity-weighted average particle diameter $\bar{x}_{DLS}$ is used for evaluation.

For transmission electron microscopy (TEM), DGEBA–IF-WS_2 suspension was dissolved in acetone (approx. 1:100 by mass), then a droplet of this solution was placed on a TEM grid and allowed to dry. The image was gathered in a Schottky-field-emission TEM (*JEOL 2200FS TEM/STEM*) operating at 200 kV.

Dynamic mechanical analysis (DMA) was done in tension (device *Eplexor 500* from *Gabo Qualimeter Testanlagen GmbH*, Germany) on samples of roughly $60 \times 10 \times 4\,mm^3$. The specimens were deformed statically by 0.2 % and dynamically at 10 Hz by 0.015 % while heating them at 1 °C/min to 200 °C. The glass-transition temperature T_g was defined as the temperature at which the loss modulus E'' was maximum. The rubber equilibrium modulus E_r was defined as the average complex modulus at temperatures between $T_{\min(E)} - 5\,°C$ and $T_{\min(E)} + 5\,°C$ during a DMA measurement, where $T_{\min(E)}$ is the temperature where the complex modulus is minimum.

The mass density ρ of neat epoxies was determined at 23 °C using the immersion technique according to ISO 1183 Method A [17].

Tensile tests were performed on neat epoxy at 1 mm/min in accordance with ISO 527-1 [18]. Eight specimens per material were machined by water-jet cutting to geometry 1A as given in ISO 527-2 [19] before post-curing and their sides and edges were ground with P400 sand paper to remove notches. The mechanical energy density at yield $U_{y,t}$ and at break $U_{b,t}$ were calculated by numerically integrating the engineering stress σ_t over the engineering strain ϵ_t until the yield and break point, respectively.

Plane-strain compression (PSC) tests were conducted on tested fracture-toughness testing specimens of all investigated materials as described by Williams and Ford [20]: Five 4 mm thick samples per material were compressed by a 3 mm wide stamp at 0.5 mm/min. The first maximum of the engineering stress was used as the plane-strain compressive yield stress $\sigma_{y,PSC}$. While this test is not as accurate as a tensile test, it allows measuring a parameter for the yield stress of materials that would otherwise fail before yielding. Moreover, no additional material is needed, which allowed measuring IF-WS_2-filled epoxies.

The fracture toughness K_{Ic} of the materials was measured in single-edge-notched bending (SENB) tests on specimens of $65 \times 15 \times 4\,mm^3$ according to ISO 13586 [21] at a test speed of 5 mm/min. A pre-crack was introduced by manually tapping a sharp blade into the machined notch at room temperature. The pre-cracks of most samples did not fulfill the recommendations of the ISO 13586 with regards to their length or symmetry, but nevertheless all samples were tested and evaluated. The plastic zone radius r'_y was estimated from the fracture toughness K_{Ic} and $\sigma_{y,PSC}$ via: [22]

$$r'_y = \frac{1}{6\pi}\left(\frac{K_{Ic}}{\sigma_{y,PSC}}\right)^2 \tag{6.1}$$

Selected nanocomposite fracture surfaces were sputter-coated with 5 nm Au (sputtering machine *EM ACE600 High Vacuum Sputter Coater* from *Leica*) before their investigation with a scanning electron microscope (SEM). The SEM (*NovaNanoSEM 230* from *FEI*) had a Schottky field-emission electron source operating at a voltage of 2 kV (beam current 57 pA), imaging secondary electrons with an in-lens detector at roughly 3×10^{-4} Pa pressure. All images were taken from regions close to the pre-crack.

The atomic force microscopy (AFM) (*MultiMode 8* from *Bruker*) was used with a 100-µm scanner in the *Peak-Force Tapping* mode in order to measure the surface topography of fracture surfaces. The used AFM probes (*ScanAsyst-Air* from *Bruker*) had a relatively soft triangular silicon-nitride cantilever (nominal spring constant 0.4 N/m) and a sharp tip (nominal tip radius 2 nm). All images were taken from regions close to the pre-crack.

6.5 Results

6.5.1 Dispersion quality

Fig. 6.1 shows a TEM image of a typical IF-WS_2 agglomerate. Its size, the diameters of the primary particles and the imperfections of the crystal structures are all well comparable to TEM images of commercial IF-WS_2 published elsewhere [6–8], indicating that the used NPs are comparable to the commercial product.

After one run through the 3RM, the average agglomerate size $\bar{x}_{\mathrm{DLS}}$ was 240 nm to 290 nm as measured via DLS. After two runs, it was 220 nm to 250 nm and after the third run 210 nm to 240 nm. These $\bar{x}_{\mathrm{DLS}}$ values are somewhat larger than those reported elsewhere (160 nm to 180 nm [7] or 170 nm to 190 nm [8]), which indicates that the laboratory-made IF-WS_2 NPs were more

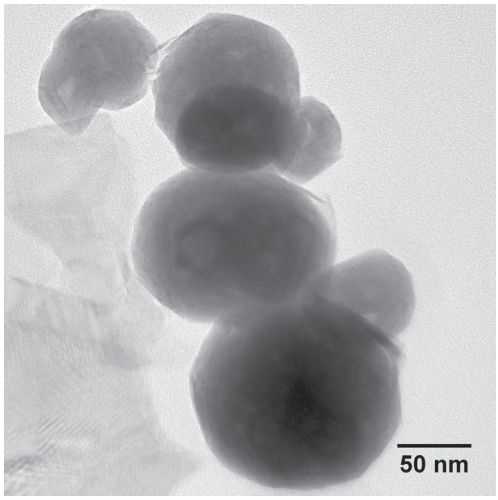

Figure 6.1: TEM image of the used IF-WS_2 NPs

difficult to disperse than the commercial product. Nevertheless, the dispersion quality should still be sufficient for further investigation.

6.5.2 Thermal characterization

Fig. 6.2 shows the T_g values of all materials as determined via DMA. With the exception of EP/MTHPA–89, the T_{post} of all materials was well above their T_g, so that it can be assumed that they were fully cured. An even higher T_{post} for EP/MTHPA-89 would increase its cure conversion even further, but was found to lead to partial degradation and thus discarded.

The materials with the higher curing agent contents had higher T_g values in all cases, which confirms the assumption that they were closer to stoichiometry and had a more densely cross-linked molecular network than the others [8]. In agreement with earlier reports [8], the addition of IF-WS_2 had no significant effect on the T_g.

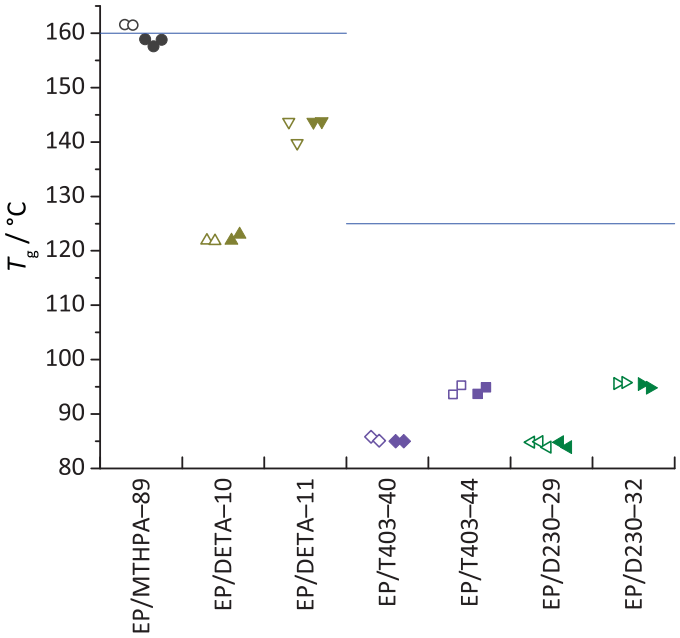

Figure 6.2: Glass-transition temperature T_g of the investigated neat (open symbols) and IF-WS_2 filled (filled symbols) epoxies. The lines give the respective post cure temperature T_{post}.

The molecular mass per cross-link M_c (basically the inverse of the cross-link density) can be calculated from the DMA data by an empirical formula: [8, 9, 23–25]

$$\log_{10}\frac{E_r}{3\ \mathrm{MPa}} = 293\frac{\rho}{M_c}\frac{\mathrm{mol}}{\mathrm{cm}^3} \tag{6.2}$$

M_c can also be estimated from theoretical considerations under a few assumptions from M_{EP}, M_{anh}, M_{DETA}, *AHEW* and the ratio of the amount of amine hydrogens to epoxide groups λ (derivation given in the Supporting Information):

$$M_{c,MTHPA}(\lambda = 1) = M_{EP} + M_{anh} \tag{6.3}$$

$$M_{c,DETA}(\lambda) = \frac{5M_{EP} + \lambda \cdot M_{DETA}}{8\lambda - 5} \tag{6.4}$$

$$M_{c,T403}(\lambda) = \frac{6M_{EP} + 6\lambda \cdot AHEW}{10\lambda - 6} \tag{6.5}$$

$$M_{c,D230}(\lambda) = \frac{6M_{EP} + 4\lambda \cdot AHEW}{9\lambda - 6} \tag{6.6}$$

Fig. 6.3 shows the measured M_c and compares it to that estimated. Qualitatively, the two values agree reasonably well with each other. Considering that the measured M_c was lower than theoretically possible, in particular for the DETA-cured epoxies, it is likely that eq. (6.2) underestimates M_c, which is not surprising, given that it is considered a "rather crude empirical relationship" [23]. Nevertheless, it is still useful for a relative comparison of different epoxy systems.

As expected, the stoichiometric materials always had a lower M_c (i.e., a higher crosslink density) than their sub-stoichiometric counterparts. The M_c values spanned a large range of 270 g/mol to 520 g/mol (measured) or 340 g/mol to 620 g/mol (estimated). This M_c range is much larger than investigated elsewhere (393 g/mol to 464 g/mol [9], 369 g/mol to 479 g/mol [8]) so that it should allow better evaluation of the M_c's effect on the K_{Ic}.

6.5.3 Tensile properties

Fig. 6.4 shows representative tensile-testing curves of neat epoxy samples of all investigated materials and fig. 6.5 shows the respective maximum stresses $\sigma_{m,t}$ and Young's moduli E_t measured. The PEA-cured epoxies showed clear yielding before failure, so that $\sigma_{m,t}$ can be seen as their yield stress and the strain at the maximum stress $\epsilon_{m,t}$ can be seen as their yield strain. In contrast, the epoxies made with MTHPA or DETA curing agents failed before yielding, so that their $\sigma_{m,t}$ does not reflect their actual yield stress and $\epsilon_{m,t}$ not their

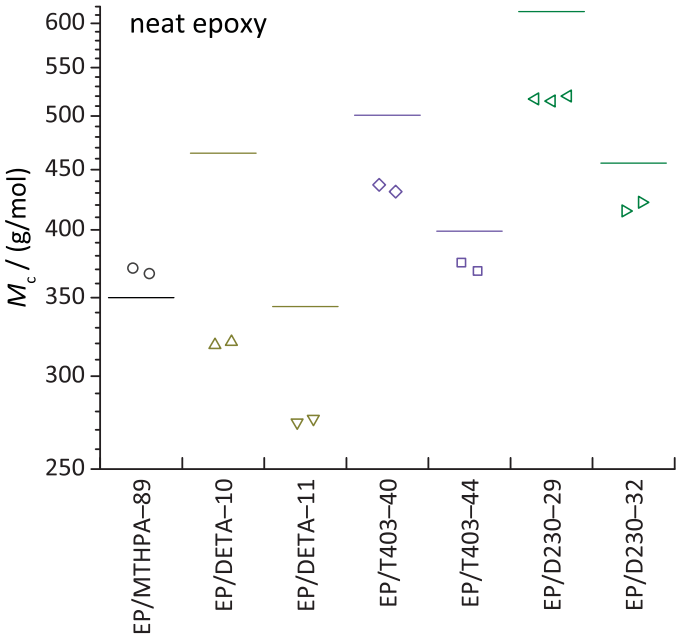

Figure 6.3: Molecular mass per crosslink M_c of neat epoxies as measured via DMA using eq. (6.2) (symbols) and as estimated theoretically (lines)

yield strain. The clearly different yielding behavior of the PEA-cured epoxies is likely due to their very flexible curing agent molecules.

The variations in both $\sigma_{m,t}$ and E_t are generally rather small, despite the large M_c differences. Notably, E_t strongly correlates positively with M_c, that is to say, the less densely cross-linked materials exhibited the higher E_t. In fact, all sub-stoichiometric materials had a higher $\sigma_{m,t}$ and a higher E_t than the (more densely cross-linked) stoichiometric ones. This was observed earlier [8, 25–27] and two different explanations were given: One explanation was that the curing agents are more flexible than the DGEBA, so that less curing agent might result in a stiffer molecular network [8]. However, this does not hold for DETA, which has very short alkyl chains between its amine groups and is therefore not more flexible than the DGEBA. Moreover, it is noteworthy that

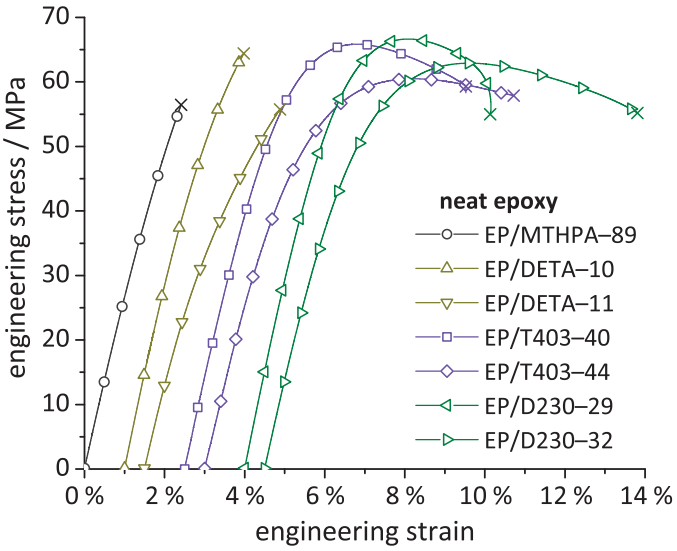

Figure 6.4: Tensile stress–strain curves of the investigated epoxy systems. The curves are horizontally off-set for clarity.

the EP/D230–29 (rather flexible curing agent molecule, high M_c) was significantly stiffer than EP/MTHPA–89 (very inflexible curing agent molecule, low M_c). The second, more plausible explanation is that more highly cross-linked epoxies shrink less after post-curing and thus contain more free volume [25]. This is confirmed by the ρ measurements, which consistently showed higher ρ for sub-stoichiometric epoxies (data in the Supporting Information).

6.5.4 Plane-strain compression tests

PSC tests are useful for measuring the yield stress of materials that fail before yielding in tensile tests [9]. Although the MTHPA- and DETA-cured epoxies also failed before yielding in the PSC tests, the curve shapes of EP/MTHPA–89 and EP/DETA–10 suggested that they were close to yielding (data shown in the Supporting Information), so that $\sigma_{y,PSC}$ is likely a representative value for

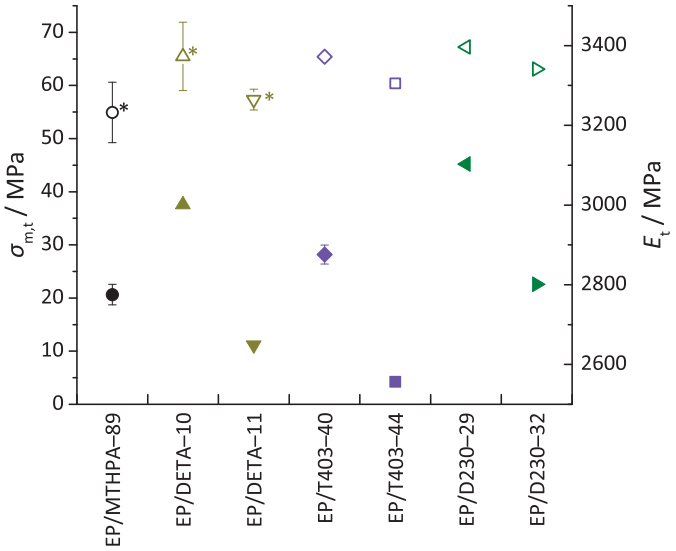

Figure 6.5: Maximum stress $\sigma_{m,t}$ (open symbols) and Young's modulus E (filled symbols) as determined in tensile tests for the investigated epoxy systems. Error bars are given only if they are larger than the respective symbols. The $\sigma_{m,t}$ values that are marked with an asterisk (*) are likely not representative for the material's yield stress.

the yield stresses of these materials. EP/DETA–11, in contrast, seems to have failed significantly prior to yielding, so that its $\sigma_{y,PSC}$ is likely not representative for the yield stress. Fig. 6.6 shows the results from the PSC tests. The $\sigma_{y,PSC}$ is clearly higher than the materials' tensile yield stress, but it is nevertheless useful for a relative comparison.

Again, the $\sigma_{y,PSC}$ was generally higher for sub-stoichiometric materials. The IF-WS_2 filler did not affect the $\sigma_{y,PSC}$ significantly. The materials that were cured with the rather flexible PEA curing agents had a significantly lower $\sigma_{y,PSC}$ than the others. Notably, the $\sigma_{y,PSC}$ correlates very strongly with ρ (*sample Pearson correlation coefficient* $r = 0.96$), indicating that the residual free volume within the epoxy determines its yield stress.

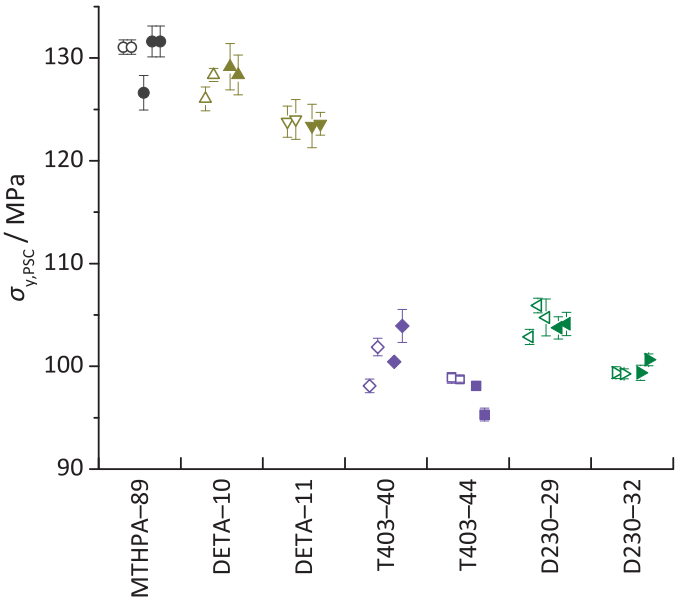

Figure 6.6: First stress maximum in PSC tests $\sigma_{y,PSC}$ for all neat (open symbols) and IF-WS_2-filled (filled symbols) materials. The $\sigma_{y,PSC}$ of EP/DETA–11 is likely not representative for the material's actual yield stress.

6.5.5 Fracture toughness

Fig. 6.7 shows the K_{Ic} results of all materials. The reproducibility was generally very good. The epoxy system and its stoichiometry had a much higher influence on the K_{Ic} than the IF-WS_2 NPs. The stoichiometric PEA systems yielded the highest K_{Ic} values, while the sub-stoichiometric PEA systems were much more brittle. In contrast, the EP/DETA–10 was a little tougher than EP/DETA–11. EP/MTHPA–89 was the most brittle of the investigated materials.

The addition of IF-WS_2 increased only the K_{Ic} of EP/D230–29 significantly. It had minor effects on the K_{Ic} of most epoxy systems, and even significantly embrittled EP/T403–44.

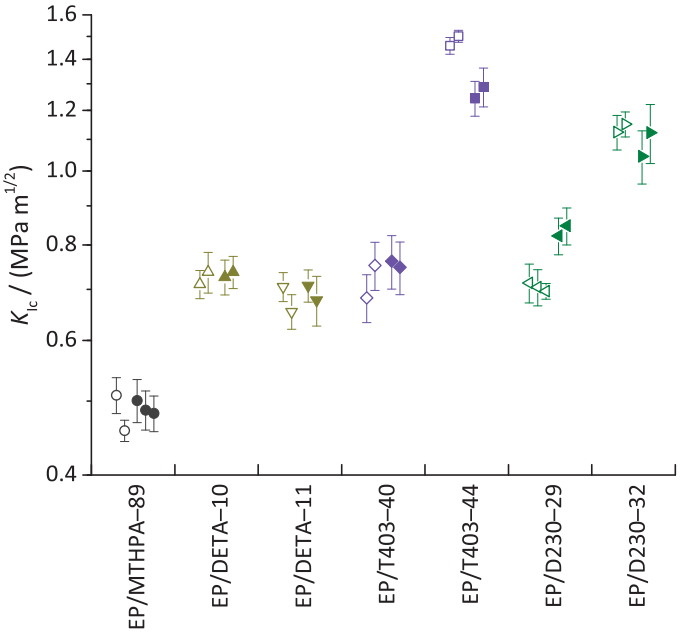

Figure 6.7: Fracture toughness K_{Ic} of investigated neat (open symbols) and IF-WS_2-filled (filled symbols) epoxies

6.6 Fractography

The fracture surfaces of EP/MTHPA–89, EP/D230–29 and EP/T403–44 were investigated with both SEM and AFM. The differences in the SEM images were rather small (fig. 6.8), despite the large differences between these materials in both the K_{Ic} and the toughening effect of the IF-WS_2 NPs. The NP filler created multiple microcracks in the brittle EP/MTHPA–89, while both EP/D230–29 and EP/T403–44 showed clear conic-section-shaped crack lines from secondary cracks as they have been reported elsewhere [7, 8, 28]. These crack lines have frequently been seen as a sign for a toughening effect, often denoted *crack pinning,crack-front bowing* or *crack deflection* [29]. However, as

fig. 6.8 shows, these lines appear regardless of whether the material has been toughened or not and should thus not be over-interpreted.

There are contradicting reports in literature on how the fracture-surface roughness correlates with the fracture toughness [30]. While there are reports stating that the roughness of epoxy–WS_2 fracture surfaces correlates with the fracture toughness [31], this was not always observed [8]. Table 6.2 lists two different roughness values of selected fracture surfaces as measured via AFM: R_{rms} is the root-mean-square roughness and d_A is the change in surface area, i.e., $d_A = (A_{\mathrm{surf}}/A_{\mathrm{proj}}) - 1$, where A_{surf} is the measured surface area and A_{proj} is the projected image area.

As observed elsewhere [8], the fracture surfaces always became significantly rougher as NPs were added, even if the K_{Ic} decreased, and the magnitude of this roughening did not correlate with the toughening effect. Notably, EP/D230–29 had the lowest R_{rms} of the investigated materials, but the highest d_A, indicating that its fracture surfaces were rather smooth overall but had a rough at small length scales. This suggests that d_A might be a more useful parameter for the investigation of NP toughening effects than traditional roughness parameters. As can be seen from the respective images (given in the Supporting Information), EP/D230–29 did not exhibit large secondary cracks

Table 6.2: Roughnesses R_{rms} and d_A of selected fracture surfaces compared to their fracture toughness K_{Ic}

material	K_{Ic} / MPa $\sqrt{\mathrm{m}}$	R_{rms} / nm	d_A / 10^{-4}
EP/MTHPA–89 neat	0.457 ± 0.015	10.5	7.0
EP/MTHPA–89 filled	0.501 ± 0.032	71.5	38.6
EP/T403–44 neat	1.500 ± 0.027	15.0	4.9
EP/T403–44 filled	1.244 ± 0.065	108	46.0
EP/D230–29 neat	0.696 ± 0.016	9.3	28.6
EP/D230–29 filled	0.847 ± 0.047	35.3	87.4

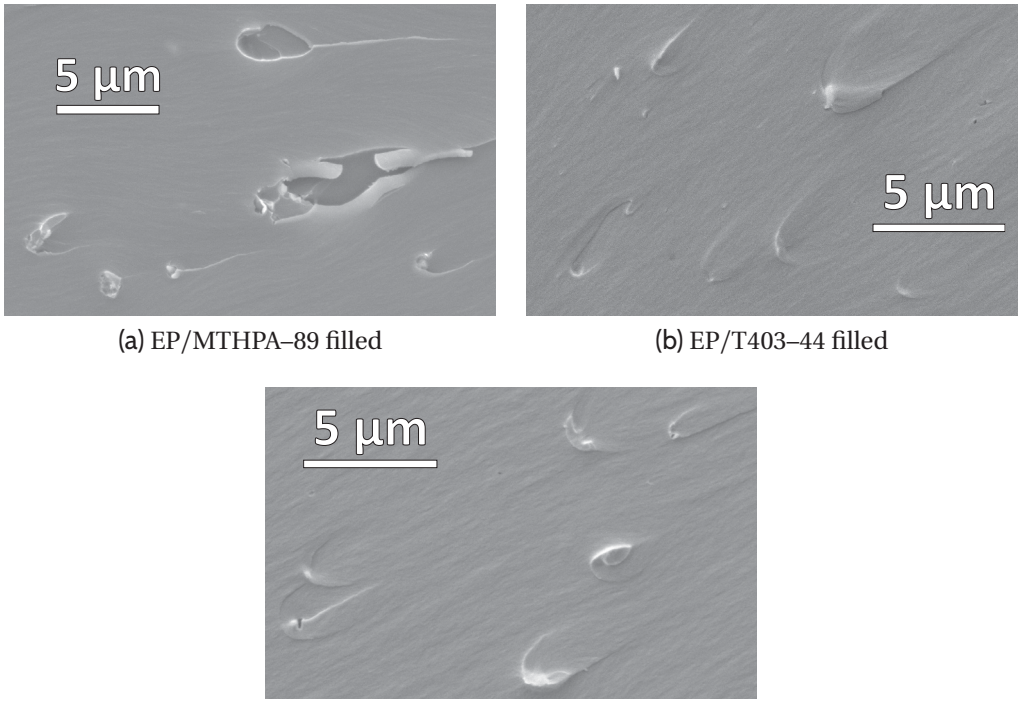

(a) EP/MTHPA–89 filled

(b) EP/T403–44 filled

(c) EP/D230–29 filled

Figure 6.8: SEM images of selected fracture surfaces of nanocomposites with 0.5 % IF-WS_2 by mass each

with tail formation, other than the other two. It rather appeared to experience more particle debonding. Both the debonding and the subsequent deformation of the debonded epoxy matrix are considered important toughening mechanisms [9], so that this might explain the superior toughening effect of IF-WS_2 in EP/D230–29.

6.7 Discussion

The toughening effect, that is to say, the change in the mean K_{Ic} when compared to the neat-epoxy reference, will be given by $d_K = \big(\langle K_{\mathrm{Ic}}\rangle - \langle K_{\mathrm{Ic,neat}}\rangle\big)/\langle K_{\mathrm{Ic,neat}}\rangle$, where $\langle\ldots\rangle$ stands for the arithmetic mean. The d_K measured in the present work is lower than those reported elsewhere [7, 8]: The toughening effect on EP/T403–40 was smaller and the embrittling effect on EP/T403–44 was higher as is highlighted in fig. 6.9. It is unclear whether this is due to the different source of the IF-WS_2 or due to the worse dispersion quality. However, the relative effect of IF-WS_2 on d_K is comparable, so that the conclusions drawn here are likely valid for commercial IF-WS_2 as well.

6.7.1 ANOVA

When the MTHPA-cured epoxy is disregarded, the experiments performed represent a full $2\times2\times3$ factorial experiment with two replicates per factorial point. An analysis of variance (ANOVA) can thus help to support the made suggestions with statistical data. The factors are the ratio of the amount of amine hydrogens to epoxide groups λ (factor A), the mass fraction of IF-WS_2 (B) and the curing agent type (C), and we investigate the linear effect of each of these factors on the mean of the K_{Ic} as well as the linear interactions between them.

Table 6.3 shows the most important ANOVA results: the sum of squares (SS), the degrees of freedom (df), the mean squares (MS), and the F-, p- and η_p^2-values, the latter two being the most important for interpretation: The p-value gives the probability that the measured effect of the respective factor is just coincidence, and η_p^2 gives what proportion of the total variance is associated with this factor.

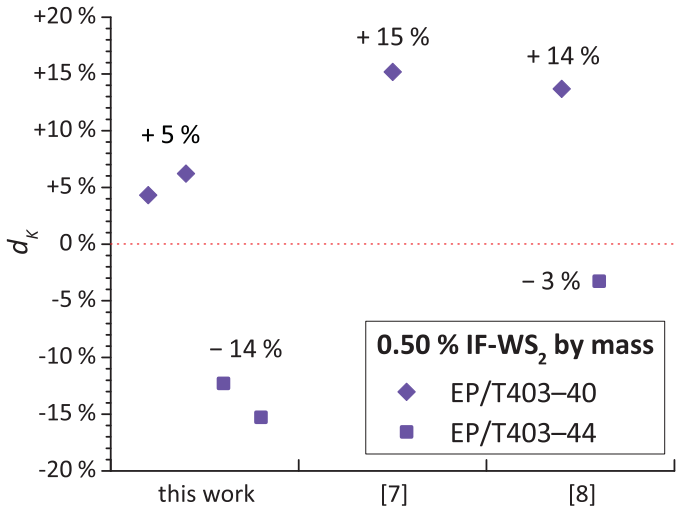

Figure 6.9: Relative fracture toughness change d_K after addition of $0.5\,\%$ IF-WS_2 by mass to EP/T403-40 and EP/T403-44, respectively, in this work and in reference works that used commercial IF-WS_2 NPs [7, 8], respectively

Table 6.3: ANOVA results for effects on K_{Ic}

Factor	SS	df	MS	F	p	η_p^2
model	1.64	11	0.15	133	*	0.99
A: λ	0.58	1	0.58	518	*	0.35
B: IF-WS_2	*	1	*	*	0.81	*
C: curing agent	0.45	2	0.23	202	*	0.27
A–B	0.026	1	0.026	23.5	0.0003	0.016
A–C	0.50	2	0.25	222	*	0.030
B–C	0.022	2	0.011	9.68	0.0027	0.016
A–B–C	0.017	2	0.008	7.47	0.0069	0.010
corrected total	1.66	24				

* $<10^{-5}$

The high η_p^2 of the model shows that the K_{Ic} can be modeled very well by these three factors. Within the chosen parameter window, the type (C) and amount (A) of curing agent are by far the most important factors determining the material's K_{Ic}, while no clear statement can be made on whether the addition of IF-WS_2 per se improves the K_{Ic}. There is some interaction between factors A and C, meaning that the importance of the stoichiometry for the K_{Ic} depends on the curing agent. The significant interactions of B with the other two factors (A–B, B–C and A–B–C) means that the toughening effect of the IF-WS_2 depends to comparable extents on the curing agent type, on its quantity, and on the combination of these. These data thus confirm that the toughening effect of IF-WS_2 depends strongly on the respective epoxy system.

6.7.2 Correlation of material properties

The main purpose of this work was to find out which material properties are determining for the toughening effect of IF-WS_2. One hypothesis was that the molecular defect fraction might be one crucial factor [8]. However, if this was the case, then all sub-stoichiometric epoxy systems would be expected to profit in a similar way from the IF-WS_2, irrespectively of the particular curing agent type as they all have a significantly increased defect fraction. Since this is not the case (cf. fig. 6.7 and tab. 6.3), it is unlikely that the molecular defect fraction itself is of major importance for the toughening effect.

Another hypothesis was that the M_c is the most important factor determining the toughening effect. It is noteworthy that the only epoxy system that increased significantly in its fracture toughness with IF-WS_2 addition, D230–29, was also that with the highest M_c. This confirms to some extent the earlier observation that epoxy systems with high M_c can be toughened more effectively with IF-WS_2 NPs [8]. Indeed, there seems to be a high correlation between d_K and M_c for PEA-cured epoxy systems ($r = 0.96$), however, the correlation

is much smaller for the other epoxy systems ($r = 0.21$) or the entire data set ($r = 0.48$), as is shown in fig. 6.10.

Table 6.4 shows the correlations of the d_K with the means of the measured material properties. Overall, d_K correlates most strongly with E_t and to a smaller extent with r'_y, K_{Ic}, M_c and the strain at maximum stress $\epsilon_{m,t}$.

The high correlation of d_K with E_t is somewhat surprising, considering that the measured differences in E_t were rather small, but it supports to some extent an earlier modeling work that predicted an important influence of E_t as well [11].

The fact that K_{Ic} correlates somewhat negatively with d_K shows that brittle epoxies can be toughened more successfully than tough ones. However, this correlation is much less pronounced than observed elsewhere [8], so that it does not seem as if there was a unique relationship. One mechanism that could explain the influence of the K_{Ic} on d_K is the size of the plastic zone r'_y at crack initiation during an SENB test, in particular when compared to the agglomerate sizes and the distances between agglomerates: If the plastic zone is significantly larger than the NP agglomerates or if it contains multiple NP agglomerates, it is possible that the NPs are essentially negated. The obtained r'_y ranged from 0.6 µm (EP/MTHPA–89) to 12.2 µm (EP/T403–44). It is thus possible that the IF-WS_2 NPs can affect the crack initiation of the brittle material much better than that of the tough material. However, the correlation of r'_y with d_K is only slightly higher than that of the K_{Ic}, so that this hypothesis does not seem to explain the observations either.

Once again, the correlations are much higher if only PEA-cured epoxy systems are concerned and very small if only non-PEA-cured epoxy systems are concerned. This shows that the NPs work entirely differently in the PEA-cured epoxy systems than in the other investigated epoxy systems, which may be explained with their different yielding behavior (cf. fig. 5.7). In particular, M_c, E_t, $\sigma_{m,t}$, $\epsilon_{m,t}$ and $U_{y,t}$ correlate very strongly with d_K for PEA-cured epoxies, sug-

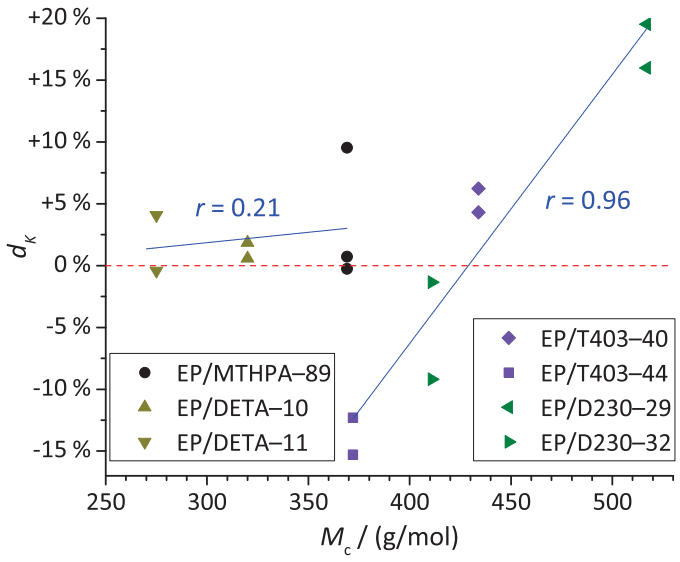

Figure 6.10: Relative fracture toughness change d_K after addition of 0.5 % IF-WS_2 by mass over the molecular mass per cross-link M_c. These values correlate strongly for the PEA-cured epoxy systems, but not for the others.

gesting that weakly cross-linked, stiff materials that yield at low strains, high elastic energies and high stresses can be toughened most successfully. However, this statement does not hold true if all investigated epoxies are taken into account.

These data do not show satisfying correlation of any material property with the toughening effect to draw clear conclusions for the entire dataset. The PEA-cured epoxies behave so differently that it is difficult to make any general statements. It seems as if the toughening effect was determined either by a combination of several material properties or by material properties that were not measured in this work.

Table 6.4: Correlation coefficients r for the correlation of the arithmetic means of material properties with d_k, for all investigated materials as well as only for PEA-cured materials and only for other materials, respectively

Property	r		
	all	PEA	other
K_{Ic}	−0.55	−0.82	−0.21
r'_{y}	−0.60	−0.84	−0.20
M_{c}	0.48	0.96	0.21
T_{g}	−0.02	−0.88	0.28
E_{t}	0.79	0.96	0.01
$\sigma_{\mathrm{m,t}}$	0.32	0.97	−0.15
$\epsilon_{\mathrm{m,t}}$	−0.41	−0.94	−0.21
$U_{\mathrm{y,t}}$	−0.34	−0.98	−0.27
$U_{\mathrm{b,t}}$	−0.23	−0.61	−0.27
ρ	0.16	0.78	−0.10
$\sigma_{\mathrm{y,PSC}}$	0.20	0.87	0.05

6.8 Conclusions

The laboratoy-made IF-WS_2 NPs are comparable to the commercial product, but they tend to form larger agglomerates and have an inferior effect on the material's K_{Ic}. The investigated epoxy systems vary greatly in their T_{g}, their M_{c} and their K_{Ic}, and to a lesser degree in their tensile properties and their $\sigma_{\mathrm{y,PSC}}$. The addition of IF-WS_2 does not affect the T_{g} or the $\sigma_{\mathrm{y,PSC}}$ significantly.

The K_{Ic} seems to be mostly determined by the particular epoxy system, i.e., the type and amount of curing agent used. The toughening effect of the IF-WS_2 on the K_{Ic} can be positive or negative, depending on the particular combination of curing agent type and quantity. Crack lines can be observed on fracture surfaces independently of whether the K_{Ic} increases or decreases. This makes it questionable to what extent crack lines can be seen as a sign for

a toughening effect. Likewise, the fracture surface roughness does not necessarily correlate with the K_{Ic}, but the fracture surface area might be more useful than assumed so far.

The polyetheramine-cured epoxy systems behave significantly differently to the others in the way the IF-WS_2 NPs affect the K_{Ic}, so that it is difficult to make general statements. It seems that stiff and brittle epoxy systems with low cross-link density and yield strain can be toughened by IF-WS_2 most effectively. However, the very strong correlation of the toughening effect with the amount of curing agent, the K_{Ic} and the M_c cannot be confirmed, suggesting that none of these factors alone determines the toughening effect, but rather a combination of several factors or a factor that has not yet been considered. Likewise, the data do not support the hypothesis that the molecular defect fraction was determining for the toughening effect.

Acknowledgements

The authors appreciate the help of Anja Huch and Marcel Rees for their experimental support. Furthermore, we want to thank the Huntsman Corporation for kindly delivering materials.

Supporting Information

Supporting Information related to this chapter can be found in section 8.5.

References

[1] L. Rapoport, Y. Bilik, Y. Feldman, *et al.*, "Hollow nanoparticles of WS_2 as potential solid-state lubricants", *Nature*, vol. 387, pp. 791–793, 1997. DOI: 10.1038/42910.

[2] C. Shahar, D. Zbaida, L. Rapoport, *et al.*, "Surface functionalization of WS_2 fullerene-like nanoparticles", *Langmuir*, vol. 26, no. 6, pp. 4409–4414, 2010. DOI: 10.1021/la903459t.

[3] V. Sorkin, H. Pan, H. Shi, S. Y. Quek, and Y. W. Zhang, "Nanoscale transition metal dichalcogenides: Structures, properties, and applications", *Crit. Rev. Solid State Mater. Sci.*, vol. 39, no. 5, pp. 319–367, 2014. DOI: 10.1080/10408436.2013.863176.

[4] M. Shneider, L. Rapoport, A. Moshkovich, *et al.*, "Tribological performance of the epoxy-based composite reinforced by WS_2 fullerene-like nanoparticles and nanotubes", *Phys. Status Solidi A*, vol. 210, no. 11, pp. 2298–2306, 2013. DOI: 10.1002/pssa.201329162.

[5] L. Rapoport, O. Nepomnyashchy, A. Verdyan, *et al.*, "Polymer nanocomposites with fullerene-like solid lubricant", *Adv. Eng. Mater.*, vol. 6, no. 1–2, pp. 44–48, 2004. DOI: 10.1002/adem.200300512.

[6] M. Shneider, H. Dodiuk, R. Tenne, and S. Kenig, "Nanoinduced morphology and enhanced properties of epoxy containing tungsten disulfide nanoparticles", *Polym. Eng. Sci.*, vol. 53, no. 12, pp. 2624–2632, 2013. DOI: 10.1002/pen.23517.

[7] D. Haba, A. J. Brunner, and G. Pinter, "Dispersion of fullerene-like WS_2 nanoparticles within epoxy and the resulting fracture mechanics", *Compos. Sci. Technol.*, vol. 119, pp. 55–61, 2015. DOI: 10.1016/j.compscitech.2015.09.013.

[8] D. Haba, M. Barbezat, S. Ayalur-Karunakaran, *et al.*, "Significance of epoxy network properties for the toughening effect of flaky and fullerene-like WS_2 nanoparticles", *J. Polym. Sci., Part B: Polym. Phys.*, vol. 54, no. 17, pp. 1738–1747, 2016. DOI: 10.1002/polb.24077.

[9] T. H. Hsieh, A. J. Kinloch, K. Masania, A. C. Taylor, and S. Sprenger, "The mechanisms and mechanics of the toughening of epoxy polymers modified with silica nanoparticles", *Polymer*, vol. 51, no. 26, pp. 6284–6294, 2010. DOI: 10.1016/j.polymer.2010.10.048.

[10] M. K. Umboh, T. Adachi, T. Nemoto, M. Higuchi, and Z. Major, "Non-stoichiometric curing effect on fracture toughness of nanosilica particulate-reinforced epoxy composites", *J. Mat. Sci.*, vol. 49, no. 21, pp. 7454–7461, 2014. DOI: 10.1007/s10853-014-8450-6.

[11] M. Salviato, M. Zappalorto, and M. Quaresimin, "Plastic shear bands and fracture toughness improvements of nanoparticle filled polymers: A multiscale analytical model", *Composites, Part A*, vol. 48, pp. 144–152, 2013. DOI: 10.1016/j.compositesa.2013.01.006.

[12] M. Shneider, H. Dodiuk, S. Kenig, and R. Tenne, "The effect of tungsten sulfide fullerene-like nanoparticles on the toughness of epoxy adhesives", *J. Adhes. Sci. Techn.*, vol. 24, no. 6, pp. 1083–1095, 2010. DOI: 10.1163/016942409X12584625925268.

[13] A. Buchman, H. Dodiuk-Kenig, A. Dotan, R. Tenne, and S. Kenig, "Toughening of epoxy adhesives by nanoparticles", *J. Adhes. Sci. Technol.*, vol. 23, no. 5, pp. 753–768, 2009. DOI: 10.1163/156856108X379209.

[14] Spetter and Tremel, DE 10 2015 016 878.9, 2016.

[15] "ISO 3001:1999. platics – epoxide compounds – determination of epoxide equivalent", International Organization for Standardization, Geneva, CH, Standard, Oct. 1999.

[16] "ISO 22412:2008(E). particle size analysis – dynamic light scattering (DLS)", International Organization for Standardization, Geneva, CH, Standard, May 2008.

[17] "ISO 1183-1:2004. plastics – methods for determining the density of non-cellular plastics – part 1: Immersion method, liquid pyknometer method and titration method", International Organization for Standardization, Geneva, CH, Standard, Feb. 2004.

[18] "ISO 527-1:2012. plastics – determination of tensile properties – part 1: General principles", International Organization for Standardization, Geneva, CH, Standard, Feb. 2012.

[19] "ISO 527-2:2012. plastics – determination of tensile properties – part 2: Test conditions for moulding and extrusion plastics", International Organization for Standardization, Geneva, CH, Standard, Feb. 2012.

[20] J. G. Williams and H. Ford, "Stress–strain relationships for some unreinforced plastics", *J. Mech. Eng. Sci.*, vol. 6, no. 4, pp. 405–417, 1964. DOI: 10.1243/JMES_JOUR_1964_006_055_02.

[21] "ISO 13586:2000(E). plastics – determination of fracture toughness (G_{IC} and K_{IC}) – linear elastic fracture mechanics (LEFM) approach", International Organization for Standardization, Geneva, CH, Standard, Mar. 2000.

[22] A. J. Kinloch and R. J. Young, "Fracture mechanics", in *Fracture behaviour of polymers*. London, New York: Springer, 2013, ch. 3, p. 91, ISBN: 978-94-017-1594-2.

[23] L. E. Nielsen, "Cross-linking-effect on physical properties of polymers", *J. Macromol. Sci., Part C: Polym. Rev.*, vol. 3, no. 1, pp. 69–103, 1969. DOI: 10.1080/15583726908545897.

[24] D. C. Timm, A. J. Ayorinde, and R. F. Foral, "Epoxy mechanical properties: Function of crosslink architecture", *Br. Polym. J.*, vol. 17, no. 2, pp. 227–232, 1984.

[25] R. J. Morgan, F.-M. Kong, and C. M. Walkup, "Structure–property relations of polyethertriamine-cured bisphenol-a-diglycidyl ether epoxies", *Polymer*, vol. 25, no. 3, pp. 375–386, 1984. DOI: 10.1016/0032-3861(84)90291-X.

[26] F. Fernandez-Nograro, A. Valea, R. Llano-Ponte, and I. Mondragon, "Dynamic and mechanical properties of DGEBA/poly(propylene oxide) amine based epoxy resins as a function of stoichiometry", *Eur. Polym. J.*, vol. 32, no. 2, pp. 257–266, 1996. DOI: 10.1016/0014-3057(95)00122-0.

[27] B. Burton, D. Alexander, H. Klein, *et al.*, *Epoxy formulations using Jeffamine polyetheramines*, Huntsman, USA, 2005.

[28] D. Haba, M. Barbezat, and A. J. Brunner, "Secondary crack formation as fracture mechanism in nanocomposites of epoxy and fullerene-like WS_2", in *Proc. NAP (Lviv, Ukraine, September 2015)*, vol. 4, 2015, 02NNSA03-1–02NNSA03-3.

[29] M. Quaresimin, M. Salviato, and M. Zappalorto, "Toughening mechanisms in nanoparticle polymer composites: Experimental evidences and modeling", in *Toughening mechanisms in composite materials*, Q. Qin and J. Ye, Eds., Woodhead Publishing, 2015, pp. 113–133, ISBN: 978-1-78242-279-2. DOI: 10.1016/B978-1-78242-279-2.00004-4.

[30] M. Quaresimin, K. Schulte, M. Zappalorto, and S. Chandrasekaran, "Toughening mechanisms in polymer nanocomposites: From experiments to modelling", *Comp. Sci. Technol.*, vol. 123, pp. 187–204, 2016. DOI: 10.1016/j.compscitech.2015.11.027.

[31] M. Shtein, R. Nadiv, N. Lachman, H. D. Wagner, and O. Regev, "Fracture behavior of nanotube–polymer composites: Insights on surface roughness and failure mechanism", *Comp. Sci. Technol.*, vol. 87, pp. 157–163, 2013. DOI: 10.1016/j.compscitech.2013.07.016.

7 Conclusions

This Thesis deals with the toughening effect of tungsten disulfide (WS_2) nanoparticles (NPs) on epoxy, in particular with that of inorganic, fullerene-like WS_2 (IF-WS_2) NPs. Earlier works have reported a significant toughening effect that they explained with the formation of a *nodular* morphology, which results in a region of higher modulus in the vicinity of the IF-WS_2 NPs [1]. The aim of this work was to investigate whether this claimed toughening effect can be confirmed and generalized, and what mechanisms might be responsible for it.

As pointed out in chapter 2, the nodular morphology in epoxy reported elsewhere [2, 3] is unlikely to exist but rather seems to be an artifact from atomic force microscopy (AFM) caused by a high surface roughness and not sufficiently sharp AFM tips. This becomes obvious when the AFM tip radius is reduced and the size of the apparent nodules changes. Super-sharp AFM tips (nominal tip radius below 1 nm) are necessary to image epoxy fracture surfaces without any nodules [4]. While nodular morphology is still repeatedly reported in recent publications [5–7], none of these works held to the suggestions made in sec. 2.5.6, so that these claims must be taken with care.

AFM in the *Peak-Force Tapping* mode was found capable of measuring the modulus distribution in epoxy, but this measurement is even more sensitive to the surface roughness if high lateral resolution is desired: The surface roughness has to be below 1 nm to avoid this artifact (chapter 2). The only surface preparation technique that was found to give sufficiently smooth sur-

faces was ultramicrotome cutting. If smooth surfaces are investigated, the modulus can be measured to a precision of approx. 300 MPa and at a resolution of approx. 10 nm (chapter 4). At this resolution, no modulus inhomogeneities were measured in bulk epoxy and neither in the close proximity to NP fillers. In a nutshell, the claimed nodular morphology does not seem to exist, nor do the claimed modulus inhomogeneities in the vicinity of IF-WS_2 NPs.

Surface functionalization of the WS_2 NPs is possible with silane modifiers, but is not necessarily successful, as can be shown via X-ray photoelectron spectroscopy (XPS) (chapter 3). Likewise, it does not seem to improve the WS_2's dispersibility within epoxy nor their toughening effect (chapter 4), other than stated elsewhere [1, 8]. This is not unexpected, however, since the surface of WS_2 is already very non-polar so that further functionalization might not affect the miscibility with an epoxy resin. The surface functionalization actually deteriorates the IF-WS_2 NPs' dispersion quality after sonication within ethanol, which could be measured well via DLS and modeled by an exponential approach function. Consequently, surface functionalization of IF-WS_2 does not seem to be useful for its use in epoxy.

Three-roll milling was found to be much more effective in dispersing IF-WS_2 NPs within epoxy than sonication, while at the same time having less degradation effect on the epoxy resin (chapter 4). The average IF-WS_2 agglomerate size obtained after 3RM within epoxy was 160 nm to 240 nm. This is still significantly larger than the approx. 100 nm IF-WS_2 primary particle size, but considering that the IF-WS_2 forms aggregates, it might not be possible to obtain a significantly smaller agglomerate size without milling the NPs.

Epoxy can be toughened with WS_2 NPs, but the success depends strongly on the investigated epoxy system, in particular on the type and amount of curing agent used (chapters 5 and 6). The highest obtained fracture toughness improvements were +25 % in the critical stress-intensity factor K_{Ic} and

+62 % in the critical strain-energy release rate G_{Ic} (both in chapter 4), but reductions by −15 % in the K_{Ic} and by −27 % in the G_{Ic} were observed as well (in chapter 6). The earlier work by Shneider *et al.* [1] that reported respectable toughening effects was carried out on an epoxy system that was cured with a sub-stoichiometric amount of T403 curing agent. This material is much more brittle than the stoichiometric epoxy system and is likely not very relevant for practical use. It is thus questionable whether WS_2 NPs can be useful as toughening agents at all. The used laboratory-made IF-WS_2 is mostly comparable to the commercial IF-WS_2, but it is more difficult to disperse and has an inferior effect on the epoxy's fracture toughness (chapter 6).

Generally, IF-WS_2 does not differ greatly from flaky WS_2 with respect to its effect on epoxy's fracture toughness (chapter 5) and it is questionable whether its toughening effect is significantly different from that of any other NP filler with similar size, shape and surface chemistry. It is thus doubtful that these rather expensive NPs might become an interesting option for a toughening agent for thermosetting polymers. In fact, its high mass density might make it an inferior choice to many alternatives, depending on the application. However, WS_2 NPs are also used as additives for other purposes, most importantly as tribologic additives [9, 10], so that even minor toughening effects can be relevant as an additional benefit. Whether or not a given epoxy system's fracture toughness increases with addition of WS_2 NPs cannot yet be forecast reliably and must thus still be tested individually.

References

[1] M. Shneider, H. Dodiuk, R. Tenne, and S. Kenig, "Nanoinduced morphology and enhanced properties of epoxy containing tungsten disulfide nanoparticles", *Polym. Eng. Sci.*, vol. 53, no. 12, pp. 2624–2632, 2013. DOI: 10.1002/pen.23517.

[2] C. M. Sahagun, "Molecular network development of a thermosetting epoxy–amine polymer", PhD Thesis, University of Southern Mississippi, 2012.

[3] M. R. VanLandingham, R. F. Eduljee, and J. R. Gillespie, "Relationships between stoichiometry, microstructure, and properties for amine-cured epoxies", *J. Appl. Polym. Sci.*, vol. 71, pp. 699–712, 1999.

[4] D. Haba, M. Barbezat, and A. J. Brunner, "AFM investigation of epoxy fracture surfaces indicating nanoplasticity", in *Proc. NAP (Lviv, Ukraine, September 2015)*, vol. 4, 2015, 01MAN01-1–01MAN01-4.

[5] S. F. Foster, E. A. Hoff, G. W. Curtzwiler, *et al.*, "Chemorheology investigation of a glassy epoxy thermoset on tensile plastic flow and fracture morphology", *J. Polym. Sci., Part B: Polym. Phys.*, vol. 53, no. 19, pp. 1333–1344, 2015. DOI: 10.1002/polb.23764.

[6] A. Bahrami, X. Morelle, L. D. H. Minh, *et al.*, "Curing dependent spatial heterogeneity of mechanical response in epoxy resins revealed by atomic force microscopy", *Polymer*, vol. 68, pp. 1–10, 2015. DOI: 10.1016/j.polymer.2015.04.084.

[7] S. Morsch, Y. Liu, S. B. Lyon, and S. R. Gibbon, "Insights into epoxy network nanostructural heterogeneity using AFM-IR", *ACS Appl. Mater. Interfaces*, vol. 8, no. 1, pp. 959–966, 2016. DOI: 10.1021/acsami.5b10767.

[8] C. Shahar, D. Zbaida, L. Rapoport, *et al.*, "Surface functionalization of WS_2 fullerene-like nanoparticles", *Langmuir*, vol. 26, no. 6, pp. 4409–4414, 2010. DOI: 10.1021/la903459t.

[9] M. Shneider, L. Rapoport, A. Moshkovich, *et al.*, "Tribological performance of the epoxy-based composite reinforced by WS_2 fullerene-like nanoparticles and nanotubes", *Phys. Status Solidi A*, vol. 210, no. 11, pp. 2298–2306, 2013. DOI: 10.1002/pssa.201329162.

[10] L. Rapoport, Y. Bilik, Y. Feldman, *et al.*, "Hollow nanoparticles of WS_2 as potential solid-state lubricants", *Nature*, vol. 387, pp. 791–793, 1997. DOI: 10.1038/42910.

8 Annex

8.1 Supporting Information for Publication 1

8.1.1 Manufacturing of other materials

In addition to the epoxy samples described in the main article, we investigated a series of additional materials that were frequently claimed to be either homogeneous or particularly inhomogeneous.

There are contradicting reports on the roughness of fracture surfaces of amorphous thermoplastics, namely PS and PMMA. In order to clarify this apparent contradiction, we conducted measurements on commercial PMMA, delivered by *Evonik Röhm GmbH* with the trade name *Plexiglas*, as well as on a PS sample from our lab.

It was mentioned by various authors that UP resins were intrinsically inhomogeneous due to the free-radical chain-growth polymerization reaction. In order to test this statement, we mixed 100 parts of *Aropol K 530 TB*, a pre-accelerated isophthalic-based UP resin mixture delivered by *Ashland*, with 1.50 parts of *Trigonox 42 PR*, a *tert*-butyl 3,5,5-trimethylhexaneperoxoate delivered by *AkzoNobel*. The mixture was stirred at 6000 rpm, degassed, and cured at 60 °C for 2 h.

Likewise, we created a so-called inter-penetrating network (IPN), a mixture of the epoxy and the UP resin, which were cured simultaneously. Such IPNs were shown to exhibit strong inhomogeneities. For that purpose, we prepared a standard epoxy mixture and separately a UP resin mixture, both in the same way as mentioned above and in the main article. The two mixtures were then mixed with each other 1:1 and cured at 60 °C for 8 h. At this temperature, the epoxy part can cure only partly. This

plate is hence supposed to be extraordinarily inhomogeneous. The resulting plate was very brittle.

8.1.2 Fracture surface of polystyrene

There were different reports on the shape of fracture surfaces of polystyrene (PS). Authors were claiming that they were extremely flat, exhibiting no surface features at all, while others claimed that they had a distinct nodular morphology. As can be seen in fig. 8.1 we found our PS fracture surfaces to be extremely rough when compared with epoxy fracture surfaces. The apparent nodular morphology is present, but is mostly covered by more dominant surface features.

8.1.3 Correlation between peak force and modulus

It is explained in the main article that the inhomogeneously measured modulus is most likely due to a variation in the tip–sample contact area. Another possible explanation could be the fact that the actual contact force F_{peak} is not perfectly constant during the scan.

Theoretically, small variations in F_{peak} should not affect the measured modulus. However, as experience shows the measured modulus does partly depend on F_{peak}, probably due to the fact that the system does not perfectly agree with the DMT model. One could therefore argue that the deviation in F_{peak} from its nominal value is the reason for the modulus to be affected by artifacts. This deviation is the *peak-force*

Figure 8.1: AFM height image of a PS fracture surface, captured in soft contact. The surface is extremely rough.

error ΔF_{peak}. Depending on the surface roughness and the measurement settings, ΔF_{peak} can easily exceed 10 % of F_{peak}.

The assumption that ΔF_{peak} causes the apparent modulus variations is partly supported by the comparison of the trace and retrace scans. In a perfect measurement, those scans would agree perfectly well with each other. As we can see in fig. 8.2 they agree well indeed, but there is some skewness in the modulus images that seems to be related to ΔF_{peak}: In positions where ΔF_{peak} is positive, the AFM tip presses stronger into the sample, which might cause the artificially highly measured modulus. The question is if this effect is the only reason for the variations in the modulus?

ΔF_{peak} is a measure for the control quality and hence a function of the vertical distance between two measured pixels: If the height difference between two adjacent pixels is large, ΔF_{peak} will be high as well. That means that we can reduce ΔF_{peak} by scanning at very small scan sizes: There are more pixels measured per nanometer, and the vertical distance between those is reduced as well.

In the example given in fig. 8.3, the scan size was chosen as small as $100 \times 200\,\text{nm}^2$ (at 512×256 pixels). The vertical distance between two adjacent pixels in that image was always well below 1 nm. The remaining variance in ΔF_{peak} was mainly due to noise and had only little correlation with the topography. In contrast, the modulus was still the same as the one measured at normal scan sizes. If the modulus inhomogeneities were caused by variations in F_{peak}, they would change strongly with the scan size, which is definitely not the case. This demonstrates that those apparent inhomogeneities are not due to variations in F_{peak}.

8.1.4 PS reference sample

In this article, we compare the variance in the measured moduli of the individual materials to that of the PS reference sample. To the sake of completeness, the PeakForce Tapping images of this reference are given in fig. 8.4. Some contamination is visible on each of the images. These areas were excluded for the modulus calibration.

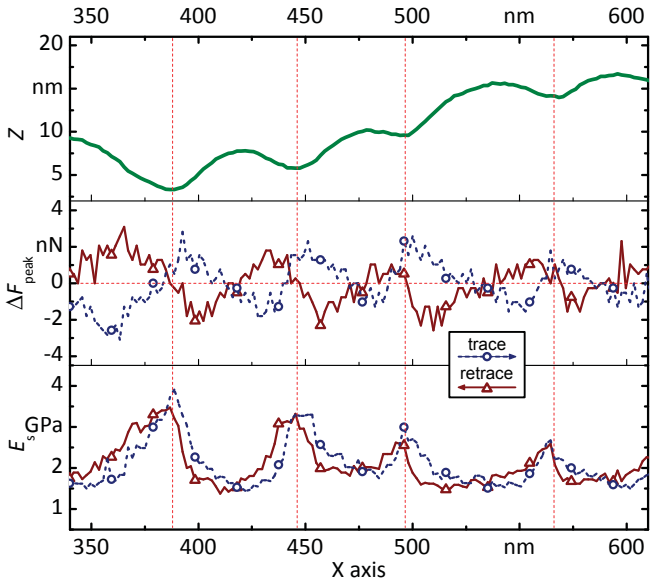

Figure 8.2: Z, ΔF_{peak} and E_{s} profile curves of one scan line of the epoxy fracture surface, both in trace (O) and in retrace direction (Δ). The E_{s} peaks are slightly skewed towards the side where ΔF_{peak} is higher.

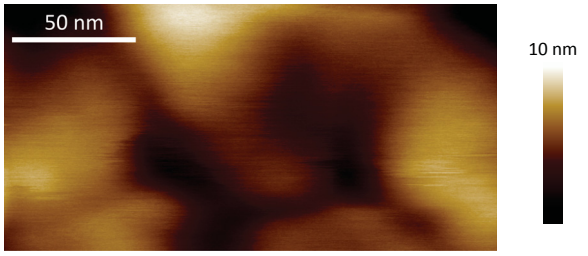

(a) Height Z

(b) Peak-force error ΔF_{peak}

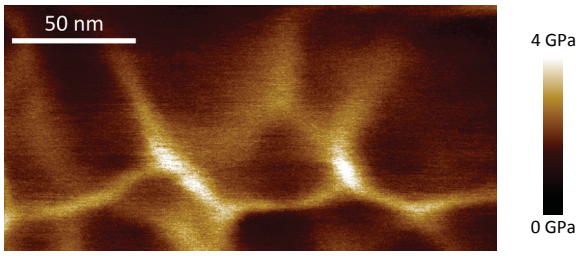

(c) Modulus E_{s}

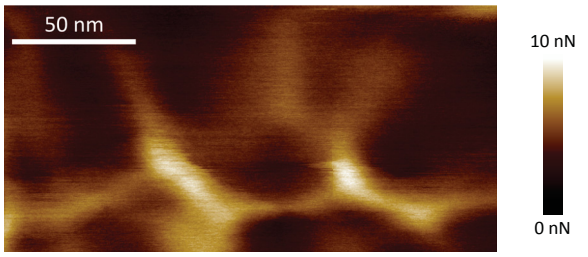

(d) Adhesion F_{adh}

Figure 8.3: Peak-Force Tapping image of the epoxy fracture surface, scanned at a very low scan size of $200 \times 100\,\mathrm{nm}^2$. While the peak-force error is strongly reduced, the apparent modulus inhomogeneities remain.

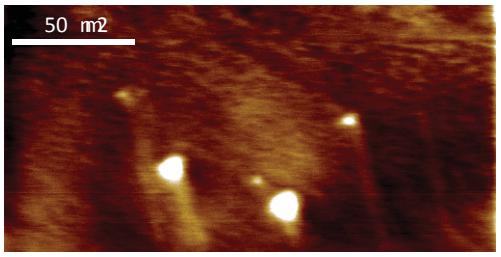

(a) Height Z

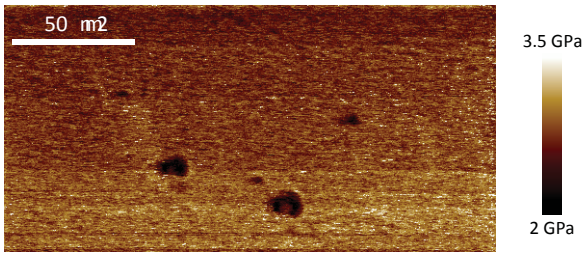

(b) Modulus E_s

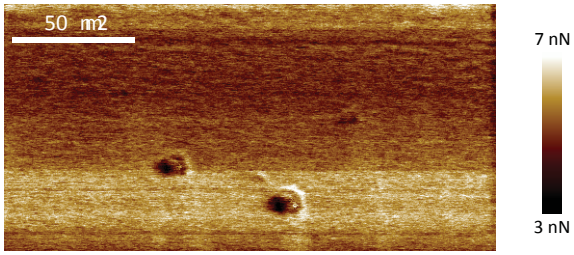

(c) Adhesion F_{adh}

Figure 8.4: Peak-Force Tapping images of the PS reference.

8.2 Supporting Information for Publication 2

8.2.1 IR spectra

It is stated in the main article that the IR spectra of the functionalized IF-WS_2 in KBr did not differ qualitatively from those of unfunctionalized IF-WS_2 in KBr, nor from those of fresh KBr. Fig. 8.5 highlights the fact that there is no qualitative change in the weak IR bands at 2962 cm^{-1}, 2922 cm^{-1} and 2852 cm^{-1}, which have been attributed to $-CH_3$ and $-CH_2-$ groups from the functionalization [1]. The quantitative differences are too small to draw conclusion from. The IR spectra do therefore not provide proof of successful functionalization.

8.2.2 Titration curves not shown in the main article

The titration curves of AATMS-1-rest-EtOH, AATMS-1 and AATMS-3 are given in fig. 8.6, together with the respective theoretical titration curves approximated by the software [2]. AATMS-3 is basic at the beginning, while AATMS-1 is acidic, which agrees with the results of the respective EtOH rests. However, the curve shapes are not that well defined and the measured amounts of diamine/diammonium far exceed the expected amounts. This might be due to the IF-WS_2 interacting in the acid–base reaction during the titration. It seems, therefore, that acid–base titration is only useful for determining the residual modifier left in the solvent, while it does not seem to be useful for measuring the amount of modifier in a IF-WS_2 powder directly.

8.2.3 Theoretical titration curve of a diprotic base

This section describes the calculation of the theoretical titration curve of a diprotic base. Here, B stands for an unprotonated diprotic base, A^- stands for the acid rest of the strong acid AH that is added during the titration, K_W is the dissociation constant of H_2O and the K_B are the base dissociation constants:

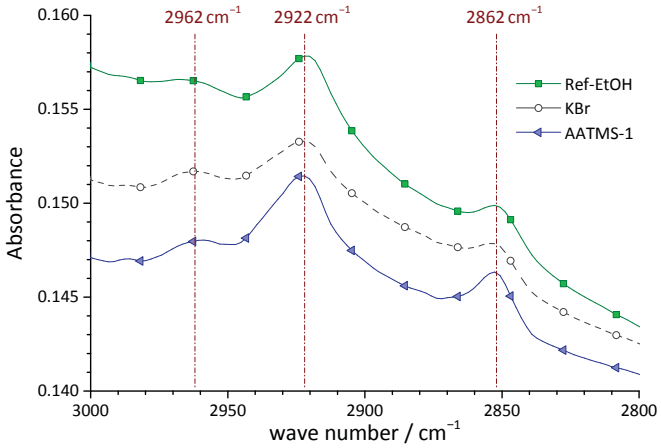

Figure 8.5: Transmission IR spectra; no qualitative differences between functionalized IF-WS_2, unfunctionalized IF-WS_2 and fresh KBr

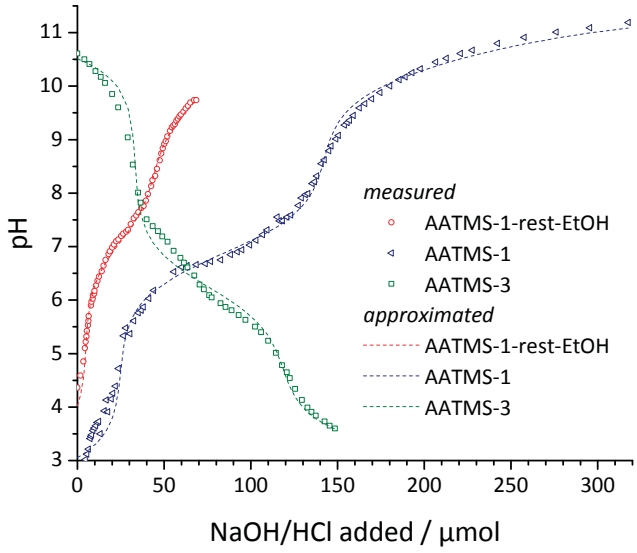

Figure 8.6: Measured titration curves of AATMS-1-rest-EtOH, AATMS-1 and AATMS-3 and theoretical titration curves fitted to these data

$$\begin{aligned} B + H_2O &\xleftrightarrow{K_{B1}} BH^+ + OH^- \\ BH^+ + H_2O &\xleftrightarrow{K_{B2}} {BH_2}^{2+} + OH^- \\ 2\,H_2O &\xleftrightarrow{K_W} H_3O^+ + OH^- \\ AH + H_2O &\longrightarrow A^- + H_3O^+ \end{aligned}$$

The K_B are calculated by $K_B = K_W/K_A$ from the respective acid dissociation constants K_A, which can be looked up in literature [3]. The charges must stay balanced:

$$c_{H_3O^+} + c_{BH^+} + 2\, c_{{BH_2}^{2+}} = c_{A^-} + c_{OH^-} \tag{8.1}$$

where c denominates the concentration. The nominal (initial) concentration of each substance will be denominated with F:

$$F_{AH} = c_{A^-} \tag{8.2}$$

$$F_B = c_B + c_{BH^+} + c_{{BH_2}^{2+}} \tag{8.3}$$

The individual concentrations are interrelated via the law of mass action:

$$K_{B1} = \frac{c_{OH^-} \cdot c_{BH^+}}{c_B} \quad \Leftrightarrow \quad c_B = \frac{c_{OH^-} \cdot c_{BH^+}}{K_{B1}} \tag{8.4}$$

$$K_{B2} = \frac{c_{OH^-} \cdot c_{{BH_2}^{2+}}}{c_{BH^+}} \quad \Leftrightarrow \quad c_{BH^+} = \frac{c_{OH^-} \cdot c_{{BH_2}^{2+}}}{K_{B2}} \tag{8.5}$$

$$K_W = c_{H_3O^+} \cdot c_{OH^-} \tag{8.6}$$

Dividing eq. (8.4) by eq. (8.3) gives:

$$\frac{c_B}{F_B} = \frac{c_{OH^-} \cdot c_{BH^+}/K_{B1}}{c_B + c_{BH^+} + c_{{BH_2}^{2+}}} \tag{8.7}$$

Including eq. (8.4) and eq. (8.5) gives:

$$\frac{c_B}{F_B} = \frac{c_{OH^-} \cdot c_{OH^-} \cdot c_{BH_2^{2+}} / (K_{B1} \cdot K_{B2})}{c_{OH^-} \cdot c_{BH^+} / K_{B1} + c_{OH^-} \cdot c_{BH_2^{2+}} / K_{B2} + c_{BH_2^{2+}}} \tag{8.8}$$

Further including eq. (8.5) gives:

$$\frac{c_B}{F_B} = \frac{c_{OH^-}^2 \cdot \cancel{c_{BH_2^{2+}}}}{\cancel{K_{B2}} \cdot c_{OH^-} \cdot c_{OH^-} \cdot \cancel{c_{BH_2^{2+}}} / \cancel{K_{B2}} + K_{B1} \cdot c_{OH^-} \cdot \cancel{c_{BH_2^{2+}}} + K_{B1} \cdot K_{B2} \cdot \cancel{c_{BH_2^{2+}}}} \tag{8.9}$$

Using a similar approach we get:

$$\frac{c_{BH^+}}{F_B} = \frac{c_{OH^-} \cdot K_{B1}}{c_{OH^-}^2 + K_{B1} \cdot c_{OH^-} + K_{B1} \cdot K_{B2}} \tag{8.10}$$

$$\frac{c_{BH_2^{2+}}}{F_B} = \frac{K_{B1} \cdot K_{B2}}{c_{OH^-}^2 + K_{B1} \cdot c_{OH^-} + K_{B1} \cdot K_{B2}} \tag{8.11}$$

Inserting eq. (8.2), eq. (8.6), eq. (8.10) and eq. (8.11) into eq. (8.1) leads to:

$$\frac{K_W}{c_{OH^-}} + F_B \cdot \frac{c_{OH^-} \cdot K_{B1} + 2 \cdot K_{B1} \cdot K_{B2}}{c_{OH^-}^2 + K_{B1} \cdot c_{OH^-} + K_{B1} \cdot K_{B2}} = F_{AH} + c_{OH^-} \tag{8.12}$$

$$\begin{aligned} \Leftrightarrow \quad 0 &= c_{OH^-}^4 + c_{OH^-}^3 \cdot (F_{AH} + K_{B1}) + \dots \\ &\cdots + c_{OH^-}^2 \cdot (K_{B1} \cdot K_{B2} + F_{AH} \cdot K_{B1} - F_B \cdot K_{B1} - K_W) + \dots \\ &\cdots + c_{OH^-} \cdot (F_{AH} \cdot K_{B1} K_{B2} - 2 \cdot F_B \cdot K_{B1} K_{B2} - K_W K_{B1}) - K_W K_{B1} K_{B2} \end{aligned} \tag{8.13}$$

With eq. (8.13) it is possible to calculate c_{OH^-} iteratively for any amount of strong acid (e.g. HCl) added, and the pH can be calculated by:

$$\mathrm{pH} = -\log_{10}\left(c_{H_3O^+} \cdot \frac{1}{\mathrm{mol}}\right) = -\log_{10}\left(\frac{K_W}{c_{OH^-}} \cdot \frac{1}{\mathrm{mol}}\right) \tag{8.14}$$

Note, however, that the calculations in the main article were done with a titration-curve-fitting software that takes even more factors into account, e.g., the ion activity [2].

8.2.4 TGA of untempered powders

As mentioned in the main article, all measurements shown were done on powders tempered at 100 °C for 1 hour. Fig. 8.7 shows TGA curves of *untempered* HTCS-1, after tempering it in vacuum at 50 °C, 80 °C and 100 °C, respectively, for 1 hour each. Significant mass was lost already below 200 °C depending on the tempering temperature. As the modification with HTCS was done at room temperature, the surface functionalization reaction had not fully finished before the measurements. The residual unreacted HTCS reacting during the TGA measurement resulted in evaporation of HCl causing significant mass loss. As XPS and TG/MS measurements showed, no HCl was measurable after tempering at 100 °C for 1 h.

8.2.5 TG/MS results and discussion

TG/MS measurements were done on AATMS-3 and HTCS-3 in order to obtain additional information on the origin of the mass loss in the TGA; the analyzed ratios of ion mass m to ion charge q were chosen in a way to analyze possible traces of CO_2, H_2O, HCl and ammonium compounds in the gas (see fig. 8.8).

The strongest MS signals were detected for m/q of 28 and 14. As these did not change with temperature, however, it is very likely that they are due to N_2 traces in the He flow gas rather then due to CO. The same is true for an m/q of 16 which is most likely $O^{+\bullet}$. The fact that the signals for m/q of 35 and 36 do not change with temperature indicates that no HCl was created, so that we can assume that the silanzation reaction of HTCS-3 has finished after tempering.

The strongest signals that correlate with the derivative of the mass loss are those with m/q of 17 and 18, which are created by OH^+ and NH_3, and by H_2O and NH_4^+, respectively. This suggests that much of the mass loss is indeed due to H_2O. The ratio between the signals with m/q of 17 and 18 are constant in the case of HTCS-3, but not in the case of AATMS-3; here, the signal with m/q of 18 increases disproportionately around 300 °C, which indicates an additional NH_4^+ signal and supports the assumption that the large mass loss peak is due to decomposition of AATMS under secession of ammonium.

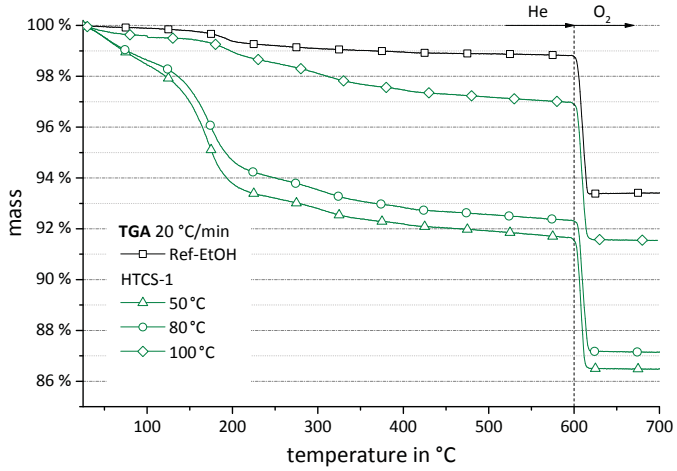

Figure 8.7: TGA curves of HTCS-1 after tempering at different temperatures

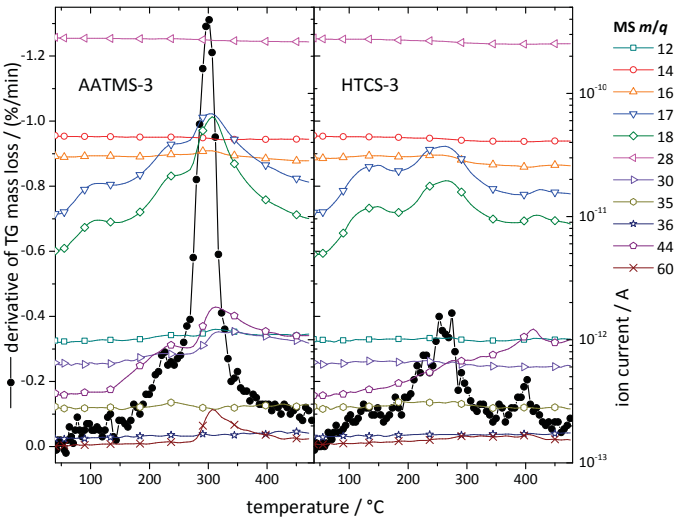

Figure 8.8: TG/MS results of AATMS-3 (left) and HTCS-3 (right); the right axis gives the MS ion current for all measured m/q ratios

There are many possible fragments that could produce a signal with an m/q of 44, e.g., $C_2H_6N^+$. However, the signal originates most likely mainly from $CO_2^{+\bullet}$. This indicates that there is a steady removal of some organic species from both samples, enabled by O traces in the gas flow.

Finally, signals from m/q of 30 and 60 were detected, which indicate $CH_2NH_2^+$ and $H_2N(CH_2)_2NH_2^{+\bullet}$. The facts that these were only seen in the AATMS-modified sample and that they appear most strongly around 300 °C support this interpretation further.

These data suggest that the functionalization of AATMS-3 and HTCS-3 was successful and support the assumptions that the TGA mass loss is mainly due to H_2O and CO_2 and in the case of AATMS-3 also due to succession of ammonium compounds.

8.2.6 SEM imaging of IF-WS_2 powders

Additional SEM images are given in fig. 8.9; arrows highlight visible agglomerates. While there is some difference visible between samples sonicated for different times, the final agglomerate size seems to be relatively large, likely due to inevitable reagglomeration of the nanoparticles upon drying.

References

[1] C. Shahar, D. Zbaida, L. Rapoport, *et al.*, "Surface functionalization of WS_2 fullerene-like nanoparticles", *Langmuir*, vol. 26, no. 6, pp. 4409–4414, 2010. DOI: 10.1021/la903459t.

[2] I. G. R. Gutz, *CurTiPot – pH and acid–base titration curves: Analysis and simulation freeware*, version 4.

[3] W. M. Haynes, "Dissociation constants of organic acids and bases", in *CRC handbook of chemistry and physics*, 95th, Boca Raton: CRC Press, 2014, pp. 5–94, ISBN: 978-1-4822-0867-2.

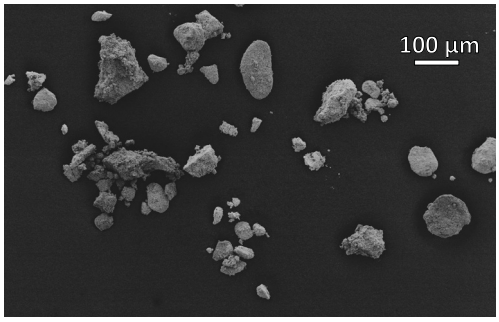

(a) IF-WS_2 as delivered

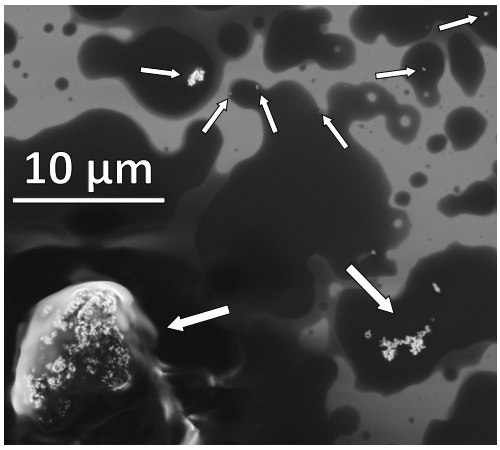

(b) Ref-EtOH after 10 s of sonication

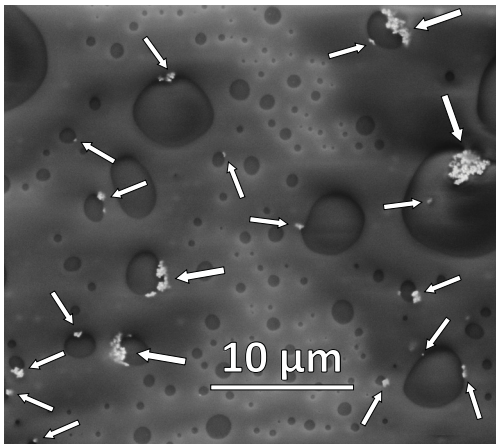

(c) Ref-EtOH after 60 min of sonication

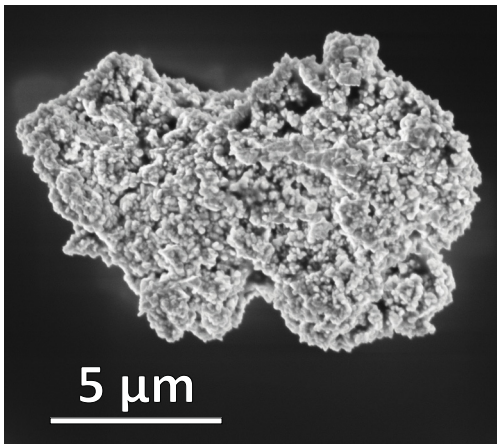

(d) HTCS-1 after 25 s of sonication

Figure 8.9: SEM images of IF-WS_2 samples on Si wafers

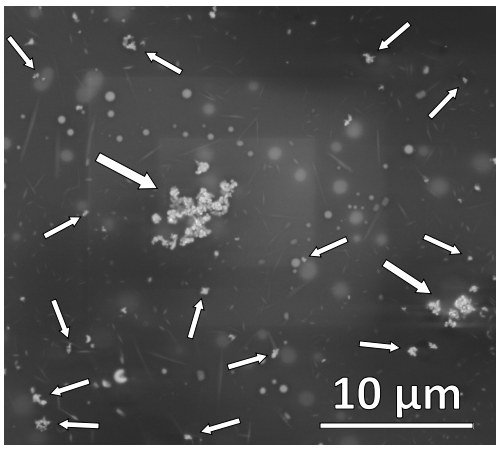

(e) HTCS-1 after 60 min of sonication

Figure 8.9: (continued) SEM images of IF-WS_2 samples on Si wafers

8.3 Supporting Information for Publication 3

8.3.1 Thermo-oxidative degradation of DGEBA

Ultraviolet–visible UV/Vis spectroscopy was done to quantify the discoloration of the DGEBA after sonication (spectrophotometer *Cary 50 Bio* from *Varian*). The sonicated DGEBA was filled in a 10 mm thick quartz cuvette for the measurement and the results were corrected for the cuvette's absorption.

Infrared (IR) spectroscopy was done in attenuated total reflection (ATR-IR) to investigate the chemical changes of the DGEBA caused by sonication (spectrophotometer *Tensor* from *Bruker*; 4000 cm^{-1} to 400 cm^{-1} with 1.9 cm^{-1} step size, 64 scans).

Sonicating neat DGEBA results in a clearly visible color change, indicating that some material damage takes place. Depending on the lighting conditions, some yellowness was visible after 1 min to 3 min, indicating material degradation. After 10 min, the yellowness was already clearly visible (see fig. 8.10). In those literature reports where IF-WS_2 were dispersed within epoxy, the sonication times were as long as 60 min [1] or 240 min [2], even though it was stated elsewhere that already 2 min of sonication damages IF-WS_2 particles [3].

The color change can be quantified in the form of UV/Vis spectra as in fig. 8.11: Neat, unsonicated DGEBA absorbs light below 305 nm, likely due to its aromatic rings. After just 4 min of sonication there is already some measurable color change. From the UV/Vis spectra it becomes obvious how severe the color change is after

Figure 8.10: Photography of neat DGEBA after different sonication times, given in minutes.

longer sonication times. After 60 min of sonication, light is absorbed over the whole visible light spectrum, resulting in a brownish color.

ATR-IR was done on each of the samples in fig. 8.11, but no monotonically changing bands could be seen, despite the good signal-to-noise ratio of these measurements. The IR spectra of DGEBA before and after 60 min of sonication and the difference between the two are given in fig. 8.12 as an example. There are barely any differences between these two spectra. The largest difference is a 0.3 % increase in the C–O–C streching peak at 828 cm^{-1}. In particular, neither did the IR band of the epoxide group at 914 cm^{-1} decrease, nor that of the ether group at 1033 cm^{-1}, which are arguably the weakest links in the DGEBA molecule. It does, therefore, not seem as if the chemical composition of the DGEBA changed strongly due to sonication. Likewise, mechanical tests indicated that sonication does not affect the mechanical properties of the cured material significantly.

Mailhot *et al.* reported that thermo-oxidative degradation of amine-cured epoxy results in strong discoloration but barely alters the obtained IR spectra [4]. They reasoned that highly UV/Vis-absorbing products are formed in concentrations not large enough to be detected by IR analysis. However, these authors observed discoloration after heating cured epoxy plates to 100 °C for several days [4], but already a few minutes of sonication seem to be sufficient for the same effect here. While the DGEBA's average temperature during sonication was permanently around 90 °C to 100 °C, it is known that sonication can locally cause temperatures of up to 5000 K [5]. While smaller molecules like ethanol limit the temperature increase by vaporization, DGEBA degrades before it vaporizes. It is therefore likely that the observed yellowing is indeed due to thermo-oxidative degradation and it is unlikely that even best cooling conditions could avoid it. However, this might have only minor effects on the material's mechanical properties as probably only small fractions of the DGEBA have degraded.

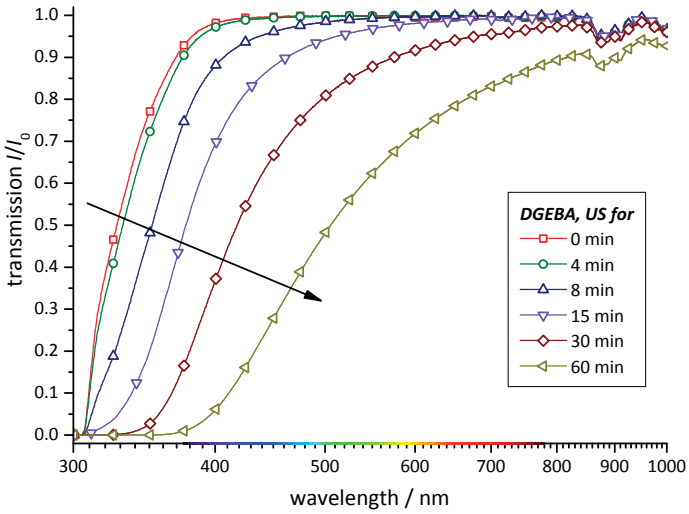

Figure 8.11: UV/Vis spectra of DGEBA after differently long sonication times. The yellowing is clearly measurable.

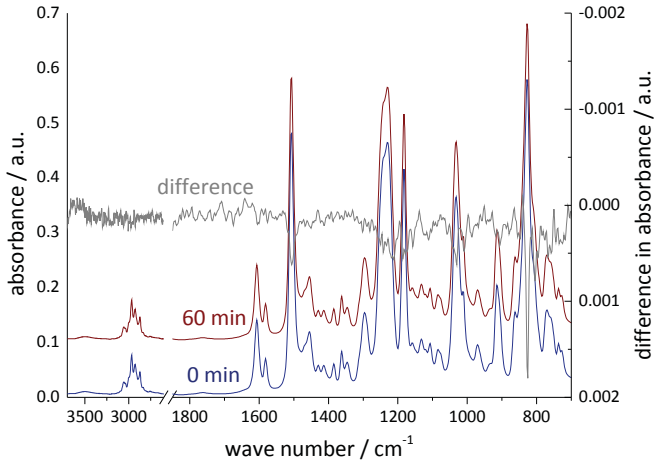

Figure 8.12: IR spectra of DGEBA before and after $60\,\mathrm{min}$ of sonication and the difference between the two. The absorbance spectrum of the DGEBA after $60\,\mathrm{min}$ of sonication is vertically shifted for clarity.

8.3.2 Structures of silane surface modifiers and curing agent

The structure formulas of the used silane surface modifiers and the used curing agent Jeffamine T-403 are given in fig. 8.13.

8.3.3 Transmission electron microscopy

For transmission electron microscopy (TEM), a drop of ethanol–IF-WS_2 suspension (sonicated for 60 min) was placed on a TEM grid and allowed to dry. The images were gathered in a Schottky field emission TEM (*JEOL 2200FS TEM/STEM*) operating at 200 kV. Figure 8.14 shows representative images of an individual primary particle and of a small agglomerate, respectively. However, it is unclear whether the agglomerate shown there has existed already in the ethanol suspension or formed upon drying on the TEM grid.

8.3.4 Conic-section-shaped crack lines due to secondary cracks

It was stated in the main article that the initiation of secondary cracks around a particle might explain the conic-section-shaped crack lines visible in SEM micrographs. This hypothesis will be dealt with in more detail here.

Consider a particle with radius R_0 embedded in a brittle matrix. In a fracture mechanics test, a crack (denominated *primary* crack) propagates through this matrix with a given velocity v_p in the same plane as the center of the particle. When this crack is a given distance A apart from the particle, the stress field in front of the propagating primary crack and the stress concentration around the rigid particle [6] cause a *secondary* crack to initiate at the particle–matrix interface, which then propagates radially with a velocity v_s. After initiation, the secondary crack propagates due to the same macroscopic stresses as the primary crack, thus it will be propagating in a nearly parallel plane. For the sake of simplicity, let's assume that both velocities v_p and v_s are constant (but not necessarily equal), that they propagate both in parallel planes and that the secondary crack propagates in all radial directions with the same velocity. Mind that none of these assumptions will generally be true.

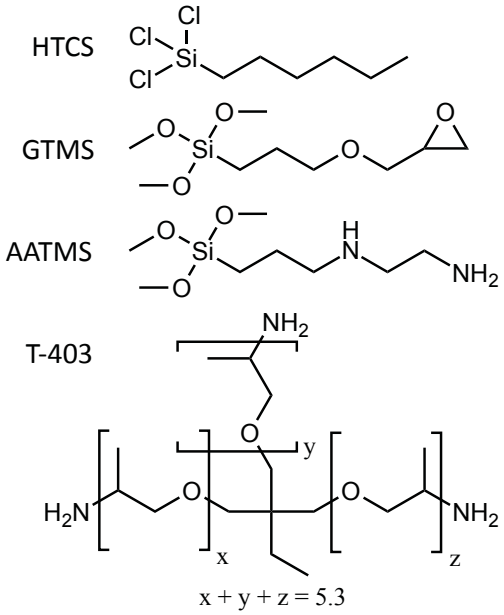

Figure 8.13: Silane surface modifiers and curing agent Jeffamine T-403

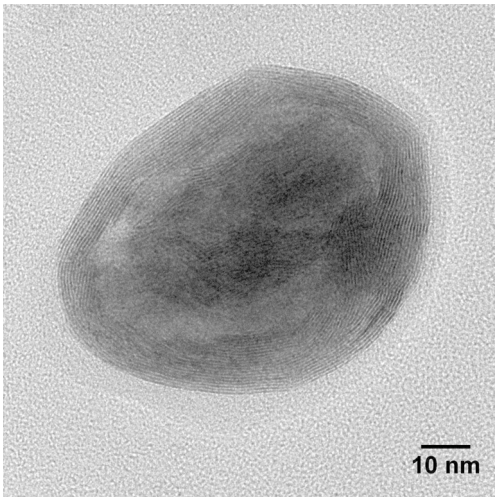

(a) Individual primary particle

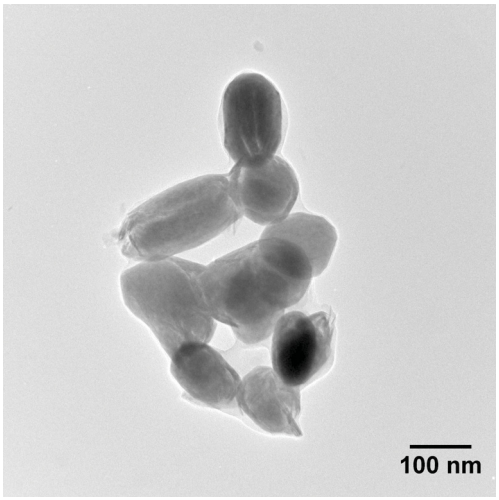

(b) Small agglomerate

Figure 8.14: Representative TEM images of the used IF-WS_2

A graphical representation of this situation is given in fig. 8.15. At time t after the initiation of the secondary crack, the distance of the secondary crack from the center of the particle is $R(t) = R_0 + v_s \cdot t$. As the origin is in the center of the particle, the position of the primary crack is $x_p(t) = v_p \cdot t - A$. The intersection of $x_p(t)$ and $R(t)$ is given by $\underline{r}(t)$, which describes the shape of the resulting crack line.

Note that for

$$v_p = v_s \quad \Rightarrow \quad R(t) - R_0 = x_p(t) + A \quad \Leftrightarrow \quad R(t) = x_p(t) + (A + R_0) \tag{8.15}$$

which describes a parabola with its focus in the center of the particle. For $v_p > v_s$, this would result in an ellipse, and for $v_p < v_s$ it would result in a hyperbola. Animations of these three possible crack line formations are available in the online version of this article.

8.3.5 AFM nanomechanical imaging of ASA

A sample of acrylonitrile–styrene–acrylate (ASA, trade name *Luran S*) was cryo-ultramicrotomed at −110 °C and imaged with AFM the same way as described in the main article in order to measure how precisely the AFM can measure modulus differences on plane surfaces of known samples. Figure 8.16a shows a topographic image of the created surface. The elastomeric regions are visible as clear depression in the elsewise very smooth surface. Figure 8.16b shows height and modulus images of a smooth region on this surface where a modulus inhomogeneity can be observed. This inhomogeneity is supposedly due to a submerged elastomeric particle that results in a more compliant region on the surface. The height difference of approx. 4 nm in this region is smaller than the nominal AFM tip radius (8 nm, so that the DMT model is reasonably well suitable, and the measured modulus image supports this assumption. The rectangular region visible in the center of fig. 8.16b is due to a small, permanent deformation by an earlier AFM scan at this position.

These measurements show that local modulus (or rather, stiffness) inhomogeneities can indeed be measured with this AFM technique given that the surface

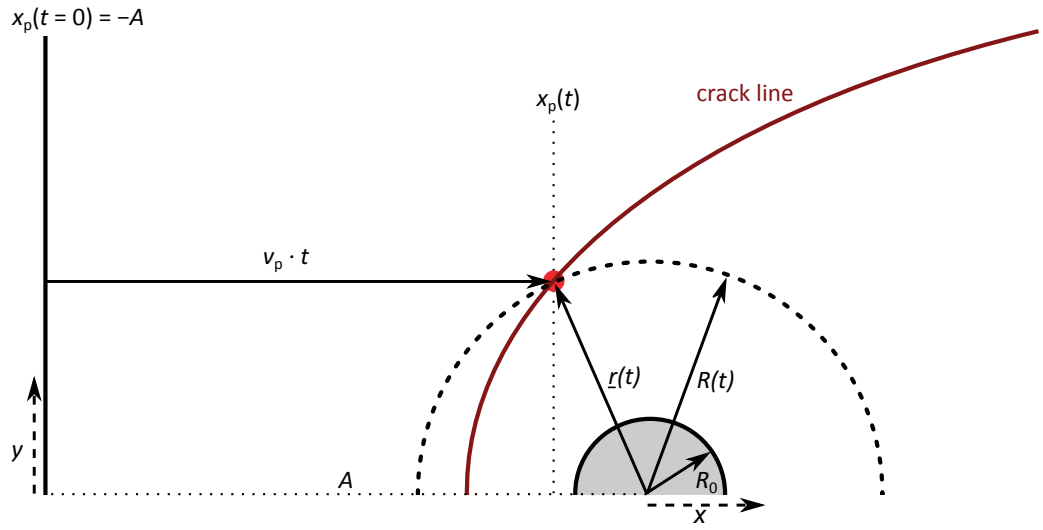

Figure 8.15: Geometric representation of the creation of a conic-section-shaped crack line. The line to the left represents the position of the primary crack, the filled half-circle represents the nanoparticle and the dashed half circle represents the position of the secondary crack.

is sufficiently smooth. A stiffness difference corresponding to an apparent modulus difference of a few hundred MPa can clearly be discerned from the bulk stiffness/modulus.

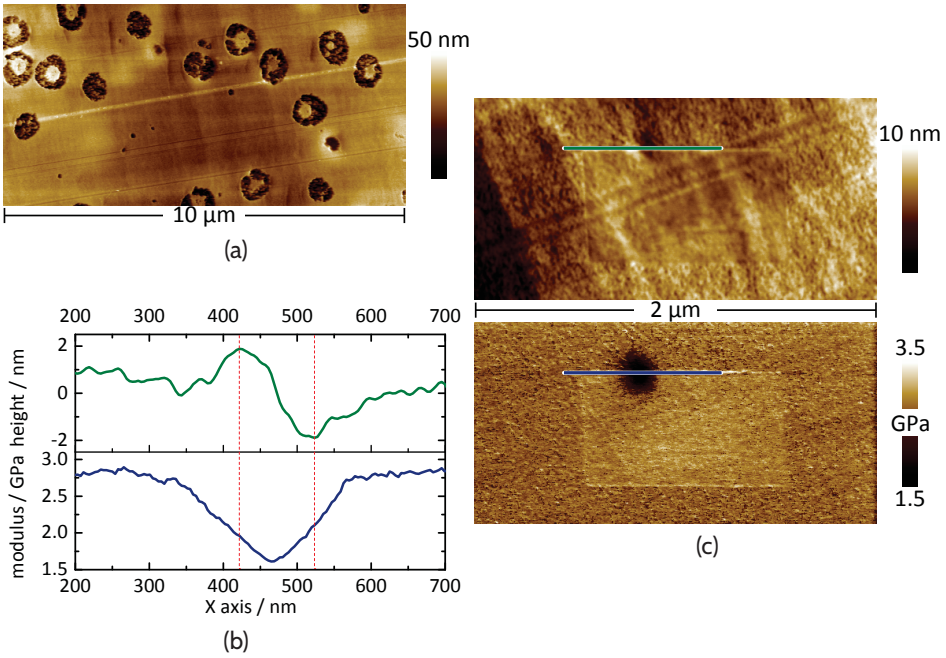

Figure 8.16: (a) AFM height image of cryo-ultramicrotomed ASA. (b) AFM height and modulus images of a smooth region therein. (c) Profile curves of the lines highlighted in (b). Images courtesy of the authors.

8.3.6 Additional fractographic images

This section shows a series of additional fractographic images in order to help the reader get a better image of the obtained dispersion quality and the observed fracture phenomena. Figure 8.17 shows that small agglomerates and individual primary particles exist also in the sonicated sample, but they are very sparse. Likewise, the images of the samples produced by 3RM (fig. 8.18 to 8.22) show that larger agglomerates are present in each material. However, the distribution is clearly much more narrow than in the sonicated nanocomposite.

Fractography does reveal certain differences between the individual nanocomposites. For instance, the fracture surface of EP/GTMS seems to be rather smooth and the rather homogeneously dispersed nanoparticles tend to detach from the epoxy

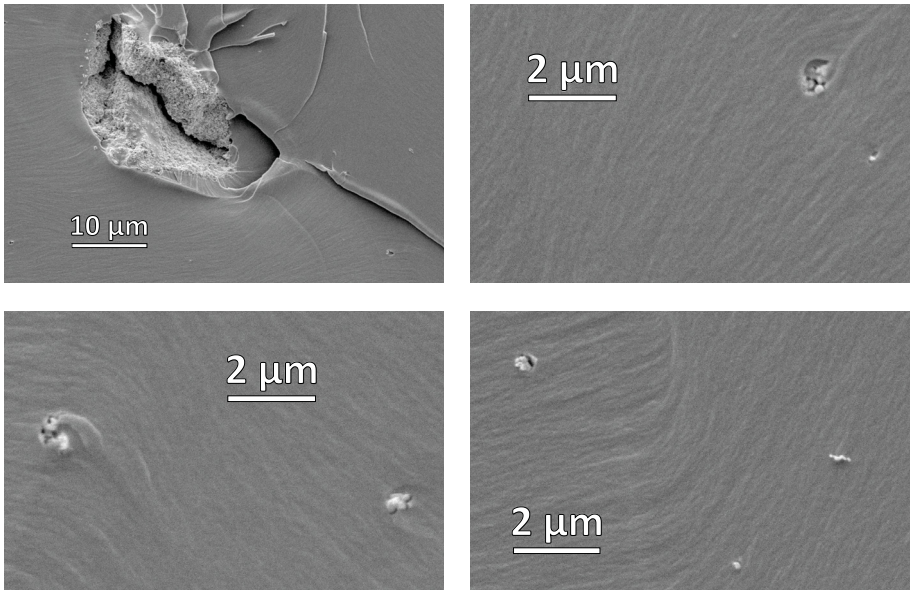

Figure 8.17: Fractographic images of sonicated EP/IF-WS_2

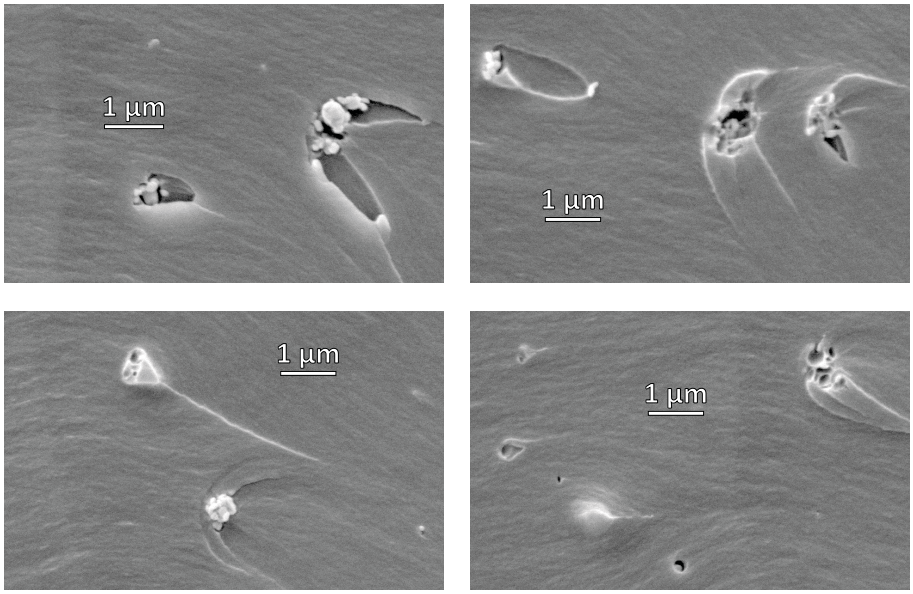

Figure 8.18: Fractographic images of EP/Ref-EtOH

matrix (fig. 8.19). In contrast, the fracture surface of EP/HTCS-1 seems to be much rougher, establishing multiple crack lines, and the less perfectly dispersed nanoparticles tend to adhere to the matrix (fig. 8.20). While this might explain the differences in the measured standard deviation, the effect on the mean fracture toughness is rather small.

Table 8.1: G_{Ic} and K_{Ic} of those n samples that were evaluated in this work and according to ISO 13586, respectively. The values in brackets give the respective sample standard deviation (e.g., 144.9(227) stands for 144.9 ± 22.7).

	this work			ISO 13586		
	G_{Ic} / (J/m^2)	K_{Ic} / (MPa$\sqrt{\text{m}}$)	n	G_{Ic} / (J/m^2)	K_{Ic} / (MPa$\sqrt{\text{m}}$)	n
neat epoxy 1	144.9(227)	0.698(57)	11	155.9(269)	0.731(71)	8
neat epoxy 2	139.1(163)	0.677(38)	18	145.9(179)	0.689(44)	7
IF-WS_2 sonicated	160.8(109)	0.742(25)	10	170.1(375)	0.753(52)	7
IF-WS_2 3RM	206.7(511)	0.791(96)	11	288.7	0.938	1
Ref-EtOH	213.3(313)	0.804(56)	11	216.8(344)	0.812(58)	8
Ref-$CHCl_3$	230.1(247)	0.858(55)	10	216.6(125)	0.824(33)	4
GTMS-1	217.1(301)	0.804(55)	10	196.1(276)	0.723(136)	10
GTMS-3	224.6(115)	0.834(19)	10	235.6(77)	0.851(9)	2
HTCS-1	206.3(278)	0.799(63)	10	202.0(231)	0.793(54)	4
HTCS-3	214.5(214)	0.827(38)	8	254.7(568)	0.903(100)	5
AATMS-1	206.9(245)	0.793(52)	11	201.1(248)	0.784(56)	8
AATMS-3	216.5(320)	0.826(73)	10	289.0(1063)	0.960(175)	2

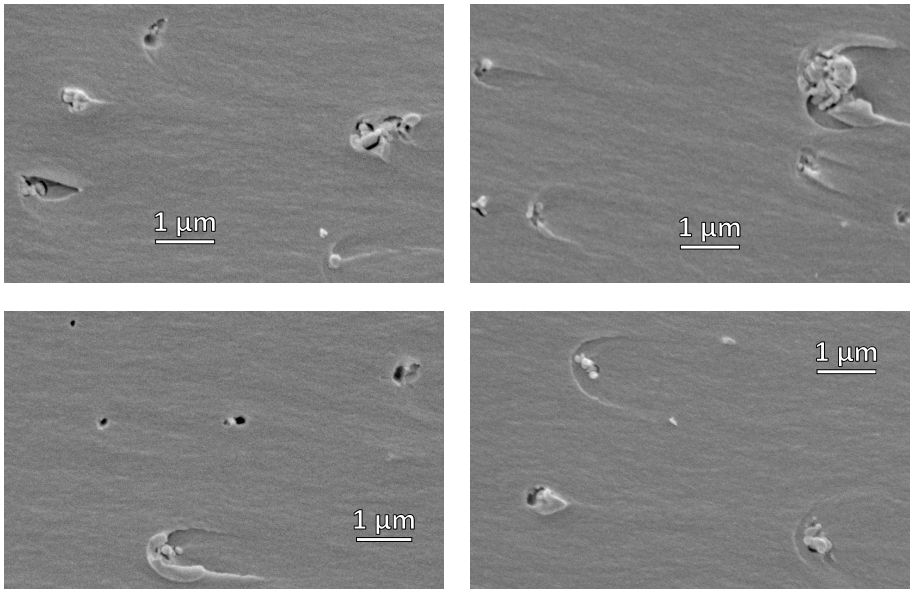

Figure 8.19: Fractographic images of EP/GTMS-3

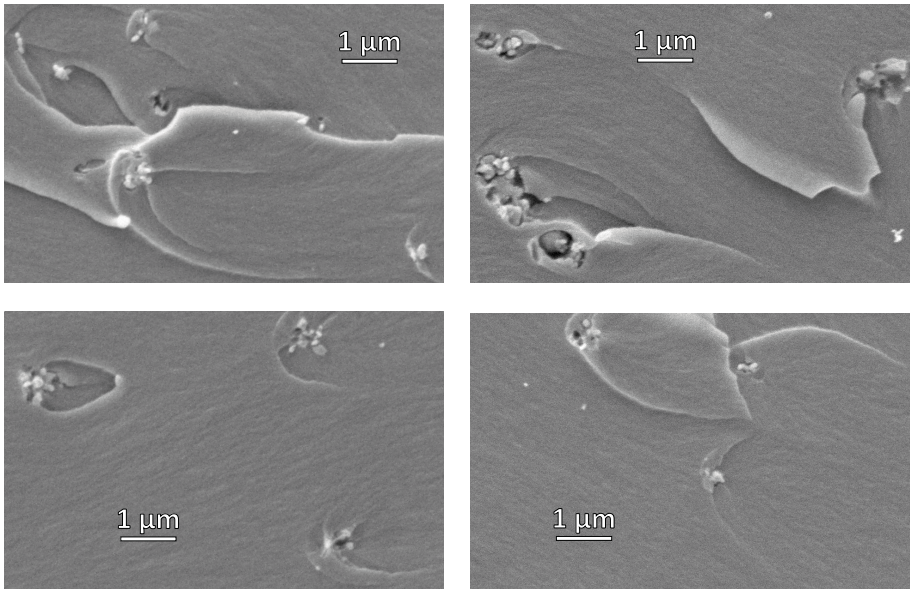

Figure 8.20: Fractographic images of EP/HTCS-1

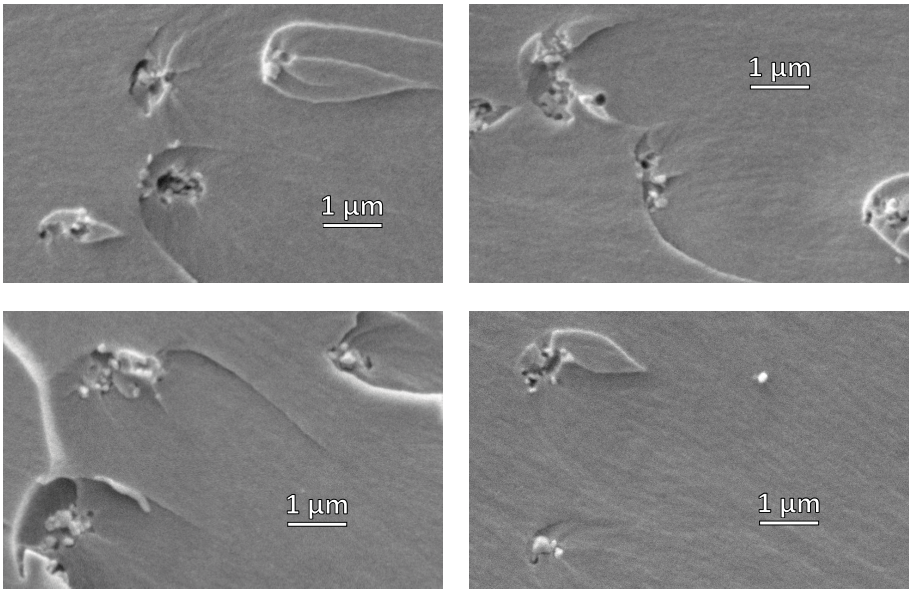

Figure 8.21: Fractographic images of EP/AATMS-1

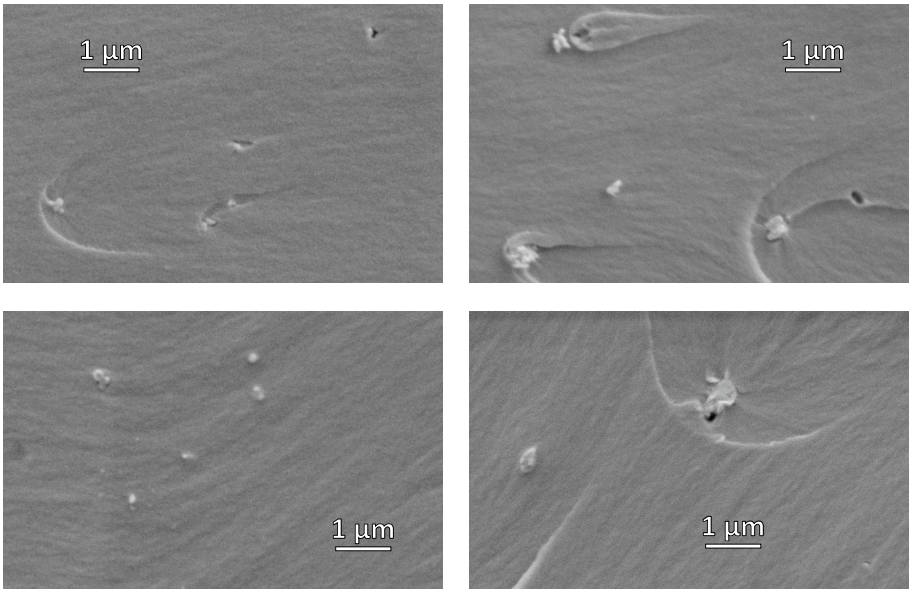

Figure 8.22: Fractographic images of EP/AATMS-3

8.3.7 Individual results of the fracture mechanics tests

According to the respective ISO standard, ISO 13586, the majority of the samples would have to be excluded, either because the average pre-crack length $\langle a_0 \rangle$ was not within 0.45 to 0.55 times the specimen width w, or because the difference between the longest part of the pre-crack along the pre-crack front, $\max(a_0)$, and its shortest part, $\min(a_0)$, was more than 10 % of $\min(a_0)$. However, as most measured values agreed very well with each other, only a few were actually excluded in the present work (mostly because of a split pre-crack). Table 8.1 lists the fracture toughness results used in this work compared to those one would obtain when evaluating strictly according to ISO 13586, and table 8.2 lists all individual samples' results. Generally, the average values agree quite well with each other, indicating that both evaluations are reasonable.

Table 8.2: Individual fracture mechanics test results. The initial pre-crack lengths at different positions are denominated with a_0 and the specimen width is denominated with w. The last two columns indicate which measurements were to be excluded according to ISO 13586, and which ones were excluded in the present work, respectively. A: Sample broken before measurement. B: Measurement rejected due to inadequate average pre-crack length. C: Measurement rejected due to slanted pre-crack. D: Other criteria of ISO 13586 not met. E: Measurement rejected due to split pre-crack.

Material sample	K_{Ic} / (MPa$\sqrt{\text{m}}$)	G_{Ic} / (J/m^2)	$\frac{\langle a_0 \rangle}{w}$	$\frac{\max(a_0)-\min(a_0)}{\min(a_0)}$	rejected ISO	rejected this work
neat epoxy 1						
1	0.796	176.3	0.54	4.3 %		
2	0.719	152.9	0.44	7.1 %	B	
3	0.659	128.4	0.64	9.2 %	B	
4	0.633	120.6	0.52	7.4 %		
5	0.631	119.8	0.48	10.3 %	C	
6	0.642	121.6	0.52	12.9 %	C	
7					A	A
8	0.785	178.8	0.51	5.4 %		
9	0.761	166.7	0.67	4.0 %	B	
10	0.759	170.3	0.51	6.8 %		
11	0.680	133.6	0.52	6.6 %		
12	0.709	156.5	0.61	5.5 %	B	
neat epoxy 2						
1	0.683	145.7	0.46	7.6 %		
2	0.687	152.0	0.69	12.6 %	B, C	
3	0.657	137.1	0.52	6.7 %		

Table 8.2: (continued) A: Sample broken before measurement. B: Measurement rejected due to inadequate average pre-crack length. C: Measurement rejected due to slanted pre-crack. D: Other criteria of ISO 13586 not met. E: Measurement rejected due to split pre-crack.

Material sample	K_{Ic} / (MPa$\sqrt{m}$)	G_{Ic} / (J/m^2)	$\frac{\langle a_0 \rangle}{w}$	$\frac{\max(a_0)-\min(a_0)}{\min(a_0)}$	rejected ISO	rejected this work
4	0.725	131.1	0.61	7.3 %	B	
5	0.653	157.8	0.53	5.2 %		
6	0.677	118.6	0.50	17.2 %	C	
7	0.721	139.2	0.51	4.0 %		
8	0.667	153.5	0.44	14.2 %	B, C	
9	0.655	135.3	0.60	5.2 %	B	
10	0.628	128.3	0.48	11.9 %	C	
11	0.643	116.2	0.60	7.1 %	B	
12	0.620	124.7	0.57	14.7 %	B, C	
13	0.620	114.3	0.49	4.1 %		
14	0.713	159.4	0.51	7.5 %		
15	0.666	129.7	0.43	11.7 %	B, C	
16	0.749	167.6	0.55	8.3 %		
17	0.723	153.5	0.50	12.2 %	C	
18	0.740	176.9	0.56	3.0 %	B	
IF-WS_2 sonicated						
1	0.753	159.4	0.52	1.9 %		
2	0.862	252.7	0.50	6.8 %		E
3	0.723	156.2	0.55	10.8 %	B, C	
4	0.781	178.8	0.41	6.8 %	B	
5	0.703	142.1	0.51	3.9 %		
6	0.713	146.4	0.52	9.5 %		
7	0.772	172.2	0.57	6.0 %	B	
8	0.754	166.4	0.46	2.2 %		
9	0.736	162.7	0.51	7.7 %		
10	0.881	233.5	0.67	4.6 %	B	B, E
11	0.732	162.9	0.55	6.2 %	B	
12	0.749	161.3	0.47	4.7 %		
IF-WS_2 3RM						
1	0.820	221.2	0.63	4.9 %	B	
2	0.757	170.7	0.57	24.8 %	B, C	
3	0.726	166.6	0.50	22.1 %	C	
4	0.934	279.2	0.44	5.5 %	B	
5	0.740	191.5	0.78	1.7 %	B	
6	0.705	161.4	0.67	1.0 %	B	
7	0.938	288.7	0.49	5.6 %		
8	0.885	265.6	0.51	12.7 %	C	
9					A	A
10	0.832	217.5	0.48	13.6 %	C	
11	0.677	157.4	0.63	9.6 %	B	
12	0.691	154.4	0.50	16.2 %	C	
Ref-EtOH						

Table 8.2: (continued) A: Sample broken before measurement. B: Measurement rejected due to inadequate average pre-crack length. C: Measurement rejected due to slanted pre-crack. D: Other criteria of ISO 13586 not met. E: Measurement rejected due to split pre-crack.

Material sample	K_{Ic} / (MPa$\sqrt{\text{m}}$)	G_{Ic} / (J/m^2)	$\frac{\langle a_0 \rangle}{w}$	$\frac{\max(a_0)-\min(a_0)}{\min(a_0)}$	rejected ISO	rejected this work
1	0.845	230.3	0.48	5.0 %		
2	0.811	207.0	0.54	7.8 %		
3	0.925	283.5	0.45	7.7 %		
4	0.736	189.7	0.56	8.8 %	B	
5					A	A
6	0.754	182.3	0.55	6.3 %		
7	0.763	183.4	0.50	16.9 %	C	
8	0.779	186.7	0.54	7.1 %		
9	0.795	208.5	0.58	11.0 %	C	
10	0.770	202.5	0.52	8.1 %		
11	0.867	247.1	0.61	13.0 %		
12	0.797	225.0	0.53	5.2 %		
Ref-$CHCl_3$						
1	0.942	281.8	0.44	3.8 %	B	
2	0.780	203.2	0.53	3.8 %		
3	0.835	219.6	0.47	6.5 %		
4	0.825	211.1	0.49	6.3 %		
5	0.781	199.3	0.66	6.2 %	B	
6	0.851	221.2	0.61	3.3 %	B	
7					A	A
8	0.899	241.0	0.61	3.8 %	B	
9	0.895	245.7	0.64	2.1 %	B	
10	0.858	232.5	0.48	7.2 %		
11	0.917	245.2	0.58	8.8 %	B	
12	0.959	290.2	0.74	1.3 %	D	E
GTMS-1						
1	0.930	284.9	0.61	8.7 %		
2					A	A
3	0.523	160.2	0.50	7.0 %		
4	0.775	216.0	0.75	4.6 %		
5					A	A
6	0.769	202.2	0.54	5.1 %		
7	0.826	227.1	0.47	8.2 %		
8	0.766	193.0	0.63	6.6 %		
9	0.780	201.2	0.62	8.5 %		
10	0.774	194.9	0.48	9.4 %		
11	0.797	223.4	0.60	3.4 %		
12	0.792	210.3	0.62	6.2 %		
GMTS-3						
1	0.835	219.9	0.67	3.0 %	B	
2	0.830	229.0	0.52	13.2 %	C	
3	0.837	231.6	0.47	10.5 %	C	

Table 8.2: (continued) A: Sample broken before measurement. B: Measurement rejected due to inadequate average pre-crack length. C: Measurement rejected due to slanted pre-crack. D: Other criteria of ISO 13586 not met. E: Measurement rejected due to split pre-crack.

Material sample	K_{Ic} / (MPa $\sqrt{m}$)	G_{Ic} / (J/m^2)	$\frac{\langle a_0 \rangle}{w}$	$\frac{\max(a_0)-\min(a_0)}{\min(a_0)}$	rejected ISO	rejected this work
4	0.810	213.8	0.41	5.0 %	B	
5	0.831	216.8	0.65	16.2 %	B, C	
6	0.858	241.1	0.53	6.5 %		
7	0.956	302.4	0.65	3.6 %	B	E
8					A	A
9	0.801	205.0	0.44	3.8 %	B	
10	0.864	239.3	0.54	13.3 %	C	
11	0.844	230.2	0.49	4.9 %		
12	0.831	219.4	0.49	10.1 %	C	
HTCS-1						
1	0.690	165.0	0.55	18.1 %	B, C	
2	0.821	209.0	0.57	12.7 %	B, C	
3	0.845	228.5	0.70	9.0 %	B	B, E
4	0.877	262.6	0.77	3.1 %	B	B, E
5	0.807	208.7	0.50	9.9 %		
6	0.846	238.2	0.67	12.8 %	B, C	
7	0.714	169.0	0.50	8.4 %		
8	0.812	207.5	0.50	7.6 %		
9	0.902	253.0	0.61	4.5 %	B	
10	0.839	222.8	0.47	4.4 %		
11	0.765	188.2	0.48	10.4 %	C	
12	0.797	201.7	0.57	7.3 %	B	
HTCS-3						
1	0.825	222.8	0.66	3.5 %	B	
2	1.055	342.0	0.48	9.4 %		E
3	0.793	194.3	0.54	7.0 %		
4	0.852	222.5	0.59	6.9 %	B	
5					A	A
6	0.881	236.1	0.50	8.3 %		
7	0.846	225.6	0.55	6.9 %		
8					A	A
9	0.851	237.2	0.65	6.8 %	B	
10	0.762	177.9	0.53	17.0 %	C	
11	0.808	199.9	0.53	12.1 %	C	
12	0.938	275.4	0.48	9.4 %		E
AATMS-1						
1	0.793	210.0	0.70	3.4 %	B	
2	0.856	246.3	0.53	5.8 %		
3	0.861	243.9	0.56	4.2 %	B	
4	0.734	185.5	0.51	5.4 %		
5	0.863	231.4	0.47	8.2 %		
6	0.751	192.7	0.46	6.8 %		

Table 8.2: (continued) A: Sample broken before measurement. B: Measurement rejected due to inadequate average pre-crack length. C: Measurement rejected due to slanted pre-crack. D: Other criteria of ISO 13586 not met. E: Measurement rejected due to split pre-crack.

Material sample	K_{Ic} / (MPa$\sqrt{\text{m}}$)	G_{Ic} / (J/m^2)	$\frac{\langle a_0 \rangle}{w}$	$\frac{\max(a_0)-\min(a_0)}{\min(a_0)}$	rejected ISO	rejected this work
7	0.797	214.1	0.61	9.9 %	B	
8	0.744	182.3	0.52	3.9 %		
9	0.824	204.0	0.53	4.5 %		
10	0.727	182.0	0.53	6.6 %		
11	0.770	184.1	0.53	9.3 %		
12	0.673	149.3	0.68	12.5 %	B, C	B, C
AATMS-3						
1	0.710	257.9	0.56	6.2 %	B	
2	0.830	182.0	0.53	15.9 %	C	
3	0.729	174.4	0.52	10.2 %	C	
4	0.802	198.8	0.69	6.0 %	B	
5	1.084	364.2	0.45	3.8 %		
6					A	A
7	0.897	249.9	0.66	6.8 %	B	
8	0.812	203.4	0.44	6.3 %	B	
9	0.915	259.3	0.63	7.8 %	B	
10	0.955	286.3	0.76	6.9 %	B	B, E
11	0.837	213.9	0.54	5.1 %		
12	0.823	208.8	0.47	17.2 %	C	

References

[1] M. Shneider, H. Dodiuk, R. Tenne, and S. Kenig, "Nanoinduced morphology and enhanced properties of epoxy containing tungsten disulfide nanoparticles", *Polym. Eng. Sci.*, vol. 53, no. 12, pp. 2624–2632, 2013. DOI: 10.1002/pen.23517.

[2] A. Buchman, H. Dodiuk-Kenig, A. Dotan, R. Tenne, and S. Kenig, "Toughening of epoxy adhesives by nanoparticles", *J. Adhes. Sci. Technol.*, vol. 23, no. 5, pp. 753–768, 2009. DOI: 10.1163/156856108X379209.

[3] M. Redlich, A. Katz, L. Rapoport, *et al.*, "Improved orthodontic stainless steel wires coated with inorganic fullerene-like nanoparticles of WS_2 impregnated in electroless nickel-phosphorous film", *Dent. Mater.*, vol. 24, no. 12, pp. 1640–1646, 2008.

[4] B. Mailhot, S. Morlat-Thérias, M. Ouahioune, and J.-L. Gardette, "Study of the degradation of an epoxy/amine resin, 1", *Macromol. Chem. Phys.*, vol. 206, no. 5, pp. 575–584, 2005. DOI: 10.1002/macp.200400395.

[5] E. B. Flint and K. S. Suslick, "The temperature of cavitation", *Science*, vol. 253, no. 5026, pp. 1397–1399, 1991. DOI: 10.1126/science.253.5026.1397.

[6] T. H. Hsieh, A. J. Kinloch, K. Masania, A. C. Taylor, and S. Sprenger, "The mechanisms and mechanics of the toughening of epoxy polymers modified with silica nanoparticles", *Polymer*, vol. 51, no. 26, pp. 6284–6294, 2010. DOI: 10.1016/j.polymer.2010.10.048.

8.4 Supporting Information for Publication 4

8.4.1 Crystal structure of flaky WS_2

The crystal structure of the flaky WS_2 was determined by X-ray diffraction (XRD). The powder diffraction patterns were obtained using a *PANalytical X'Pert PRO* system equipped with a Cu tube, a Johannson monochromator (Cu–$K_{\alpha 1}$, 154.06 pm) and an *X'Celerator* linear detector operating in Bragg–Brentano geometry ($\theta/2\theta$). The diffraction patterns were recorded between 5° and 120° with a step size of 0.016° (2θ) and a scan speed of 0.3 °/min.

Fig. 8.23 shows the diffraction pattern of the flaky WS_2 together with a calculated diffraction pattern based on the structural data presented elsewhere [1–3]. This pattern suggests that the powder consists mainly of WS_2 with the crystal structures $P6_3/mmc$ and $R\bar{3}m$, in similar quantities. The unit cells of these WS_2 polytypes are usually denoted by 2H (hexagonal) and 3R (rhombohedral), respectively. Besides these structures, there are signals that can be assigned to WO_3 and SO_2, which seems reasonable, given that traces of these molecules have been reported earlier on the surfaces of IF-WS_2 NPs as well [4].

8.4.2 Estimation of the cross-link density

For estimating the cross-link density, we define a cross-link in a thermosetting polymer as an atom that is connected to the molecular network by three or more covalent bonds. In a sub-stoichiometric system ($\lambda < 1$), nearly every primary and secondary amine group can be expected to react with an epoxide group. Assuming that all amine groups in T403 are primary amines, every T403 molecule would thus react six times with a DGEBA molecule. If each of these connected to the molecular network, this would mean that all three amine groups in T403 would form one cross-link and the central methanetriyl group in T403 would form one cross-link.

However, if some of the DGEBA molecules react only once, the amine groups they bond to have only two connections to the molecular network and thus do not form a cross-link. Every DGEBA molecule is expected to react at least once as unreacted

molecules are much more mobile than those that have already reacted once (this assumption can be made only for $\lambda \gg 0.5$).

In order to facilitate the calculation, every amine group is expected to react with at least one DGEBA molecule that reacts twice. If an amine group reacted with two DGEBA molecules that both do not react a second time, then the methanetriyl group of the molecule it belongs to would not form a cross-link either. However, for each such amine group, another amine group would react with two DGEBA molecules that would both react twice so that this amine group does form an additional cross-link. Consequently, this assumption does not affect the number of cross-links calculated in total.

For n_{EP} epoxide groups, there are only $n_{\mathrm{NH2}} = \lambda \cdot n_{\mathrm{EP}}/2$ amine groups available, so that $(1-\lambda) \cdot n_{\mathrm{EP}}$ DGEBA molecules react only once and thus, that many amine groups do not form cross-links. Hence, n_{NH2} amine groups form $n_{\mathrm{NH2}} - (1-\lambda) \cdot n_{\mathrm{EP}} = n_{\mathrm{NH2}} \cdot (3 - 2/\lambda)$ cross-links in addition to the $n_{\mathrm{NH2}}/3$ cross-links in the curing agent's central methanetriyl group, so $n_{\mathrm{NH2}} \cdot (10/3 - 2/\lambda)$ cross-links in total.

The mass of epoxy resin per amount of epoxide groups (usually called *epoxy equivalent weight, EEW*) is M_{EP} and the mass of curing agent per amount of amine groups is $M_{\mathrm{NH2}} = 2 \cdot AHEW$, where *AHEW* is the curing agent's *amine hydrogen equivalent weight*. Therefore, a mixture with n_{NH2} amine groups consists of curing agent of the mass $n_{\mathrm{NH2}} \cdot M_{\mathrm{NH2}}$ and epoxy resin of the mass $n_{\mathrm{EP}} \cdot M_{\mathrm{EP}} = 2/\lambda \cdot n_{\mathrm{NH2}} \cdot M_{\mathrm{EP}}$, so its total mass is $n_{\mathrm{NH2}} \cdot (M_{\mathrm{NH2}} + 2/\lambda \cdot M_{\mathrm{EP}})$. The mixture's mass per cross-link M_{c} can hence be estimated to be

$$M_{\mathrm{c}}(\lambda) = \frac{6M_{\mathrm{EP}} + 3\lambda \cdot M_{\mathrm{NH2}}}{10\lambda - 6} \tag{8.16}$$

8.4.3 Background to DQ NMR measurements and their evaluation

In highly mobile media such as polymer melts or dilute polymer solutions, the chain dynamic order parameter S is close to zero in a large time scale due to the isotropic nature of motion. However, cross-links in networks (or other constraints in other systems) introduce an anisotropic character, especially at longer times, since chain

segments have a restricted conformational space. This results in a non-zero value of S and the value itself which depends on the extent of this anisotropicity and the resulting persistent orientation. A global dynamic order parameter of all the segments would then be a measure of the extent of constraints (e.g., of cross-links in networks), provided that the anisotropicity is induced only by these constraints and other factors remain the same.

^{1}H dipole–dipole coupling is also directly proportional to the orientation-dependence of the inter-nuclear vector of the interaction spins with the magnetic field. Practically, structural averaging due to multiple segments, and time-averaging due to fast segmental motions result in an averaged residual dipolar coupling D_{res}, which can be exclusively accessed by DQ NMR. In chemically simple monomers, i.e., assuming a homogeneous spin system, D_{res} can be used as a reliable probe to study the dynamic order parameter, i.e., the amount of motional restrictions like cross-links.

While different methods exist for determining D_{res}, DQ NMR [5] and relaxometry [6] are the most frequently used methods. Among the two, the unique advantage of DQ NMR is the ability to excite two different time-dependent signal functions and subsequent manipulation resulting in delineating structural effects from dynamic effects, resulting in a model-free approach to study the structure. The two signal functions are (i) the DQ build-up curve[1] $S_{\mathrm{DQ}}(\tau)$, which contains signals from coupled spins embedding D_{res} and decay contributions related to multiple quantum coherences at longer times (given in fig. 8.24 as $\triangle$), and (ii) the decaying curve S_{ref} (given in fig. 8.24 as $\square$) containing higher order contributions as well as contributions from uncoupled mobile spins such as defects.

In the absence of contributions from non-coupled spins which are dynamic in nature, a normalized curve S_{nDQ} exclusively embedding DQ coherences (i.e., D_{res}) can be obtained from (8.17).

[1] Although MQ coherences do contribute at longer times, their contribution is negligible at short times so that the signal is dominated by DQ coherences.

$$S_{\mathrm{nDQ}} = \frac{S_{\mathrm{DQ}}}{S_{\mathrm{DQ}} + S_{\mathrm{ref}}} \equiv \frac{S_{\mathrm{DQ}}}{S_{\Sigma\mathrm{MQ}}} \tag{8.17}$$

Such a normalized curve reaches an overall intensity of 0.5 in the long-time limit, however fails to do so in presence of relaxation contributions due to motion. Such contributions can be easily identified from the log-time tail in a semi-log plot of $S_{\Sigma\mathrm{MQ}}$ over the DQ excitation time τ_{DQ} and fitted to a single exponential $S_{\mathrm{defect,1}} = A \cdot \exp(-2\tau_{\mathrm{DQ}}/T_{2,\mathrm{A}})$, which can then be subtracted from $S_{\Sigma\mathrm{MQ}}$ to get S_{nDQ} as follows:

$$S_{\mathrm{nDQ}} = \frac{S_{\mathrm{DQ}}}{S_{\Sigma\mathrm{MQ}} - S_{\mathrm{defect}}} \tag{8.18}$$

In cases where S_{nDQ} still does not reach 0.5 in the long time limit, a second defect contribution can easily be identified from the tail of the signal ($S_{\mathrm{DQ}} - S_{\mathrm{ref}} - S_{\mathrm{ref}} \equiv S_{\mathrm{diff}} - S_{\mathrm{defect}}$) and can be fitted similarly to get $S_{\mathrm{defect,2}} = B \cdot \exp(-2\tau_{\mathrm{DQ}}/T_{2,\mathrm{B}})$. S_{nDQ} can then be similarly obtained by

$$S_{\mathrm{nDQ}} = \frac{S_{\mathrm{DQ}}}{S_{\Sigma\mathrm{MQ}} - S_{\mathrm{defect,1}} - S_{\mathrm{defect,2}}} \tag{8.19}$$

The total defect fraction is given by the sum of A and B.

The obtained normalized DQ build-up curves are fitted using an appropriate function to derive D_{res}, where any *a priori* information on the system can be taken into account. Thermosets such as epoxy are formed from nearly monodisperse molecules, thus cross-linking does not introduce much heterogeneity. However, the differences in mobility of the two molecules namely DGEBA and T403 can be reflected as distinct D_{res} specially at high temperatures where thermal effects on dynamics can become more pronounced. This can be seen in the work of Martin-Gallego *et al.* [7] where a broad distribution is seen at lower temperatures while two distinct modes are seen at higher temperatures.

A simple (inverted) Gaussian build-up of DQ coherences [8] was assumed and the best fit was seen for the two-component Gaussian build-up given in (8.20), as is shown in fig. 8.25.

$$S_{\mathrm{nDQ}}(D_{\mathrm{res},1}, D_{\mathrm{res},2}, f) = 0.5\, f \cdot \left[1 - \exp\left(-\frac{2}{5} D_{\mathrm{res},1}^2 \tau_{\mathrm{DQ}}^2\right)\right] + 0.5\,(1-f) \cdot \left[1 - \exp\left(-\frac{2}{5} D_{\mathrm{res},2}^2 \tau_{\mathrm{DQ}}^2\right)\right] \tag{8.20}$$

Such bimodal fits were previously used in highly homogeneous but strongly bimodal end-linked PDMS elastomers [5] and filled elastomers [9]. This heterogeneity arising from a single network chain has been identified earlier [7] but not noted. This can also be supported by a nearly constant fraction of the two components irrespective of the stoichiometry.

8.4.4 Fracture toughness results

Table 8.3 lists the fracture mechanics results of the neat epoxy samples that were only partly given in the main article.

As mentioned in the main article, the pre-cracks of most SENB samples did not fulfill the recommendations of the ISO 13586 with regards to their length or symmetry: ISO 13586 recommends to discard a result if the average length a_0 of the pre-crack of the measured sample is shorter than $0.45b$ or longer than $0.55b$, where b is the sample's width, or if the difference between the shortest and the longest part of the pre-crack is more than 10 % of a_0 [10]. However, these recommendations were ignored as more than two thirds of the results would have to be excluded. Instead, results were discarded only if they were clear outliers.

For the sake of completeness, table 8.4 lists the fracture toughness results presented in the main article, without excluding any outliers (*all samples*) as well as after excluding all results as recommended in ISO 13586, respectively. Furthermore, it gives the number of samples n that were measured in total, that were evaluated for the main article and that fulfilled the recommendations of the ISO 13586, respectively. While the mean values are always comparable, the standard deviation depends strongly on which results are evaluated.

Table 8.3: Fracture toughness results of neat epoxy

W_{T403}	K_{Ic} / (MPa $\sqrt{m}$)	G_{Ic} / (J/m^2)
38 phr	0.598 ± 0.058	119.6 ± 14.7
38 phr	0.703 ± 0.137	176.4 ± 69.5
40 phr	0.682 ± 0.049	140.8 ± 21.3
40 phr	0.752 ± 0.054	178.8 ± 36.8
42 phr	0.938 ± 0.082	410.1 ± 65.4
42 phr	0.990 ± 0.069	313.4 ± 49.8
42 phr	0.927 ± 0.054	283.1 ± 36.2
44 phr	1.458 ± 0.037	753.2 ± 30.0
44 phr	1.447 ± 0.024	758.2 ± 26.9
44 phr*	1.500 ± 0.027	799.4 ± 18.9
46 phr	1.486 ± 0.034	792.2 ± 33.7

* DGEBA passed through the 3RM five times

8.4.5 Additional fractographic images

Figures 8.26, 8.27, 8.28 and 8.29 show additional fractographic images to support the conclusions in the main article. Flaky WS_2 exhibits significantly larger agglomerates than IF-WS_2 and results in more numerous and more distant crack lines.

References

[1] W. J. Schutte, J. L. De Boer, and F. Jellinek, "Crystal structures of tungsten disulfide and diselenide", *J. Solid State Chem.*, vol. 70, no. 2, pp. 207–209, 1987. DOI: 10.1016/0022-4596(87)90057-0.

[2] P. M. Woodward, S. A. W., and V. T., "Structure refinement of triclinic tungsten trioxide", *J. Phys. Chem. Solids*, vol. 56, no. 10, pp. 1305–1315, 1995. DOI: 10.1016/0022-3697(95)00063-1.

[3] B. Post, R. S. Schwarz, and I. Fankuchen, "The crystal structure of sulfur dioxide", *Acta Cryst.*, vol. 5, pp. 372–374, 1952. DOI: 10.1107/S0365110X5200109X.

Table 8.4: Fracture toughness results of all measurements (no outliers excluded) and for those that fulfilled the recommendations of ISO 13586 only. Column n lists how many samples were measured in total, evaluated for the present work, and fulfilled the requirements of ISO 13586, respectively. The values in brackets give the respective sample standard deviation (e.g., 119.6(147) stands for 119.6 ± 14.7).

		all samples		ISO 13586		
w_{NP}	W_{T403}	K_{Ic} / (MPa $\sqrt{m}$)	G_{Ic} / (J/m^2)	K_{Ic} / (MPa $\sqrt{m}$)	G_{Ic} / (J/m^2)	n
0 %	38 phr	0.598(58)	119.6(147)	0.663(37)	138.5(5)	12-12-2
0 %	38 phr	0.703(137)	176.4(695)	0.762(169)	208.0(872)	12-12-6
0 %	40 phr	0.682(49)	140.8(213)	0.691(55)	140.2(259)	17-17-5
0 %	40 phr	0.752(54)	178.8(368)	0.775(21)	190.8(153)	11-11-3
0 %	42 phr	0.938(82)	410.1(654)	0.976(7)	411.7(665)	12-12-3
0 %	42 phr	0.990(69)	313.4(498)	0.982(78)	306.0(544)	12-12-3
0 %	42 phr	0.927(54)	283.1(362)	0.913(24)	269.7(96)	10-10-3
0 %	44 phr	1.458(37)	753.2(300)	1.473(34)	773.6(259)	12-12-5
0 %	44 phr	1.430(59)	740.7(608)	1.444(27)	760.8(321)	10-9-3
0 %*	44 phr	1.472(98)	769.8(996)	1.496(34)	796.0(189)	11-10-5
0 %	46 phr	1.443(79)	763.4(586)	1.486(27)	785.7(268)	11-11-3
flaky WS_2						
0.25 %	38 phr	0.686(101)	150.7(374)	0.660(155)	143.5(302)	12-10-3
0.50 %	38 phr	0.756(52)	167.2(236)	0.774(2)	180.3(117)	12-12-3
1.00 %	38 phr	0.782(57)	183.8(266)	0.892	240.7	12-12-1
0.25 %	40 phr	0.623(297)	157.7(797)	0.781(73)	199.6(356)	10-10-3
0.50 %	40 phr	0.745(82)	177.5(392)	0.775(51)	202.3(312)	12-12-3
1.00 %	40 phr	0.737(56)	198.5(276)	0.704(30)	174.6(145)	12-12-3
0.25 %	42 phr	1.067(114)	378.0(871)	1.110(125)	386.9(935)	12-12-4
0.50 %	42 phr	0.931(318)	332.5(1352)	1.065(81)	389.5(607)	11-11-2
1.00 %	42 phr	0.905(437)	322.0(1686)	1.121(42)	402.6(561)	10-10-3
0.25 %	44 phr	1.478(42)	785.9(393)	1.505(25)	809.3(164)	12-12-4
0.50 %	44 phr	1.433(118)	647.7(710)	1.305	541.8	12-11-1
1.00 %	44 phr	1.410(68)	708.2(840)	1.464(9)	757.9(249)	12-12-3
IF-WS_2						
0.25 %	38 phr	0.673(48)	142.0(195)	0.698(39)	156.6(132)	11-11-4
0.50 %	38 phr	0.696(58)	143.8(205)	0.755(39)	166.4(200)	11-11-2
0.25 %	40 phr	0.733(53)	167.9(197)	0.762(17)	177.0(117)	12-12-2
0.50 %	40 phr	0.815(95)	198.1(310)	0.784(36)	186.3(193)	12-12-4
0.25 %	42 phr	0.974(58)	306.8(400)	0.975(57)	308.5(418)	12-12-5
0.50 %	42 phr	0.984(154)	354.2(1194)	0.904(57)	293.1(500)	10-9-3
0.25 %	44 phr	1.415(56)	780.9(655)	1.479(41)	858.4(266)	11-11-2
0.50 %	44 phr	1.420(76)	755.5(695)	1.451(33)	771.2(458)	12-12-5

* DGEBA passed through the 3RM five times

[4] D. Haba, T. Grießer, U. Müller, and A. J. Brunner, "Critical investigation of the silane surface functionalization of fullerene-like WS_2", *J. Mater. Sci.*, vol. 50, no. 15, pp. 5125–5135, 2015. DOI: 10.1007/s10853-015-9039-4.

[5] K. Saalwächter, P. Ziegler, O. Spyckerelle, *et al.*, "^{1}H multiple-quantum nuclear magnetic resonance investigations of molecular order distributions in poly(dimethylsiloxane) networks: Evidence for a linear mixing law in bimodal systems", *J. Chem. Phys.*, vol. 119, no. 6, pp. 3468–3482, 2003.

[6] P. Sotta, C. Fülber, D. E. Demco, B. Blümich, and H. W. Spiess, "Effect of residual dipolar interactions on the NMR relaxation in cross-linked elastomers", *Macromolecules*, vol. 29, no. 19, pp. 6222–6230, 1996. DOI: 10.1021/ma960141e.

[7] M. Martin-Gallego, A. González-Jiménez, R. Verdejo, M. A. Lopez-Manchado, and J. L. Valentín, "Epoxy resin curing reaction studied by proton multiple-quantum NMR", *J. Polym. Sci., Part B: Polym. Phys.*, vol. 53, no. 18, pp. 1324–1332, 2015. DOI: 10.1002/polb.23767.

[8] K. Saalwächter, "Proton multiple-quantum NMR for the study of chain dynamics and structural constraints in polymeric soft materials", *Prog. Nucl. Magn. Reson. Spectrosc.*, vol. 51, no. 1, pp. 1–35, 2007. DOI: 10.1016/j.pnmrs.2007.01.001.

[9] R. S. Maxwell, S. C. Chinn, D. Solyom, and R. Cohenour, "Radiation-induced cross-linking in a silica-filled silicone elastomer as investigated by multiple quantum ^{1}h NMR", *Macromolecules*, vol. 38, no. 16, pp. 7026–7032, 2005. DOI: 10.1021/ma047625s.

[10] "ISO 13586:2000(E). plastics – determination of fracture toughness (G_{IC} and K_{IC}) – linear elastic fracture mechanics (LEFM) approach", International Organization for Standardization, Geneva, CH, Standard, Mar. 2000.

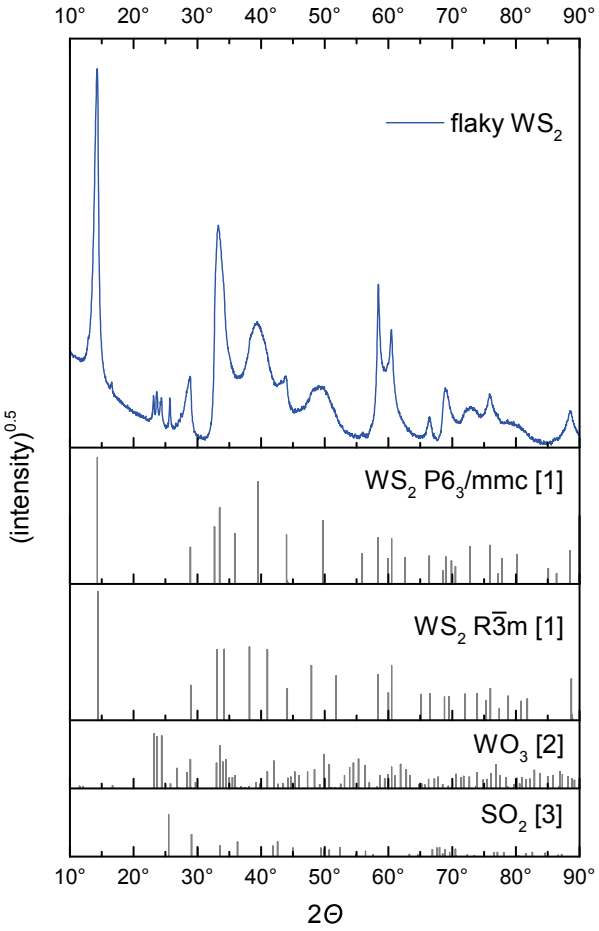

Figure 8.23: XRD spectrum of the flaky WS_2 and of reference materials [1–3]

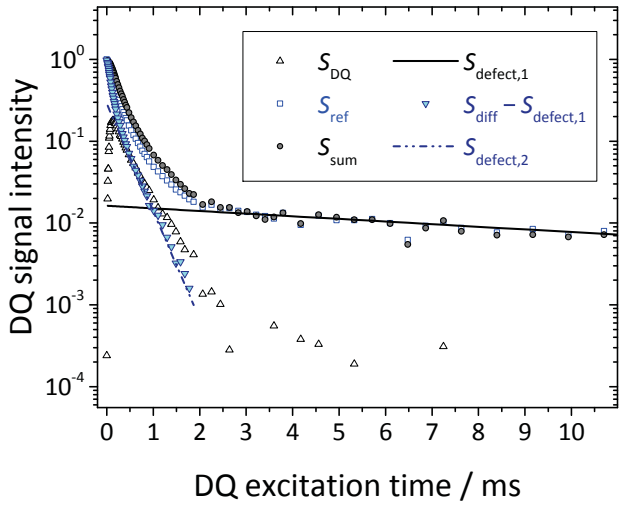

Figure 8.24: Evaluation steps for DQ NMR data using the data of neat epoxy made with $38\,\mathrm{phr}$ T403. The long-time tail of $S_{\mathrm{sum}} = S_{\mathrm{ref}} + S_{\mathrm{DQ}}$ is fitted by the mono-exponential function $S_{\mathrm{defect},1}$. Subsequently, $S_{\mathrm{diff}} = S_{\mathrm{ref}} - S_{\mathrm{DQ}}$ is subtracted by $S_{\mathrm{defect},1}$ and the tail of the result is fitted by $S_{\mathrm{defect},2}$.

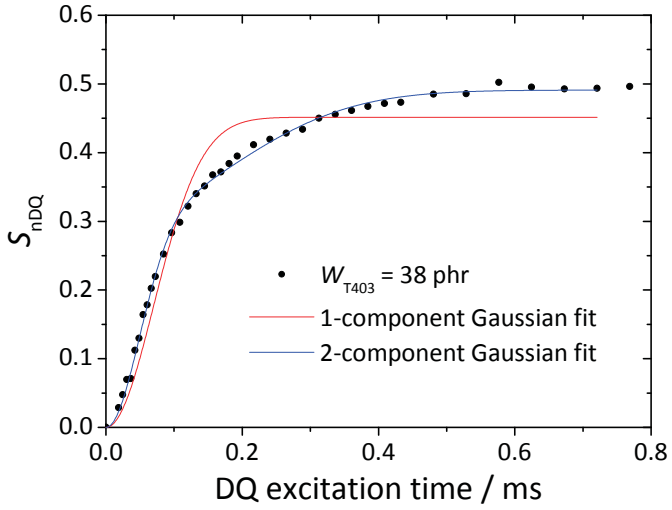

Figure 8.25: The normalized DQ curve $S_{\mathrm{nDQ}} = S_{\mathrm{DQ}}/(S_{\mathrm{sum}} - S_{\mathrm{defect}})$ can be fitted much better by the bimodal Gaussian model (8.20) than by a mono-functional Gaussian model

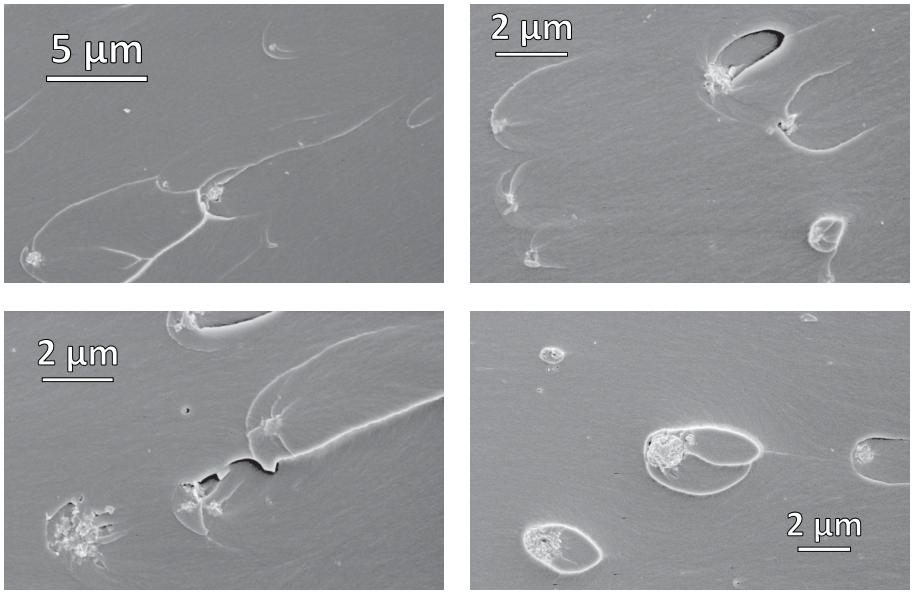

Figure 8.26: SEM images of the fracture surfaces for $w_{\text{flaky}} = 1.00\,\%$ and $W_{\text{T403}} = 40\,\text{phr}$

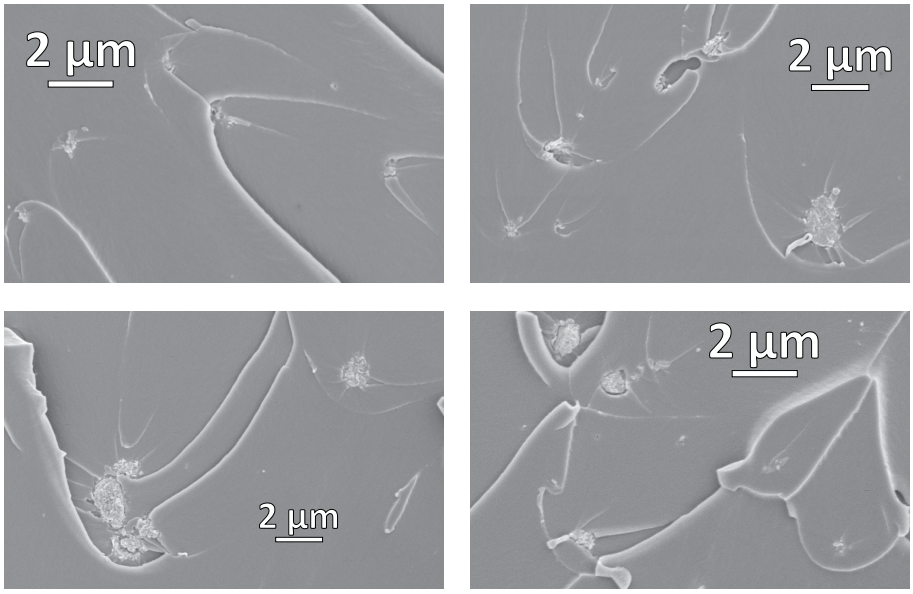

Figure 8.27: SEM images of the fracture surfaces for $w_{\text{flaky}} = 1.00\,\%$ and $W_{\text{T403}} = 44\,\text{phr}$

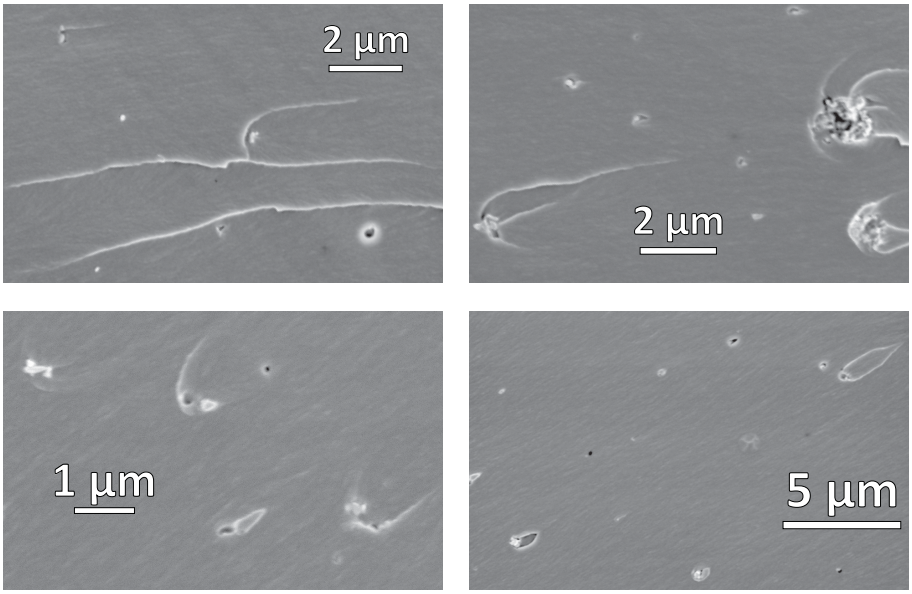

Figure 8.28: SEM images of the fracture surfaces for $w_{\mathrm{IF}} = 0.50\,\%$ and $W_{\mathrm{T403}} = 40\,\mathrm{phr}$

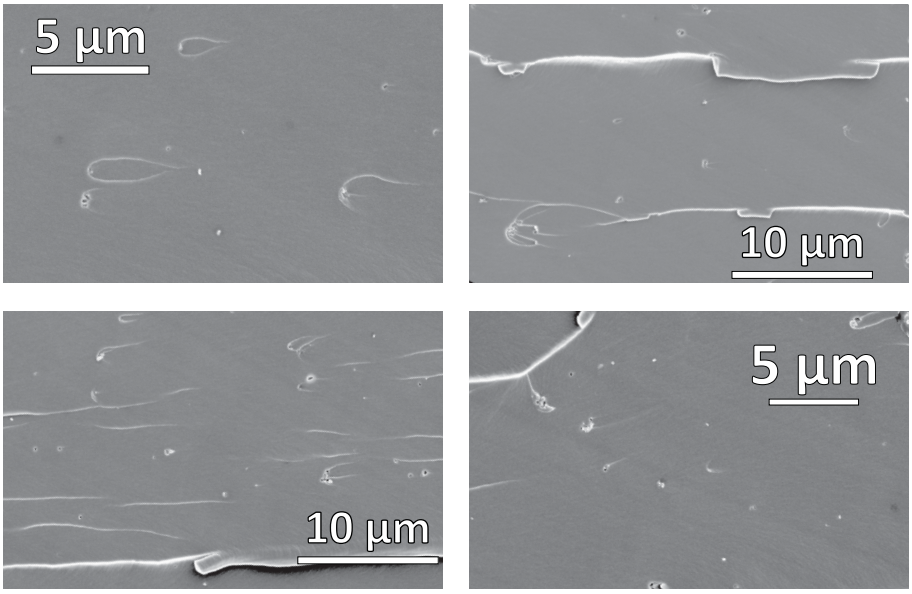

Figure 8.29: SEM images of the fracture surfaces for $w_{\mathrm{IF}} = 0.50\,\%$ and $W_{\mathrm{T403}} = 44\,\mathrm{phr}$

8.5 Supporting Information for Publication 5

8.5.1 Estimation of the cross-link density

The cross-link density will be estimated similarly to how it was done elsewhere [1]: We define a cross-link in a thermosetting polymer as an atom that is connected to the molecular network by three or more covalent bonds individually. We will assume that every anhydride group or single amine hydrogen will react with an epoxide group. As in the main article, the ratio of the amount of amine hydrogen atoms n_{aH} to the amount of epoxide groups n_{EP} will be described with $\lambda = n_{\mathrm{aH}}/n_{\mathrm{EP}}$. The structures of the molecules are given in fig. 8.30.

MTHPA

The anhydride system is the easiest system to investigate as only the stoichiometric case must be considered. Under the mentioned assumptions, every epoxide group would react twice, forming a cross-link. An epoxy resin with n_{EP} epoxide groups has a mass of $m_{\mathrm{EP}} = n_{\mathrm{EP}} \cdot M_{\mathrm{EP}}$, where M_{EP} is its mass per amount of epoxide groups (also known as the epoxy equivalent weight, EEW). If a stoichiometric quantity of anhydride curing agent is added, the amount of anhydride groups n_{anh} must be equal to n_{EP}, so that the mass of this curing agent must be $m_{\mathrm{anh}} = n_{\mathrm{anh}} \cdot M_{\mathrm{anh}} = n_{\mathrm{EP}} \cdot M_{\mathrm{anh}}$, where M_{anh} is its *anhydride equivalent weight*. The molecular mass per cross-link of the anhydride system can thus be estimated to be

$$M_{\mathrm{c}} = \frac{m_{\mathrm{EP}} + m_{\mathrm{anh}}}{n_{\mathrm{EP}}} = M_{\mathrm{EP}} + M_{\mathrm{anh}} \tag{8.21}$$

Amine curing agents

In contrast, the amine groups are what form the cross-links in amine-cured epoxy. Under the stated assumptions, every DETA molecule would form three cross-links, every D230 molecule would form two cross-links and every T403 molecule would

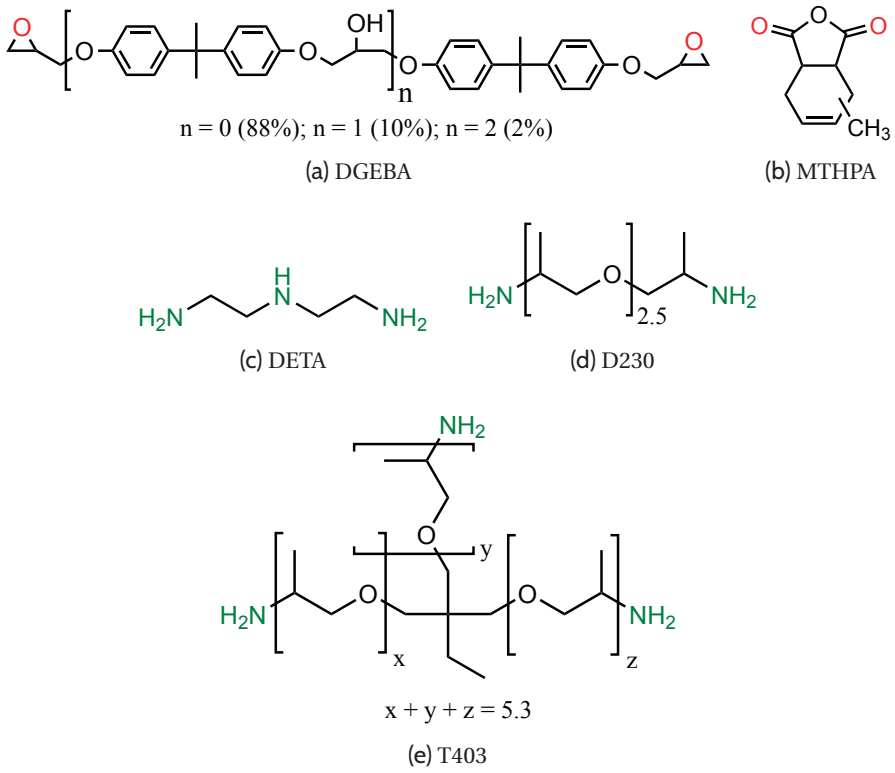

Figure 8.30: Molecular structures of the DGEBA epoxy resin and the four used curing agents

form three cross-links in addition to the one cross-link it already has in form of its central methanetriyl group.

However, if some of the DGEBA molecules react only once (as is the case for $\lambda < 1$), the amine groups they bond to have only two connections to the molecular network and thus do not form a cross-link. Every DGEBA molecule is expected to react at least once as unreacted molecules are much more mobile than those that have already reacted once (this assumption can be made only for $\lambda \gg 0.5$). In order to facilitate

the model, every amine group is expected to react with at least one DGEBA molecule that reacts twice[1].

DETA In the case of DETA, the amount of amine groups is $n_{\text{amine}} = 3/5 \cdot n_{\text{aH}} = 3/5 \cdot \lambda \cdot n_{\text{EP}}$, so that $(1-\lambda) \cdot n_{\text{EP}}$ DGEBA molecules react only once and thus, that many amine groups do not form cross-links. Hence, n_{amine} amine groups form $n_{\text{c}} = n_{\text{amine}} - (1-\lambda) \cdot n_{\text{EP}} = n_{\text{amine}} \cdot [8/3 - 5/(3\lambda)]$ cross-links.

DETA has a molecular mass M_{DETA}, so that its mass per amount of amine groups is $M_{\text{amine}} = M_{\text{DETA}}/3$. A mixture of DGEBA and DETA with n_{amine} amine groups contains DETA with a mass of $m_{\text{DETA}} = n_{\text{amine}} \cdot M_{\text{amine}} = n_{\text{amine}} \cdot M_{\text{DETA}}/3$ and DGEBA with a mass of $m_{\text{EP}} = n_{\text{EP}} \cdot M_{\text{EP}} = 5/(3\lambda) \cdot n_{\text{amine}} \cdot M_{\text{EP}}$, so that the total mass of the mixture is $m_{\text{total}} = m_{\text{EP}} + m_{\text{amine}} = n_{\text{amine}} \cdot (5/(3\lambda) \cdot M_{\text{EP}} + M_{\text{DETA}}/3)$. Consequently, the mass of the mixture per cross-link is:

$$M_{\text{c,DETA}}(\lambda) = \frac{m_{\text{total}}}{n_{\text{c}}} = \frac{n_{\text{amine}} \cdot (5/(3\lambda) \cdot M_{\text{EP}} + M_{\text{DETA}}/3)}{n_{\text{amine}} \cdot [8/3 - 5/(3\lambda)]} = \frac{5M_{\text{EP}} + \lambda \cdot M_{\text{DETA}}}{8\lambda - 5} \tag{8.22}$$

Polyetheramine curing agents The cross-link density of the PEA-cured epoxies can be calculated in a similar way as that of the DETA-cured epoxies (described in section 8.5.1), but the amount of amine groups is now $n_{\text{amine}} = 1/2 \cdot n_{\text{aH}} = 1/2 \cdot \lambda \cdot n_{\text{EP}}$. Hence, n_{amine} amine groups form $n_{\text{amine}} - (1-\lambda) \cdot n_{\text{EP}} = n_{\text{amine}} \cdot (3 - 2/\lambda)$ cross-links. In the case of T403, additional $n_{\text{amine}}/3$ cross-links are formed due to its central methanetriyl group (cf. fig. 8.30e), making $n_{\text{amine}} \cdot (10/3 - 2/\lambda)$ cross-links in total for T403.

As the PEA curing agents are not as pure as DETA is, we will use their *amine hydrogen equivalent weights* (*AHEW*) instead of their molecular masses for the further considerations: $M_{\text{amine}} = 2 \cdot AHEW$. Therefore, a mixture with n_{amine} amine groups consists of curing agent of the mass $n_{\text{amine}} \cdot M_{\text{amine}}$ and epoxy resin of the

[1] This assumption serves only for facilitation and does not affect the result: If an amine group reacts with two DGEBA molecules that both do not react a second time, this removes one cross-link, but for each time this happens, another amine group will react once more, thus creating one cross-link, so that the total number of cross-links is unchanged.

mass $n_{EP} \cdot M_{EP} = 2/\lambda \cdot n_{amine} \cdot M_{amine}$, so its total mass is $n_{amine} \cdot (2/\lambda \cdot M_{EP} + M_{amine})$. The mixture's mass per cross-link M_c can hence be estimated to:

$$M_{c,D230}(\lambda) = \frac{6M_{EP} + 4\lambda \cdot AHEW}{9\lambda - 6} \tag{8.23}$$

and

$$M_{c,T403}(\lambda) = \frac{6M_{EP} + 6\lambda \cdot AHEW}{10\lambda - 6} \tag{8.24}$$

8.5.2 Plane-strain compression curves

Fig. 8.31 shows examples of stress–strain curves during PSC tests. The PEA-cured epoxies showed clear yielding and failed at significantly higher stresses and strains. EP/MTHPA–89 and EP/DETA–10 failed close to the presumable yield stress, so that their $\sigma_{y,PSC}$ is likely close to the actual yield stress. EP/DETA–11 failed even earlier, so that its $\sigma_{y,PSC}$ might underestimate its actual yield stress.

8.5.3 Mass density

Fig. 8.32 shows the mass densities ρ of the neat epoxy references. All sub-stoichiometric epoxy systems had a higher ρ than the stoichiometric ones cured with the same curing agent. This shows that the more highly cross-linked materials shrink less after post-curing and thus contain more free volume at room temperature, which in turn results in a lower E.

8.5.4 AFM images

Fig. 8.33 shows AFM images of fracture surfaces that were used to calculate the roughness parameters listed in the main article. Notably, the material that was successfully toughened, EP/D230–29, was that with the lowest roughness, the strongest fine structure and with the smallest secondary cracks.

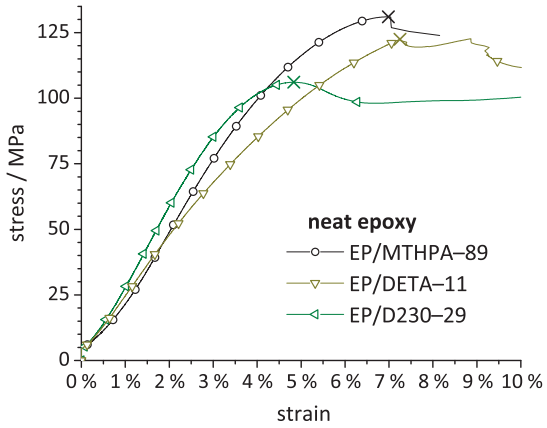

Figure 8.31: Examples of raw data from PSC tests. The crosses show which values were used for $\sigma_{y,PSC}$. While some materials failed before yielding (e.g., EP/DETA–11), $\sigma_{y,PSC}$ seems to reflect the actual yield stress reasonably well.

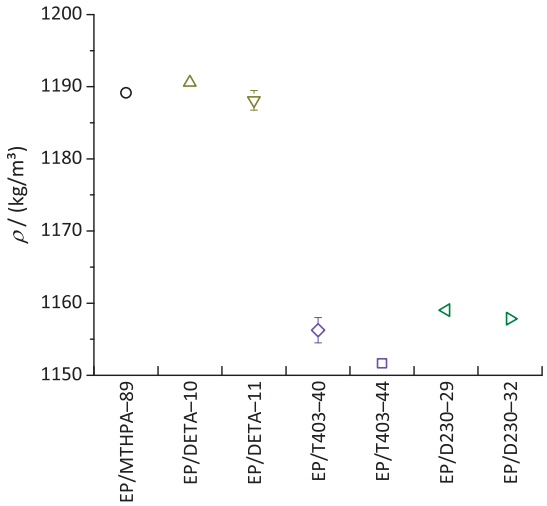

Figure 8.32: Mass densities ρ of neat epoxy references. Error bars are given only if they are larger then the symbols.

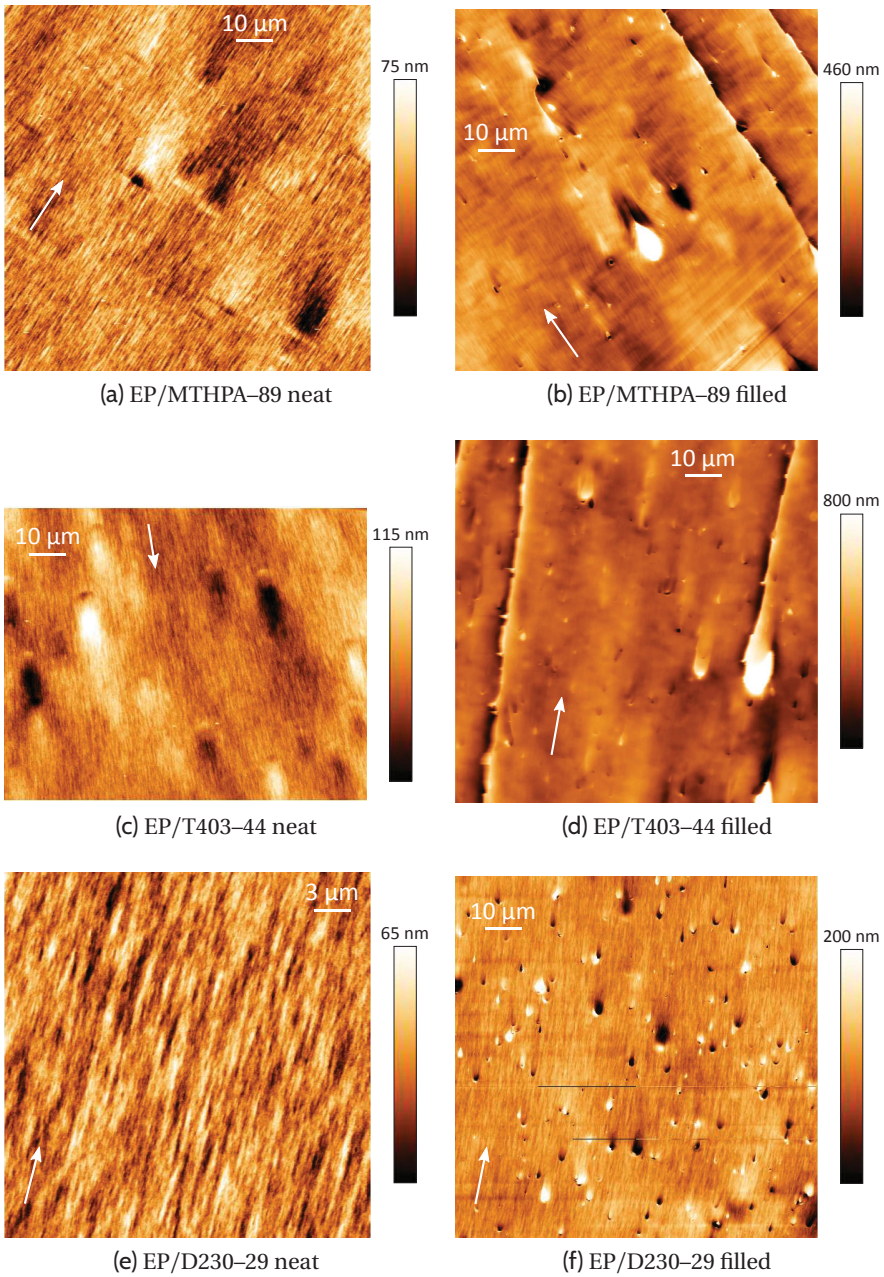

(a) EP/MTHPA–89 neat (b) EP/MTHPA–89 filled

(c) EP/T403–44 neat (d) EP/T403–44 filled

(e) EP/D230–29 neat (f) EP/D230–29 filled

Figure 8.33: AFM images of selected fracture surfaces. Filled systems contained 0.5 % of IF-WS_2 each. Arrows indicate the crack propagation direction.

8.5.5 ANOVA

The main article lists the most important ANOVA results. One of the key assumptions for a statistical analysis like that is that the ANOVA output data form a normal distribution around the predicted values. Fig. 8.34 shows a *normal probability plot*, indicating that the ANOVA data meet the requirements of a normal distribution.

8.5.6 Correlation of material properties

Fig. 8.35 shows the correlation of d_K with the K_{Ic}. While there is some trend that more brittle epoxy can be toughened more effectively than tough epoxy, once again the correlation is high only for the PEA-cured materials.

References

[1] D. Haba, M. Barbezat, S. Ayalur-Karunakaran, *et al.*, "Significance of epoxy network properties for the toughening effect of flaky and fullerene-like WS_2 nanoparticles", *J. Polym. Sci., Part B: Polym. Phys.*, vol. 54, no. 17, pp. 1738–1747, 2016. DOI: 10.1002/polb.24077.

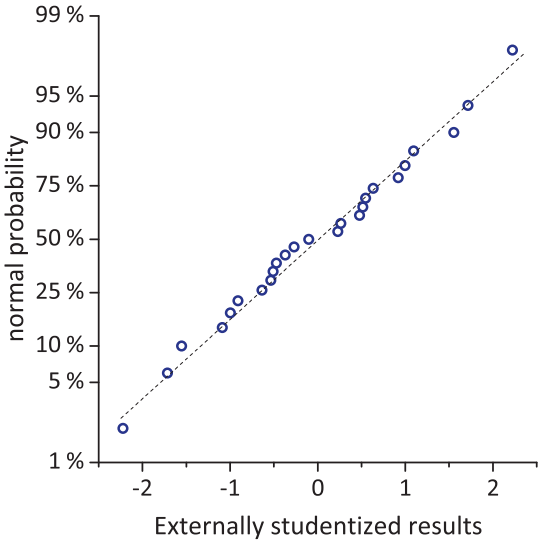

Figure 8.34: Normal probability plot of the ANOVA-modeled K_{Ic} data. When studentized according to the suggested model, the data fit the normal distribution nicely.

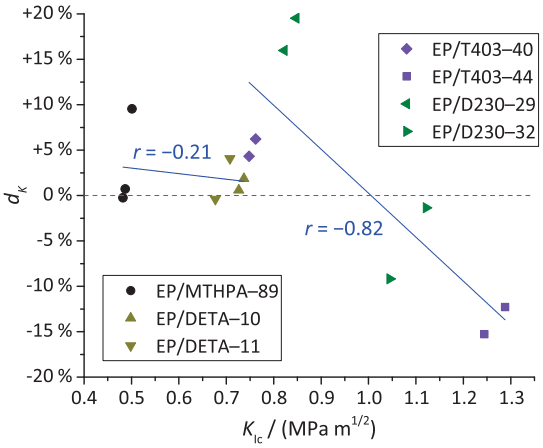

Figure 8.35: Fracture toughness change d_K over the fracture toughness K_{Ic}. The correlation is high ($r = -0.82$) if only PEA-cured epoxies are considered, but rather low for the entire data set.

List of Variables

$\langle \ldots \rangle$	average over all elements of the enclosed expression
A	(in chapters 1 and 5) area
A	(in section 8.3) distance between a crack and a NP at $t = 0$
A	(in section 8.4) molar fraction of component A
A_{surf}	surface area
A_{proj}	projected area
a	crack length
a_0	pre-crack length
b	width of an SENB specimen
B	(in section 8.4) molar fraction of component B
c	concentration
$2c$	(in chapter 1) mean inter-particle distance
$\hat{c}_{\text{v}}$	coefficient of variation
D	translational diffusion coefficient
d	(in chapter 1) particle diameter
d	(in chapter 2) tip–sample distance
d	(in chapter 3) average agglomerate diameter
d_A	change in surface area with respect to projected area
d_{def}	deformation ($= d_0 - d$)
d_K	change in $K_{\text{Ic}}$with respect to neat epoxy reference
D_{res}	residual dipolar coupling
e	Euler's number (2.71828…)
E, E_{t}	tensile Young's modulus
E'	storage modulus
E''	loss modulus
E^*	(in chapter 1) complex modulus
E^*	(in chapter 2) reduced modulus

E_r	rubber equilibrium modulus
E_s	sample Young's modulus
$\bar{E}_s$	mean Young's modulus in an image
f	(in chapter 1) fracture-mechanics geometry factor
f	(in section 8.4) molar fraction of one component
F	(in chapter 2) force
F	(in section 8.2) nominal initial concentration
F	(in chapter 6) F value calculated in an F test
F_{adh}	adhesion force
F_{peak}	peak force
G	strain-energy release rate
G_{Ic}	critical strain-energy-release rate
$h\nu$	radiation energy
k	spring constant of an AFM probe
K	dissociation constant
k_B	Boltzmann constant
K_I	stress-intensity factor
K_{Ic}	critical stress-intensity factor
m	ion mass
M_{amine}	mass of curing agent per amount of amine groups
M_{anh}	anhydride equivalent weight
m_{anh}	mass of anhydride curing agent
M_c	molecular mass per cross-link
$M_{c,D230}$	estimated molecular mass per cross-link for D230
$M_{c,DETA}$	estimated molecular mass per cross-link for DETA
$M_{c,MTHPA}$	estimated molecular mass per cross-link for MTHPA
$M_{c,T403}$	estimated molecular mass per cross-link for T403
M_{DETA}	molecular mass of DETA
M_{EP}	mass of DGEBA per amount of epoxide groups (i.e., EEW)
M_{NH2}	mass of curing agent per amount of amine groups

N	number of pixels in an image
n	(in chapter 1) number density
n	(in chapter 2) index of a pixel in an image
n	(in chapter 3) average number of particles per agglomerate
n_{aH}	amount of amine hydrogen atoms
n_{amine}	amount of amine groups
n_{anh}	amount of anhydride groups
n_{c}	amount of cross-links
n_{end}	final average number of particles per agglomerate
n_{EP}	amount of epoxide groups
n_{NH2}	amount of amine groups
p	p value calculated in a statistical significance test
q	ion charge
R	radius
r	sample Pearson correlation coefficient
$\underline{r}$	shape of a crack line
R_0	particle radius
R_{a}	average roughness
R_{rms}	root-mean-square roughness
r_{tip}	AFM tip radius
r'_{y}	plastic zone radius
S	chain dynamic order parameter (for details on S_{DQ}, S_{nDQ}, S_{ref}, $S_{\Sigma\mathrm{MQ}}$, S_{diff} and S_{defect} see section 8.4)
s	standard deviation
T	temperature
t	time
T_{g}	glass-transition temperature
$T_{\min(E)}$	temperature where the complex modulus is minimum in a DMA measurement
T_{post}	post-cure temperature

U	mechanical energy
U_b, $U_\mathrm{b,t}$	mechanical energy density at break in a tensile test
U_y, $U_\mathrm{y,t}$	mechanical energy density at yield in a tensile test
V	average agglomerate volume
v_s	velocity of the secondary crack
v_p	velocity of the primary crack
w	mass fraction
w	(in chapter 1 and section 8.4) width of a fracture mechanics specimen
W	relative curing agent quantity by mass
W_T403	relative quantity of T403 by mass
$\bar{x}_\mathrm{DLS}$	average particle diameter as measured via DLS
x_p	position of the primary crack
Z	height
α	ratio of current dispersion quality to final dispersion quality
Δ	difference
δ	loss angle
∂	partial derivative
ϵ, ϵ_t	engineering strain in a tensile test
ϵ_b	engineering strain at break
$\epsilon_\mathrm{m,t}$	maximum engineering strain in a tensile test
ϵ_y	engineering strain at yield
η	viscosity
η_p^2	measure for the effect size in an ANOVA
Θ	scatter angle
λ	ratio of amine hydrogen atoms to epoxide groups
ν	Poisson's ratio
π	circle number (3.14159…)
ρ	mass density
σ, σ_t	engineering stress in a tensile test

$\sigma_{m,t}$	maximum engineering stress in a tensile test
σ_y	engineering stress at yield
$\sigma_{y,PSC}$	yield stress measured in a plane-strain compression (PSC) test
σ_{yy}	nominal normal stress
τ	time constant
φ_p	particle volume fraction

List of Acronyms

The following table lists the acronyms used in the present work. It does not include trade names like *RTESPA*, company names like *BASF*, states like *USA*, SI units like MPa or chemical symbols like EtOH or WS_2. When chemical symbols are used in the work, they are used in a different font type in the text to facilitate their differentiation from the other acronyms.

1MI 1-methyl imidazole

3RM three-roll mill

AATMS 3-(2-aminoethylamino)propyltrimethoxysilane

AFM atomic force microscopy *or* atomic force microscope

AHEW amine hydrogen equivalent weight

ANOVA analysis of variance

ASA acrylonitrile–styrene–acrylate

ATR attenuated total reflection

CFRP C-fiber-reinforced polymer

D230 Jeffamine D-230

DETA diethylenetriamine

df degrees of freedom

DGEBA diglycidyl ether of bisphenol A

DLS dynamic light scattering

DMA dynamic mechanical analysis

DMT Derjaguin–Muller–Toporov

DOI digital object identifyer

DQ double-quantum

EEW epoxy equivalent weight

EP epoxy

ETD Everhart-Thornley detector

FRP fiber-reinforced polymer

GTMS 3-glycidoxypropyltrimethoxysilane

HTCS hexyltrichlorosilane

IF-WS_2 inorganic, fullerene-like WS_2

IPN inter-penetrating network

IR infrared

ISO International Organization for Standardization

LEFM linear-elastic fracture mechanics

MS mass spectroscopy

MS (in chapter 6) mean squares

MTHPA methyl-tetrahydrophthalic anhydride

NMR nuclear magnetic resonance

NP nanoparticle

NT nanotube

PEA polyetheramine

phr parts by mass per hundred parts of resin

PMMA polymethylmethacrylate

PS polystyrene

PSC plane-strain compression

PTFE polytetrafluoroethylene

SE secondary electron

SEM scanning electron microscope *or* scanning electron microscopy

SENB single-edge-notched bending

SI International System of Units

SS sum of squares

SSA specific surface area

T403 Jeffamine T-403

TEM transmission electron microscope *or* transmission electron microscopy

TGA thermogravimetric analysis

TG/MS thermogravimetric analysis with mass spectrometry

TLD through-the-lens detector

UP unsaturated polyester

UV/Vis ultraviolet–visible

XPS X-ray photoelectron spectroscopy

XRD X-ray diffraction

List of Figures

List of Tables